BULGARIAN CHEMICAL COMMUNICATIONS

Preface

The Second Crystallographic Symposium **(NCS'10)** was organized by the Faculty of Chemistry of Sofia University "St.Kl.Ohridski", under the aegis of the Bulgarian Crystallographic Society (**BCS**). In accordance with the resolutions of the First Crystallographic Symposium (**NCS'09**), the event scope was extended with international paticipation. The organizers of **NCS'10** invited leading researchers from abroad to inspire the interdisciplinary audience and attract young researchers to this important field of science. The invited speakers were Prof. Bernt Krebs (University of Münster, Germany), Prof. Mois Aroyo (University of the Basque Country, Bilbao, Spain), Prof. Boriana Mihailova (University of Hamburg, Germany), Prof. Ramiza Rastsvetaeva (Institute of Crystallography RAS, Moscow, Russia), Dr. Stanislav Ferdov (University of Minho, Portugal), and Dr. Milen Gateshki (Application Specialist, PANalytical).

Main purpose of the meeting was to create background for the crystallographic community in Bulgaria to meet and share knowledge and experience in modern crystallographic approaches of matter study achieved by scientists from national research institutes and universities in the fields of crystallography, crystal chemistry, crystal physics, mineralogy and materials science.

NCS'10 offered the opportunity for young scientists in various disciplines of Crystallography to present their research and exchange new ideas during the round table discussions. The most outstanding presentations from young scientists in all topics were awarded.

NCS'10 was organized with the assistance of University of Sofia – Faculty of Chemistry; Earth and Man Museum, Sofia; UNION project; Geological Institute – BAS; Institute of General and Inorganic Chemistry – BAS; Institute of Mineralogy and Crystallography – BAS. Invaluable help was received by our sponsors – PANalytical, TEAM OOD, Labexpert.

NCS'10 included three days of presentations and discussions, while giving the chance to see the crystal collection of "The Earth and Man National Museum" in Sofia at the same time. The Scientific program of the Second National Crystallographic Symposium was composed of Keynote invited lectures, Oral presentations and Poster session.

NCS'10 was attended by almost 100 participants from different institutes of Bulgarian Academy of Sciences, Sofia University, Plovdiv University, University of Mining and Geology and Bourgas University.

Reported were 22 oral presentations and 30 posters reflecting the recent state of the crystallographic studies in Bulgaria, including presentations of considerable number of young scientists.

The contributions presented at the Second National Crystallographic Symposium were given the opportunity to be published in a special issue of the Journal "**Bulgarian Chemical Communications**". The acceptance of the papers was based on the Journal's normal reviewing procedure with Guest editor Prof. Tony Spassov.

We very much hope that this issue representing the accepted full text papers reveals the high quality work of the Bulgarian crystallographers and is a good basis for provoking business interest in investment in production of high technological materials.

We are looking forward to successful organization of the Third National Crystallographic Symposium (http://bgcryst.com/symp11/) to be held in Sofia, October 3–5, Sofia.

Prof. Tony Spassov,

Guest editor of the special issue of the Journal Bulgarian Chemical Communications.

Crystallography online: Bilbao Crystallographic Server

M. I. Aroyo[1]*, J. M. Perez-Mato[1], D. Orobengoa[1], E. Tasci[1], G. de la Flor[1], A. Kirov[2]

[1] Depto. Fisica de la Materia Condensada, Universidad del Pais Vasco, 48040 Bilbao, Spain
[2] Condensed Matter Department, Sofia University, 15064 Sofia, Bulgaria

The *Bilbao Crystallographic Server* is a web site with crystallographic databases and programs available online (www.cryst.ehu.es). It has been operating for more than ten years and new applications are being added regularly. The programs available on the server do not need a local installation and can be used free of charge. The server gives access to general information related to crystallographic symmetry groups (generators, general and special positions, maximal subgroups, Brillouin zones, etc.). Apart from the simple tools for retrieving the stored data, there are programs for the analysis of group-subgroup relations between space groups. There are also software package studying specific problems of solid-state physics, structural chemistry and crystallography.

Key words: Bilbao Crystallographic Server, crystallographic symmetry, online tools.

1. INTRODUCTION

The *Bilbao Crystallographic Server* is a web site with crystallographic databases and programs available online. The server has been operating since 1998, and new programs and applications are being added regularly [23, 2, 3]. The programs available on the server do not need a local installation and can be used free of charge. The only requirement is an Internet connection and a web browser. The *Bilbao Crystallographic Server* is accessible at www.cryst.ehu.es.

The server is built on a database core, and contains different shells. The set of databases includes data from *International Tables for Crystallography*, Vol. A: Space-group symmetry (hereafter referred to as *IT*A)[12], and the data on maximal subgroups of space groups as listed in Part 1 of *International Tables for Crystallography*, Vol. A1: Symmetry relations between space groups (hereafter referred to as *IT*A1)[13]. There is an access to the crystallographic data for the subperiodic layer and rod groups (*International Tables for Crystallography*, Vol. E: Subperiodic groups [14]) and their maximal subgroups. A database on incommensurate structures incorporating modulated structures and composites, and a **k**-vector database with Brillouin-zone figures and classification tables of the wave vectors for all space groups are also available.

The innermost shell is formed by simple retrieval tools which serve as an interface to the databases. They allow the access to the information on space groups or subperiodic groups in different types of formats: HTML, text ASCII or XML. The second shell contains applications which are essential for problems involving group-subgroup related space groups $G > H$ (supergroups of space groups, chains of maximal subgroups relating G and H, splittings of Wyckoff positions for group-subgroup pairs). Then, follows a shell with programs on representations of point and space groups including the computation of spacegroup representations, their correlations for $G > H$, etc. Parallel to the crystallographic software a shell with programs facilitating the study of specific problems related to solid-state physics, structural chemistry and crystallography is also developed. For example, the program PSEUDO provides an online tool for systematic pseudosymmetry search based on group-subgroup relations between space groups. The detection of pseudosymmetry can be very useful in predicting phase transitions, including the identification of ferroic materials or the detection of false symmetry assignments in crystal structure determination [11, 21, 22]. The performance and efficiency of the program has been greatly improved by including a powerful cross-check of Wyckoff compatibility relations of the possible high-symmetry structures [9]. The automatic symmetry-mode analysis done by AMPLIMODES can be very useful for establishing the driving mechanisms of structural phase transi-

tions or the fundamental instabilities at the origin of the distorted phases [25, 26]. Given the high- and the low-symmetry structure the program determines the atomic displacements that relate them, defines a basis of symmetry-adapted modes, and calculates the amplitudes and polarization vectors of the distortion modes of different symmetry frozen in the structure. In that shell one can also find a computer program that calculates the phonon extinction rules for inelastic neutron scattering experiments. Given the space group and the phonon symmetry specified by the wave vector, NEUTRON [17] examines the inelastic neutron scattering activity of the corresponding phonons for all possible types of scattering vectors. The systematic selection rules are also useful in the interpretation of the results of thermal diffuse scattering.

The aim of the present contribution is to report on the different databases and basic programs of the server related to the crystallographic groups, their group-subgroup relations and representations. Part of these databases and programs have been already described in [2, 3], and here we follow closely these presentations. They are completed by the description of the new developments until 2010. The presentation of the relevant databases and retrieval tools that access the stored crystallographic symmetry information is given in Section 2. The discussion of the accompanying applications related to group-subgroup and group-supergroup relations between space groups can be found in Section 3. The Section 4 introduces the basic programs for representations of crystallographic groups available on the Bilbao Crystallographic Server.

2. SPACE-GROUPS DATABASES AND RETRIEVAL TOOLS

The databases form the core of the Bilbao Crystallographic Server and the stored information is used by all computer programs available on the server. The space-group database includes information on the following symmetry items: generators and representatives of the general position of each space group specified by its *IT*A number and Hermann-Mauguin symbol; special Wyckoff positions including the Wyckoff letter, Wyckoff multiplicity, the site-symmetry group and the set of coset representatives, as given in *IT*A; the Reflection conditions including the general and special conditions. The programs and databases of the Bilbao Crystallographic Server use specific settings of space groups (hereafter referred to as standard or default settings) that coincide with the conventional space-group descriptions found in *IT*A. For space

groups with more than one description in *IT*A, the following settings are chosen as standard: unique axis b setting, cell choice 1 for monoclinic groups, hexagonal axes setting for rhombohedral groups, and origin choice 2 (origin in $\bar{1}$) for the centrosymmetric groups listed with respect to two origins in *IT*A. The data from the databases can be accessed using the simple retrieval tools that use as input the number of the space group (*IT*A numbers). There is also a possibility to select the group from a table with *IT*A numbers and Hermann-Mauguin symbols. The output of the program GENPOS contains the list with the generators or the general positions and provides the possibility to obtain the same data in different settings either by specifying the transformation matrix to the new basis or selecting one of the 530 settings listed in Table 4.3.2.1 of *IT*A. The list with the Wyckoff positions for a given space group in different settings can be obtained using the program WYCKPOS. The Wyckoff-position representatives for the non-standard settings of the space groups are specified by the transformed coordinates of the representatives of the corresponding default settings. The program NORMALIZER gives access to the data on the Euclidean and affine normalizers of space groups (*cf.* Part 15 of *IT*A) specified by a set of coset representatives of their decomposition with respect to the space groups. The assignments of the Wyckoff positions to Wyckoff sets are retrieved by the program WYCKSETS (*cf.* Table 14.2.3.2 of *IT*A).

2.1. Database on maximal subgroups

All maximal non-isomorphic subgroups and maximal isomorphic subgroups of indices 2, 3 and 4 of each space group can be retrieved from the database using the program MAXSUB[1]. Each subgroup *H* is specified by its *IT*A number, the index in the group *G* and the transformation matrix-column pair (P, p) that relates the default bases **a′**, **b′**, **c′** of *H* and **a**, **b**, **c** of *G*:

$$(\mathbf{a'}, \mathbf{b'}, \mathbf{c'}) = (\mathbf{a}, \mathbf{b}, \mathbf{c})\, \boldsymbol{P} \qquad (2.1.1)$$

The column $\boldsymbol{p} = (p_1, p_2, p_3)$ of coordinates of the origin O_H of *H* is referred to the coordinate system of *G*.

The different maximal subgroups are distributed in classes of conjugate subgroups. For certain applications it is necessary to represent the subgroups *H* as subsets of the elements of *G*. This is achieved by an option in MAXSUB which transforms the gener-

---

[1] A subgroup $H < G$ is maximal if no subgroup Z exists for which $H < Z < G$ holds.

al-position representatives of *H* by the corresponding matrix-column pair $(\boldsymbol{P}, \boldsymbol{p})^{-1}$ to the coordinate system of *G*. A link provides the splittings of all Wyckoff positions of *G* with respect to those of *H*.

Maximal subgroups of index higher than 4 have indices p, p^2 or p^3, where p is a prime. They are isomorphic subgroups and are infinite in number. In *IT*A1 the isomorphic subgroups are listed not individually but as members of series under the heading 'Series of maximal isomorphic subgroups'. The program SERIES provides the access to the database of maximal isomorphic subgroups of the *Bilbao Crystallographic Server*. Apart from the parametric *IT*A1 descriptions of the series, its output provides the individual listings of all maximal isomorphic subgroups of indices as high as 27 for all space groups except for the cubic ones where the index is 125. The format and content of the subgroup data are similar to those of MAXSUB access tool. In addition, there is a special tool (under 'define a maximal index' on the SERIES web form) that permits the online generation of maximal isomorphic subgroups of any index up to 131 for all space groups. (Note that these data are only online generated and do not form part of the (static) database on isomorphic subgroups.)

2.2. Subperiodic groups

Recently, we have started with the development of a database for the subperiodic groups with symmetry information as listed in *International Tables for Crystallography* Vol. E: Subperiodic Groups [14]. For the moment the *Bilbao Crystallographic Server* provides a free online access to a database for the layer and rod groups including generators, general and special positions. The structure of this database and the retrieval programs are similar to the *IT*A database. In addition, the complete information on maximal subgroups of layer groups [5] and rod groups is made available: Similar to the *IT*A1 database, all maximal non-isotypic subgroups as well as maximal isotypic subgroups of index 2, 3 and 4 are listed individually. The conjugacy relations of the subgroups in the original group are indicated. The transformation to the conventional coordinate system of the subgroup is available as a 3×3 matrix for the change of basis and a column for the origin shift. Each subgroup can be further specified by its general-position representatives referred to the basis of the group. The symmetry information has been stored in a provisional CIF-format. For the extension of the existing CIF-core dictionary a list of data names has been developed which refer to the specific requirements of the subgroup tables of the layer groups.

2.3. Brillouin zones and wave-vectors classification

The determination, classification, labeling and tabulation of irreducible representations (irreps) of space groups is based on the use of wave vectors **k**. The **k**-vector database available on the *Bilbao Crystallographic Server* contains figures of the Brillouin zones and tables which form the background of a classification of the irreps of all 230 space groups. In this compilation the symmetry properties of the wave vectors are described by the so-called reciprocal-space groups which are isomorphic to symmorphic space groups [27], see also [4]. This isomorphism allows the application of crystallographic conventions in the classification of the wave vectors (and henceforth in the irreps of the space groups). For example, the different symmetry types of **k**-vectors correspond to the different kinds of point orbits (Wyckoff positions) in the symmorphic space groups; the unit cells with the asymmetric units given in *IT*A can serve as Brillouin zones and representation domains, *etc*. The advantages of the reciprocal-space group approach compared to the traditional schemes of wave-vector classification can be summarized as follows:

• The asymmetric units given in *IT*A serve as representation domains which are independent of the different shapes of the Brillouin zones for different ratios of the lattice parameters.

• For the non-holohedral groups the representation domain is obtained from that of the corresponding holohedral group by extending the parameter ranges, not by introducing differently labeled special wave vector points, lines or planes of symmetry.

• A complete list of the special sites in the Brillouin zone is provided by the Wyckoff positions of *IT*A. The site symmetry of *IT*A corresponds to the little co-group of the wave vector; the number of branches of the star of the wave vector follows from the multiplicity of the Wyckoff position.

• All wave-vector stars giving rise to the same type of irreps are related to the same Wyckoff position and designated by the same Wyckoff letter.

The available figures and the wave-vector data based on the reciprocal-space group symmetry are compared with the representation domains and the k-vector tables of the widespread tables of space-group representations by Cracknell, Davies, Miller and Love [10] (hereafter referred to as CDML). The retrieval tool KVEC of the k-vector database uses as input the *IT*A-number of the space group. The output contains wave-vector tables and figures. There are several sets of figures and tables for the same space group when its Brillouin-zone shape depends on the lattice parameters of the reciprocal lattice. The

k-vector data are the same for space groups of the same arithmetic crystal class.

In the tables, the **k**-vector data as listed by CDML are compared with the Wyckoff-position description as given in *ITA*. Each **k**-vector type is specified by its label and coordinates as listed in CDML. The corresponding Wyckoff positions are described by their Wyckoff letters, multiplicities, and site symmetry groups. Their parameter description contains also the parameter ranges chosen in such a way that each orbit of the Wyckoff position of *ITA*, *i.e.* also each **k**-orbit, is listed *exactly once*. No ranges for the parameters are listed in CDML. Symmetry points, lines of symmetry or planes of CDML which are related to the same Wyckoff position are grouped together. The wave-vector coordinates of CDML refer always to primitive basis irrespective whether the conventional description of the space group is with respect to a centred or primitive basis. For that reason, in the case of space groups with centred lattices the wave-vector coordinates with respect to a basis that is dual to the conventional basis in direct space are also included in the tables. (For space groups with primitive lattices, the wave-vector coordinates referred to a primitive basis coincide with those referred to the dual basis.)

An additional tool allows the complete characterization of any wave vector of the reciprocal space (not restricted to the first Brillouin zone): given the **k**-vector coordinates referred either to primitive

(CDML) or conventional dual basis, the program assigns the **k**-vector to the corresponding wave-vector symmetry type, specifies its CDML label, calculates the little co-group and the arms of the **k**-vector stars. In the figures, the Brillouin zones of CDML and the conventional unit cells of *ITA* are displayed. The asymmetric units play the role of the representation domains of the Brillouin zones and they are chosen often in analogy to those of *ITA*. The names of **k**-vector points, lines, and planes of CDML are retained in this listing. New names have been given only to points and lines which are not listed in CDML.

Example: Brillouin zones and special k-vectors of the arithmetic crystal class $\overline{4}m2I$. The following example illustrates the relation between the traditional and the reciprocal-space group descriptions of the wave-vector types of space-group irreps. The included figures and tables form part of the output of the access tool KVEC.

The are two space groups belonging to the arithmetic crystal class $\overline{4}m2I$: $I\overline{4}m2 - D_{2d}^9 (119)$ and $I\overline{4}c2 - D_{2d}^{10}(120)$. The **k**-vector types of that arithmetic crystal class are described with respect to the corresponding reciprocal space group which is isomorphic to $I\overline{4}2m(121)$. Depending on the relations between the lattice constants a, b and c, there are two topologically different bodies of the Brillouin
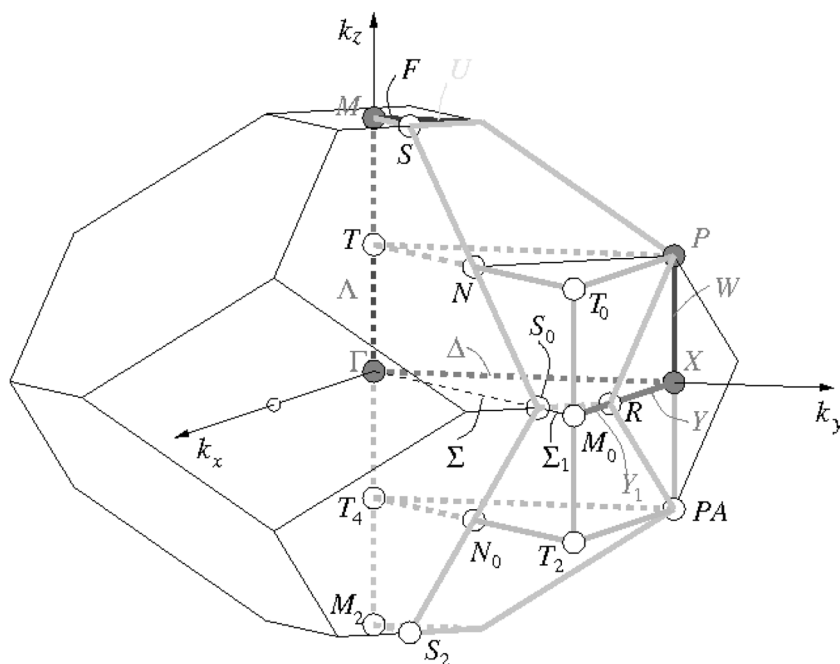
Fig. 1. Brillouin zone, asymmetric unit and representation domain of CDML for the arithmetic crystal class $\overline{4}m2I : c > a$: space groups $I\overline{4}m2 - D_{2d}^9 (119)$ and $I\overline{4}m2 - D_{2d}^{10}(120)$; reciprocal-space group $I\overline{4}2m^*$, No. 121: $c^* < a^*$. The representation domain of CDML is different from the asymmetric unit.

zone displayed in Fig. 1 and Fig. 2 by thin black lines; the first one has 24 vertices, 48 lines and 14 faces, the other has 18 vertices, 28 lines and 12 faces. The shape of the unit cell of *IT*A is always a parallelepipedon with 8 vertices, 12 edges and 6 faces. Similarly, the representation domains of CDML are more complicated than the asymmetric units of *IT*A, see Fig. 1 and Fig. 2.

The representatives of the **k**-vectors symmetry points or of symmetry lines, as well as the edges of the representation domain of CDML and of the chosen asymmetric unit are brought out in colors. A **k**-vectors symmetry point is designated by a red or cyan if it belongs to the asymmetric unit or to the representation domain of CDML. Points listed by CDML are not colored if they are part of a symmetry line or symmetry plane only. The color of the line is pink for an edge of the asymmetric unit which is not a symmetry line and it is red for a symmetry line of the asymmetric unit. The color of the line is brown with the name in red for a line which is a symmetry line as well as an edge of the asymmetric unit. The edges of the representation domains of CDML (displayed in the same figure) are colored in light blue. The corresponding symmetry points and lines are colored cyan. Edges of the representation domain or common edges of the representation domain and the asymmetric unit are colored dark blue with the letters in cyan if they are symmetry

lines of the representation domain but not of the asymmetric unit. To save space we have included only part of the list of k-vector relations for the arithmetic class $\bar{4}m2I$ in the table shown in Fig. 3 (a screen-shot of the output of the access tool KVEC), corresponding to Fig. 1. The **k**-vector parameters of CDML (second column) of the table in Fig. 3 are different from those of *IT*A (last column) because in CDML the data are always referred to a primitive basis, whereas in *IT*A they are referred to a centered basis. The parameter ranges (last column) are chosen such that each k-vector orbit is represented exactly once.

One takes from the table given in Fig. 3 that different k labels of CDML (first column) may correspond to the same Wyckoff position may belong to the same type of **k** vectors, *i. e.* may belong to the same type of **k** and they give rise to the same type of irreps. Due to the special shape of the representation domain of CDML the special wavevector line corresponding to the Wyckoff position 8 *i* (..m) (fourth column) is split into two parts, *SM* and *F*. In the *IT*A description $SM \cup F$ corresponds to one line $[GMM_0]$, $(x, x, 0)$, with $0 < x < 1/2$. The splitting of the 8 *i* line into two parts is a consequence of the Brillouin-zone shape for the specific values of the lattice parameters. This is confirmed from Fig. 2 where the corresponding special line *SM* is not split.
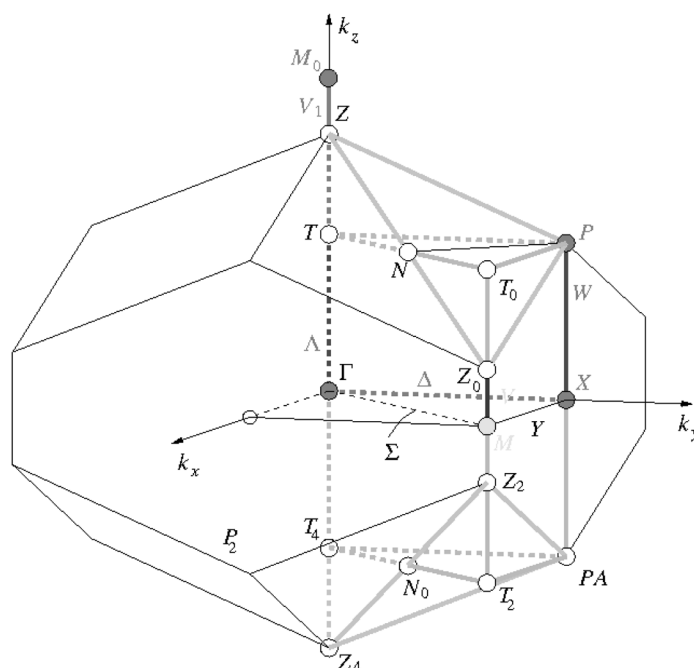
Fig. 2. Brillouin zone, asymmetric unit and representation domain of CDML for the arithmetic crystal $\bar{4}m2I$: $c < a$: space groups $I\bar{4}m2 - D_{2d}^9$ (119) and $I\bar{4}c2 - D_{2d}^{10}$ (120) ; reciprocal-space group $I\bar{4}2m^*$, No. 121: $c^* > a^*$. The representation domain of CDML is different from the asymmetric unit.

k-vector description			Wyckoff Position		ITA description	
CDML*		Conventional-ITA	ITA		Coordinates	
Label	Primitive					
GM	0,0,0	0,0,0	a	2	-42m	0,0,0
M	1/2,1/2,-1/2	0,0,1	b	2	-42m	0,0,1/2
X	0,0,1/2	1/2,1/2,0	c	4	222.	0,1/2,0
P	1/4,1/4,1/4	1/2,1/2,1/2	d	4	-4..	0,1/2,1/4
LD	u,u,-u	0,0,2u	e	4	2.mm	0,0,z : 0 < z < 1/2
DT	0,0,u	u,u,0	f	8	.2.	0,y,0 : 0 < y < 1/2
Y	-u,u,1/2 ex	1/2+u,1/2-u,0	g	8	.2.	x,1/2,0 : 0 < x <= r
U	1/2,1/2,-1/2+u ex	u,u,1	g	8	.2.	0,y,1/2 : 0 < y < g=1/2-r
U~Y$_1$=[R M$_0$]			g	8	.2.	x,1/2,0 : r < x < 1/2
Y+Y$_1$			g	8	.2.	x,1/2,0 : 0 < x < 1/2
W	u,u,1/2-u	1/2,1/2,2u	h	8	2..	0,1/2,z : 0 < z < 1/4
N	0,1/2,0 ex	1/2,0,1/2	i	8	..m	1/4,1/4,1/4
SM	-u,u,u ex	2u,0,0	i	8	..m	x,x,0 : 0 < x <= s$_1$
F	1/2-u,1/2+u,-1/2+u ex	2u,0,1	i	8	..m	x,x,1/2 : 0 < x < s=1/2-s$_1$
F~SM$_1$=[S$_0$ M$_0$]			i	8	..m	x,x,0 : s$_1$ < x < 1/2
SM+SM$_1$=[GM M$_0$] ex			i	8	..m	x,x,0 : 0 < x < 1/2

Fig. 3. List of **k**-vector symmetry types (selection) for the arithmetic crystal class $\bar{4}m2I$: $c > a$: space groups $I\bar{4}m2 - D_{2d}^9$ (119) and $I\bar{4}c2 - D_{2d}^{10}$ (120); reciprocal-space group $I\bar{4}2m^*$, No. 121 (*cf.* Fig. 1).

3. GROUP-SUBGROUP RELATIONS OF SPACE GROUPS

3.1. Subgroups of space groups

If two space groups G and H form a group–subgroup pair $G > H$, it is always possible to represent their relation by a chain of intermediate maximal subgroups Z_k: $G > Z_1 > \cdots > Z_n = H$. For a specified index of H in G there are, in general, a number of possible chains relating both groups, and a number of different subgroups $H_j < G$ isomorphic to H. We have developed two basic tools for the analysis of the group–subgroup relations between space groups: SUBGROUPGRAPH [15], and HERMANN [8]. Given the space-group types G and H, and an index [i], both programs determine all different subgroups H_j of G with the given index, and their distribution into classes of conjugate subgroups with respect to G. Due to its importance in a number of group–subgroup problems, the program COSETS is included as an independent application. It performs the decomposition of a space group in cosets with respect to one of its subgroups. Apart from these basic tools, there are two complementary programs which are useful in specific crystallographic problems that involve group–subgroup relations between space groups.

The program CELLSUB calculates the subgroups of a space group for a given multiple of the unit cell. The common subgroups of two or three space groups are calculated by the program COMMONSUBS. In the following we will consider in more details the program SUBGROUPGRAPH which is the main program for the study of the group-subgroup relations between space groups. For a description of the rest of the programs of the group-subgroup shell the reader is referred to Ref. [2].

3.1.1. The program SUBGROUPGRAPH

The program is based on the data for the maximal non-isomorphic subgroups of index 2, 3 and 4 and isomorphic subgroups of indices up to 9 of the space groups. These data are transformed into a graph with 230 vertices corresponding to the 230 space-group types. If two vertices in the graph are connected by an edge, the corresponding space groups form a group–maximal-subgroup pair.

The specification of the group–subgroup pair $G > H$ leads to a reduction of the total graph to a subgraph with G as the top vertex and H as the bottom vertex, see the example at the end of this subsection. In addition, the $G > H$ subgraph, referred to as the general $G > H$ graph, contains all possible groups Z_k which appear as intermediate maximal

subgroups between *G* and *H*. It is important to note that in the general *G* > *H* graphs the space-group symbols indicate space-group types, *i.e.* all space groups belonging to the same space-group type are represented by one node on the graph. Such graphs are called *contracted*. The contracted graphs have to be distinguished from the *complete* graphs where all space groups occurring in a group–subgroup graph are indicated by different space-group nodes.

The number of the vertices in the general *G* > *H* graph may be further reduced if the index of *H* in *G* is specified. The obtained subgraph is again of contracted type. For the cases of specified indices, the program SUBGROUPGRAPH produces also complete graphs that are equal for subgroups of a conjugacy class; the different orientations and/ or origin shifts of the conjugate subgroups Hs are manifested by the different transformation matrices $(\boldsymbol{P}, \boldsymbol{p})_s$ listed by the program.

Input Information

- The space groups *G* and *H* can be introduced by their *ITA* numbers or by their Hermann-Mauguin symbols chosen from a list provided by the program.
- The index of *H* in *G* is optional.

Output Information

- Group-subgroup pair *G* > *H* with non-specified index.

1. The list of the possible intermediate space groups Z_k relating *G* and *H*.

2. A contracted graph.

Each space-group type in the list corresponds to one node in the graph, and the maximal subgroups are the neighbors (successors) of this node. Group–subgroup relations occurring in both directions are represented by nodes connected by two lines with opposite arrows. Maximal isomorphic subgroups are shown by loop edges (nodes connected to themselves), *cf*. Fig. 4.

- Group-subgroup pair *G* > *H* with specified index

1. A list with all possible chains of maximal subgroups relating *G* and *H* with this index. (The program has no access to the data on maximal isomorphic subgroups with indices higher than 9).

2. The graphical representation.

The graphical representation contains the intermediate groups that connect *G* and *H* with the specified index. This graph is a subgraph of the general graph of maximal subgroups with unspecified index and is also of contracted type.

For a given index of *H* in *G*, the different subgroups H_j of that index are calculated and distributed into classes of conjugate subgroups of *G*. The subgroups of a conjugacy class form a block where each subgroup is specified by the corresponding transformation matrix-column pair $(\boldsymbol{P}, \boldsymbol{p})_j$ that relates the default bases of *G* and H_j. There is also a link to a list of the elements of the subgroups transformed to the basis of the group *G*, which allows the identification of those elements of *G* that are retained in the subgroup. The list of transformation

Fig. 4. General contracted graph for *P*622 (No. 177) > *C*2 (No. 5) as given by the program SUBGROUPGRAPH. The nodes of the graph correspond to the space-group types that can appear as intermediate groups in the chain of the group-subgroup pair *P*622 > *P*2. Each edge of the graph corresponds to a maximal subgroup pair of the indicated index [*i*]. Isomorphic subgroups (of indices up to 7) are shown as loops.

matrices that give the same (identical) subgroup is accessible under a separate link (*cf.* Fig. 7).

The graph contains the intermediate space groups Z_k for the pair $G > H$ but contrary to the graph of the previous step, the different isomorphic subgroups are represented by different nodes, *i.e.* the graph is a complete one. All isomorphic subgroups H_j are given at the bottom of the graph. Their labels are formed by the symbol of the subgroup followed by a number given in parenthesis which specifies the class of conjugate subgroups to which the subgroup H_j belongs.

Note that for group–subgroup pairs with high indices, where a lot of intermediate maximal subgroups occur, the resulting complete graph with all subgroups H_j can be very complicated and difficult to overview. Alternatively, a more simple graph associated to a single specific subgroup H_j (identical for all subgroups within a conjugacy class) can also be obtained.

Example: Consider the group–subgroup relations between the groups $G = P622$, No. 177, and $H = C2$, No. 5. If no index is specified then the graph of maximal subgroups that relates $P622$ and $C2$ is represented as a table indicating the space-group types of the possible intermediate space groups Z_k, and the corresponding indices. The contracted general $P622 > C2$ graph is shown in Fig. 4. Two edges with opposite arrows between a group–subgroup pair correspond to group–subgroup relations in both directions, *e.g.*, the pair $P62$ and $P64$. When the index $[i]$ of the subgroup in the group is specified, the resultant graph is reduced to the chains of maximal subgroups that correspond to the value of $[i]$. For example, in Fig. 5 the contracted graph $P622 > C2$
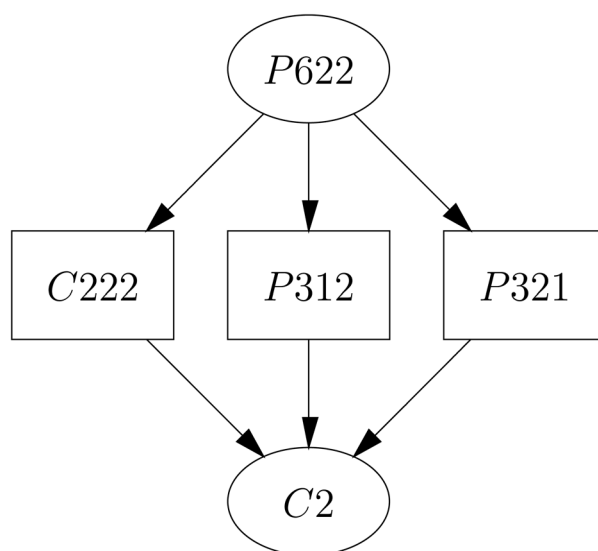
Fig. 5. Contracted graph for $P622$ (No. 177) > $C2$ (No. 5), index 6, as given by the program SUBGROUPGRAPH. The nodes of the graph correspond to space-group types. Each edge of the graph corresponds to a maximal subgroup pair.

of index 6 is shown. The data in Fig. 7 and the complete graph shown in Fig. 6 indicate that there are six different $C2$ subgroups of $P622 > C2$ of index 6, distributed in two classes of conjugate subgroups. One of the conjugacy classes consists of the three different subgroups of space-group type $C2$ whose twofold axes point along $[1\bar{1}0]$, $[120]$ and $[\bar{2}\bar{1}0]$ of $P622$. The other three subgroups with two-fold axes along $[100]$, $[010]$ and $[\bar{1}\bar{1}0]$ of $P622$ give rise to the second class of conjugate subgroups. The cor-
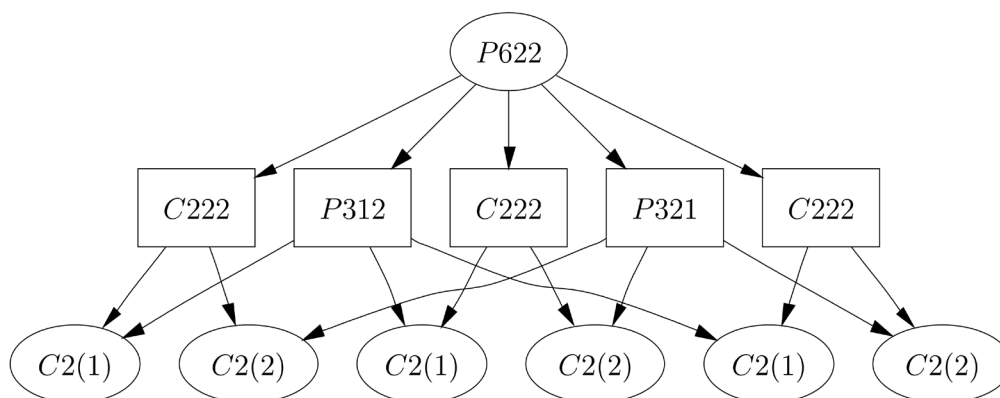
Fig. 6. Complete graph for $P622$ (No. 177) > $C2$ (No. 5), index 6, as given by the program SUBGROUPGRAPH. The nodes represent space groups and not space-groups types. The six subgroups of the type $C2$ are distributed into two classes of conjugate subgroups which are indicated in the parentheses after the space-group symbol. The three subgroups $C2(1)$ with twofold axes along $[1\bar{1}0]$, $[120]$ and $[\bar{2}\bar{1}0]$ of $P622$ belong to the same conjugacy class. They have equal complete single graphs, which differ from the graph of the subgroups $C2(2)$ of the second conjugacy class. The latter corresponds to subgroups whose twofold axes point along $[100]$, $[010]$ and $[\bar{1}\bar{1}0]$ of $P622$.

Class 1

N	Chain [indices]	Chain with HM symbols	Transformation	Transform with	Identical
1	177 021 005 [3 2]	$P622 > C222 > C2$	$\begin{pmatrix} -1 & -1 & 0 & 0 \\ 0 & -2 & 0 & 0 \\ 0 & 0 & 1 & 0 \end{pmatrix}$	matrix 1	to group 1
2	177 021 005 [3 2]	$P622 > C222 > C2$	$\begin{pmatrix} 0 & 2 & 0 & 0 \\ -1 & 1 & 0 & 0 \\ 0 & 0 & 1 & 0 \end{pmatrix}$	matrix 2	to group 2
3	177 021 005 [3 2]	$P622 > C222 > C2$	$\begin{pmatrix} -1 & 1 & 0 & 0 \\ -1 & -1 & 0 & 0 \\ 0 & 0 & 1 & 0 \end{pmatrix}$	matrix 3	to group 3

Class 2

N	Chain [indices]	Chain with HM symbols	Transformation	Transform with	Identical
4	177 150 005 [2 3]	$P622 > P321 > C2$	$\begin{pmatrix} 2 & 0 & 0 & 0 \\ 1 & 1 & 0 & 0 \\ 0 & 0 & 1 & 0 \end{pmatrix}$	matrix 4	to group 4
5	177 021 005 [3 2]	$P622 > C222 > C2$	$\begin{pmatrix} 1 & 1 & 0 & 0 \\ -1 & 1 & 0 & 0 \\ 0 & 0 & 1 & 0 \end{pmatrix}$	matrix 5	to group 5
6	177 021 005 [3 2]	$P622 > C222 > C2$	$\begin{pmatrix} -1 & 1 & 0 & 0 \\ -2 & 0 & 0 & 0 \\ 0 & 0 & 1 & 0 \end{pmatrix}$	matrix 6	to group 6

Fig. 7. Screen-shot of the list of the six subgroups $C2$ (No. 5) of $P622$ (No. 177), index 6, as given by the program SUBGROUPGRAPH. The subgroups $(C2)_j, j = 1, \ldots, 6$ are distributed in two conjugacy classes and each subgroup is specified by its transformation matrix $(\boldsymbol{P}, \boldsymbol{p})_j$.

responding transformations can be read from the screen-shot table shown in Fig. 7. (Note that the standard setting for $C2$ is the UNIQUE AXIS b setting.) The complete graph $P622 > C2$, index 6 (Fig. 6), also shows that there are two different maximal subgroup chains to each subgroup $C2$. The subgroups of a conjugacy class have the same complete single graphs, while the complete graphs of subgroups of different conjugacy classes differ in general.

3.2. Supergroups of space groups

The problem of the determination of the supergroups of a given space group is of rather general interest. For several applications it is not sufficient to know only the space-group types of the supergroups of a given group; it is necessary to have available all different supergroups $G_r > H$ which are isomorphic to G, and are of the same index $[i]$. In the literature there are few papers treating the supergroups of space groups in detail [18, 29]. In *ITA* one finds only listings of minimal supergroups of space groups which, in addition, are not explicit:

they only provide for each space group H the list of those space-group types in which H occurs as a maximal subgroup (*cf*. Section 2.1). It is not trivial to determine all supergroups $G_r > H$ if only the types of the minimal supergroups are known. The Bilbao Crystallographic Server offers two basic programs [16] that solve that problem for a given finite index $[i]$: (i) the program MINSUP, which gives all minimal supergroups of indices 2, 3, 4, 5, 7 and 9 of a given space group; and (ii) the program SUPERGROUPS, which calculates all different supergroups of a given space-group type and a given index. Similar to the case of subgroups, we have developed two complementary programs that involve the calculation of supergroups of space groups. The program CELLSUPER calculates the supergroups of a space group for a given $[i_L]$ index, while the program COMMONSUPER is for the computation of common supergroups of two or more space groups.

The following discussion concerns the two basic programs MINSUP and SUPERGROUPS. For details on the complementary programs for group-su-

pergroup relations between space groups the reader is referred to Ref. [2].

3.2.1. The programs MINSUP and SUPERGROUPS

The determination of all supergroups G_r of a given space-group type G and an index [i] of a space group H can be done by inverting the data on the subgroups H_s of G of index [i]. For that it is first necessary to determine all subgroups $H_s < G$ of the same index and distribute them into classes of conjugate subgroups with respect to G. It is sufficient to choose a representative H_r from each class of conjugate subgroups, specified by $(\boldsymbol{P}, \boldsymbol{p})_r$, and apply $(\boldsymbol{P}, \boldsymbol{p})_r^{-1}$ to the group G in order to obtain the supergroup G_r. Further supergroups may be generated by the coset representatives of the decomposition of $N_A(H)$ relative to $(N_A(H) \cap N_A(G))$. In order to obtain all supergroups of a given space group type and index it is sufficient to apply the procedure to one representative of each class of conjugate subgroups $H_s < G$ of index [i].

Input Information of MINSUP

• The *IT*A number (or the Hermann-Mauguin symbol) of the group for which the minimal supergroups have to be determined.

• The type of supergroup, it can be chosen from a table (returned by the program) which contains: the *IT*A number of the minimal supergroup, its Hermann-Mauguin symbol and the index of the group in the supergroup. There is also a link to the list with the transformation matrices that relate the basis of the supergroup with that of the subgroup.

• It is necessary to select the type of the normalizers of the group and the supergroup. By default the Euclidean normalizers of general cell metrics are used as listed in Tables 15.2.1.3 and 15.2.1.4 of *IT*A. The affine normalizers of the space groups (except triclinic and monoclinic) are also accessible.

Input Information of SUPERGROUPS

• The *IT*A numbers of the space groups G and H, and their index.

• The type of the normalizers of the group and the supergroup. As in the case of MINSUP, the spacegroup normalizers used by default are the Euclidean normalizers. Also, there is a possibility for the user to use the affine normalizers given in *IT*A or to provide a specific one.

Output Information of MINSUP and SUPERGROUPS

1. The transformation matrix $(\boldsymbol{P}, \boldsymbol{p})$ that relates the default basis of the supergroup with that of the subgroup.

2. One representative from each coset in the decomposition of the supergroup G with respect to the group H.

3. The full cosets of the decomposition $G : H$. The elements of G are listed with respect to the default basis of the subgroup H.

From the considerations given above it should have become clear that the aim of the presented procedure and the supergroup programs is to solve the following 'purely' group-theoretical problem: Given a group–subgroup pair of space groups, $G > H$, determine all supergroups G of H, isomorphic to G. The procedure does not include any preliminary checks on the compatibility of the metric of the studied space group with that of a supergroup. As a consequence, in some particular cases when the supergroups and the groups belong to different crystal systems, it may happen that the determined supergroups are not space groups but just affine groups isomorphic to space groups (*cf.* [18]).

The number of supergroups of a space group H of a finite index is not always finite. This is the case of a space group H whose normalizer $N(H)$ contains continuous translations in one, two or three independent directions (*cf. IT*A, Part 15). As typical examples one can consider the infinitely many centrosymmetrical supergroups of the polar groups: there are no restrictions on the location of the additional inversion centre on the polar axis. For such group–supergroup pairs there are up to three parameters r, s and t in the transformation matrix and in the translational part of the coset representatives. The different values of the parameters corresponds to different supergroups of the same space-group type.

3.3. Relations of Wyckoff positions for a group–subgroup pair of space groups

Consider two group–subgroup related space groups $G > H$. Atoms which are symmetrically equivalent under G, *i.e.* belong to the same orbit of G, may become non-equivalent under H, (*i.e.* the orbit splits) and/or their site symmetries may be reduced. The orbit relations induced by the symmetry reduction are the same for all orbits belonging to a Wyckoff position, so one can speak of Wyckoff-position relations or splitting of Wyckoff positions. Theoretical aspects of the relations of the Wyckoff positions for a group–subgroup pair of space groups $G > H$ have been treated in detail by Wondratschek [28]. Part 3 of *IT*A1 contains the tables of the Wyckoff-position splittings for all space groups and their maximal subgroups. However, for certain applications it is more comfortable to have the appropriate computer tools for the calculations of the Wyckoff-position splittings for $G > H$: for example, when H is not a maximal subgroup of G, or when the space groups $G > H$ are related by transformation matrices different from those listed in the tables of *IT*A1. The program WYCKSPLIT [20] calculates

the Wyckoff-position splittings for any group–subgroup pair. In addition, the program provides further information on Wyckoff-position splittings that is not listed in *IT*A1, namely, the relations between the representatives of the orbit of *G* and the corresponding representatives of the suborbits of *H*.

3.3.1. The program WYCKSPLIT

The program WYCKSPLIT calculates the splitting of the Wyckoff positions for a group–subgroup pair *G* > *H*, given the corresponding transformation relating the coordinate systems of *G* and *H*. The additional data on the explicit correspondence between the representatives of the orbit of *G* and the corresponding representatives of the suborbits of *H* are calculated by comparing the values of the fixed parameters and the variable parameter relations in both sets.

Input Information
• The specification of the space groups *G* and *H* by their *IT*A numbers.
• The transformation matrix–column pair (***P***, ***p***) that relates the basis of *G* to that of *H*. The user can input a specific transformation or can be linked to the *IT*A1 database for the maximal subgroups of *G*. In the case of a non-maximal subgroup, the program SUBGROUPGRAPH provides the transformation matrix(ces) for a specified index of *H* in *G*. The transformations are checked for consistency with the default settings of *G* and *H* used by the program.
• The Wyckoff positions W_G to be split can be selected from a list. In addition, it is possible to calculate the splitting of any orbit specified by the coordinate triplet of one of its points.

Output Information
1. The splittings of the selected Wyckoff positions W_G into Wyckoff positions W_H^I of the subgroup, specified by their multiplicities and Wyckoff letters.
2. The correspondence between the representatives of the Wyckoff position and the representatives of its suborbits is presented in a table where the coordinate triplets of the representatives of W_G are referred to the bases of the group and of the subgroup.

4. REPRESENTATIONS OF CRYSTALLOGRAPHIC POINT GROUPS AND SPACE GROUPS

The *Bilbao Crystallographic Server* provides several programs facilitating the application of representation theory to specific problems of solid-state physics and crystallography-related fields. The computing packages support certain essential (and more involved from a mathematical point of view) steps in the related group-theoretical studies. The server offers access to the basic modules for handling space-group (REPRES) and point-group (POINT) representations, it enables the study of the correlations between irreps of group-subgroup related space groups (CORREL) and the decomposition of Kronecker direct products of space-group irreps (DIRPRO). In the following, we explain the necessary input data and provide details on the output results of the basic programs REPRES and POINT. For a presentation of the rest of the programs treating representations of crystallographic groups and the group-theoretical background of the developed programs, the reader is referred to Ref. [3].

4.1. Space-group representations

There exist several reference sets of tables of space-groups irreps (see *e.g.* CDML, and the references therein). However, the available data have important drawbacks related to the lack of full space-group representations due to the limitations and/or specificity in the choice of the **k**-vectors. In addition, the used space-group settings are often not compatible with those of *IT*A. These disadvantages are overcome by the program REPRES which computes the irreps of space groups explicitly: For any space group *G* and a **k**-vector, the corresponding little group G^k, the allowed (small) irreps of G^k and the matrices of the full-group irreps are constructed. As part of the working environment of the Bilbao Crystallographic Server, the program REPRES provides the irrep data in a format suitable for its further use as input for other programs on the server.

4.1.1. The program REPRES

REPRES calculates the irreps of space groups following a general scheme based on a normal-subgroup induction method: the irreps of a space group *G* are constructed starting from those of its translation subgroup T_G which is a normal subgroup of *G*, $T_G \lhd G$. The main steps of the procedure involve the construction of all irreps of T_G and their distribution into orbits under *G*, determination of the corresponding little groups and the allowed (small) irreps and finally, construction of the irreps of *G* by induction from the allowed irreps. The most involved step in the procedure is the determination of the allowed irreps of the little group. In the majority of books on irreps of space groups this problem is solved by applying the theory of the so-called *projective representations*. Here we have preferred another approach for the construction of the allowed irreps which is a slight modification of an induction procedure originally proposed by Zak

[30]. It is based on the fact that all space groups are *solvable groups*, *i. e.* for every space group one can construct a composition series $G \triangleright H_1 \triangleright H_2 \ldots \triangleright T$ such that all factor groups H_i/H_{i+1} are cyclic groups of order 2 or 3.

Input Information

• Space group data: As an input the program needs the specification of the space group G which can be defined by its sequential *IT*A number. Here, as well as in the rest of programs of the *Bilbao Crystallographic Server* the default settings of the space groups are used for the calculations. The program REPRES can treat space groups in unconventional settings, once the transformation matrixcolumn pair $(\boldsymbol{P}, \boldsymbol{p})$ to the corresponding default setting is known.

• **k**-vector data: There are two different ways to introduce the **k**-vector: either by choosing it from a table where the different symmetry types of wave vectors are listed explicitly, or by typing in the **k**-vector coefficients directly. The program accepts **k**-vector coefficients referred to different coordinate systems of the reciprocal space. For its internal calculations REPRES uses **k**-vector coefficients (k_1, k_2, k_3) referred to a basis which is dual to the default ITA settings of the space groups (called conventional k-vector coefficients). The program accepts also **k**-vector coefficients referred to a primitive basis of the reciprocal lattice as given for example, in CDML tables of space-group irreps. If a non-conventional setting for the space group is chosen (2.1.1), then the corresponding 'non-conventional' **k**-vector coefficients

$$(k'_1, k'_2, k'_3) = (k_1, k_2, k_3)\boldsymbol{P},$$

can be given as input data. Note that the program does not accept variables (free parameters) as coefficients of the wave vector.

Output Information

1. Information on the space group G:

• Non-translational generators of G listed as matrix-column pairs (W, w), *i.e.* in (3. 4) matrix form consisting of a (3×3) matrix part W and a (3×1)-column part w:

$$(W, w) = \begin{pmatrix} W_{11} & W_{12} & W_{13} & w_1 \\ W_{21} & W_{22} & W_{23} & w_2 \\ W_{31} & W_{32} & W_{33} & w_3 \end{pmatrix};$$

The sequence of generators follows that of *IT*A for the conventional settings of the space groups;

• List of the coset representatives (W, w) of the decomposition of G with respect to T_G (known also as *translational coset representatives* given in (3×4) matrix form. The numbers coincide with the sequential numbers of the general-position coordinate triplets listed in *IT*A.

2. **k**-vector data:

The program lists the input values of the **k**-vector coefficients followed by the corresponding conventional coefficients (k_1, k_2, k_3). The coefficients of the arms of the wave-vector star *****k** are referred also to the basis that is dual to the default setting of the space group. The program also asignes a label to the given **k**-vector according to the classification scheme of CDML.

3. Information on the little group G^k:

• A set of coset representatives of G with respect to the little group G^k;

• A set of non-translational generators and a set of translational coset representatives of G^k given as (3×4) matrices;

• Little-group irreps presented in a matrix form for the translational coset representatives of G^k in a consecutive order. The labels of the irreps follow the classification scheme of CDML. The (complex) matrix elements are specified by their moduli and phase angles in degrees [○].

4. Full-group representations:

The program lists the characters of the full-group representations for all translational coset representatives of the group G. In addition, the pairs of full-group irreps that form physically-irreducible representations are also indicated.

As an option, the program can list the full-group irreducible representations of the non-translational generators of the space group (or any element of the space group specified by the user) in a blockmatrix form: for a given representation and a generator, the program prints out the induction matrix whose non-zero entries, specified by its row and column indices, indicate a matrix block corresponding to a little-group matrix.

Example: Irreps of $P4_2/mbc$ (No. 135) for $\mathbf{k} = \mathbf{T}(0.37, 1/2, 1/2)$

The input data consists in the specification of the space group $P4_2/mbc$ by its *IT*A number, No. 135, and the data for **k**-vector coefficients, $\mathbf{k} = \mathbf{T}(0.37, 1/2, 1/2)$.

The discussion of the output follows the order of the results as they appear in the output file.

1. *Space-group information* block:

(a) The generators of $P4_2/mbc$ (with the exception of the generating translations) are listed in the same sequence as they appear in *IT*A: $(1, o), (2_z, o), (4_z, \tau_1), (2_y, \tau_2) (\bar{1}, o)$, with $o = (0, 0, 0)$, $\tau_1 = (0, 0, 1/2)$ and $\tau_2 = (1/2, 1/2, 0)$.[2]

---

[2] To make the description more compact we use a symbolic notation for the space-group elements.

(b) Decomposition of $P4_2/mbc$ relative to its translation subgroup with coset representatives as given in *ITA*: $(1, o)$, $(2_z, o)$, $(4_z, \tau_1)$, $(4_z^3, \tau_1)$, $(2_x, \tau_2)$, $(2_y, \tau_2)$, $(2_{xx}, \tau_1 + \tau_2)$, $(2_{x\bar{x}}, \tau_1 + \tau_2)$, $(\bar{1}, o)$, (m_z, o), $(\bar{4}_z, \tau_1)$, $(\bar{4}_z^3, \tau_1)$, (m_x, τ_2), (m_y, τ_2), $(m_{xx}, \tau_1 + \tau_2)$ $(m_{x\bar{x}}, \tau_1 + \tau_2)$.

2. **k**-*vector information* block:

(a) The input **k**-vector coefficients **T**(0.37, 1/2, 1/2) followed by the corresponding conventional coefficients. (In all space groups with primitive lattices, the **k**-vector coefficients, referred to a primitive basis of the reciprocal space (CDML), coincide with the conventional k-vector coefficients.)

(b) The **k**-vector star: *T = {(0.37, 1/2, 1/2), (0.63, 1/2, 1/2), (1/2, 0.37, 1/2), (1/2, 0.63, 1/2)}.

(c) The little group $G^T = P2_1am$ is specified by the coset representatives of its decomposition with respect to the translation subgroup: $(1, o)$, $(2_x, \tau_2)$, (m_z, o), (m_y, τ_2). The little co-group $\bar{G}^T = \{1, 2_x, m_y, m_z\}$ is isomorphic to the point group $2mm$.

(d) The coset representatives of the decomposition of $P4_2/mbc$ relative to $P2_1am$ are as follows: $\{(1, o), (2_z, o), (4_z, \tau_1)$, and $(4_z^3, \tau_1)\}$.

3. *Allowed irreps* of G^T

As the little group G^T is non-symmorphic and the k vector is on the surface of the Brillouin zone, it is not possible to derive directly the allowed irreps of $P2_1am$ from the point-group irreps of the little co-group $2mm$. The program determines the allowed irreps following the composition series for the little group $P2_1am$: $P2_1am \triangleright Pm \triangleright T$.

The little group of the **k**-vector has 4 allowed irreps:

$P2_1am$	$(1, o)$	$(2_x, \tau_2)$	(m_x, o)	(m_x, τ_2)
$D^{T, 1}$	1	ε_1	1	ε_1
$D^{T, 2}$	1	ε_1	$\bar{1}$	ε_2
$D^{T, 3}$	1	ε_2	$\bar{1}$	ε_1
$D^{T, 4}$	1	ε_2	1	ε_2

$\varepsilon_1 = exp(i113.4)$ and $\varepsilon_2 = exp(i293.4)$

4. *Full-group irreps*

The (complex) characters of the full-group irreps for all translational coset representatives of $P4_2/mbc$ are represented by by their moduli and phase angles in degrees [○]. The physically irreducible representations are formed by the pairs $\{D^{*T, 1}, D^{*T, 4}\}$ and $\{D^{*T, 2}, D^{*T, 3}\}$.

The matrices of the full-group irreps for the non-translation generators are presented in a blockmatrix form. The program lists separately the induction matrix $M (W, w)$ and the corresponding blocks of the little-group representation matrices specified by the row-column indices of the nonzero entries of M

(W, w). For example, the matrix of the full-group irrep for the generator $(\bar{1}, o)$ of $P4_2/mbc$ (No. 5 in the list of generators)

$$D^{*T,1}(\bar{1}, o) = \begin{pmatrix} 0 & 1 & 0 & 0 \\ 1 & 0 & 0 & 0 \\ 0 & 0 & 0 & 1 \\ 0 & 0 & \bar{1} & 0 \end{pmatrix}$$

is presented as a (4×4) induction matrix

$$M(\bar{1}, o) = \begin{pmatrix} 0 & 1 & 0 & 0 \\ 1 & 0 & 0 & 0 \\ 0 & 0 & 0 & 1 \\ 0 & 0 & 1 & 0 \end{pmatrix},$$

with the following (1×1) blocks:

Block (1, 2) = (1.000, 0.0);
Block (2, 1) = (1.000, 0.0);
Block (3, 4) = (1.000, 180.0);
Block (4, 3) = (1.000, 180.0).

4.2. Point group representations

The information about the 32 (non-magnetic) crystallographic point groups plays a fundamental role in many applications of crystallography. In the literature, there exists a lot of information about crystallographic point groups and their representations. Some complete tables are given in Koster et al. [19], Bradley & Cracknell [7], Altmann & Herzig [1] (and the references therein). In our case, a selection of these data have been recalculated and is now available online via the *Bilbao Crystallographic Server*. The point-group databases are part of the core shell of the server. They provide essential information for a point-group analysis in applications related to crystallographic, solid-state or phase transitions problems. The information about the irreps of the 32 point groups is obtained from the program REPRES for the particular case of **k** = Γ(0, 0, 0). The generated point-group data have been stored as an XML database of the server.

4.2.1. The program POINT

The program POINT displays a set of tables for each of the 32 crystallographic point groups which are specified by their international (Hermann-Mauguin) and Schoenflies symbols:

1. Character table. The character table provides the characters of the ordinary irreps of the chosen point group. The irreps are labelled in the notation of Mulliken [24] and by the Γ labels introduced by Bethe [6], see also Koster et al. [19]. The matrices

of the degenerate irreps as calculated by REPRES are also accessible. The number of point-group elements in a conjugacy class is indicated by the listed multiplicity. In addition, the transformation properties of the cartesian tensors of rank 1 (vectors and axial vectors) and 2 are displayed. (The tensor of rank 0 belongs always to the totally symmetric irrep and is not listed explicitly). Cartesian tensors that transform according to two- or three-dimensional irreps are joined by brackets.

2. Subgroup table. The point-group types of the subgroups of a point group are listed with the corresponding indices with respect to the initial point group.

3. Irrep multiplication table. The table shows the decomposition into irreducible constituents of the Kronecker (direct) product of any pair of point-group irreps.

4. Tensor representations. A physical property can be represented by a tensor which transforms, in general, according to a reducible representation. Any reducible representation can be decomposed into irreducible constituents applying the so-called reduction ("magic") formula:

$$\Gamma \sim \bigoplus_i n_i \Gamma_i, \text{ where } n_i = \frac{1}{|\bar{G}|} \sum_g \chi(g) \chi_i^*(g).$$

Here, Γ represents a reducible representation expressed in terms of its irreps Γ_i. The multiplicity of the irrep is given by n_i, $|\bar{G}|$ is the order of the point group and $\chi(g)$ and $\chi_i(g)$ are the corresponding characters of the reducible representation Γ and the irrep Γ_i.

The tensor-representation tables one finds the decompositions into irreducible constituents of representations related to some important tensors (and their powers), such as the vector V (polar) or the pseudovector A (axial), their symmetrized $[V^2]$ or antisymmetrized squares, *etc*.

5. Selection rules for fundamental transitions. The table displays the selection rules for infrared and Raman vibrational (phonon) transitions. The data in the first row of each table (specified by the trivial irrep label) corresponds to the usual infrared and Raman selection rules.

6. Subduction from the rotation group irreps. Given a representation of the rotation group of dimension $2l+1$, $l = 0, \ldots, 9$, the table lists the point-group irreps which appear in its subduction to the chosen point group.

5. CONCLUSIONS

The *Bilbao Crystallographic Server* site provides a free online interface for different crystallographic databases and programs at www.cryst.ehu.es. The working enviroment is divided into several

shells according to different topics, from simple retrieval tools for access to crystallographic data to more sophisticated solid-state applications. The programs available on the server do not need a local installation the only requirement is an Internet connection and a web browser. The programs on the *Bilbao Crystallographyc Server* have user-friendly interfaces with links to documentation an online help for each of the consecutive steps in a calculation. One of the important advantages of the server is that the different programs can communicate with each other, so that the output of some programs is used directly as input dato to other. In that way the server has turned into a workin environment with the appropiate tools for treating problems of theoretical crystallography, solid-state physics and crystal chemistry.

REFERENCES

1. S. L. Altmann, P. Herzig, Point Group Theory Tables. Oxford, Clarendon Press, 1994.
2. M. I. Aroyo, J. M. Perez-Mato, C. Capillas, E. Kroumova, S. Ivantchev, G. Madariaga, A. Kirov, H. Wondratschek, *Z. Kristallogr*., **221**, 15 (2006a).
3. M. I. Aroyo, A. Kirov, C. Capillas, J. M. Perez-Mato, H. Wondratschek, *Acta Crystallogr. A*, **62**, 115 (2006b).
4. M. I. Aroyo, H. Wondratschek, *Z. Kristallogr*., **210**, 243 (1995).
5. M. I. Aroyo, H. Wondratschek, in: Jahrestagung DGK-DGKK abstracts, Jena, 2004.
6. H. A. Bethe, *Ann. Physik*, **3**, 133 (1929) (in German).
7. C. J. Bradley, A. P. Cracknell, The Mathematical Theory of Symmetry in Solids, Oxford, Clarendon Press, 1972.
8. C. Capillas, PhD Thesis, Universidad del Pa´ıs Vasco, 2006.
9. C. Capillas, E. S. Tasci, G. de la Flor, D. Orobengoa, J. M. Perez-Mato, M. I. Aroyo, *Z. Kristallogr*., in press.
10. A. P. Cracknell, B. L. Davies, S. C. Miller, W. F. Love, Kronecker Product Tables. Volume 1, General Introduction and Tables of Irreducible Representations of Space Groups, New York, IFI/Plenum, Abbreviated CDML, 1979.
11. J. M. Igartua, M. I. Aroyo, J. M. Perez-Mato, *Phys. Rev. B*, **54**, 12744 (1996).
12. International Tables of Crystallography, Vol. A, Space-Group Symmetry, T. Hahn (ed.), 5th ed., Dordrecht, Kluwer Academic Publishers, 2002 Abbreviated: IT A.

13. International Tables for Crystallography, Vol. A1, Symmetry Relations between Space Groups, H. Wondrtaschek, U. Müller (eds.), Dordrecht, Kluwer Academic Publishers, 2004 Abbreviated: IT A1..

14. International Tables for Crystallography, Vol. E, Subperiodic Groups. V. Kopsky, D. Litvin (eds.), Dordrecht: Kluwer Academic Publishers, 2002 Abbreviated: IT E..

15. S. Ivantchev, E. Kroumova, G. Madariaga, J. M. Perez-Mato, M. I. Aroyo, *J. Appl. Cryst.*, **33**, 1190 (2000).

16. S. Ivantchev, E. Kroumova, M. I. Aroyo, J. M. Perez-Mato, J. M. Igartua, G. Madariaga, H. Wondratschek, *J. Appl. Cryst.*, **35**, 511 (2002).

17. A. K. Kirov, M. I. Aroyo, J. M. Perez-Mato, *J. Appl. Cryst.*, **36**, 1085 (2003).

18. E. Koch, *Acta Cryst*. A, **40**, 593 (1984).

19. G. F. Koster, J. O. Dimmock, R. G. Wheeler, H. Statz, Properties of the Thirty-two Point Groups, Cambridge, M.I.T. Press, 1963.

20. E. Kroumova, M. I. Aroyo, J. M. Perez-Mato, *J. Appl. Cryst.*, **31**, 646 (1998).

21. E. Kroumova, M. I. Aroyo, J. M. Perez-Mato, J. M. Igartua, S. Ivantchev, *Ferroelectrics*, **241**, 295 (2000).

22. E. Kroumova, M. I. Aroyo, J. M. Perez-Mato, *Acta Cryst. B*, **58**, 921 (2002).

23. E. Kroumova, J. M. Perez-Mato, M. I. Aroyo, S. Ivantchev, G. Madariaga, H. Wondratschek, in: Abstracts of 18th European Crystallographic Meeting, Praha, Czech Republic, 1998a.

24. R. S. Mulliken, *Phys. Rev.*, **43**, 279 (1933).

25. D. Orobengoa, C. Capillas, M. I. Aroyo, J. M. Perez-Mato, *J. Appl. Cryst. A*, **42**, 820 (2009).

26. J. M. Perez-Mato, Orobengoa, M. I. Aroyo, *Acta Cryst. A*, **66**, 558 (2010).

27. G. Wintgen, *Math. Ann.*, **118**, 195 (1941) (in German).

28. H. Wondratschek, *Mineralogy and Petrology*, **48**, 87 (1993).

29. H. Wondratschek, M. I. Aroyo, *Acta Cryst. A*, **57**, 311 (2001).

30. J. Zak, *J. Math. Phys.*, **1**, 165 (1960).

КРИСТАЛОГРАФИЯ ОНЛАЙН: БИЛБАО КРИСТАЛОГРАФСКИ СЪРВЪР

М. И. Аройо[1,*], Х. М. Перес-Мато[1], Д. Оробенгоа[1], Е. Тасци[1],
Г. де ла Флор[1], А. Киров[2]

[1] Катедра Физика на кондензираната материя, Баски Университет, 48040 Билбао, Испания
[2] Катедра Физика на кондензираната материя, Софийски Университет, 15064 София, България

(Резюме)

Билбао Кристалографски Сървър е уебсайт с кристалографски база данни и програми, достъпни онлайн (www.cryst.ehu.es). В продължение на повече от 10 години сървърът предоставя кристалографска информация, като предлаганите данни и програми постоянно се обновяват и разширяват. Програмите на сървъра не се нуждаят от локално инсталиране и могат да бъдат използвани безплатно. Билбао Кристалографски Сървър предоставя свободен достъп до информация от общ характер свързана с кристалографските групи на симетрия (генератори, общи и специални Wyckoff позиции, зони на Brillouin и т.н.). Освен приложенията за директно четене на съхраняваните данни, сървърът разполага с програми за анализ на връзките група–подгрупа за пространствените групи, техните представяния и т.н. Има също така програмни продукти за изучаване на специфични проблеми от физиката на твърдото тяло, структурна химия и кристалография.

Fundamental absorption edge of pure and doped magnesium sulfite hexahydrate (MgSO$_3$.6H$_2$O) single crystals

Zh. Bunzarov[1], I. Iliev[2], T. Dimov[2], P. Petkova[2]*

[1] Sofia University, Department of Physics
[2] Shumen University, Department of Natural Sciences

Absorption spectra of magnesium sulfite hexahydrate (MgSO$_3$.6H$_2$O), pure and doped with Co and Ni have been studied in the spectral range of the fundamental absorption edge. The investigations have been carried out from 208 nm to 230 nm with linear polarized light $\vec{E}//\bar{c}$, $\vec{E} \perp \bar{c}$ ($\bar{c}$ is the optical axis of MgSO$_3$.6H$_2$O) which propagates in the direction ($1\bar{2}10$). The influence of the Co and Ni ions on the spectral position of the absorption edge has been proved. The structure of the absorption edge manifests good expressed linear dichroism in the mentioned direction. The peculiarities of the linear dichroism in dependence of the impurity ions in the crystal lattice of MgSO$_3$.6H$_2$O are analyzed and discussed.

Key words: magnesium sulfite hexahydrate, fundamental absorption edge, linear dichroism.

INTRODUCTION

The magnesium sulfite hexahydrate (MgSO$_3$.6H$_2$O) crystals are of the crystallographic class C$_3$ (without a center of symmetry). The crystal symmetry suggests presence of nonlinearity, piezo- and pyro-electric properties and gyrotropy as well [1], [2]. The unit cell of MgSO$_3$.6H$_2$O contains an octahedron Mg (H$_2$O)$_6^{2+}$ and a pyramidal ion SO$_3^{2-}$ [3], [4], [5]. The density measurements of MgSO$_3$.6H$_2$O are presented in [5].

Single crystals of MgSO$_3$.6H$_2$O (pure and doped with Ni, Co and Zn) for the time being are grown only by the original method developed in the Laboratory for Crystal growth at the Faculty of Physics of Sofia University.

The impurities provoke changes of electrical, optical and magnetic properties of MgSO$_3$.6H$_2$O [6], [7], [8]. The influence of Ni and Co impurities on the absorption spectra has been investigated in direction ($1\bar{2}10$) with linear polarized light $\vec{E}//\bar{c}$, $\vec{E} \perp \bar{c}$ (c is the optical axis of MgSO$_3$.6H$_2$O).

Absorption spectra of magnesium sulfite hexahydrate (MgSO$_3$.6H$_2$O), pure and doped with Co and Ni have been studied in the spectral range of the fundamental absorption edge in the present paper. The ions Co^{2+}, Ni^{2+} are in the same isomorphous order with Mg^{2+}. Therefore the ions

Co^{2+} and Ni^{2+} can replace Mg^{2+} ions in the crystal lattice of MgSO$_3$.6H$_2$O. The concentration of Ni and Co has been found by the analytical chemistry methods and it amounts to 0.17 weight %.

The optical spectra give an opportunity to obtain information about the fine spectral structures, the transition selection rules and the impurity states in the forbidden band [9].

The anisotropy of the crystal is conditioned by the particles in the crystal lattice, by their mutual dispositions and by the character of the chemical connection. The linear dichroism in the optical spectra is a result of the crystal anisotropy and can be determined by measurements of the absorption coefficient with linear polarized light $\vec{E}//\bar{c}$ and $\vec{E} \perp \bar{c}$. The linear dichroism appears in all spectral regions in the optical spectra of MgSO$_3$.6H$_2$O.

The Co^{2+} and Ni^{2+}-ions influence considerably on the optical spectra at the fundamental absorption edge of MgSO$_3$.6H$_2$O.

EXPERIMENTAL RESULTS

The structure around 210–220 nm in the optical spectra of MgSO$_3$.6H$_2$O is the fundamental absorption edge. The forbidden band width can be determined from the position of edge.

The optical spectra are measured with linear polarized light from 208 nm to 230 nm for pure and

* To whom all correspondence should be sent:
E-mail: Petya232@abv.bg

Ni doped $MgSO_3.6H_2O$ and from 200 nm to 280 nm for Co doped $MgSO_3.6H_2O$. The spectra are presented at Fig. 1, Fig. 2, Fig. 3. The wave vector of the incident light is $kII(1\bar{2}10)$, $\vec{k} \perp \bar{c}$.

The absorption coefficient spectra at the fundamental edge have a typical unusual form – a rapid value decreasing to the short length wave (Fig.1, 2, 3). The part of the spectrum to the longer waves belongs structurally to the fundamental absorption edge.

The spectral positions of the fundamental edges of pure and doped $MgSO_3.6H_2O$ for light polarization $\vec{E}II\bar{c}$, $\vec{E} \perp \bar{c}$ are presented in Table 1.

The absorption coefficient spectra are most strongly influenced by the presence of Ni and Co in the spectral region of the fundamental edge. The impurities cause a displacement of edge spectral positions for $\vec{E}II\bar{c}$, $\vec{E} \perp \bar{c}$ to the longer light wave.

Fig. 3. Absorption spectra of MgSO3.6H₂O: Co for light polarizations $\vec{E} \perp \bar{c}$ and $\vec{E}II\bar{c}$

The value change of the absorption coefficient in the vicinity of the fundamental edge is proportional to the impurity atoms concentration.

The optical structure at the edge for $\vec{E} \perp \bar{c}$ has a doublet character (Fig. 1, 2, 3).

The presence of linear dichroism ($\Delta\alpha$) shows that the crystal anisotropy influences essentially the absorption of pure and doped $MgSO_3.6H_2O$. The linear dichroism in the region of the fundamental edge is characterized with a maximum at: 218.6 nm for $MgSO_3.6H_2O$; 220.0 nm for $MgSO_3.6H_2O$: Ni and 247.2 nm for $MgSO_3.6H_2O$: Co, (Fig.4, 5, 6).

The linear dichroism changes its sign in the short wave range for $MgSO_3.6H_2O$: Ni and in the long wave range for $MgSO_3.6H_2O$:Co.

Fig. 1. Absorption spectrum of $MgSO_3.6H_2O$ for light polarization $\vec{E} \perp \bar{c}$ and $\vec{E}II\bar{c}$

DISCUSSION

The analysis of the spectra in Fig. 2, 3 shows that the Ni and Co-ions influence on the position of the absorption edge and change the value of the absorption coefficient.

The linear dichroism in the optical spectra of $MgSO_3.6H_2O$ is well expressed. It is a result of the selection rules for the transitions from the valence subbands to the conduction band.

The difference in the magnitude of the maximum in the linear dichroism at the edge for pure and doped $MgSO_3.6H_2O$ can be explained by the different coefficients of the edge impurity displacement for both polarizations.

The position change of the maximum in the linear dichroism explains the disturbances in $MgSO_3.6H_2O$ conditioned by Co and Ni presence. Ni^{2+} and Co^{2+} ions create additional vacancies in the crystal lattice. These vacancies cause the arising of

Fig. 2. Absorption spectrum of $MgSO_3.6H_2O$: Ni for light polarization $\vec{E} \perp \bar{c}$ and $\vec{E}II\bar{c}$

Table 1. Spectral positions of the fundamental edges of pure and doped $MgSO_3.6H_2O$ for light polarization $\vec{E} // \bar{c}$, $\vec{E} \perp \bar{c}$ at room temperature

$MgSO_3.6H_2O$	216.7 nm for $\vec{E}//\bar{c}$	221.7 nm for $\vec{E} \perp \bar{c}$
$MgSO_3.6H_2O$:Ni	221.5 nm for $\vec{E}//c$	223.4 nm for $\vec{E} \perp \bar{c}$
$MgSO_3.6H_2O$:Co	233.6 nm for $\vec{E}//\bar{c}$	256.9 nm for $\vec{E} \perp \bar{c}$

random strains and Coulomb interaction [10] which contribute to the change of the local electric fields [11] and smear the low energy periphery structure of the absorption edge [12].

The appearance of Ni and Co impurity states in the forbidden band is one of the basic mechanisms for the explanation of the spectral position change of the absorption edge. It can be concluded on the basis of the absorption spectra around the fundamental edge of pure crystal, that the edge displacement is caused by impurity levels which are localized at the minimum of the conduction band. The additional impurity states influence the character of electron transitions as a result of a deformation of the band structure at the bottom of the conduction band. The influence manifests itself as a change of the spectral positions of the edge structure to the longer waves.

The experimental absorption spectrum in the vicinity of the fundamental edge of $MgSO_3.6H_2O$: Ni is described with Urbach's rule [14].

The theory shows that the linear dichroism contains information about the electron transitions [13]. The changes of the value and the sign of the linear dichroism in the spectral range of fundamental edge in accordance with the theory is an indication that the band-band electron transitions are influenced by the presence of Ni^{2+} and Co^{2+}-ions. Therefore the

sign-changed shape of the linear dichroism spectrum (Fig. 5, 6) is a consequence of the unparallelism of the moments of the interband transitions. This unparallelism can be considered as a result of the asymmetry of the spin-orbit interaction in the Ni and Co-ions. The asymmetry can be caused by the internal crystal field [15].
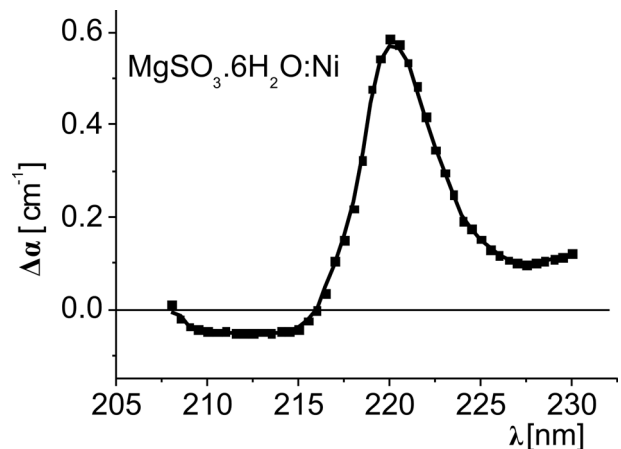
Fig. 5. Linear dichroism spectrum at the absorption edge of $MgSO_3.6H_2O$: Ni
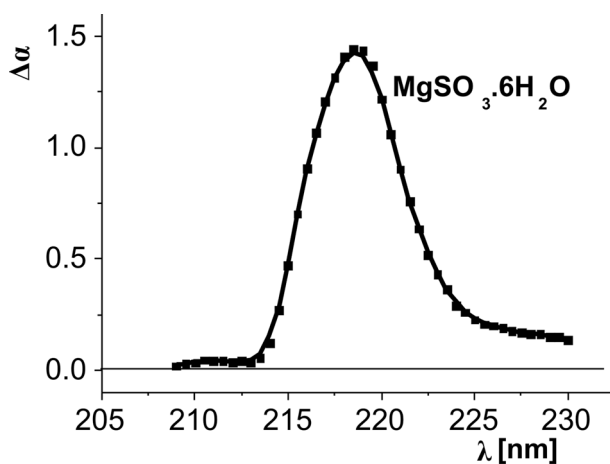
Fig. 4. Linear dichroism spectrum at the absorption edge of $MgSO_3.6H_2O$
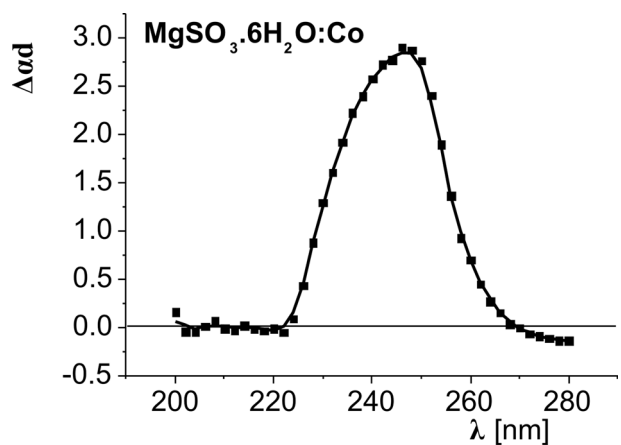
Fig. 6. Linear dichroism spectrum at the absorption edge of $MgSO_3.6H_2O$: Co

The established difference of the maximum positions in the linear dichroism spectra $\Delta\alpha(\lambda)$ (Fig. 5, 6) is a result of the additional spin-orbit splitting of the valence band due to the ions of the transition metals Co and Ni located in the crystal lattice of $MgSO_3.6H_2O$ [16].

The energy band scheme of $MgSO_3.6H_2O$ is not developed. It can be concluded on the basis of the experimental spectra that the energy gap of $MgSO_3.6H_2O$ is direct. We assume that the valence band is split in two subbands (A and B) due to the spin-orbit interaction. The transitions from subband A are allowed only for polarization $\vec{E}\perp\vec{c}$. The transitions from subband B are allowed for both polarizations ($\vec{E}\perp\vec{c}$, $\vec{E}II\vec{c}$).

The change of the edge spectral positions of $MgSO_3.6H_2O$ for $\vec{E}II\vec{c}$, $\vec{E}\perp\vec{c}$ in presence of Ni and Co is caused by the impurity states arising in the forbidden band near to the bottom of the conduction band. The transitions from these levels determine the edge displacing but the selection rules are the same as by the pure $MgSO_3.6H_2O$.

CONCLUSIONS

1. Absorption spectra of pure and Ni and Co doped $MgSO_3.6H_2O$ have been measured in the spectral range of the fundamental absorption edge with linear polarized light $\vec{E}II\vec{c}$ and $\vec{E}\perp\vec{c}$ in direction ($1\bar{2}10$).

2. It has been established that the forbidden band of $MgSO_3.6H_2O$ is direct. It has been also experimental proved that the Ni and Co cause a displacement of edge spectral positions to the longer light wave and a value change of the absorption coefficient in the vicinity of the fundamental edge.

3. The linear dichroism due to the crystal anisotropy is established and analyzed in the vicinity of the fundamental absorption edge. It is proved

that the impurities influence the linear dichroism spectrum.

REFERENCES

1. H. A. Klasens, W. Perdok and P Terpstra, *Rec. Trav. Chim. Pays Bas* **54**, 728 (1935).
2. Z. Bunzarov, S. M. Saltiel, T. Kovachev, L. Ljutov, D. Russev, in: Proceedings of SPIE 3052 SPIE, Bellingham, WA, 1996, 197.
3. H. Flack, *Acta Cryst. B* **29**, 656 (1973).
4. L. Andersen and O. Lindqvist, *Acta Cryst. C* **40,** 584 (1984).
5. G. Gianluca, G. Lyutov, L. Lyutov, *Bul. Journal of Chem. Comm.* (to be published).
6. Zh. Bunzarov., P. Petkova, T. Dimov, I. Iliev., *Coll. Papers, Physics, Shumen University* **1**, 39 (2004).
7. P. Petkova, Zh. Bunzarov, I. Iliev, T. Dimov, in: ROCAM'09 Brasov, Romania, 2009, in press.
8. Zh. Bunzarov, T. Dimov, P. Petkova, I. Iliev, in: American Institute of Physics, Conference Proceedings 1162, 2009, 210.
9. M. Aven, J. S. Prener, Physics and Chemistry of II-VI Comp., Moskva, Mir, 1970.
10. J. Pankove, Opt. Processes in Semiconductors, Moskva, Mir, 1973, p. 53.
11. P. Radovanovic, D. Gamelin, in: Proc. of SPIE, 4809, 2002, p. 51.
12. D. Redfield, A. Afromovitz, *Appl. Phys. Letters* **11**, 138 (1967).
13. Ch. Cantor, P. Schimmel, Biophys. Chem., Part II, Moskva, Mir, 1984, p. 28.
14. J. D. Dow, D. Redfield, *Phys. Rev. B* **5,** 594 (1972).
15. J. Coleman, R. Coleman, *Journal of Biolog. Chem.*, **247**, 4723 (1972).
16. H. Bethe, Intermediate quantum mechanics, Moskva, Mir, 1982, p. 153.

АБСОРБЦИОННИ ЕФЕКТИ ОКОЛО РЪБА НА ПОГЛЪЩАНЕ НА НЕЛЕГИРАНИ И ЛЕГИРАНИ МОНОКРИСТАЛИ ОТ МАГНЕЗИЕВ СУЛФИТ ХЕКСАХИДРАТ (MgSO$_3$.6H$_2$O)

Ж. Бунзаров[1], И. Илиев[2], Т. Димов[2], П. Петкова[2]

[1] Софийски университет „Св. Кл. Охридски“, Физически факултет
[2] Шуменски университет „Еп. К. Преславски“, Факултет по природни науки

(Резюме)

Изследвани са спектрите на поглъщане на магнезиев сулфит хексахидрат (MgSO$_3$.6H$_2$O), нелегиран и легиран с кобалт и никел, в спектралния диапазон около ръба на поглъщане. Изследванията са проведени от 208 nm до 230 nm с линейно поляризирана светлина $\vec{E} \| \bar{c}$, $\vec{E} \perp \bar{c}$ ($\bar{c}$ е оптичната ос на кристала MgSO$_3$.6H$_2$O). Светлината се разпространява по направление ($1\bar{2}10$). Доказано е влиянието на Co и Ni йони върху спектралното положение на ръба на поглъщане. Структурата при ръба на поглъщане проявява добре изразен линеен дихроизъм, когато светлината се разпространява в направление ($1\bar{2}10$). Анализирани и дискутирани са особеностите в линейния дихроизъм, дължащи се на примесните йони в кристалната решетка на MgSO$_3$.6H$_2$O.

Structure of LaSrFeO₄: neutron diffraction, Mössbauer spectroscopy and modeling

L. Dabrowski[1], D. Neov[2]*, V. Antonov[2], M. Machkova[3], S. Neov[2], V. Kozhukharov[3]

[1] Atomic Energy Institute, 05-400 Otwock, Swierk, Poland
[2] Institute for Nuclear Research and Nuclear Energy, Bulgarian Academy of Sciences, 1784 – Sofia, Bulgaria
[3] University of Chemical Technology and Metallurgy, 1756 – Sofia, Bulgaria

Mössbauer spectroscopy and neutron diffraction experiments were carried out for study of LaSrFeO₄, synthesized by wet chemical method. The data obtained were interpreted on the basis of *ab initio* quantum-mechanical modeling. The experimental results from Mössbauer spectroscopy and model calculations show that occupational distribution of La and Sr atoms on (4e) Wyckoff positions of I4/mmm space group (confirmed by neutron diffraction) is not random as previously assumed, but predominantly in double layers of either La or Sr. The distribution of each double layer is however random. The quantum mechanical model calculations of La and Sr arrangement along the *c*-axis explain the presence of two Mössbauer sextets at low temperature despite the unique position of Fe in the unit cell.

Key words: Mössbauer spectroscopy, neutron diffraction, modeling

INTRODUCTION

The increased interest towards LaSrFeO₄ in recent years is invoked by the possibility of using this material as a cathode in solid oxide fuel cells (SOFC), operating at high temperature. The compound possesses high electron-ion conductivity, significant oxygen diffusion, thermo-mechanical stability and other properties suitable for SOFC cathode application. The compound crystallizes in K_2NiF_4 – type structure and constitutes a particular case of Ruddlesden-Popper phases $A_{n+1}B_nO_{3n+1}$ with n = 1. From the viewpoint of its structure the question if La^{3+} ion (ionic radius R = 1.03 Å) and Sr^{2+} (R = 1.18 Å) randomly occupy the same Wyckoff crystallographic position (4e) in tetragonal space group I4/mmm despite the difference in their effective ionic radii and valence, needs further experimental and model investigations. The diffraction experiments [1–3] provide rather averaged information about the local distribution of the atoms, whereas the Mössbauer spectroscopy is sensitive to the coordination polyhedron of atoms surrounding the Fe (forming the first coordination sphere). Mössbauer spectrum cumulates also the influence of more distant atoms around Fe atom that form the second coordination sphere. Hence,

the complementary data from both experimental methods and model calculations of fine parameters of the structure of LaSrFeO₄ could explain better the observed physical properties.

Practically all authors report random distribution of La and Sr ions in the „rock-salt" layers between "perovskite" layers formed by adjacent FeO_6 octahedra. Although seemingly natural, such distribution needs further unconventional assumptions in order to explain the experimentally obtained peculiarities of Mössbauer spectra and their temperature dependence. Additional argument for carrying out our investigation is the rather strong dependence of the Neel temperature (T_N) from the method of compound synthesis. In particular, depending on which one is used – solid-state reaction at various temperature regime or wet chemical method, T_N deduced from the Mössbauer experiments varies from 300 to 380 K [3–6]. At the same time, electrical resistivity covers much wider range, $2.6 \cdot 10^2 – 2.4 \cdot 10^3$ Ω.cm (almost tenfold variation) [5]. Because of the fact that crystal structure remains unchanged (in the experimental uncertainty range), such high variations indicate possible different oxygen content, different oxidation state of iron and different distribution of the cations in La-Sr-O rock-salt layers. All mentioned factors are strongly affected by the compound synthesizing conditions, namely by maximal temperature of synthesis and if oxidizing or reducing atmosphere was applied.

---

* To whom all correspondence should be sent:
E-mail: dneov@abv.bg

The goal of the current study was applying neutron diffraction, Mössbauer spectroscopy together with first-principle quantum-mechanical modeling to reach more reliable interpretation of LaSrFeO$_4$ structural data.

EXPERIMENT

Synthesis of LaSrFeO$_4$ was carried out by a nitrate-citrate method. Highly pure La$_2$O$_3$, Sr(NO$_3$)$_2$ and Fe(NO$_3$)$_3$.9H$_2$O were used as starting materials. The oxides and nitrates in respective stoichiometric ratio were dissolved in aqueous solution of nitric acid at heating and stirring. After complete dissolution citric acid in molar ratio 3.3:1 in relation to metal ions was added. The obtained clear solution was concentrated and dried at 200 °C. After drying, the self-combustion of the dry residue gave powdered precursors. A thermal treatment at temperatures from 700 to 1100 °C for 2 hours and simultaneous thermogravimetry/ differential thermal analysis (TG/DTA) was performed to observe the thermal decomposition of precursors. The TG/DTA measurements were made using Q-1500-D derivatograph at heating rate of 10 °C/min in the temperature range from 15 °C to 1000 °C in air atmosphere. The ceramic powder was pressed to bars and sintered at 1250 °C for 5 h and at 1400 °C for 1 h. Phase composition of obtained ceramic powders was characterized by X-ray diffraction. The microstructure of sintered samples was observed by scanning electron microscopy (SEM) using JEOL-JSM-35CF microscope.

Neutron diffraction (*ND*) experiment was carried out on E9 – Fine Resolution Powder Diffractometer at the BER II reactor of Helmholtz Centre Berlin for Materials and Energy. The powder sample 5g in weight was measured at room temperature. The wavelength of neutron beam was $\lambda = 0.1797$ nm. The structure was refined using FullProf program [7], by minimization of the weighted sum: $\chi^2 = \Sigma_i w_i [y_{iobs}(2\theta) - y_{ical}(2\theta)]^2$.

Mössbauer spectroscopy measurements were implemented using a standard transmission technique with a source of ^{57}Co in Pd. The sample was mounted in close-cycle helium cryostat and the resonance γ-ray absorption spectra were measured in the temperature range from 9.3 K to 295 K. Calibration of the velocity scale was made by ARMCO iron as standard absorber.

MODELLING

The model calculations were performed via the ultrasoft pseudopotentials and a plane wave basis set as implemented in the Quantum Espresso (QE) integrated suite of computer codes [8]. The generalized gradient approximation (GGA) of Perdew, Burke and M. Ernzerhof (PBE) [9] was used. The applied pseudopotentials with QE were ultrasoft, generated by the Vanderbilt scheme [10] and taken from the QE distribution [8]. The wave functions at each k-point are represented by the numerical coefficients of a finite set of plane waves, determined by a kinetic energy cut-off. The k-point sets were generated automatically, following the Monkhorst – Pack (MP) scheme [11]. To decrease the number of k-points needed to sample the Brillouin zone, the crystallographic symmetry of the sample was considered. The computation of interatomic forces was performed by the Hellmann-Feynman theorem [12]. Hubbard corrections (GGA+U) as implemented in QE approach were performed in order to take into account the strong on-site Coulomb interaction (U) presented in the localized 3d electrons of Fe, and in turn to describe well the band gap. In the present work, the GGA+U corrections of Dudarev et al. [13] are used, which depends on the effective Coulomb interaction U$_{eff}$=U−J, with J being the screened exchange energy. The used in calculations value for U$_{eff}$ was taken to be 4.5 eV [13]. A Gaussian electron energy level smearing with width of 0.08 eV was introduced.

The initial calculations started with convergence studies to determine the kinetic energy cut-off and the size of the MP grid. Iterations using self-consistent field (SCF) cycles were performed until the difference of the total energy was checked less than 10^{-5} eV. The forces in the unit cell and the lattice vectors were relaxed using ground state structural optimization via the Broyden algorithm as implemented in the QE. Calculations were performed until the interatomic force became less than 7×10^{-3} eV/Å and the cell pressure (for the lattice constant calculations) was less than 0.05 kbar.

EXPERIMENTAL RESULTS AND DISCUSSION

Rietveld analysis of neutron diffraction data of LaSrFeO$_4$ collected at room temperature [3], Fig. 1, was performed using scattering lengths 8.24, 7.02, 9.450 and 5.803 fm [10^{-15}m], for La, Sr, Fe and O nuclei, respectively. The background of multidetector data was approximated by six parameters polynomial curve.

The fit with tetragonal I4/mmm space group, i.e. K$_2$NiF$_4$-type structure [14], Fig. 2, was successful. The Bragg R-factor was 4.52 and $\chi^2 = 3.05$. The calculated unit cell parameters are a = b = 3.8694 Å and c = 12.7322 Å, respectively. These values are in agreement with the previously reported data, which depending on the synthesis conditions lie in the

range: a = 3.86–3.88 Å, and c = 12.687–12.760 Å, [1,2]. The atomic positions, isotropic temperature factors (B) and the occupancy of equivalent positions are given in Table 1.

The calculated axial and equatorial bond lengths Fe-O2$_{axial}$ = 2.172Å and Fe-O1$_{eq}$ = 1.935Å in FeO$_6$ octahedron differ by nearly 10%, but the axial symmetry along the c-axis is preserved and the angle O2-Fe-O2 is exactly 180°. Surprisingly high is the difference between the isotropic temperature factors of oxygen O1 (B = 0.699 Å^2) and O2 (B = 1.724 Å^2) as is shown in Table 1. This difference seems to be characteristic for all A-substituted R-P phases [4–6]. Most probably, it is a direct result of the quasi-random distribution (as calculated by *ab initio* modeling) of La^{3+} and Sr^{2+}-ions in the rock-salt layer (bilayer) around the apical oxygen (O2) of FeO$_6$ octahedron. The different arrangement, effective ionic radii and electrical charge of La^{3+} (R=1.032Å) and Sr^{2+} (R = 1.18 Å) disturb the equilibrium position of O2, what is registered by neutron scattering as a higher value of the Debye-Waller factor. The significant influence of La and Sr distribution on the resonance γ-spectra was observed by low temperature Mössbauer experiment, as well.

Neutron diffraction data of LaSrFeO$_4$ point to tetragonal structure in which lanthanum and strontium atoms are distributed randomly among the (4e) Wyckoff positions. Moreover, from diffraction data it follows that the Fe atoms are crystallographically equivalent and hence experimentally undistinguishable. Fig. 3 shows the Mössbauer resonance absorption spectrum of LaSrFeO$_4$ measured at 9.3 K. A model of two sextets with equal effective magnetic field (H$_{eff}$), isotrope shift (IS) and different quadroupole splitting (Q) plus a small contamination singlet was accepted. Fig. 3 and Table 2 illustrate a good coincidence with the experimental data. A posible interpretation of this result can be done by the admission (in contradiction with diffraction data) of two non equivalent Fe ions in the unit cell. In reality, the variable distribution of La^{3+} and Sr^{2+} ions in the second coordination sphere of Fe ions influences (as follows from the model calculations) the spatial electrons distribution, as well as,
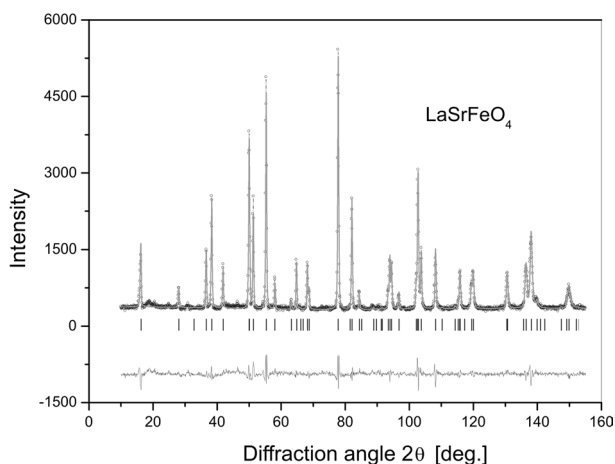
Fig. 1. Neutron diffraction spectrum of LaSrFeO$_4$. Peak positions and difference curve are shown below the experimental points and fitting curve
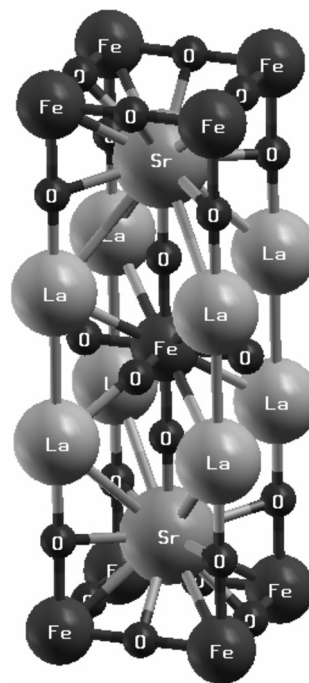
Fig. 2. Crystal structure of LaSrFeO$_4$

Table 1. Crystal structure parameters of LaSrFeO$_4$, obtained by Rietveld analysis of neutron diffraction data, T = 298 K; La and Sr ions occupy the Wyckoff position (4e)

Atom	Atomic positions			B	Occupancy	
	x	y	z			
La, Sr	0.	0.	0.3580(5)	0.643	4	(4e)
Fe	0.	0.	0.	0.565	2	(2a)
O1	0.	0.5	0.	0.699	4	(4c)
O2	0.	0.	0.1703(7)	1.724	4	(4e)
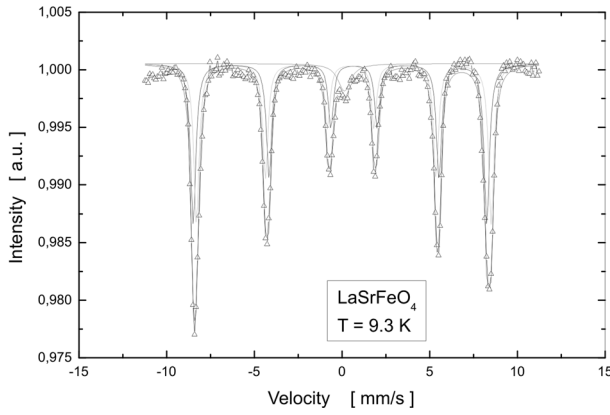
Fig. 3. Mössbauer spectrum of LaSrFeO$_4$ at 9.3 K. The singlet is due to <5% contamination phase
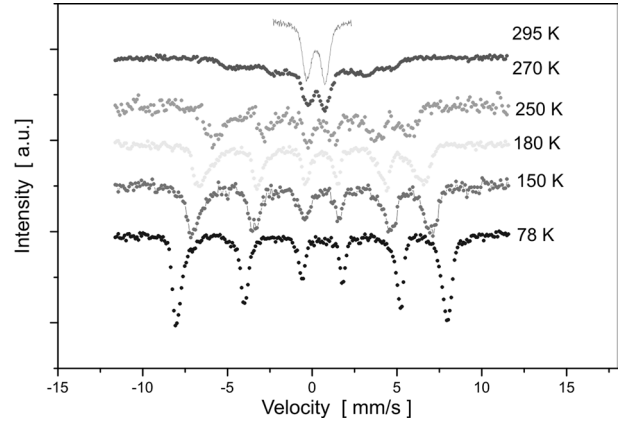
Fig. 4. Mössbauer spectra of LaSrFeO$_4$ measured in the interval 78–295 K

the position of the apical oxygen O2, thus changing the symmetry and intensity of the electrical field in FeO$_6$ octahedron. The Q value of the sextets is relatively stable as a function of T below the liquid nitrogen temperature and converges to nearly equal value above 150 K. The obtained values of isomer shift are characteristics for high spin state of Fe^{3+} (S=5/2).

Mössbauer spectra collected in the temperature interval from 78 K to 295 K are presented in Fig. 4. The Mössbauer spectroscopy measurements at room temperature reveal a small quantity of Fe^{4+} in the studied sample in good accordance with [2], where by direct chemical method (titration) Fe^{4+} content of about 10% was detected in LaSrFeO$_4$. The best fit of resonance curve at T = 295 K was done by two-component quadroupole doublet. Taking into account the unique position of Fe ions in the structure, a model with equal Q and different IS of constituent doublets was applied. The values of Q and IS

of components are given in Table 2. The presence of two doublets: IS = 0.42 mm/s and 0.27 mm/s is a contribution from the different oxidation states of iron atoms. According to [2], these two components can be attributed to Fe^{3+} and mixed Fe^{3+} – Fe^{4+} state of iron, respectively. The deduced parameters of hyperfine interactions parameters H$_{eff}$, Q and IS are summarized in Table 2.

MODEL OF THE LOCAL MICROSTRUCTURE

The crystal structure of LaSrFeO$_4$, [1–3], is tetragonal, space group No 139 – I4/mmm. Every Fe atom is followed by oxygen and then either La or Sr atoms along the Z axis. All possible local configurations are numbered by 1 to 4 as follows: (1) La-O-Fe-O-La, (2) La-O-Fe-O-Sr, (3) Sr-O-Fe-O-La and (4) Sr-O-Fe-O-Sr, respectively. Such configurations

Table 2. Mössbauer hyperfine interactions parameters calculated from the data presented in Fig. 2 and Fig. 3.

T [K]		H [T]	Q [mm/s]	IS (δ) [mm/s]	
9.3	Sextet 1	52.00	−0.40	0.377	
	Sextet 2	52.21	−0.195	0.391	
	Singlet	–		0.226	
78	Sextet 1	49.30	−0.39	0.376	
	Sextet 2	49.47	−0.20	0.446	
150	Sextet 1	42.06	−0.28	0.378	
	Sextet 2	44.55	−0.29	0.391	
180	Sextet 1	38.44	−0.284	0.344	
	Sextet 2	41.68	−0.29	0.367	
295	Doublet 1	–	−1.09	0.27	56%
	Doublet 2	–	−1.00	0.42	44%

Table 3. Positioning of atoms in the perovskite unit cell. X,Y,Z are the coordinates in case of local configurations (2) La-Sr and (3) Sr-La (I4/mmm symmetry) and XYZ' are the coordinates in case local configurations (1) La-La and (4) Sr-Sr (P4/mmm symmetry)

Atom	X	Y	Z	Z'
O	0.0	0.0	0.1706	0.1729
	0.0	0.0	0.8294	0.82710
O	0.5	0.5	0.3294	0.3539
	0.5	0.5	0.6706	0.6461
O	0.0	0.5	0.0	0.0
	0.5	0.0	0.0	0.0
O	0.5	0.0	0.5	0.5
	0.0	0.5	0.5	0.5
Fe	0.0	0.0	0.0	0.0
	0.5	0.5	0.5	0.5
Sr	0.0	0.0	0.3581	0.3690
	0.0	0.0	0.6419	0.6310
La	0.5	0.5	0.1419	0.1630
	0.5	0.5	0.8581	0.8370

should lead to different environment for the Fe atoms and hence Mössbauer effect should distinguish three different sextets since configurations (2) and (3) are equivalent in the terms of local environment and lead to the same sextet. In case of random distribution of La and Sr atoms in the crystal unit cell all configurations (1)–(4) should take place with equal frequency and all three sextets should be present. If configurations (1) and (4) are more likely we should observe two sextets and if only (2) and (3) are eligible we should observe only one sextet contrary to the experiment. It should be noticed in addition, that configurations (2) and (3) disrupt the local symmetry along *c*-axis – the inversion substitutes La atom with Sr and the opposite. Furthermore, La³⁺ and Sr²⁺ have different ionic radii and it is rather doubtful that their unique positions in the unit cell are preserved after substitution. Atomic positions in the unit cell are arranged in Table 3 in the case of local configurations (1) La-La and (4) Sr-Sr.

The computer simulation of the local configurations (1) and (4) mentioned before, revealed that strontium and lanthanum positions, as well some of oxygen positions listed in Table 3 are not stable. Minimum of the internal energy is reached if they are slightly displaced along the c-axis; these new values are designated in Table 3 by Z'. Such change of the atomic positions causes the change of the space group from I4/mmm to P4/mmm, as well.

To find the most suitable positions of La atoms substituted by Sr ones, different structures representing the geometrically equivalent positions were tested. In order to obtain results for the stability of the different structures, calculations were

performed for a fixed volume with relaxation of the atomic positions. The most stable configuration was found to be the structure where the Sr and La atoms are grouped in double layers, randomly distributed between perovskite layers formed by FeO₆ octahedra.

When the concentration of Sr and La equals to ½ (the case of LaSrFeO₄), the ratio of probability of configurations (1) or (4) – P_{1+4} and probability of configurations (2) or (3) – P_{2+3} can be represented by the Boltzman factor $P_{1+4}/P_{2+3} = \exp(-V/2kT)$. The configuration potential $V \approx -0{,}22$ eV was calculated under the assumption of finding the atoms in their X, Y and Z' equilibrium positions, given in Table 3. At room temperature the Boltzman factor is $\exp(V/2kT) \approx 70.5$ hence the low-symmetry configurations (2) and (3) should not take place. It should be noted that this conclusion refers to the equilibrium state of LaSrFeO₄ which is not necessary the case. Taking into account the moderate maximal temperature at which the sample was synthesized and assuming equilibrium temperature of the compound of about 600K, we obtain factor $\exp(V/2kT) \approx 8{,}4$. Therefore, from this result it follows that low symmetry configurations should be observed with very low intensity or not observed at all.

LOCAL CHARGE DENSITY DISTRIBUTION

For both practical and theoretical point of view it is important to determine how the electron density around Fe ions changes at the substitution of La by Sr. Lanthanum has one 5d electron and two 6s electrons or 3 valence electrons. The rest of the electrons (54 = 57–3) belong to the "core" and do not participate in chemical bonds. Using *"ab initio"* methods for
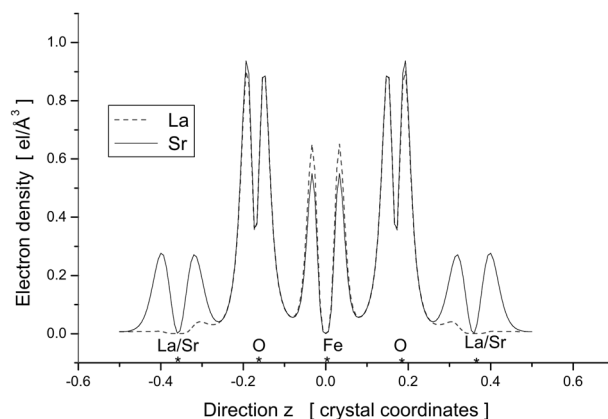
Fig. 5. Local distribution of the electron density along (001) direction for La-O-Fe-O-La and Sr-O-Fe-O-Sr configurations

calculation of electronic structure of Sr-containing compounds it is common to take into consideration not only two 5s electrons of strontium but also six 4p electrons or eight electrons altogether. Charge distribution corresponding to local configuration (1) and (4) is depicted in Fig. 5.

Comparing the charge distribution in both cases we observe significant influence of La and Sr on the electron density around Fe atoms, Fig. 5. Evidently, the wide accepted opinion that the oxygen is shielding Fe ion from the influence of La and Sr is not justified in the case of LaSrFeO$_4$. The electron density around Fe is higher in presence of La atom. The model calculations of electron density distribution clearly demonstrate the influence of atoms from the second coordination sphere of Fe-ion on the electric field in FeO$_6$ octahedron thus providing a plausible explanation of the observed two Mössbauer sextets at low temperature.

CONCLUSIONS

Results of neutron diffraction and Mössbauer spectroscopy study of LaSrFeO$_4$, synthesized by nitrate citrate method, were compared with quantum mechanical model calculations. The random substitution of lanthanum by strontium, although widely accepted, was found to be energetically non favorable. It was found that the internal energy is minimal in the case when La^{3+} and Sr^{2+} ions form La-La and Sr-Sr bilayers in the rock-salt layers which are randomly distributed in the structure. The data from low temperature Mössbauer spectroscopy were interpreted on the basis of established K$_2$NiF$_4$ – type crystal structure. A model of two sextets verified by model calculations of electron density distribution was used for deconvolution of the resonance absorption spectra.

REFERENCES

1. J. Soubeyroux, P. Courbin, L. Fournes, D. Fruchart, G. Le Flem, *J. Solid State Chem.* **31**, 313 (1980).
2. A. Jenings, S. Skinner and Ő. Helgason, *J. Solid State Chem.*, **175**(2), 207 (2003).
3. S. Neov, L. Dabrowski, N. Velinov, M. Machkova, D. Neov, I. Tobolik-Jarzebska, O. Prokhnenko, in: 7th International Conference of the Balkan Physical Union, Alexandroupolis, Greece, 9–13 September 2009, AIP Conference Proceedings, A. Angelopoulos, T. Fildisis (eds), vol. 1203, 2009, p. 246.
4. T. Omata, K. Ueda, H. Hosono, *Phys. Rev. B*, **49**(15), 10194 (1994-I).
5. T. Omata, K. Ueda, N. Ueda, M. Katada, S. Fujitsu, T. Hashimoto, H. Kawazoe, *Solid State Comm.*, **88**(10), 807 (1993).
6. M. Shimada, M. Koizumi, *Mat. Res. Bull.*, **11**, 1237 (1976).
7. J. Rodriguez-Carvajal, FullProf Version 3.5d Oct. 1998, LLB (CEA-CNRS).
8. P. Giannozzi, et al., *J. Phys. Condens. Matter.*, **21,** 395502 (2009), available via http://www.quantum-espresso.org.
9. J. Perdew, K. Burke, M. Ernzerhof, *Phys. Rev. Lett.*, **77,** 3865 (1996).
10. D. Vanderbilt, *Phys. Rev. B*, **41,** 7892 (1990).
11. H. Monkhorst, J. Pack, *Phys. Rev.* B, **13,** 5188 (1976).
12. R. Feynman, *Phys. Rev.*, **56** 340 (1939).
13. S. Dudarev, G. Botton, S. Savrasov, C. Humphreys, A. Sutton, *Phys. Rev. B*, **57**, 1505 (1998).
14. S. Ruddlesden, P. Popper, *Acta Cryst.*, **10**, 538 (1957).

СТРУКТУРА НА LaSrFeO₄: НЕУТРОННА ДИФФРАКЦИЯ, МЬОСБАУРЕВА СПЕКТРОСКОПИЯ И МОДЕЛИРАНЕ

L. Dabrowski[1], Д. Неов[2]*, В. Антонов[2], М. Мачкова[3], С. Неов[2], В. Кожухаров[3]

[1] *Atomic Energy Institute, 05-400 Otwock, Swierk, Poland*
[2] *Институт за ядрени изследвания и ядрена енергетика, Българска академия на анауките, 1784 София, България*
[3] *Химикотехнологичен и металургичен университет, 1756 – София, България*

(Резюме)

Повишеният интерес към сложните окиси на преходните метали с перовскитна и перовскитоподобна структура през последните години е предизвикан от откриването на високо-температурната свръхпроводимост, а също така от възможността за приложението на тези окиси в високотемпературните горивни клетки (SOFC). В настоящето изследване бяха извършени опити по Мьосбаурова спектроскопия и неуронна дифракция върху съединението LaSrFeO₄, представляващо частен случай на Рудлесден-Попер фаза $A_{n+1}B_nO_{3n+1}$ с n=1. Синтезът на LaSrFeO₄ беше проведен по сравнително рядко използван метод от разтвори на изходните вещества. Получните данни бяха обяснени на базата на квантово-механично моделиране по метода *ab initio*. Експериментът по Мьосбаурова спектроскопия и моделните пресмятания показват че La и Sr атоми не се разпределят случайно в Уайкоф позициите (4e) на I4/mmm пространствена група както се предполагаше предварително, а преимуществено в двойни слоеве съставени от La или Sr. Тези двойни слоеве обаче не следват определена последователност в кристала. Моделните пресмятания на разположението на лантан и стронциевите атоми по оста *c* обяснява съществуването на два Мьосбаурови секстета при ниски температури въпреки единствената кристалографска позиция на желязото в елементарната клетка.

Cysteine modified silica submicrospheres as a new sorbent for preconcentration of Cd (II) and Pb (II)

I. Dakova[1],*, P. Vasileva[2], I. Karadjova[1]

[1] *Department of Analytical Chemistry*
[2] *Department of General and Inorganic Chemistry, Faculty of Chemistry, University of Sofia*
"St. Kliment Ohridski", 1 James Bourchier blvd., Sofia, Bulgaria

In this research, submicronsized silica (SiO₂) spheres with uniform spherical morphology are grown using the Stöber sol-gel process and subsequently, functionalized with (3-aminopropyl)-trimethoxysilane (APS). These spheres are further modified by chemical binding with L-cysteine (SiO₂-CYS). The composition, structure, morphology and surface properties of the particles obtained are characterized by using elemental analysis, SEM, XRD, Zeta potential and N_2 adsorption measurements. Experiments performed showed that SiO₂-CYS particles permit fast and quantitative sorption of Cd (II) and Pb (II) in the pH range 7-8 and could be used for the separation and preconcentration of Cd (II) and Pb (II) in water samples. Sorption procedure developed is characterized with high concentration factors and ensures quantification of 0.01 µg/L Cd and 0.1 µg/L Pb in various types of water samples. Relative standard deviation for the concentration range 0.01–1 µg/L Cd and 0.1–10 µg/L Pb varied between 4 and 11% for both elements. Analytical method is applied for the determination of Cd and Pb in river, lake and sea water and verified by parallel analysis using ICP-MS

Key words: amine functionalized silica submicrospheres, L-cysteine modification, solid-phase extraction, trace lead and cadmium, surface waters.

INTRODUCTION

High concentration of minerals (approximately 3%) and very low content of metal ions in highly salted sea lakes and sea waters are the two major problems that preclude the application of simple, direct instrumental approach for their analysis [1]. Therefore, the isolation and enrichment of analytes is a key stage of each analytical procedure for the determination of ultra trace concentrations. Methods based on solid phase extraction (SPE) are widely used for this purpose. The efficiency of SPE procedure depends mainly on the nature and properties of the sorbent material [2]. Among the many types of solid phases used in SPE, silica is the most common due to its advantageous characteristics of thermal and mechanical stability, no swelling and hydroxyl reactive groups [3]. Effectiveness and selectivity of the adsorbent may be improved by introducing suitable functional agents capable to react with the silanol groups on the silica surface [4]. Functionalization of silica particle surfaces is com-

monly achieved using layer-by-layer assembly [5], physical adsorption [6] and silane coupling agents [7,8]. In recent years, silica particles chemically modified with various ligands like 3-aminopropyltriethoxysilane [9], 8-hydroxyquinoline [10], thiourea [11], glycerol [12], thioacetamide [13], alizarin violet [14]. 2-aminothiazole [15] and etc. have been proposed in various SPE procedures. (3-aminopropyl)-trimethoxysilane (APS) functionalization is the most preferred method for obtaining exposed amine groups on silica surface. Cysteine (CYS) can be easily immobilized onto silica surface, previously functionalized with amine groups and in the same time it is a suitable ligand for metal ions sorption due to the presence of three functional groups (HSCH₂CH(NH₂)COOH) in the molecule. CYS has been already used to modify surface of the controlled pore glass [16], porous carbon [17], poly(hydroxyethylmethacrylate) microbeads [18] and silica gel [19]. However, the use of submicronsized silica spheres modified by cysteine for separation and preconcentration of trace metal ions has not been reported in the literature.

In the present work, we focus our attention on the synthesis and characterization of L-cysteine

---

* To whom all correspondence should be sent:
E-mail: idakova@chem.uni-sofia.bg

modified silica submicrospheres and their application for separation and preconcentration of trace analytes. Submicronsized SiO_2 spheres with uniform spherical morphology are prepared using a variation of the method developed by Stöber et al. [20]. Subsequently, the surface of these spheres is functionalized with (3-aminopropyl)-trimethoxysilane and further modified by chemical binding of L-cysteine to the functionalized surface using the bifunctional reagent (glutaraldehyde) (SiO_2-CYS particles). The characterization studies showed that SiO_2-CYS possess high affinity toward Cd (II) and Pb (II), ensuring very fast process of quantitative sorption. This new sorbent was successfully applied for SPE and determination of Cd and Pb in surface waters.

EXPERIMENTAL

Reagents

Tetraethylorthosilicate (TEOS, 99%, Fluka, Germany), ammonia (25 wt. % NH_3 in water), absolute ethanol (EtOH, 99.6%), doubly distilled water (DDW) and 3-aminopropyltrimethoxysilane, (APS Fluka, Germany) were used to prepare the bare silica (SiO_2) and amine-functionalized (SiO_2-NH_2) spheres.

The stock standard solutions of Cd (II), and Pb (II) (1000 µg/mL) were Titrisol, Merck (Darmstadt, Germany) in 2% HNO_3. All reagents used were of analytical reagent grade. Working standard solutions were daily prepared by appropriate dilution with DDW. L-cysteine, hydrochloric acid, nitric acid and glutaraldehyde (GLA, 25 wt.%) were provided from Sigma–Aldrich, Germany and used to prepare the cysteine-modified silica sorbent (SiO_2-CYS). The following buffer solutions were used for pH adjustment: CH_3COONa/CH_3COOH for pH 5–6 and KH_2PO_4 /NaOH for pH 7 and 8. All solutions used in the experiments were prepared using DDW.

Apparatus and characterization

Flame atomic absorption spectrometry (FAAS) measurements were carried out on a Perkin Elmer Zeeman 1100 B spectrometer (Überlingen, Germany) with an air/acetylene flame. The instrumental parameters were optimized in order to obtain maximum signal-to-noise ratio. Electrothermal AAS (ETAAS) measurements were carried out on a Perkin-Elmer (Norwalk, CT, USA) Zeeman 3030 spectrometer with an HGA-600 graphite furnace. The light sources used were hollow cathode lamps for Pb and electrodeless discharge lamps for Cd. Optimal instrumental parameters as recommended by the manufacturer are used. Elemental analysis was carried out with an universal CHNOS elemental analyzer Vario EL III (Elementar Analysensysteme GmbH, Germany). The centrifuge K-1000 (KUBOTA Corporation, Osaka, Japan) was used to separate silica microspheres and extracted metal solution in batch experiments. A microprocessor pH-meter (Hanna Instruments, Portugal) was used for pH measurements. X-ray diffraction (XRD) patterns were measured using Siemens D500 instrument with the CuKα radiation ($\lambda = 1.54$Å) in 2θ ranging from 15° to 85°. Scanning Electron Microscopy (SEM) of the silica particles was carried out using a JEOL JSM 5510 instrument operating at 10kV. A Nano ZS Zetasizer (Malvern Instruments Ltd.) was used to determine zeta (ζ) potential of the particles. The specific surface areas were determined by the BET method through N_2 adsorption at 77K.

Synthesis methods

Figure 1 presents the scheme of preparation of SiO_2-CYS particles by chemical binding of L-cysteine to amine-functionalized surface of SiO_2 submicrospheres.

Sol-gel synthesis of silica submicrospheres and surface functionalization. Silica submicron-sized particles were synthesized by the modified Stöber
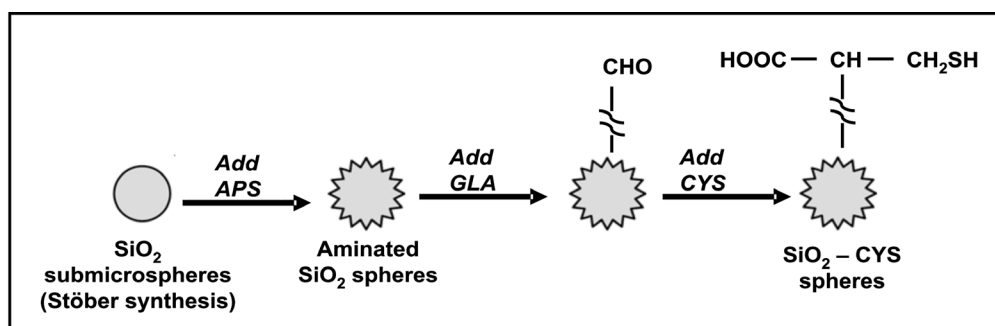
Fig. 1. Scheme of preparation of SiO_2-CYS particles

procedure [20] at optimized reaction conditions as it was described in a previous paper [21]. The reagents were mixed in two starting solutions. Firstly, TEOS (20.3 mL) was dissolved in absolute EtOH (94 mL). A second solution was prepared by mixing of ammonia solution (16.7 mL), distilled water (20.3 mL) and absolute EtOH (209 mL). The second solution was then rapidly added under magnetic stirring to the first solution and mixture was left to react for at least four hours at ambient temperature (22 °C). The final reactant concentrations were 0.25 mol/L TEOS, 0.5 mol/L NH_3 and 5 mol/L H_2O.

The silica particle surface was then functionalized with aminopropyl groups using a modified one-step process similar to that of Wu [22]. At our procedure 4 mL 3-aminopropyltrimethoxysilane (APS) was injected into the above reaction mixture and allowed to react for additional 12 h at room temperature under magnetic stirring. Upon completion of the reaction, a silica surface terminated with amine groups was obtained. For comparison, bare silica spheres without addition of APS were synthesized as well. The particles were then separated by centrifugation and purified by redispersion in ethanol (three times) and DDW (three times). Sonication was used to redisperse the particles in the desired solvents.

L-cysteine modification of aminated silica spheres. The cysteine was immobilized on the SiO_2-NH_2 using the bifunctional reagent glutaraldehyde (GLA). GLA solution (25%, 1 mL) was taken and made up to 40 mL with phosphate buffer (pH 7). SiO_2-NH_2 (1 g) was suspended in this solution and was stirred at room temperature in a nitrogen atmosphere to prevent oxidation. The reaction was allowed to continue for 1 h during which time a brown coloration was observed. The solid product was collected by filtration, washed with water and added to cysteine solution in phosphate buffer (50 mL) at pH 6. Nitrogen was slowly bubbled through the solution for five hours at room temperature (with stirring) and then the solution was left to stay for 2 days. The solid product was filtered and washed several times with DDW and dried under vacuum at room temperature. Four different types of functionalized silica samples were prepared by modification with cysteine using different SiO_2-NH_2 /CYS ratios.

Adsorption studies. Adsorption of Cd(II) and Pb(II) ions from aqueous solutions was studied in batch systems. Aqueous standard solution of (5 mL) containing investigated metal ions (1 μg/mL Cd and 10 μg/mL Pb), 5 mL of a buffer solution and 100 mg of SiO_2-CYS were mixed together in a plastic centrifuge tube. The mixture was stirred with an electric shaker for 15 min and then centrifuged at 3000 rpm for 5 min. In order to investigate the distribution ratio of elements studied, the supernatant was removed and

analyzed by FAAS as effluate. The SiO_2-CYS was washed with DDW and trace analytes were eluted from the sorbent particles by 2 mL 2 mol/L HNO_3 for 15 min. In order to investigate the degree of elution, after centrifugation the metal ions contents in the eluate was determined by FAAS.

Sorption characteristics of the sorbent

The degree of sorption, adsorption capacity and distribution ratio are calculated using the following equations:

$$E = [(C_i − C_f)/C_i] . 100$$
$$Q = (C_i − C_f) . V/m$$
$$D = Q/C_f$$

where: E is degree of sorption (%), Q is the adsorption capacity (μmol/g), D is the distribution ratio (mL/g); C_i and C_f are initial and final concentrations of metal ions (μmol/mL), respectively. V is the volume of the solution (mL) and m is the mass of SiO_2-CYS (g).

RESULTS AND DISCUSSIONS

Characterization of bare and amine-functionalized SiO_2 submicrospheres

The SiO_2 particles synthesized in this study show an X-ray diffraction pattern, typical of amorphous solids (Fig. 2.)

Fig. 3a and b illustrate typical SEM micrograph exemplifying the morphology and size distribution obtained for the bare silica (SiO_2) particles. Table 1 summarizes the main surface characteristics of the bare silica (SiO_2) and amine-functionalized (SiO_2-NH_2) particles.

The SEM image proves that the methodology employed to fabricate bare silica particles provides a
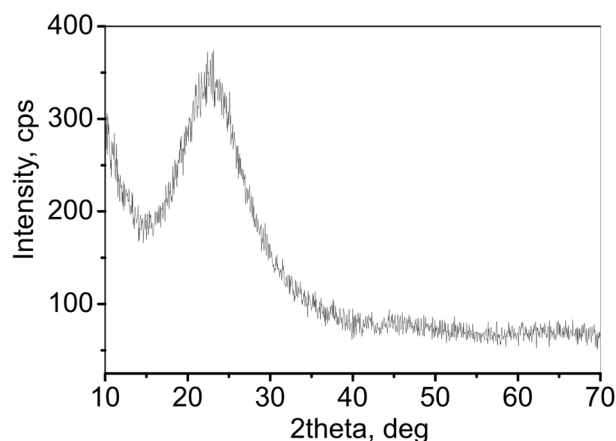
Fig. 2. X-ray diffraction pattern of bare SiO_2 particles

(a)

(b)
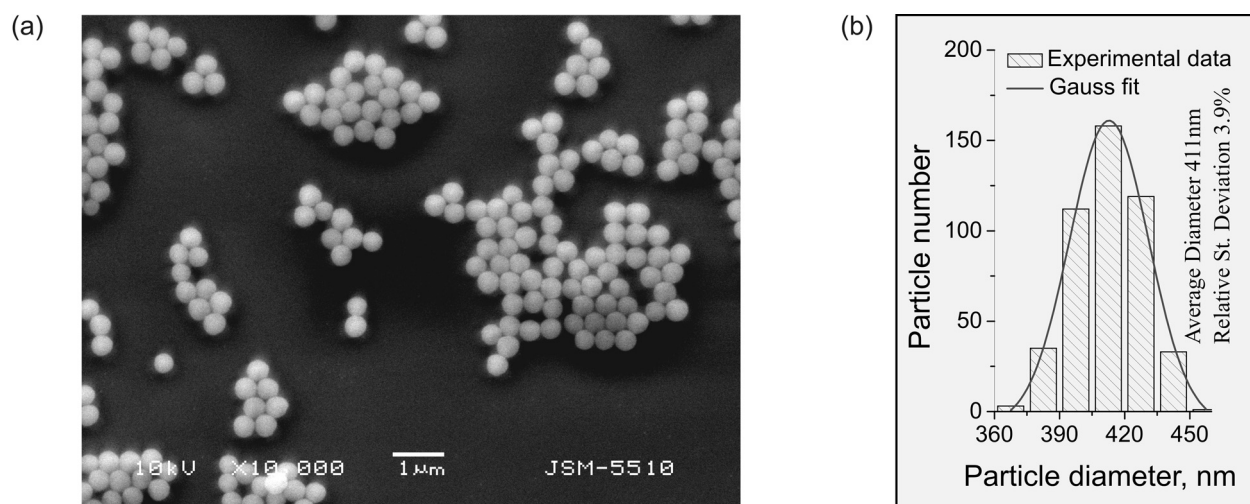
Fig. 3. (a) SEM image showing the representative morphology of synthesized via sol-gel procedure silica submicron-sized particles; (b) particle size-distribution histogram determined by counting of 450 particles from different SEM images using Image J software

reliable control on the particle form and size. Indeed, perfectly spherical and monodispese silica particles with smooth surface can be obtained at the reaction conditions of the implemented sol-gel method. The measured average size of the bare silica spheres was 411±16 nm. The process of amine-functionalization did not change the morphology of silica spheres. As it can be seen from Table 1, there is no difference in the average diameter, size distribution and specific surface area of silica particles before and after the functionalization with APS.

Assuming nonporous particles, the specific surface areas of the particles were calculated on the base of SEM particle size and compared with measured BET surface areas in Table 1. The determined BET surface areas are larger than the calculated values, but these values are on the same magnitude, suggesting nonporous nature of the particles [22].

The Zeta potential measured indicates that bare SiO_2 spheres reach $-$ 56.9 mV at pH 7. It is clearly indicated from measuring of the ζ-potential that the surface charge density of microspheres decreases (in absolute value) with decreasing pH. The ζ-potential data at pH 7 indicate that the negative surface charge on the spheres with APS on their surface is twice reduced. Moreover, the effect of basic amine groups on the silica surface is reflected in the positive value of ζ-potential at pH 2.6, which causes a considerable shift of IEP to higher pH value [22]. The ζ-potential results and data from elemental analysis of SiO_2-NH_2 particles (Table 2) confirm a successful surface functionalization of silica submicrospheres with propylamine groups.

Characterization studies of SiO_2-CYS as a sorbent for SPE

Four different adsorbents were prepared from SiO_2-NH_2 by grafting different quantities of cysteine groups on the surface of silica (Table 2). The elemental analysis was carried out on the SiO_2-NH_2 and SiO_2-CYS sorbents in order to determine C, N and S contents. It is seen that the prepared SiO_2-CYS includes O, N and S donor atoms. The experimental results presented (Table 2) suggest that SiO_2-NH_2

Table 1. Main characteristics of bare and amine-functionalized silica submicrospheres

Sample	ζ^* (mV) (at pH 7)	ζ^* (mV) (at pH 2.6)	Size (nm)	S_{BET} (m^2/g)	S_{calc} (m^2/g)
SiO_2	$-$56.9	$-$14.7	411±16	13	7
SiO_2-NH_2	$-$22.1	+50.8	409±17	12	9

*with 1mM added NaCl at 25 °C.

Table 2. Elemental analysis of the prepared SiO_2-CYS sorbents

Sorbent	SiO_2-NH_2/CYS (g/mmol)	Elemental analysis		
		C (%)	N (%)	S (%)
SiO_2-NH_2	1 : 0	4.2	1.58	–
SiO_2-CYS-0.2	1 : 0.2	7.53	1.98	1.14
SiO_2-CYS	1 : 0.4	10.99	2.57	2.90
SiO_2-CYS-0.6	1 : 0.6	10.35	2.13	2.24
SiO_2-CYS-1.0	1 : 1.0	8.87	2.04	1.25

has been successfully modified by cysteine. The results obtained showed that the sulphur content is highest in SiO_2-CYS (2.90%). The content of nitrogen and sulphur in SiO_2-CYS were estimated as 1.82 and 0.91 mmol/g sorbent, respectively.

Optimization of the experimental conditions for preconcentration of Cd(II) and Pb(II)

The acidity of sample (pH value) is an important condition for efficient retention of the trace elements on the sorbent. Its influence strongly depends on the nature of the sorbent used. The newly synthesized SiO_2-CYS contains thiol and carboxylic functional groups therefore taking into account that pKa values of -SH and -COOH groups in cysteine are about 8 and 2 respectively [23] the sorption of the investigated cations should be strongly affected by pH of the sample solution. The pH influence on the degree of sorption, distribution ratios of Cd (II) and Pb (II) and their adsorption capacities were investigated in the pH range 5–8 by batch equilibrium procedure (Table 3).

The trend observed is an increased sorption and adsorption capacities for investigated cations with increasing pH of the solution. At low pH (around 5-6) the degree of sorption and distribution ratio was generally low for investigated metal ions which might be explained with the protonation of the thiol and carboxylic functional groups thus eliminating their ability to form complexes with metal ions. The

degree of sorption for Pb (II) is > 95% in the pH range from pH 7 to pH 8, for Cd (II) quantitative sorption is achieved at pH 8. At higher pH values (>9), the decrease in the degree of sorption can be attributed partly to the formation of metal hydroxide complexes or to the dissolution of the SiO_2-CYS sorbent. Finally, pH 8 could be accepted as optimal for simultaneous sorption of Cd (II) and Pb (II) on SiO_2-CYS sorbent.

The influence of various parameters (sorption and desorption time, eluent volume and concentration) on the solid phase extraction efficiencies of SiO_2-CYS for the preconcentration of Cd(II) and Pb(II) from their solutions at pH 8 was investigated. The kinetics of the Cd(II) and Pb(II) sorption and desorption were examined in a batch system with 100 mg of the SiO_2-CYS particles for 5–40 min. The adsorbed Cd(II) and Pb(II) ions were desorbed by treatment with 2 mol/L HNO_3 at continuous stirring. It was established that the saturation values were gradually reached within 15 min, so the adsorption was sufficiently fast for practical applications. The Cd(II) and Pb(II) ions could be quantitatively eluted for 15 min.

The effect of the eluent volume on the metal desorption was investigated in the range of 1–5 mL 2 mol/L HNO_3 and the eluent acidity influence – in the range of 0.5–4.0 mol/L HNO_3. The full desorption of Cd(II) and Pb(II) was reached when the adsorbed Cd(II) and Pb(II) were eluted with 2 mL 2 mol/L HNO_3.

Table 3. Comparison of the degree of sorption (E), distribution ratio (D) and adsorption capacity (Q) of Cd(II) and Pb(II) extraction by SiO_2-CYS.

pH	Degree of sorption E (%)		Distribution ratio D (mL/g)		Adsorption capacity Q (µmol/g)	
	Cd	Pb	Cd	Pb	Cd	Pb
5	18±3	20±3	22	25	0.35	0.47
6	55±2	87±2	122	674	0.81	4.20
7	75±2	>99	305	9504	2.57	4.75
8	97±1	>99	3197	9504	8.63	4.75
9	89±2	86±2	808	667	7.92	8.2

Table 4. Comparative results for Cd and Pb content in surface waters

Sample	Cd (μg/L) [mean/RSD,%]		Pb (μg/L) [mean/RSD,%]	
	SPE (SiO$_2$-CYS)	ICP MS[*]	SPE (SiO$_2$-CYS)	ICP MS[*]
Black sea, Krapets	0.05/11	0.06/23	1.8/8	1.5/7
Black sea, Kamchia	0.03/11	<0.05	0.6/8	0.7/16
Varna lake, northwest	0.09/11	0.07/23	2.1/7	1.8/7
Beloslavsko lake, west	0.15/10	0.1/21	1.6/8	1.4/7
River Iskar (Novi Iskar)	0.09/10	0.092/9	0.2/8	0.18/7
River Iantra (V. Tarnovo)	0.03/11	0.024/15	0.1/10	0.11/7

*ICP MS results obtained in Green Analytical Methods Academic Centre, University of Plovdiv

Application of SiO$_2$-CYS sorbent

The prepared SiO$_2$-CYS was used for the determination of Cd (II) and Pb (II) in surface water samples, from defined monitoring stations in Bulgaria and shown in Table 4. After sampling, the water samples were filtered through cellulose filter membranes of 0.2 μm for the removal of suspended matter. The 100 mg SiO$_2$-CYS particles (placed in a plastic centrifuge tube) were stirred with 50 mL sea water (original pH 8.2) spiked with Cd (1 ng) and Pb (10 ng) for 15 min. After centrifugation, the supernatant is removed and the sorbent is washed twice with DDW. The loaded cations were eluted with 2 mL 2 mol/L HNO$_3$. The cation amount in the eluate is determined by ETAAS. Recoveries for investigated elements in spiked sea samples varied in the range 93–98%. Results obtained by the proposed analytical procedure were compared with direct ICP-MS measuremenst (Table 4) and very good agreement was observed.

Analytical procedure developed permits quantification of 0.01 μg/L Cd and 0.1 μg/L Pb in various types of water samples. Relative standard deviation for the concentration range 0.01–1 μg/L Cd and 0.1-10 μg/L Pb varied between 4 and 11% for both elements. Model experiments performed showed that proposed preconcentration procedure could be combined with field sampling and next transportation of water samples to the laboratory thus avoiding any sample contaminations due to the additions of conservation reagents .

CONCLUSIONS

Submicrometer silica spheres functionalized with aminopropyl groups are prepared trough a one-step process. Chemical binding of L-cysteine to the functionalized surface of the silica support using glutaraldehyde as a bifunctional reagent are made.

It is observed that the density of surface capping by thiol groups can be easily controlled by changing the ratio of SiO$_2$-NH$_2$ to L-cysteine. Its optimal value is found to be 1:0.4 g/mmol.

The new sorbent based on cysteine modified silica submicrospheres is found to be suitable for successful separation and preconcentration of Cd (II) and Pb (II) in water samples. The SiO$_2$-CYS sorbent shows a good efficiency even in the presence of complex matrices such as Black sea water and recommended preconcentration procedure could be combined with field sampling and sample transportation.

REFERENCES

1. J. -F. Peng, R. Liu, J.-F. Liu , B. He, X. -L. Hu, G. -B. Jiang, *Spectrochim. Acta B,* **62,** 499 (2007).
2. V. Camel, *Spectrochim. Acta Part B*, **58,** 1177 (2003).
3. P.K. Jal, S. Patel, B.K. Mishra, *Talanta,* **62**, 1005 (2004).
4. K. Kupiec, P. Konieczka, J. Namiesnik, *Crit. Rev. Anal. Chem.*, **39,** 60 (2009).
5. A. P. R. Johnston, E. S. Read, F. Caruso, *Nano Lett.*, **5**, 953 (2005).
6. I. Roth, F. Simon, C. Bellmann, A. Seifert, S. Spangs, *Chem.Mater.*, **18**, 4370 (2006).
7. A. P. Fhilipse, A. Vrij, *J. Colloid Interface Sci.*, **128**, 121 (1989).
8. A. van Blaadaren, A. Vrij, *J. Colloid Interface Sci.*, **156**, 1 (1993).
9. N. Tokman, S. Akman, M. Ozcan, *Talanta*, **59**, 201 (2003).
10. O. Zaporozhets, N. Petruniock, V. Sukhan, *Talanta*, **50,** 865 (1999).
11. A. Safavi, N. Iranpoor, N. Saghir and S. Momeni, *Anal. Chim. Acta*, **569,** 139 (2006).

12. Z. H. Xie, F.Z. Xie, L. Q. Guo, X.C. Lin, G. N. Chen, *J. Sep. Sci.,* **28**, 462 (2005).
13. M. A. A. Akl, I. M. Kenawy, R. R. Lasheen, *Anal. Sci.,* **21**, 923 (2005).
14. G. R. Castro, V. M. Cristante, C. C. F. Padilha, S. M. A. Jorge, A. O. Florentino, A. G. S. Prado, P. M. Padilha, *Microchim. Acta*, **160**, 203 (2008).
15. Q. He, X. Chang, X. Huang, Z. Hu, *Microchim. Acta*, **160**, 147 (2008).
16. H. A. M. Elmahadi, G. M. Greenway, *J. Anal. Atom. Spectrom.,* **8,** 1011 (1993).
17. T. C. Miller, J. A. Holcombe, *Anal. Chim. Acta*, **455,** 233 (2002).
18. A. Disbudak, S. Bektas, S. Patır, O. Genc, A. Denizli, *Sep. Pur. Techn.*, **26**, 273 (2002).
19. M. A. Abu-Daabes, N. G. Pinto, *Chem. Eng. Sci.*, **60**, 1901 (2005).
20. W. Stöber, A. Fink, E. Bohn, *J. Colloid Interf. Sci.,* **26**, 62 (1968).
21. G. Simeonova, S. Anachkov, P. Vasileva, C. Dushkin, in: Nanoscience & Nanotechnology, E. Balabanova, I. Dragieva (eds), vol. 7, Heron Press, Sofia, 2007, p. 66.
22. Z. Wu, H. Xiang, T. Kim, M. –S. Chun, K. Lee, *J. Colloid Interf. Sci.,* **304**, 119 (2006).
23. N. A. Rey, O. W. Howarth, E. C. Pereira-Maia, *J. Inorg. Biochem.*, **98**, 1151 (2004).

МОДИФИЦИРАНИ С ЦИСТЕИН СУБМИКРОННИ СФЕРИ ОТ СИЛИЦИЕВ ДИОКСИД, КАТО НОВ СОРБЕНТ ЗА КОНЦЕНТРИРАНЕ НА Cd (II) И Pb (II)

И. Дакова[1],*, П. Василева[2], И. Караджова[1]

[1] *Катедра аналитична химия*
[2] *Катедра Обща и неорганична химия, Химически факултет, Софийски университет „Св. Кл. Охридски“, бул. „Джеймс Баучър“ № 1, София, България*

(Резюме)

Силициев диоксид със субмикронни размери и перфектна сферична морфология е синтезиран по зол-гел метода на Stöber и след това е функционализиран с (3-аминопропил)-триметоксисилан (APS). Получените сферични частици са модифицирани чрез химично свързване с L-цистеин (SiO₂-CYS). Съставът, структурата, морфологияга и повърхностните им свойства са охарактеризирани с помощта на елементен анализ, SEM, XRD, измервания на ζ-потенциал и адсорбция на N₂. Показано е, че сорбцията на Cd(II) и Pb(II) върху SiO₂-CYS е бърза и количествена при pH 7, и че този сорбент може да се използва за разделяне на концентриране на Cd(II) и Pb(II) във водни проби. Предложената процедура се характеризира с висок коефициент на концентриране, а границите на откриване в различни типове водни проби за Cd и Pb са 0.01 µg/L и 0.1 µg/L, съответно. Относителното стандартно отклонение в концентрационния интервал 0.01–1 µg/L за Cd и 0.1–10 µg/L за Pb варира между 4 и 11% за двата елемента. Аналитичният метод е приложен за определяне на Cd and Pb в речна, езерна и морска вода и е верифициран чрез ICP-MS анализ.

Single crystal structure of pure and Zn ion exchanged clinoptilolite: Comparison of low temperature and room temperature structures and Cu vs. Mo radiation

L. Dimova*, B. L. Shivachev, R. P. Nikolova

Bulgarian Academy of Sciences, Institute of Mineralogy and Crystallography, 1113 Sofia, Acad. Georgi Bonchev Str., Bl. 107, Bulgaria

Natural clinoptilolite crystals were Zn ion-exchanged. The crystals were initially Na-exchanged and then the precursor was treated with 1 M $ZnCl_2$ solution for three months at 383 K to obtain the Zn exchanged form. Chemical analyses with an EDS/SEM for Zn exchanged samples showed that the cation exchange is partial and that several other cations remained in the structure. Duplicate single crystal structure refinements were performed for both Natural and Zn-exchanged clinoptilolite samples for revealing the structural peculiarities. Most of the Zn atoms are not bonded to framework oxygen. The Zn cations are located in the center of the ten-membered channel forming a disordered $[Zn(H_2O)6]$ complexes.

Key words: clinoptilolite, Zn ion-exchange, single crystal structure.

INTRODUCTION

The naturally occurring Heulandite-type zeolites, including heulandite (Heu) and clinoptilolite (CPT) are the most abundant minerals on earth, exhibiting a zeolite structure. Large, easily accessible surface deposits mainly of volcanoclastic origin, allow clinoptilolite low cost production by simple excavation. Its applications [1] range from wastewater treatment, aquacultural and agricultural applications (fertilizer), as a deodorizer and up to Fluid Catalytic Cracking (FCC) [2]. Nowadays the focus is shifted onto its ion exchange properties and potential medical and pharmaceutical applications [3–5]. For a better understanding of clinoptilolite applications a pure material is required and for single-crystal X-ray experiments large crystals are demanded. Single crystal structural studies have the advantage over powder XRD, spectroscopic and NMR studies that multiple inclusion sites (cation, anion, water etc.) can directly be distinguished. However, natural clinoptilolite rocks are rather inhomogeneous and are obtained as mixtures of phases (e.g. other zeolites, SiO_2, feldspars, clays, Fe-oxides/hydroxides) thus the occurrence of individual large clinoptilolite crystals should be thoroughly exploited. Heulandite

and clinoptilolite are isotypic (space group C2/m, $a \approx 17.7, b \approx 17.9, c \approx 7.4$ Å, $\beta \approx 116°$) [6]. Distinction between heulandite and clinoptilolite is done on the basis of the Si/Al ratio, silica-rich crystals (Si/Al > 4) are nammed clinoptilolites while aluminous ones (Si/Al<4) are heulandites [7].

The crystal structure shows the existence of three types of structural channels confined by ten- and eight-membered tetrahedral ring systems (Fig. 1). From crystal-chemistry point of view alumo-slicate framework possesses a negative charge that is equilibrated by cations located in the channels (simplified formula: $([Me^+, Me^{2+}, NxH_2O]^{6+} [Al_6Si_{30}O_{72}]^{6-})$. Detailed structural investigations on complete and partially ion exchanged on Na, K, Rb, Cs, Cd, Ag, Mn, Cu, Pb, Sr, Er, La clinoptilolite have been carried out [8-11] and summarizing the results some typical positions for cation placement in the channels have been assigned [6]. However, no detailed single crystal structural studies for Zn ion-exchanged clinoptilolite (ZnCPT) have been undertaken. The conducted by us studies revealed that CPT tolerates limited to complete Zn ion-exchange [12].

The aims of the present study are: (1) to obtain a Zn rich clinoptilolite via cation exchange; (2) to study the positioning and coordination of extra-framework Zn atoms by single-crystal X-ray methods; and (3) to compare the quality of the single-crystal data conducted under various conditions.

_____

* To whom all correspondence should be sent:
E-mail: anien@abv.bg

EXPERIMENTAL

Ion-exchange

Clinoptilolite from Beli plast deposit, Kardzhali, Bulgaria, was used for this study. For three months a set of single crystals with average size between 0.2 and 0.08 mm was treated in an aqueous NaCl solution (1 M) in a Teflon reactor with temperature slowly oscillating in an oven around 383 K. The NaCl solution was replaced weekly. The NaCl exchange is an indirect method that avoids the use of an acid treatment for the preparation of H-CPT form. The obtained Na-exchanged form was subsequently Zn-exchanged under similar conditions (1 M aqueous $ZnCl_2$ solution for three months at 383, weekly exchange of the solution and with additional pH monitoring).

X-ray single crystal analyses

Crystal of CPT and ZnCPT with approximate dimension of $0.14 \times 0.12 \times 0.12$ mm and $0.18 \times 0.12 \times 0.12$ mm respectively was placed on a glass fiber and mounted on an Enraf-Nonius *CAD-4* diffractometer and Oxford diffraction *Supernova* diffractometer equipped with Atlas CCD detector. X-ray data collection was carried out at 290 (*CAD-4* and *Supernova*) and 120 K (*Supernova*) with monochromatized Mo-Kα radiation ($\lambda = 0.71073$ Å) and Cu Kα radiation ($\lambda = 1.54184$ Å). During the low temperature data collection the sample was kept at 120 K with an Oxford Instruments Cobra controller device and a nitrogen atmosphere. The unit cell parameters were determined using 15 reflections and refined employing 22 higher-angle reflections, $18 < \theta < 20°$; the ω/2θ technique was used for data collection using CAD-4 Nonius Diffractometer Control Software [13]. For the Supernova the data reduction and analysis for these structures were carried out with the CrysAlisPro program [14]. Lorentz and polarization corrections were applied to intensity data using the WinGX [15]. The structure was solved by direct methods using SHELXS-97 [16] and refined by full-matrix least-squares procedure on F^2 with SHELXL-97 [16].

Scanning electron microscopy (SEM), energy dispersive X-ray microanalysis (EDS)

The structure of the clinoptilolite crystals was examined with the SEM Jeol JSM-840A. Chemical composition and phase changes in CPT/ZnCPT were evaluated by EDS analysis in the Link AnalyticalAN10000 analyzer.

RESULTS AND DISCUSSION

The clinoptilolite (CPTand ZnCPT) chemical composition obtained from SEM/EDS data is given in Table 1.

The obtained chemical composition of the natural single crystals is close to the ideal balance between +/– charges in the CPT structure (+/– = 5.76/5.72 = extra framework cations). Following the ion exchange with NaCl and ZnCl (aggregate time of 6 months) the Si/Al ratio is only slightly altered compared to the initial one (5.31 vs. 5.16) thus one can presume that the CPT framework is intact. The results also clearly indicate that Zn ion-exchange has taken place. If we compare the charge of the extra framework cations for CPT (5.76) and ZnCPT (5.83) we can see that Na, Ca, K, Mg, Ba charge is slightly lower than expected in Zn exchanged sample: (4.90 $Na_{0.89}Ca_{1.40}$ $K_{0.07}Mg_{0.11}Ba_{0.46}$ + 0.66 $_{Zn}$) = 5.56 (though one can argue that the result is comparable to the method error). Further, the amounts of K, Mg and Ba are almost identical in CPT and ZnCPT and as Na is a monovalent cation there is great probability that Zn ↔ Ca exchange has occurred. However, typical Ca and Zn ion coordination spheres are significantly different.

The CAD4 diffractometer Mo source is a fine focus sealed tube. The Supernova is equipped with Agilent micro-focus Mova (Mo radiation) and Nova (Cu radiation) sources. The Mova produces typically 2.5x more intense radiation flux than the Mo fine focus sealed tube while the Nova intensity is usually 3x that of the Mova.

Structure solution and refinement

As an example we are going to describe the solution of the natural CPT from Beliplast (CAD4, Mo

Table 1. Chemical composition of natural and Zn exchanged clinoptilolite

	Chemical formula		Si/Al	+/– charges
CPT	$(Na_{0.35}Ca_{1.99}K_{0.09}Mg_{0.18}Ba_{0.49})$	$Al_{5.72}Si_{30.28}O_{72}$	5.31	5.76/5.72
ZnCPT	$(Na_{0.89}Ca_{1.40}K_{0.07}Mg_{0.11}Ba_{0.46}Zn_{0.33})$	$Al_{5.83}Si_{30.17}O_{72}$	5.16	5.83/5.56
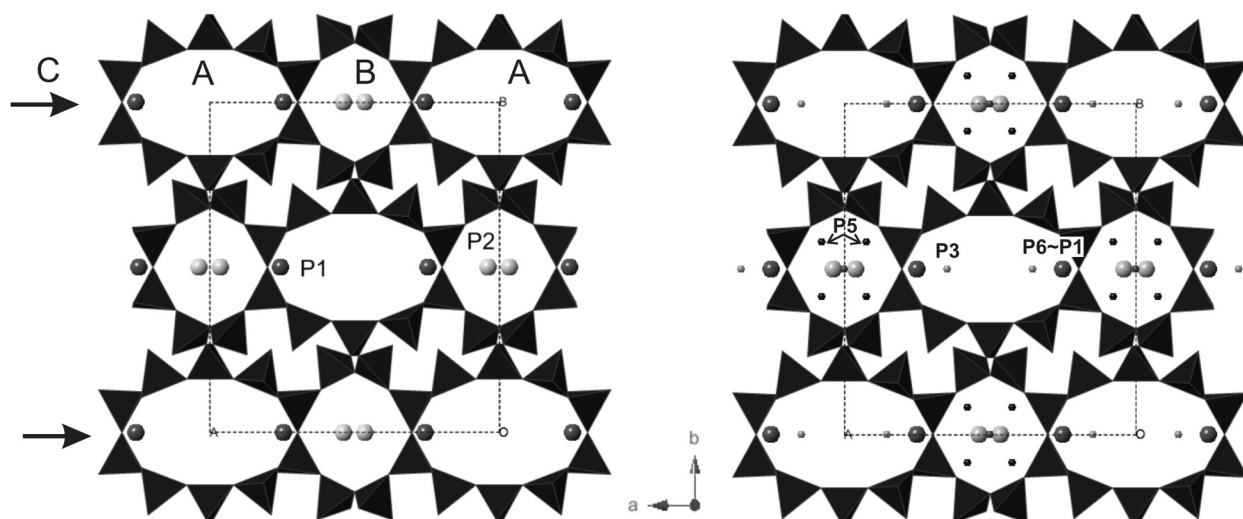
Fig. 1. Polyhedral model of a portion of the clinoptilolite structure projected parallel to the c-axis illustrating the porous structure: the ten-membered A and the eight-membered B channels are clearly visible in the projection while the eight-membered C channels, indicated by arrows, connect A and B channels in the *bc* plane. The locations of the most important extra-framework sites are also indicated.

wavelength). The "hkl" file was generated through XCAD4 as implemented in WinGX [15] and a direct methods solution using ShelX86 [16] was initiated. The resulting electron density clearly allowed the positioning of the framework atoms, Si, Al and O and in surplus located two extra framework positions (P1 and P2) with respective coordinates 0.242700, 0.0, 0.052000 and 0.461700, 0.0, 0.630300 (Fig. 1). At this stage the main statistical parameters look very promising: isotropic refinement, $R = 0.1496$, $R_w=0.1878$ $wR=0.4133$ $GOF = 2.221$. A subsequent cycles of refinement allowed the location of four electron density peaks (Q1=P3, Q2=P4, Q3=P5 and Q4=P6 with respective values of 9.16, 5.16, 4.81 and 3.15) located in the CPT channels which were clearly more pronounced than the other ones (the values of Q5 was 1.18). The P1 and P6 positions are too close to be occupied simultaneously ~0.77 Å ("forbidden positions") which is not uncommon case for CPT structures[7–9]. The resulting statistical parameters were $R = 0.1018$, $R_w=0.1423$ $wR=0.3286$ $GOF = 1.105$ (isotropic refinement), thus indicating that the model is very close to the collected data.

Now let's look in details for each accounted location. P1 is located in the A channel and is at ~2.97 and 3.14 Å from framework oxygen (Fig. 3). The position (P1) has been observed by Koyama and Takeuchi [17] and later on subsequent studies [11] have found that the position is occupied by "large" cations like potassium K. P2 is also known from literature [17] and the cation that is associated with this position is Ca (or Na). P3 is close to P1 and is

normally occupied by Na. P4 is positioned in the center of channel B (nearby P2) and is associated to coordination water (usually with occupancy around 1). P5, like P4 is located in B channel and is also reported as being coordination water. P6 is
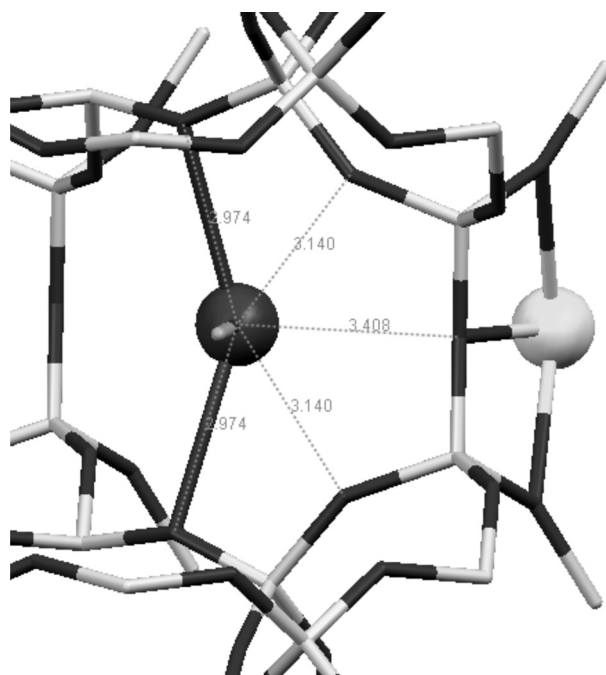
Fig. 2. P1 coordination sphere, P4 in orange, P2 in yellow, oxygen framework atoms in red and Si/Al in white. Reported contacts are in Å.

close to P1 and is associated to Na or Ba or may be an artifact from the isotropical refinement.

Thus if we crosscheck with the calculated from EDS chemical formula where we have Na, Ca, K, Mg and Ba: K/Na/Ca = P1, Ca = P2, Na = P3, Ba = P6 (forbidden with P1), P4 and P5 water. The missing Mg, according to available structural data [17] is normally positioned in the center of A channel − not allocated at this stage of refinement (or alternatively may occupy one of the observed positions P1 through P6, Figure 2).

After a few cycles of refinement an additional water position was detected. Further the occupancies of water molecules and cations were refined and finally the structure was refined anisotropically. The final refinement parameters are presented in Table 2. The same crystal was mounted on an Oxford Supernova diffractometer with ATLAS CCD and two datasets

Table 2. Crystal data

CPT-pure	CPT-pure	CPT-pure	CPT Zn exchanged	CPT Zn exchanged
CAD4	Supernova Cu	Supernova Mo Low Temperature	CAD4 Mo radiation	Supernova Cu
Monoclinic, $C2/m$	Monoclinic, $C2/m$	Monoclinic, $C2/m$	Monoclinic, $C2/m$	Monoclinic, $C2/m$
Hall symbol: –C 2y	Hall symbol: –C 2y	Hall symbol: –C 2y	Hall symbol: –C 2y	Hall symbol: –C 2y
$a = 17.229\,(4)$ Å	$a = 17.2660\,(4)$ Å	$a = 17.2032\,(4)$ Å	$a = 17.259\,(2)$ Å	$a = 17.3081\,(16)$ Å
$b = 17.931\,(5)$ Å	$b = 17.9954\,(3)$ Å	$b = 17.9697\,(3)$ Å	$b = 17.955\,(2)$ Å	$b = 17.9896\,(11)$ Å
$c = 7.388\,(2)$ Å	$c = 7.39542\,(17)$ Å	$c = 7.3827\,(2)$ Å	$c = 7.3930\,(15)$ Å	$c = 7.4020\,(6)$ Å
$\beta = 113.66\,(3)°$	$\beta = 113.731\,(3)°$	$\beta = 113.717\,(3)°$	$\beta = 113.70\,(2)°$	$\beta = 113.705\,(11)°$
$V = 2090.5\,(9)$ Å^3	$V = 2103.52\,(8)$ Å^3	$V = 2089.51\,(8)$ Å^3	$V = 2097.6\,(6)$ Å^3	$V = 2110.3\,(3)$ Å^3
$Z = 1$	$Z = 1$	$Z = 1$	$Z = 1$	$Z = 1$
$D_x = 2.189$ Mg m^{-3}	$D_x = 2.169$ Mg m^{-3}	$D_x = 2.179$ Mg m^{-3}	$D_x = 2.184$ Mg m^{-3}	$D_x = 2.189$ Mg m^{-3}
Cell parameters from 22 reflections	Cell parameters from 10 frames	Cell parameters from 10 frames	Cell parameters from 22 reflections	Cell parameters from 10 frames
$\theta = 18$–$20°$			$\theta = 16.3$–$17.7°$	
Prism, colourless	Prism, colourless	Prism, colourless	Prism, colorless	Prism, colorless
0.14×0.12×0.12 mm	0.14×0.12×0.12 mm	0.14×0.12×0.12 mm	0.18×0.12×0.12 mm	0.18×0.12×0.12 mm

Table 2. Data collection

Enraf Nonius CAD4	Oxford Supernova	Oxford Supernova	Enraf Nonius CAD4	Oxford Supernova
Radiation source: sealed tube	Radiation source: micro focus	Radiation source: micro focus	Radiation source: sealed tube	Radiation source: micro-focus
Mo $K\alpha$ radiation $\lambda = 0.71073$ Å	Cu $K\alpha$ radiation $\lambda = 1.54184$ Å	Mo $K\alpha$ radiation $\lambda = 0.71073$ Å	Mo $K\alpha$ radiation $\lambda = 0.71073$ Å	Cu $K\alpha$ radiation $\lambda = 1.54184$ Å
$T = 293(2)$ K	$T = 293(2)$ K	$T = 123(1)$ K	$T = 293(2)$ K	$T = 293(2)$ K
4830 measured reflections	4344 measured reflections	11878 measured reflections	4767 measured reflections	4218 measured reflections
2569 independent reflections	2251 independent reflections	5427 independent reflections	2579 independent reflections	2109 independent reflections
1602 reflections with $I > 2\sigma(I)$	2192 reflections with $I > 2\sigma(I)$	4021 reflections with $I > 2\sigma(I)$	1695 reflections with $I > 2\sigma(I)$	2000 reflections with $I > 2\sigma(I)$
$R_{int} = 0.061$	$R_{int} = 0.048$	$R_{int} = 0.029$	$R_{int} = 0.086$	$R_{int} = 0.039$
$\theta_{max} = 28.0°$	$\theta_{max} = 76.2°$	$\theta_{max} = 37.7°$	$\theta_{max} = 28.0°$	$\theta_{max} = 76.2°$
$\theta_{min} = 1.7°$	$\theta_{min} = 3.7°$	$\theta_{min} = 3.0°$	$\theta_{min} = 1.7°$	$\theta_{min} = 3.7°$
$h = 0 \rightarrow 22$	$h = -21 \rightarrow 18$	$h = -29 \rightarrow 25$	$h = 0 \rightarrow 22$	$h = -17 \rightarrow 21$
$k = -23 \rightarrow 23$	$k = -14 \rightarrow 22$	$k = -28 \rightarrow 30$	$k = -23 \rightarrow 23$	$k = -22 \rightarrow 13$
$l = -9 \rightarrow 8$	$l = -8 \rightarrow 9$	$l = -12 \rightarrow 12$	$l = -9 \rightarrow 8$	$l = -9 \rightarrow 6$
3 standard reflections every 120 min intensity decay: 0%	Dark frame: every 50 frames intensity decay: 0%	Dark frame: every 50 frames intensity decay: 0%	3 standard reflections every 120 min intensity decay: 1%	Dark frame: every 50 frames intensity decay: 0%

with Mo and Cu radiation were collected. The structure solution and refinement was conducted according to the above mentioned procedure and the final refinement parameters are shown in Table 2.

Zinc exchanged CPT structure solution

Using the results from SEM/EDS the main peculiarities in the CPT vs. ZnCPT composition

Table 2. Refinement

Refinement on F^2	Refinement on F^2	Refinement on F^2	Refinement on F^2	Refinement on F^2
Least-squares matrix: full	Least-squares matrix: full	Least-squares matrix: full	Least-squares matrix: full	Least-squares matrix: full
$R[F^2 > 2\sigma(F^2)] = 0.074$	$R[F^2 > 2\sigma(F^2)] = 0.072$	$R[F^2 > 2\sigma(F^2)] = 0.067$	$R[F^2 > 2\sigma(F^2)] = 0.077$	$R[F^2 > 2\sigma(F^2)] = 0.072$
$wR(F^2) = 0.238$	$wR(F^2) = 0.241$	$wR(F^2) = 0.233$	$wR(F^2) = 0.277$	$wR(F^2) = 0.218$
$S = 0.94$	$S = 1.06$	$S = 0.74$	$S = 0.98$	$S = 1.12$
2569 reflections	2251 reflections	5427 reflections	2579 reflections	2109 reflections
173 parameters	173 parameters	161 parameters	162 parameters	177 parameters
0 constraints	0 constraints	0 constraints	0 constraints	0 constraints
$w = 1/[\sigma^2(F_o^2) + (0.1579P)^2 + 2.2394P]$ where $P = (F_o^2 + 2F_c^2)/3$	$w = 1/[\sigma^2(F_o^2) + (0.1147P)^2 + 37.7576P]$ where $P = (F_o^2 + 2F_c^2)/3$	$w = 1/[\sigma^2(F_o^2) + (0.1938P)^2 + 34.2667P]$ where $P = (F_o^2 + 2F_c^2)/3$	$w = 1/[\sigma^2(F_o^2) + (0.2P)^2]$ where $P = (F_o^2 + 2F_c^2)/3$	$w = 1/[\sigma^2(F_o^2) + (0.1147P)^2 + 37.7576P]$ where $P = (F_o^2 + 2F_c^2)/3$
$(\Delta/\sigma)_{max} = 1.716$	$(\Delta/\sigma)_{max} = 14.1$	$(\Delta/\sigma)_{max} = 15$	$(\Delta/\sigma)_{max} = 0.121$	$(\Delta/\sigma)_{max} = 2.511$
$\Delta\rho_{max} = 0.84$ e Å^{-3}	$\Delta\rho_{max} = 0.68$ e Å^{-3}	$\Delta\rho_{max} = 0.57$ e Å^{-3}	$\Delta\rho_{max} = 0.89$ e Å^{-3}	$\Delta\rho_{max} = 0.88$ e Å^{-3}
$\Delta\rho_{min} = -0.90$ e Å^{-3}	$\Delta\rho_{min} = -0.62$ e Å^{-3}	$\Delta\rho_{min} = -0.83$ e Å^{-3}	$\Delta\rho_{min} = -0.90$ e Å^{-3}	$\Delta\rho_{min} = -0.93$ e Å^{-3}

Primary atom site location: structure-invariant direct methods,
Secondary atom site location: difference Fourier map
Absorption correction: none
Extinction correction: none
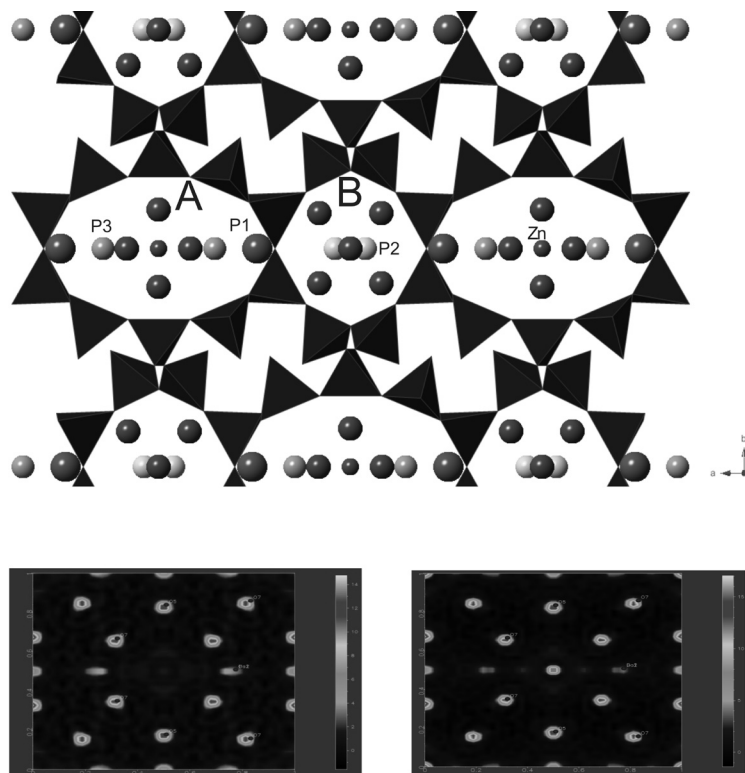
Fig. 3. *Top*: Polyhedral model of a portion of the ZnCPT structure (projected along ab plane) illustrating the porous structure: the ten-membered A and the eight-membered B channels are clearly visible in the projection. The locations of the most important extra-framework sites are also indicated. The Zn atom is located in the center of the A channel. *Bottom*: Fourier (Fobs) maps for natural clinoptilolite Mo radiation, CAD4 (left) and ZnCPT, Cu radiation, Supernova (right). The white arrow shows the absence/presence of electron density in CPT and ZnCPT.
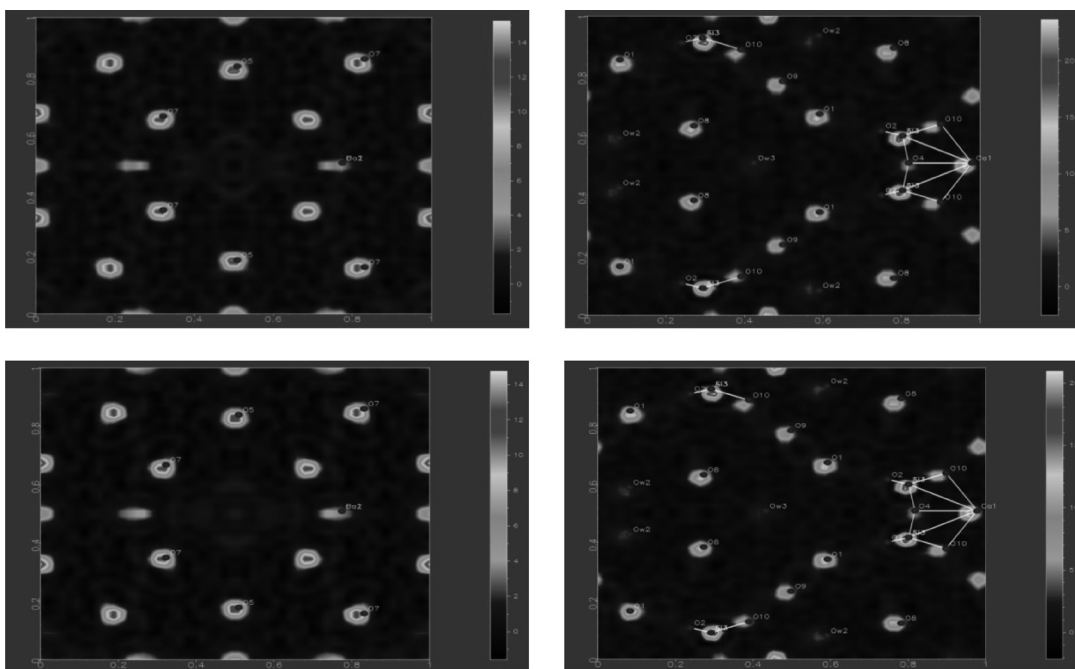
Fig. 4. Fourier maps (ab plane) of pure (top) and Zn exchanged (bottom) from CAD4 experiments Mo radiation.

are: Potassium and Barium values do not change only a reduction of Ca and Mg is observed (from ~2.00 to ~1.40 and ~0.18 to ~0.11 respectively). Thus a charge compensation of ~0.7 should be expected. Actually the results show that Na increases from ~0.4 to ~0.9 and some Zn (0.33) is also present. The compensation is approximately equal (and taking into account the Si/Al variation – or the framework charge the result is indeed very good). Thus for the structure refinement two possibilities exist (this of course is an oversimplification): the Zn replaces Ca and Mg or
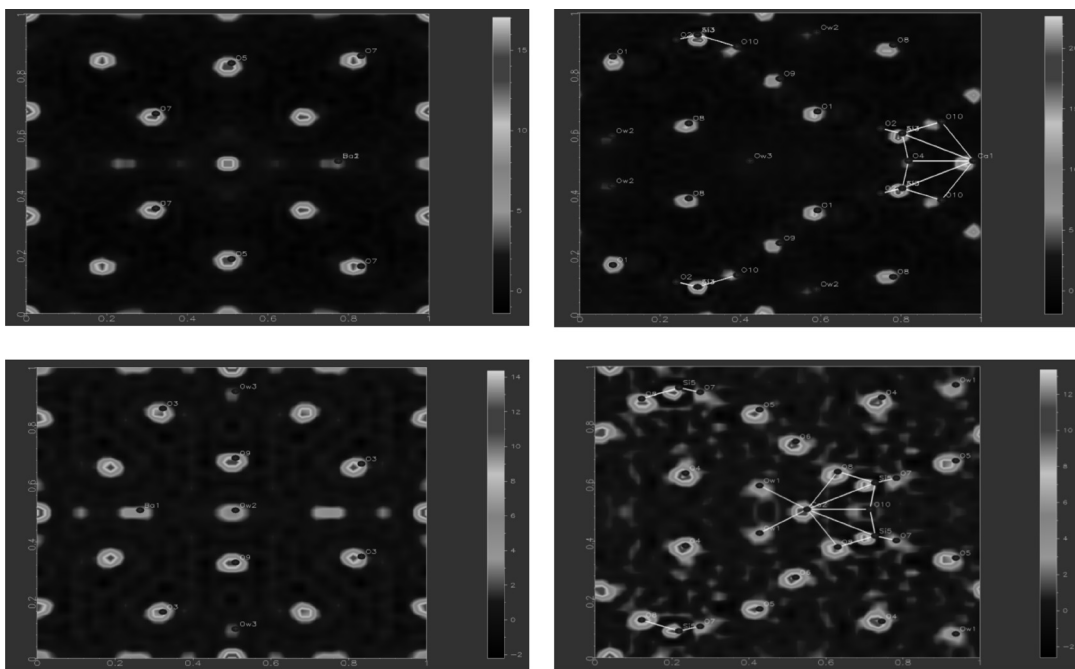
Fig. 5. Fourier maps (*ab* plane) of Zn exchanged low temperature Mo radiation (top) and Cu radiation (bottom) from Supernova experiments.

Zn is located in a different position (not observed in the structure of the pure CPT).

The crystal solution is performed as described previously and the statistics are shown in Table. 2.

The difference Fourier map clearly shows that the Zn cation occupies a new position (0 0.5 0) (Fig. 3), not observed in the natural CPT of Beli plast.

We do have 2 experiments on the CAD-4 and 3 on the Supernova (for pure and ion exchanged clinoptilolite). As expected the unit cell is monoclinic (*C2/m*) and the unit cell parameters do not change a lot from experiment to experiment and remain close to those of pure CPT. The framework atoms Si/Al and O are easily discernable in all experiments.

The difference Fourier map of pure and Zn exchanged CPT obtained from CAD4 experiments are comparable (Fig. 4). This is actually expected as the chemical variation for the whole crystal is ~2% and thus should not influence greatly data collection and refinement results. However, the difference Fourier densities maps clearly show that the more intense Cu radiation allows better positioning of the cations in the channels (Fig. 5).

CONCLUSIONS

It is visible that the experiments performed on the CAD4 (pure and ion exchanged) produce almost identical statistics as those on Oxford Supernova (CCD, Cu or Mo radiation). One may presume that pure and ion exchanged structures should be sufficiently "changed" in order to account for notable differences. On the other hand the differences are more pronounced for low temperature experiments and further more with the increase of radiation intensity e.g. Cu radiation. Thus, for accounting subtle structural variations low temperature and more intensive radiation are recommended.

REFERENCES

1. H. G. K. M. Stöcker, J.C. Jansen, J. Weitkamp, *Advanced Zeolite Science and Applications*; (in Stud. Surf. Sci. Catal., vol. 85), Elsevier: Amsterdam, 1994; Vol. 85.
2. J. Mikulec; M. Vrbova. *Clean Technol Envir*, **10**, 121 (2008).
3. G. Cerri; M. de' Gennaro; M. C. Bonferoni; C. Caramella. *Appl Clay Sci*, **27**, 141 (2004).
4. V. J. Inglezakis; M. Stylianou; M. Loizidou. *J. Phys. Chem. Solids*, **71**, 279 (2010).
5. Y. Yukselen-Aksoy. *Appl. Clay Sci.*, **50**, 130 (2010).
6. A. Godelitsas; T. Armbruster. *Micropor. Mesopor. Mat.*, **61**, 3 (2003).
7. D. S. Coombs; A. Alberti; T. Armbruster; G. Artioli; C. Colella; E. Galli; J. D. Grice; F. Liebau; J. A. Mandarino; H. Minato; E. H. Nickel; E. Passaglia; D. R. Peacor; S. Quartieri; R. Rinaldi; M. Ross; R. A. Sheppard; E. Tillmanns; G. Vezzalini. *Canadian Mineralogist*, **35**, 1571 (1997).
8. J. Stolz; P. Yang; T. Armbruster. *Micropor. Mesopor. Mat.*, **37**, 233 (2000).
9. M. E. Gunter; T. Armbruster; T. Kohler; C. R. Knowles. *Am. Mineral.*, **79**, 675 (1994).
10. P. Yang; J. Stolz; T. Armbruster; M. E. Gunter. *Am. Mineral.*, **82**, 517 (1997).
11. T. Armbruster; P. Simoncic; N. Dobelin; A. Malsy; P. Yang. *Micropor. Mesopor. Mat.*, **57**, 121 (2003).
12. L. Dimova, PhD Thesis, IMC-BAS, 2011.
13. J. C. Schoone; Duisenbe.Aj. *Acta Crystallogr. A,* **25**, S81 (1969).
14. *Oxford Diffraction (2010). CrysAlis PRO. Oxford Diffraction Ltd, Yarnton, England.*
15. L. Farrugia. *Journal of Applied Crystallography*, **32**, 837 (1999).
16. G. M. Sheldrick. *Acta Crystallogr. A*, **64**, 112 (2008).
17. K. Koyama; Y. Takeuchi. *Z. Krist.*, **145**, 216 (1977).

МОНОКРИСТАЛНА СТРУКТУРА НА ПРИРОДЕН И ЦИНКОВО ЙОНООБМЕНЕН КЛИНОПТИЛОЛИТ: СРАВНЕНИЕ НА СТРУКТУРНИТЕ РЕЗУЛТАТИ ПРИ НИСКА И СТАЙНА ТЕМПЕРАТУРА, МЕДНО И МОЛИБДЕНОВО ЛЪЧЕНИЕ

Л. Димова*, Б. Л. Шивачев, Р. П. Николова

Институт по минералогия и кристалография „Акад. Иван Костов“, Българска Академия на Науките, ул. Акад. Г. Бончев бл. 107, 1113 София

(Резюме)

Осъществен бе цинков йонообмен на монокристали на природен клиноптилолит. За получаване на цинкова форма първоначално бе приготвена натриева форма на образците. След това натриевите образци (форма) бяха третирани в продължение на три месеца с 1 M разтвор на $ZnCl_2$ при 383 K. Химическият анализ (енергийно дисперсионна спектроскопия) на цинковите образци показа частичен цинков йонообмен. Уточнена бе структурата на природния и цинково обменения клиноптилолит за изясняване на структурните промени. Повечето цинкови атоми не взаимодействат със скелетните кислородни атоми, а са разположени в центъра на десетчленния канал образувайки неподредени $[Zn(H_2O)_6]$ комплекси.

Use of time-resolved X-ray scattering methods for investigation of structural formation in polymer liquid crystals

G. K. Exner[1],*, E. Pérez[2], M. N. Krasteva[3]

[1] *Deparment of General Physics, Faculty of Physics, Plovdiv University "P.Hilendarski",*
24 Tzar Asen Street, 4000-Plovdiv, Bulgaria
[2] *Instituto de Ciencia y Tecnología de Polímeros (CSIC) 3 Juan de la Cierva, 28006 Madrid, Spain*
[3] *Department of General Physics, Faculty of Physics, 5 James Bourchier Blvd, 1126 Sofia, Bulgaria*

The paper gives general information about the advantages of using synchrotron radiation in investigation of polymer liquid crystals. Examples are given with thermotropic polymer liquid crystal Poly(heptane-1,7-diyl-4,4'-biphenyldicarboxylate). The melt formation of smectic liquid crystal phase and consequent crystallization at decreasing temperature is depicted. Detailed description of different structural parameters, derivable from appropriate analysis of the experimental results, is given. With the aim of all those parameters an overall hierarchical structuring during phase transitions could be revealed.

Since some basic terms about liquid crystals and polymer liquid crystals are given, the paper would serve as an introductory reading in the field.

Key words: Polymer liquid crystals, Time-resolved experiments, X-ray scattering, Structure formation, Phase transitions.

INTRODUCTION

Curiously till the early sixties, synchrotron radiation has been considered only as an unwanted but inescapable by-product of elementary particle acceleration. Today, it is irreplaceable tool for investigation of structure and properties of vast classes of materials. Synchrotron facilities enlarge much further the possibilities of scientific investigation, helping to reveal much more details on the structure, and providing deeper inside about the mechanism of many processes (dynamics and kinetics), information which is inaccessible with the ordinary laboratory equipment.

The present paper aims to introduce to the reader the advantages of synchrotron radiation sources by giving an example with structural transformation of thermotropic liquid crystals. We also hope that this manuscript would serve as an introductory reading in the field of polymer liquid crystals and their structural investigation at diverse conditions.

BASIC KNOWLEDGE

1. *Synchrotron radiation*. Synchrotron radiation has been firstly observed in synchrotrons (storage rings). It is an intensive electromagnetic radiation generated when high energy particles, accelerated to nearly the speed of light, are deflected in a strong magnetic field [1]. The radiation emitted by the orbital electrons covers broad range of the electromagnetic spectrum and the synchrotron radiation has continuous spectral distribution. The relativistic effects provoke a sharp forward peaking of the radiation and a large increase in the total radiated energy takes place.

The synchrotron radiation properties of interest for structural investigations could be summarized as follows [1]: continuous spectrum from infrared to hard X-rays; very high intensity of radiation and brightness of the source as compared with the conventional sources; high collimation of the beam; highly polarized radiation with an electric field vector in the orbital plane; well defined time structure which is a copy of the electron pulse structure of the beam. Owing to these synchrotron radiation features, because of the very short measurements times, one is able to investigate very fast processes (in order of nano- or even picoseconds). Because of the high brightness, together with utilization of two-dimensional detectors, one can gather very accurate and space and time discriminate experimental information. Another very important achievement is the possibility of simultaneous performance of several different experiments. For instance

---

* To whom all correspondence should be sent:
E-mail: todorova_ginka@yahoo.com

wide-angle x-ray diffraction (WAXD), small angle x-ray scattering (SAXS) and differential scanning calorimetry (DSC) can be run in the same time on only sample. Such approach leads to complete consistence of the obtained results and eliminates all doubts about the exact repetition of the experimental conditions, when each of the methods is employed separately.

2. *Liquid crystals*. Since many years, subject of great interest are structures having intermediate, between those of crystals and ordinary liquids, properties. For the sake of completeness, there are several states of matter displaying such intermediate behavior. They have common name – mesomorphic phases, divided into three main subclasses – liquid crystals, plastic crystals and condis crystals [2, 3]. In the present paper we focus our attention on liquid crystals only.

The nature of the liquid crystallinty (LC) is still not completely understood. One very important feature of liquid crystals is that the molecule (or part of it) shows rigidity. In most of the cases, one can imagine stiff rods, having lengths much greater than their diameter. Some authors [4] have proven that not only stiffness and asymmetry in shape but also electrical, steric, biphylic and flexibility molecular asymmetry play important role in LC appearance. Independently of the reason, the molecular segments giving LC are called mesogens.

Complete liquid crystals nomenclature could be found in the papers of International Union for Pure and Applied Chemistry [5, 6]. One possible division is according to the molecular weight: when the molecules are small – one deals with low-molar-mass or molecular liquid crystals (MLC), and otherwise – with polymer liquid crystals (PLC). In addition, since polymers are in fact very long molecules, there are many ways to incorporate the mesogens along the chain. According to the molecular architecture, there are more than 20 different types of PLC [2, 5, 6].

Independently of the molar mass, liquid crystallinity can appear at different conditions. One distinguishes three main types of substances – lyotropic (when LC is cased by a solvent), thermotropic (LC cased by temperature variation) and barotropic (at varying pressure).

Now let us turn attention to one very important fact. Objects having shape other than spherical may possess three types of order, giving rise to different LC phases. If the symmetry axes of the objects are on average parallel to a well-defined spatial direction (called director, $\bar{n}$) then the substance shows orientational order (OO) (One can imagine spaghetti in a box). Translational order (TO) exists, when the system stays invariant under translations in space by an integer number of specific vectors (Imagine a crystal lattice and translation with respect to any of its unit cell vectors). The third possible order is called bond orientational order (BOO). It is not connected with the chemical bonds, but with the line is space which connects two adjacent molecules. If the direction of these lines is preserved over a long range, then BOO exists in the material (One can imagine here the view from above of densely packed spaghetti. The order looks like repeated hexagons).

Nematics are structures which possess only OO (Fig. 1A). Smectics are substances which display OO and TO in at least one direction (Fig. 1B). Some of the smectic phases may have also BOO. Cholesterics are special kind of materials, which posses OO, TO in one direction and also some persistent angle of inclination of the average molecular axis of one layer to its neighboring layer (Fig. 1C).
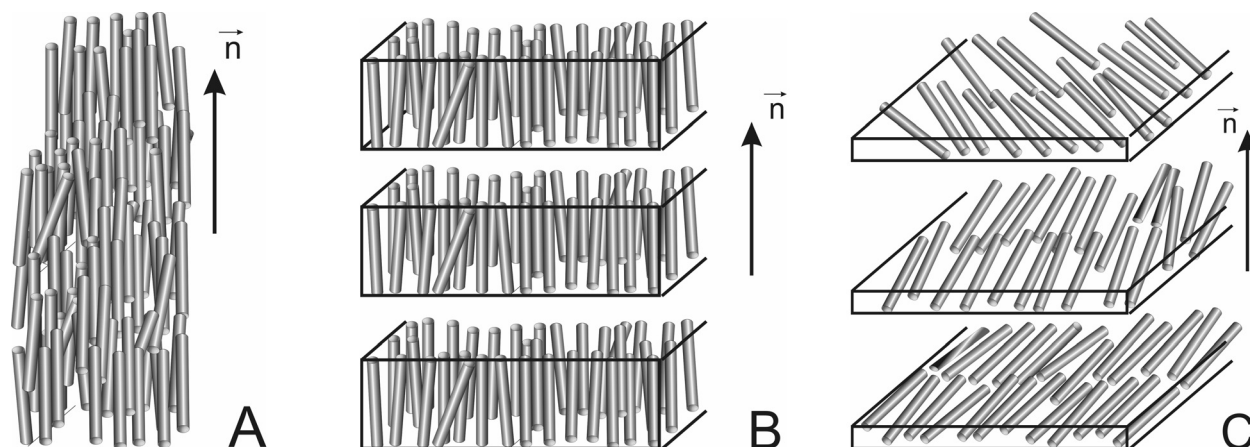
Fig. 1. A) Nematic Liquid crystal; B) Smectic liquid crystal; C) Cholesteric liquid crystal

MATERIALS AND METHODS

The investigated material is Poly(heptane-1,7-dyil-4,4'-biphenyldicarboxylate), P7MB. It belongs to the class of thermotropic main-chain liquid crystalline polyesters. Details of polymers preparation could be found elsewhere **[7].** The intrinsic viscosity of P7MB was measured in chloroform at 25 °C and it was 1.03 dL/g.

Real-time variable isothermal temperature X-ray scattering and diffraction experiments were carried out at the beam line A2, HASYLAB (Hamburg, Germany). The wave-length of the X-ray beam was $\lambda = 0.150$ nm. Details about the experimental set-up could be found in our previous papers [8, 9, 10].

P7MB forms Smectic CA liquid crystalline phase [11]. This smectic structure is stable only in a limited temperature interval. At low temperatures the smectic structure partially crystallizes and at high temperatures it melts [9, 10]. The transition isotropic melt – smectic phase takes place in several minutes and it is very fast followed by partial crystallisation. Hence, with the ordinary laboratory equipment only the final semi-crystalline phase is reachable. Using synchrotron radiation we were able to follow up the kinetics of the phase transformation and to establish the mechanisms of the observed transitions.

The data treatment in the WAXD region is based on Bragg's law

$$(d = \frac{\lambda}{2 \sin \theta} = \frac{1}{s},$$

where λ is the x-ray wavelength, θ is the position of angle at the scattering peak maximum, and s is the scattering vector at the maximum) [1, 9]. Usually, polymeric materials undergo partial phase transfor-

mation and WAXD region is used to calculate degree of crystallinity

$$(X_{cr} = \frac{\sum I_{cr}}{T_{tot}},$$

where $\sum I_{cr}$ is the sum of the integrated intensities of all crystalline reflections and I_{tot} is the total integrated intensity) [1, 9]. Fig. 2A demonstrates the time evolution of WAXS patterns at isothermal temperature $T_{iso} = 135$ °C, and Fig. 2B – the method of deconvolution [1]. For deeper inside about the meaning of the results, the reader is referred to our already published results [8, 9, 10].

MAXS scattering interval is connected with mesogenic layer spacing, d_{MAXS}. The d_{MAXS} was calculated again according to Bragg's formula and its time dependence was established. Additional information about the domain dimensions in direction perpendicular to the mesogenic planes, D_{MAXS}, could be derived from Scherrer's formula:

$$D_{MAXS} = \frac{1}{\delta s}$$

(δs is the width of the peak half maximum). Important information could be extracted also from integrated intensity, I_{MAXS}, because it corresponds to the quantity of the material, which undergoes phase transformation. Fig. 2A presents MAXS peak time evolution at $T_{iso}=135$ °C and Fig. 3A demonstrated the time dependencies of all three discussed parameters. Actually, there are two d-spacings – at initial times there is a smectic d-spacing, having higher value and later on the crystallization takes
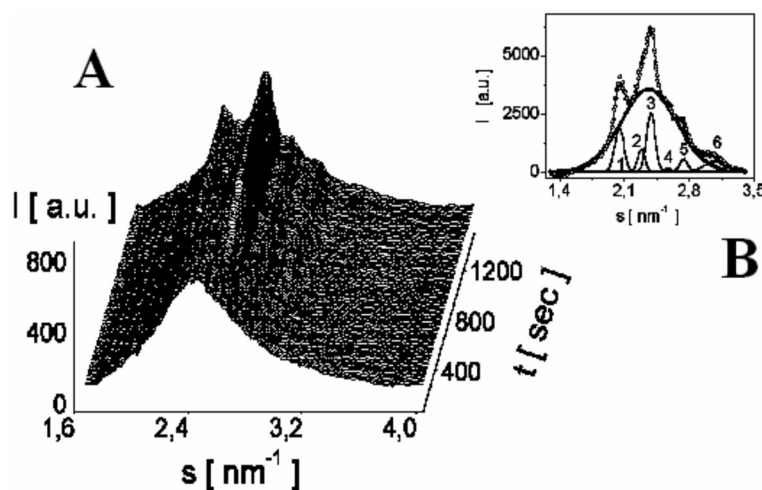
Fig. 2. A) WAXS pattern time evolution at $T_{iso}=135$ °C; B) deconvolution of the WAXD peaks
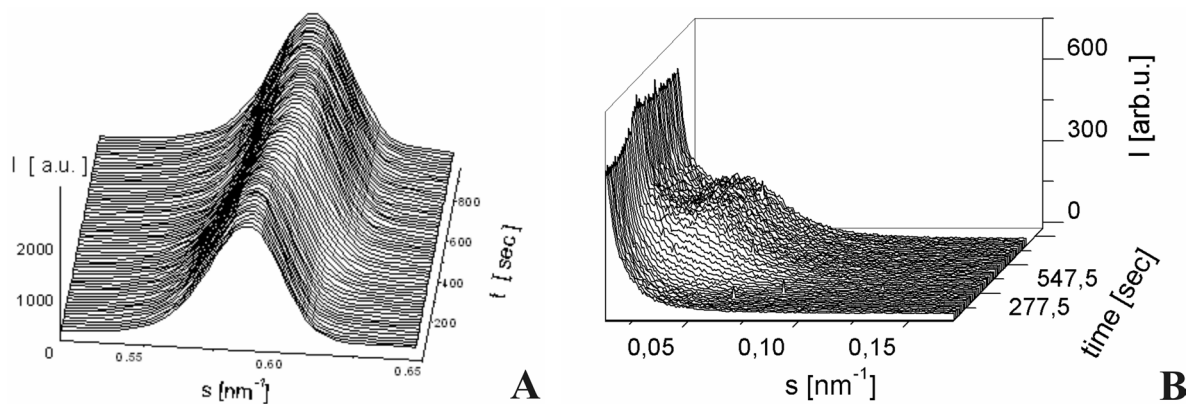
Fig. 3. MAXS (A) and SAXS (B) patterns time evolution at T_{iso}=135 °C

place (lower d-spacing). The deconvolution of both peaks was only possible because the experiments were taken at synchrotron. In the results for I_{MAXS} and D_{MAXS} different symbols show the results for each d-spacing. The detailed analysis of the curves could be found elsewhere [9, 10].

SAXS scattering interval shows whether there is a hierarchical structuring in the material. In such case so called Long period appear (SAXS peak). Its values can be determined from the position of the peak maximum in Lorentz corrected SAXS patterns, L_{Lor}, or from the maximum of the normalized one-dimensional correlation function, $\gamma_1(x)$,

$$\gamma_1(x) = \frac{\int_0^\infty s^2 I(s)\cos(2\pi xs)ds}{\int_0^\infty s^2 I(s)ds},$$
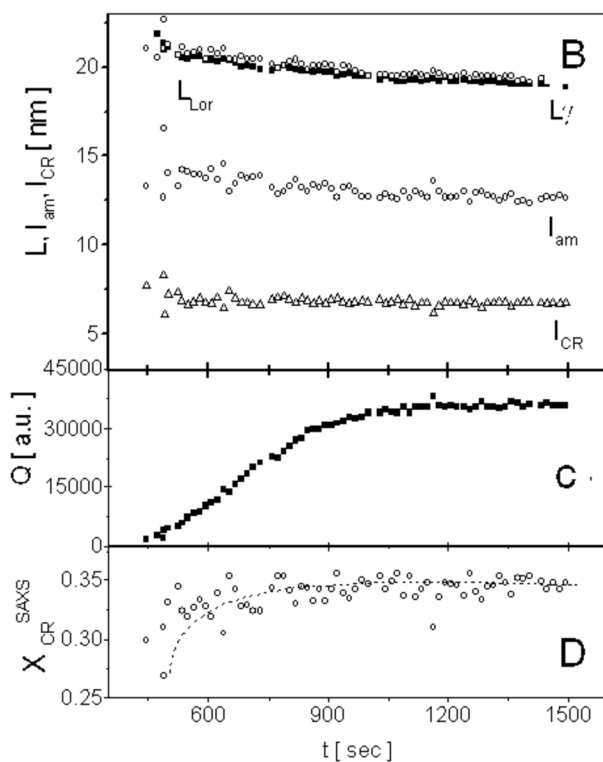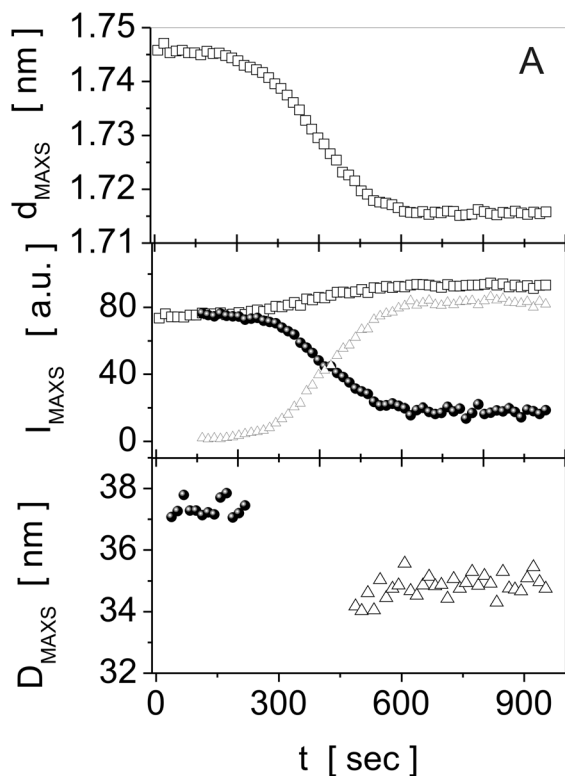
Fig. 4. d_{MAXS}, I_{MAXS}, D_{MAXS} time evolution (A); Results from one dimensional correlation function analysis of long period, crystal and amorphous layer thickness (B), Porod's invariant (C) and crystallinity with the stacks (D)

where $I(s)$ is smoothed and corrected for background SAXS intensity) [1, 10]. The analysis of $\gamma_1(x)$ gives also the degree of crystallinity within the lamellar stacks X_{cSAXS}, the lamellar thickness, l_c, the thickness of the amorphous layer, as well as the Porod's invariant, Q which is measure of the electron density difference between the present phases. For further readings see the books of Baltá-Calleja and Vonk [1] and Roe [12]. The results for P7MB are given in Fig. 4B, Fig. 4C, and Fig. 4D.

One can describe the overall picture of phase transformation only if all X-ray intervals are investigated. The exact structure determination and the mechanisms of phase transformation can be unambiguously assessed when the time (or temperature in case on non-isothermal processes) dependencies are known. In case of very fast processes, and when the changes are small (see for instance d_{MAXS}) the ordinary laboratory equipment fails to reveal the processes and only time-resolved synchrotron experiments are in help to the scientists.

CONCLUSIONS

Synchrotron radiation appears to be very useful tool for investigating thermotropic polymer liquid crystals. With its help many details about structure and the nature of the observed phase transition could be derived. SAXS, MAXS and WAXS experimental methods were performed simultaneously, which avoided the ambiguity coming from the problem with exact repetition of the experimental conditions when each method is performed at different time and with different equipment.

REFERENCES

1. F. J. Baltá-Calleja, C. G. Vonk, X-ray scattering of synthetic polymers, *Polymer Science Library 8*, Elsevier, Amsterdam-Oxford-New York-Tokyo (1989).
2. A. A. Collier (Ed.), *Luquid Crystal Polymers: From Structure to Applications*, Elsevier Applied Science, London and New York, (1992).
3. B. Wunderlich, *Thermal Analysis of Polymeric Materials*, Springer, Berlin-Heidelberg-New York (2005).
4. A. Petrov, *The lyotropic state of matter: molecular physics and living matter*, Gordon&Breach Publishers, New York (1999).
5. M. Barón, *Pure Appl. Chem.*, **73**(5), 845 (2001).
6. M. Barón, R.F.T. Stento, *Pure Appl. Chem.*, **74**(3), 493 (2002).
7. E. Pérez, A. Bello, M. M. Marugán, J. Rereña, *Polym. Commun.*, **31**, 386 (1990).
8. B. Katerska, G. Exner, E. Pérez, M. N. Krasteva, *Eur. Pol. J.*, **46**(7), 1623 (2010).
9. E. Pérez , G. Todorova, M. N. Kresteva , J. Pereña, A. Bello, M. Marugán, M. Shlouf, *Macromol. Chem. and Phys.*, **204**(14), 1791 (2003).
10. G.K. Todorova, M.N. Krasteva, E. Pérez, J.M. Perena, A. Bello, *Macromolecules*, **37**(1), 118 (2004).
11. J. Watanabe, M. Hayashi, Y. Nakata, T. Niori, M. Tokita, *Prog. Pol. Sci.*, **22**, 1053 (1997).
12. R-J. Roe, *Methods of x-ray and neutron scattering in polymer science*, Oxford University Press, New York-Oxford (2000).

ПРИЛОЖЕНИЕ НА РЕНТГЕНОВИТЕ МЕТОДИ ЗА ИЗСЛЕДВАНЕ НА СТРУКТУРНОТО ФОРМИРАНЕ В ПОЛИМЕРНИ ТЕЧНИ КРИСТАЛИ

Г. К. Екснер[1,*], Е. Перес[2], М. Н. Кръстева[3]

[1] *Катедра Обща физика, Физически факултет, ПУ „П. Хилендарски", 4000 Пловдив, България*
[2] *Институт за наука и технология на полимерите (CSIC), 28006 Мадрид, Испания*
[3] *Катедра Обща физика, Физически факултет, СУ „Св. Кл. Охридски", София, България*

(Резюме)

Настоящата статия дава обща информация относно предимствата при употреба на синхротронно лъчение за изследване на структурното формиране на полимерни течни кристали. Дадени са примери с термотропният полимерен течен кристал Poly(heptane-1,7-dyil-4,4'-biphenyldicarboxylate). Описано е формирането от стопилка на смектична течно-кристална фаза, последвано от кристализация при намаляване на температурата. Детайлно са описани различни структурни параметри, които са извлечени чрез подходящ анализ на експерименталните резултати. С помощта на разглеждане на всички тези параметри в цялост, може да се разкрие пълното йерахично структуриране по време на фазовото превръщане.

Статията може да служи и като въвеждащо четиво в областта, доколкото в нея са въведени и описани основните термини за нискомолекулните течните кристали и полимерни течни кристали.

Synthesis and crystal structure
of 2-[(2,3-dihydro-2-oxo-3-benzoxazolyl)methyl]benzoic acid

M. Gerova[1], R. Nikolova[2], B. Shivachev[2]*, O. Petrov[1]

*[1] University of Sofia "St. Kliment Ohridski", Faculty of Chemistry, Department of Applied Organic Chemistry,
1164 Sofia, 1 James Bourchier Blvd., Bulgaria*
*[2] Bulgarian Academy of Sciences, Institute of Mineralogy and Crystallography, 1113 Sofia,
Acad. Georgi Bonchev Str., Bl. 107, Bulgaria*

The synthesis, IR, NMR and X-ray structure of 2-[(2,3-dihydro-2-oxo-3-benzoxazolyl)methyl]benzoic acid – a potential new drug scaffold are reported. The compound crystallizes in the triclinic *P*-1 space group with unit cell parameters: $a = 6.716(3)$, $b = 7.828(4)$, $c = 13.283(5)$ Å, $\alpha = 78.029(12)$, $\beta = 81.360(17)$, $\gamma = 65.7100(10)$ °, $V = 621.0(4)$ Å^3, $M_w = 269.25$ and $Z = 2$. In the three-dimensional arrangement of the molecules only one classical hydrogen bond (O-H…O) is observed. Weak and C–H…O and π…π interactions are responsible for the additional stabilization and packing of the molecules in the crystal structure.

Key words: 2(3*H*)-benzoxazolone, benzoic acid, X-ray

INTRODUCTION

Benzoxazole represents an important heterocyclic scaffold, as several of its derivatives are shown to display a range of promising pharmaceutical properties such as anticonvulsant, anti-inflammatory, analgesic, antiulcer, antineoplastic, antibacterial and antifungal activities [1-3]. A number of substituted (2,3-dihydro-2-oxo-3-benzoxazolyl)alkanoic acid derivatives have been recognized as therapeutically useful cyclooxygenase inhibitors (Non-Steroidal Anti-Inflammatory Drugs, NSAIDs).

The analgesic activity of substituted 2(3*H*)-benzoxazolones was first reported by Close *et al.* [4]. Subsequently it was found, that the introduction of alkanoic acid residues at position 3 led to favorable antinociceptive compounds. Renard *et al.* [5] demonstrated that (6-acyl-2-oxo-3*H*-benzoxazol-3-yl) alkanoic acids and their esters exhibited a greater analgesic activity than aspirin. Önkol *et al.* [6, 7] indicated that [2(3*H*)-benzoxazolon-3-yl]propanamide and propanoic acid derivatives were more active than the corresponding acetic acid derivatives. In addition, Gülcan *et al.* [8] showed that 4-[5-chloro-2(3*H*)-benzoxazolon-3-yl]butanoic acid exhibits a greater analgesic potential than analogous amide

derivatives. Therefore, in the course of our research we planned to synthesize the title compound (**I**) as potential anti-inflammatory and analgesic agent and clarify its structure.

EXPERIMENTAL

Melting point of compound **I** was determined on a Boetius hot-stage microscope. The IR spectrum was recorded on a Specord 71 spectrometer. The ^{1}H-NMR spectrum was obtained on a Tesla BS 487 C spectrometer operating at 80 MHz in DMSO-d$_6$. Chemical shifts were reported in δ units (ppm) relative to tetramethylsilane as internal standard. Single crystal data was collected on a CAD-4 diffractometer.

Synthesis of 2-[(2,3-Dihydro-2-oxo-3-benzoxazolyl)methyl]benzoic acid (I)

To a stirred solution of 2(3*H*)-benzoxazolone (6.76 g, 0.05 mol) in dry N,N-dimethylformamide (DMF, 20 mL), 2 g of sodium hydride (80% suspension in oil) were added slowly. After addition was completed, the mixture was stirred for further 10 minutes. Then, phthalide (6.71 g, 0.05 mol) was added and the reaction mixture was refluxed for 6 hours, cooled, poured into 200 mL ice-water and acidified with 10% hydrochloric acid. The product

---

* To whom all correspondence should be sent:
E-mail: mgerova@chem.uni-sofia.bg

was precipitated, filtered and washed with water. Yield 7.72 g (57%). M.p. 214–216 °C (ethanol). IR (nujol, cm^{-1}): 1680, 1780 (v_{CO}); 2400–2750 (v_{CO}). ^{1}H-NMR (DMSO-d$_6$): 5.60 (s, 2H, CH$_2$), 7.0–8.1 (m, 8H, Ar**H**). Anal. Calcd. for C$_{15}$H$_{11}$NO$_4$: C 66.91; H 4.12; N 5.20. Found C 66.68; H 4.47; N 5.29.

X-ray analysis

A crystal of the title compound having approximate dimension 0.31×0.28×0.24 mm was placed on a glass fiber and mounted on an Enraf-Nonius CAD-4 diffractometer. X-ray data collection was carried out at 290 K with graphite monochromatized Mo-Kα radiation (λ = 0.71073 Å). The unit cell parameters were determined from 15 reflections and refined employing 22 higher-angle reflections, $18 < \theta < 20°$. The *ω/2θ* technique was used for data collection using Nonius Diffractometer Control Software [9]. Lorentz and polarization corrections were applied to intensity data using the WinGX [10]. The structure was solved by direct methods using SHELXS-97 [11] and refined by full-matrix least-squares procedure on F^2 with SHELXL-97 [11]. The hydrogen atom of the OH group (O4) has been located from difference Fourier map. All remaining hydrogen atoms were placed in idealized positions (C–H$_{aromatic}$ = 0.93 Å and C–H$_{methylen}$ = 0.97 Å) and were constrained to ride on their parent atoms, with U$_{iso}$(H) = 1.2U$_{eq}$(C or O).

Table 1. Crystal data and structure solution methods and refinement results for **I**

Crystal data	
C$_{15}$H$_{11}$N$_1$O$_4$	F_{000} = 280
M_r = 269.25	D_x = 1.44 Mg m^{-3}
Triclinic, *P–1*	Melting point: 487–489 K
Hall symbol: –P 1	Mo *K*α radiation λ = 0.71073 Å
a = 6.716 (3) Å	Cell parameters from 22 reflections
b = 7.828 (4) Å	θ = 18.0–19.9°
c = 13.283 (5) Å	μ = 0.11 mm^{-1}
α = 78.029 (12)°	T = 290 (2) K
β = 81.360 (17)°	Prism, yellow
γ = 65.7100 (10)°	Crystal size:
V = 621.0 (4) Å^3	0.31 × 0.28 × 0.24 mm
Z = 2	
Data collection	
Enraf Nonius CAD4 diffractometer	R_{int} = 0.028
Radiation source: sealed tube	θ$_{max}$ = 26.0°
Monochromator: graphite	θ$_{min}$ = 1.6°
T = 290(2) K	h = –8 → 8
non–profiled ω/2θ scans	k = –9 → 9
Absorption correction: none	l = –16 → 16
4782 measured reflections	3 standard reflections
2436 independent reflections	every 120 min
1801 reflections with $I > 2σ(I)$	intensity decay: –1%
Refinement	
Refinement on F^2	Secondary atom site location: difference Fourier map
Least-squares matrix: full	Hydrogen site location: inferred from neighbouring sites
$R[F^2 > 2σ(F^2)]$ = 0.039	H-atom parameters constrained
$wR(F^2)$ = 0.106	$w = 1/[σ^2(F_o^2) + (0.0507P)^2 + 0.0515P]$ where $P = (F_o^2 + 2F_c^2)/3$
S = 1.04	$(Δ/σ)_{max} < 0.001$
2436 reflections	$Δρ_{max}$ = 0.14 e Å^{-3}
181 parameters	$Δρ_{min}$ = –0.20 e Å^{-3}
0 constraints	Extinction correction: none
Primary atom site location: structure-invariant direct methods	

Scheme 1. Synthesis of the compound (I)

RESULTS AND DISCUSSION

As illustrated in Scheme 1, the preparation of 2-[(2,3-dihydro-2-oxo-3-benzoxazolyl)methyl] benzoic acid (**I**) was carried out by the reaction of 2(3*H*)-benzoxazolone with phthalide, which were refluxed in DMF in the presence of sodium hydride as base. The product **I** was isolated in good yield and purified by recrystallization from ethanol. The chemical structure of the title compound **I** was elucidated by IR, ¹H-NMR spectral data and X-ray analysis.

Crystal structure of 2-[(2,3-dihydro-2-oxo-3-benzoxazolyl)methyl]benzoic acid

Experimental conditions are summarized in Table 1. Selected bond distances and bond angles
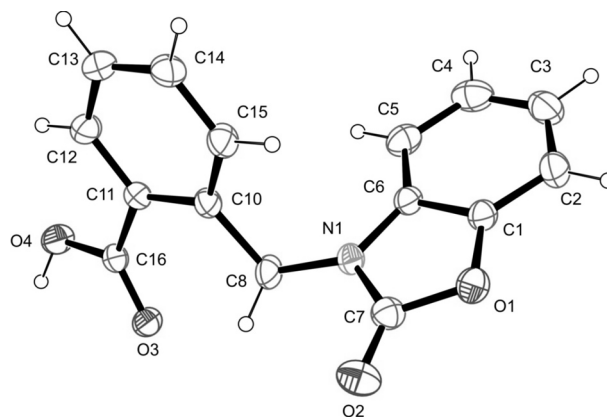
Fig. 1. A view of (I), showing the atom-numbering scheme. Displacement ellipsoids are drawn at the 50% probability level for all non-H atoms. All H atoms are rendered as spheres with arbitrary radii.

Table 2. Selected geometrical parameters for **I** (Å, °)

C1—C2	1.366 (2)	C10—C15	1.385 (2)
C1—C6	1.377 (2)	C10—C11	1.403 (2)
C1—O1	1.3797 (19)	C11—C12	1.393 (2)
C2—C3	1.381 (3)	C11—C16	1.485 (2)
C3—C4	1.378 (3)	C12—C13	1.377 (2)
C4—C5	1.386 (3)	C13—C14	1.372 (3)
C5—C6	1.373 (2)	C14—C15	1.382 (2)
C6—N1	1.391 (2)	C16—O3	1.2225 (18)
C7—O2	1.197 (2)	C16—O4	1.3092 (19)
C7—N1	1.364 (2)	O4—H4O	0.9426
C7—O1	1.377 (2)	C8—C10	1.514 (2)
C8—N1	1.4557 (19)		
C2—C1—C6	123.39 (16)	C15—C10—C11	117.77 (14)
C2—C1—O1	127.39 (15)	C15—C10—C8	120.46 (14)
C6—C1—O1	109.22 (13)	C11—C10—C8	121.75 (13)
C1—C2—C3	116.07 (18)	C12—C11—C10	119.65 (14)
C4—C3—C2	121.19 (18)	C12—C11—C16	118.29 (14)
C3—C4—C5	122.11 (18)	C10—C11—C16	121.93 (14)
C5—C6—C1	120.74 (15)	C13—C12—C11	121.07 (16)
C5—C6—N1	133.32 (15)	C14—C13—C12	119.66 (16)
C1—C6—N1	105.93 (13)	C14—C15—C10	122.14 (16)
O2—C7—N1	129.73 (17)	O3—C16—O4	122.13 (14)
O2—C7—O1	122.56 (16)	O3—C16—C11	123.27 (14)
N1—C7—O1	107.70 (14)	O4—C16—C11	114.55 (14)
N1—C8—C10	113.40 (12)	C6—N1—C8	126.57 (14)
C7—N1—C6	109.49 (13)	C7—O1—C1	107.62 (12)
C7—N1—C8	123.47 (14)		

Table 3. Hydrogen bonds and weak interactions for **I** (Å, °)

D–H···A	D(D–H)	d(H···A)	d(D···A)	<(DHA)
O(4)–H(4)···O(3)[i]	0.943	1.702	2.644(4)	177.4
C(12)–H(12)···O(4)[ii]	0.93	2.619	3.346(5)	135.5
C(5)–H(5)···O(1)[iii]	0.93	2.578	3.352(6)	141.0
Cg1···Cg1[iv]	–	–	3.529(8)	–

Symmetry codes: (i) *1-x, 1-y, -z* ; (ii) *1-x, 2-y, -z*; (iii) *-x+1, y, z* ; (iv) *-x, 1-y, -z*

*Cg*1 includes atoms C1, N1, C3, C4, C5, C6, C7, N1, O1
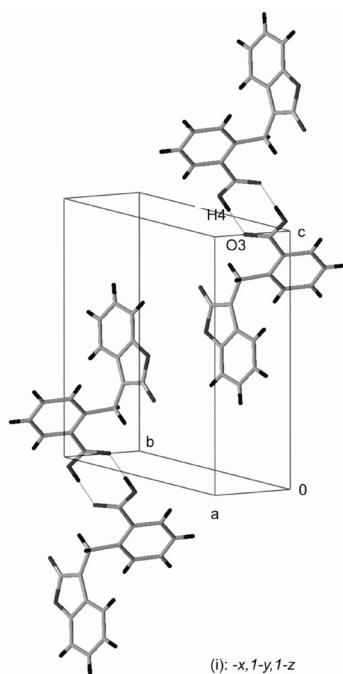
Fig. 2. A representation of the unit-cell contents of (I). Atoms involved in hydrogen bonding interactions are shown. Hydrogen bonds are rendered as dashed lines.

(i): -x,1-y,1-z

are listed in Table 2. Hydrogen bonds and weak interactions geometry are presented in Table 3. *ORTEP* [12] drawing diagram of the molecular structure with 50% probability and the atom numbering scheme is shown in Fig. 1. The data for publication were prepared with WinGX [10], *ORTEP* [12], and Mercury [13] program packages.

In the asymmetric unit of **I**, only one independent molecule is present (Fig. 1). The structural parameters of the title compound are comparable with those reported earlier [14–16]. The phenyl and benzoxazol fused ring systems are essentially planar with r.m.s. deviations of 0.008(6) and 0.018(9) Å respectively. The angle between the mean planes of the two ring systems is 71.12(3)°. In the three-dimensional arrangement of the molecules of **I** only one classical hydrogen bond was found (Fig. 2). A head-to-head O-H...O[i] (2.644(4) Å) interaction produces bicyclical dimmers. A subsequent careful examination of the intermolecular contacts shows that weak C–H...O and π...π interactions are responsible for the packing of the molecules in the crystal structure of **I**. Adjacent pairs of dimmers are connected through π...π [Cg1...Cg1[i]] interactions with shortest centroid-to-centroid distance of 3.529(8) Å (Fig. 3) [symmetry codes: (i) – x, 1 – y, 1 – z]. Two alternating C-H...O interactions of 3.346(5) Å and 3.352(6) Å produce pseudo layers along *ac* (Fig. 4).
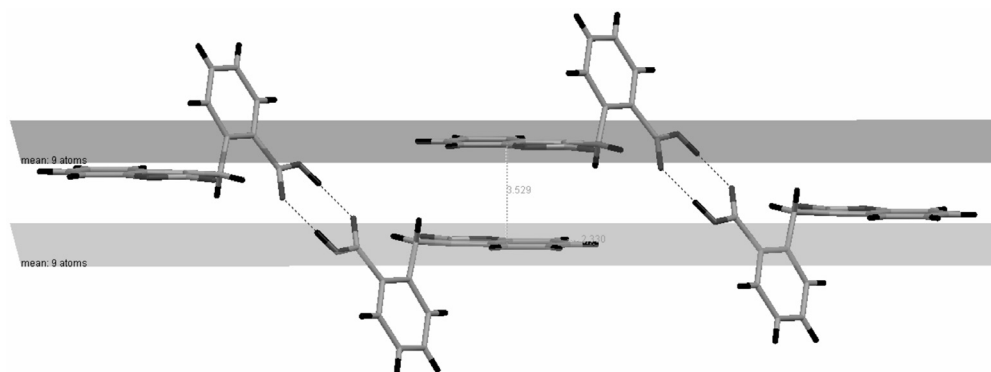
Fig. 3. A representation of the π...π interactions between the fused ring(represented by the mean planes) system in I.
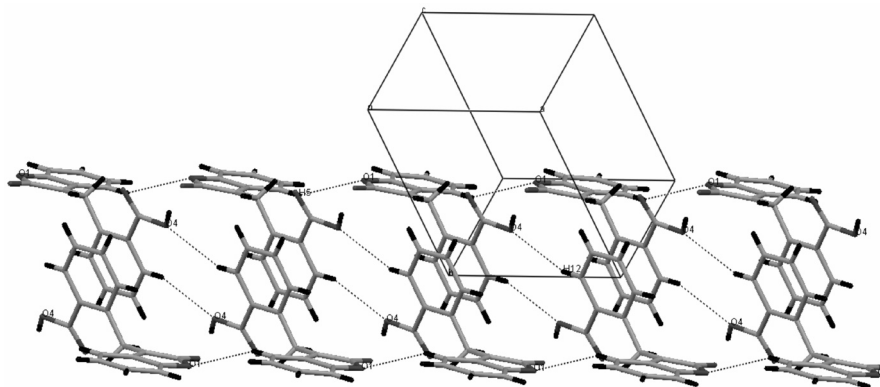
Fig. 4. A representation of C-H…O interactions interaction in I producing pseudo-layers along *ac*.

CONCLUSION

The crystallographic and spectroscopic data are in good agreement. There are no obvious discrepancies between solid-state and solution data.

SUPPLEMENTARY MATERIALS

CCDC 805276 contains the supplementary crystallographic data for this paper. This data can be obtained free of charge via www.ccdc.cam. ac.uk/data_request/cif, by e-mailing data_request@ ccdc.cam.ac.uk, or by contacting The Cambridge Crystallographic Data Centre, 12 Union Road, Cambridge CB2 1EZ, UK; fax: +44(0)1223-336033.

REFERENCES

1. J. Poupaert, P. Carato, E. Colacino, *Curr. Med. Chem.*, **12**, 877 (2005).
2. N. Gökhan, H. Erdoğan, B. Tel, R. Demirdamar, *Eur. J. Med. Chem.*, **31**, 625 (1996).
3. T. Önkol, S. Ünlü, E. Küpeli, E. Yeşilada, M. F. Şahin, *Turk J. Pharm. Sci.*, **6**, 93 (2009).
4. W. J. Close, B. D. Tiffany, M. A. Spielman, *J. Am. Chem. Soc.*, **71**, 1265 (1949).
5. P. Renard, D. Lesieur, C. Lespagnol, *Eur. J. Med. Chem., Chim. Ther.*, **15**, 453 (1980).
6. T. Önkol, S. Ito, E. Yildirim, K. Erol, M. F. Şahin, *Arch. Pharm. Pharm. Med. Chem.*, **334**, 17 (2001).
7. T. Önkol, Y. Dündar, B. Sirmagül, K. Erol, M. F. Şahin, *J. Fac. Pharm. Gazi*, **19**, 15 (2002).
8. H. O. Gülcan, E. Küpeli, S. Ünlü, E. Yeşilada, M. F. Şahin, *Arch. Pharm. Pharm. Med. Chem.*, **336**, 477 (2003).
9. Enraf-Nonius diffractometer control software, Release 5.1, 1993. Enraf-Nonius, Delft, The Netherlands.
10. L. J. Farrugia, *J. Appl. Cryst.*, **32**, 837 (1999).
11. G. M. Sheldrick, *Acta Cryst. A*, **64**, 112 (2008).
12. L. J. Farrugia, *J. Appl. Cryst.*, **30**, 565 (1997).
13. I. J. Bruno, J.C. Cole, P. R. Edgington, M. Kessler, C. F. Macrae, P. McCabe, J. Pearson, R. Taylor, *Acta Cryst. B*, **58**, 389 (2002).
14. S. Isik, Y. Köysal, M. Yavuz, M. Köksal and H. Erdogan, *Acta Cryst.* E, **60**, o2321 (2004).
15. A. Aydin, T. Önkol, M. Akkurt, O. Büyükgüngör, *Anal. Sci.: X-ray Struct. Anal.*, **21**, 119 (2005).
16. Ni Yan, X. Liu, M. K. Pallerla, J. M. Fox, *J. Org. Chem.*, **73**, 4283 (2008).

СИНТЕЗ И КРИСТАЛНА СТРУКТУРА НА 2-[(2,3-DIHYDRO-2-OXO-3-BENZOXAZOLYL)METHYL] БЕНЗОЕНА КИСЕЛИНА

М. Герова[1], Р. Николова[2], Б. Шивачев[2], О. Петров[1]

[1] *Химически Факултет, Софийски Университет, бул. „Дж. Баучер" 1, 1164 София*
[2] *Институт по минералогия и кристалография „Акад. Иван Костов",*
Българска Академия на Науките, ул. „Акад. Г. Бончев" бл. 107, 1113 София

(Резюме)

Отразени са синтезът, монокристален рентгеноструктурен, ИЧ и ЯМР спектроскопски изследвания на 2-[(2,3-dihydro-2-oxo-3-benzoxazolyl)methyl]benzoic acid. Веществото кристализира в *P*-1 пространствена група и параметри на елементарна клетка: $a = 6.716(3)$, $b = 7.828(4)$, $c = 13.283(5)$ Å, $\alpha = 78.029(12)$, $\beta = 81.360(17)$, $\gamma = 65.7100(10)$ °, $V = 621.0\ (4)$ Å^3, $M_w = 269.25$ и $Z = 2$. Тримерната подредба на молекулите се стабилизира от една (O-H…O) водородна връзка. Слаби C–H…O и π…π взаимодействия допринасят за допълнителна стабилност на кристалната структура.

Single-crystals of magnesium sulfite hexahydrate doped with nickel – structure, density and optical properties

G. Giorgi[1], G. L. Lyutov[2], L. G. Lyutov[2]*

[1] Universita Degli Studi di Siena – via A. Moro – 53100 Siena, Italy; e-mail: ciads@unisi.it
[2] Sofia University "St. Kl. Ohridski", J. Bourcher st. 1, Sofia, Bulgaria

$MgSO_3.6H_2O$ is a crystalline compound which possesses notable optical properties, which make possible its application in modern high technologies. Single-crystals of the compound can be obtained by method which combines chemical reaction and polythermic growth from low-temperature water-based solutions.

The crystallization process can be best started at temperatures 53–46 °C. At higher temperatures $MgSO_3.6H_2O$ is prone to turn into $MgSO_3.3H_2O$. Crystal growth lasts 20–25 days, where the temperature is gradually lowered to ambient by semi-automatic device.

The apparatus allows growth of crystals with maximum length of the basal edge of trigonal pyramid 30–40 mm.

For a first time we have started research on single-crystal growth of $MgSO_3.6H_2O$ with isomorphic inclusion of Ni^{2+} and Co^{2+} ions. It is supposed that these ions would influence the main physical and optical properties of the crystals, such as refractive index, range of optical transparency, magneto-optical properties etc. We have obtained single crystals of $MgSO_3.6H_2O$ with included 2–5% Ni^{2+} ions, where nickel is added by $NiCl.6H_2O$. The process starts with mixing the Mg- and Ni- bearing solution with the one containing SO_3^{2-} and $S_2O_5^{2-}$ at 50-60 °C, followed by gradual cooling the joint-solution until it reaches room temperature for a few days.

Key words: $MgSO_3.6H_2O$, dopping, Ni^{2+}, PACS: birefringence – solids – 78.20.F, density – crystalline solids – 71.20, diffraction – X-ray analysis – 61.10.H, structure – crystalline solids – 61.66.

1. INTRODUCTION

Co-crystallization depends on chemical correlation matrix – admixtures. Typical cases are shown in [1].

Co-crystallization of isomorphic and isodimorphic admixtures

Isomorphic compounds are compounds which have similar composition and crystallize in the same or similar form. In isomorphic compounds, mutual replacement of equivalent particles happens, in equivalent positions within the crystal structure. Solid solutions form by replacement in such way. In isodimorphic compounds, phase transition happens in which the admixture takes the structure of the main component. For example the compounds $NiSO_4.7H_2O$ (rhombic), $CoSO_4.7H_2O$ (monoclinic) and $CuSO_4.5H_2O$ (triclinic) can form mixed crystals, where the admixture accepts the unstable (for it) structure of the macro-component.

Co-crystallization of non-isomorphic admixtures

Non-isomorphic are ions which have different charges or different chemical characteristics. They are not replacements within the crystal structure but they are adsorbed on the surfaces of the growing crystals. That adsorption is selective and inclusion is on sectors. Such inclusions alter the shape of the crystal, because the inclusions change the speed of growth of the crystal in some directions.

Complex compounds can form well-shaped crystals, which include micro-admixtures (anomalous mixed crystals). Ions with higher charge can displace ions with lower charge near cation vacancy, thereby preserving general electro-neutrality. Such inclusion is called "hetero-valent isomorphism". That phenomenon can be used to dope crystals with admixtures, thereby giving them desired properties for usage in scintilators, lasers, piezoelectric and segnetoelectric elements.

Isotherms of co-crystallization of various systems are shown on Figure 1, where:

---

* To whom all correspondence should be sent:
E-mail: nhll@chem.uni-sofia.bg
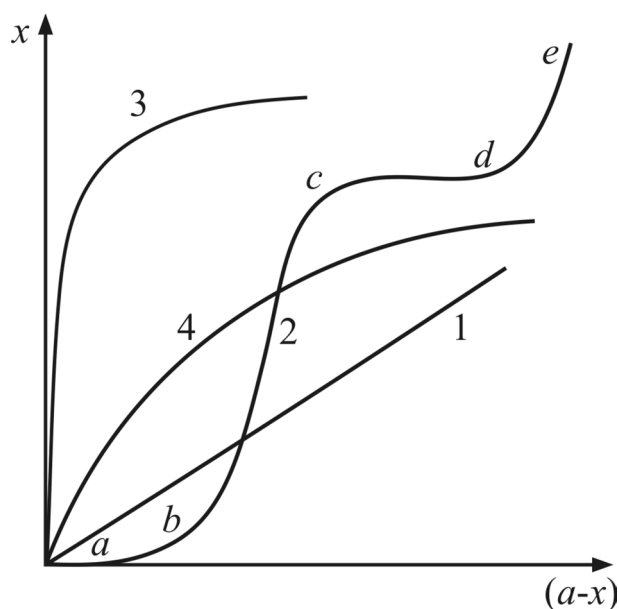
Fig. 1. Isotherms of co-crystallization of various systems. 1 – isomorphic and isodimorphic; 2 – anomalous mixed crystals with lower limit of inclusion; 3 – complex compounds of non-isomorphic admixtures; 4 – adsorption inclusion

Line 1 – Isotherm of co-crystallization of ideal mixed crystals. Equilibrium coefficient of co-crystallization can be gauged from the slope of line 1.

Line 2 – Isotherm of co-crystallization of anomalous mixed crystals, which shows the lower boundary of inclusion (*a-b*), rapid growth of the included amount (*b-c*), saturation, where the included amount does not change (*c-d*) and then sharp rapid growth of the included admixture amount (*d-e*).

Line 3 – Isotherm of co-crystallization of anomalous mixed crystals where complex ligands with high electric charge form new nucleus.

Line 4 – adsorption-based inclusion without lower boundary, observed in some rarely encountered systems.

2. EXPERIMENTAL

2.1. Method

Single-crystals of the compound can be obtained by method which combines chemical reaction and polythermic growth from low-temperature water-based solutions.

The chemical reaction is as follows [2]:

$$MgCl_2 + Na_2SO_3 \rightarrow MgSO_3 + NaCl$$
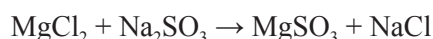
where, in order to prevent mass crystallization, HSO_3^- ions are added. They apparently widen the metastable zone and hinder the process by increasing

solubility. HSO_3^- ions can be brought into the system by adding $Na_2S_2O_5$ as follows:

$$Na_2S_2O_5 \rightarrow 2\,Na^+ + S_2O_5^{2-}$$

$$S_2O_5^{2-} + H_2O \rightarrow 2\,HSO_3^-$$
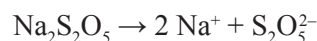
The crystallization process is the best to start at temperature 46–53 °C. At higher temperatures $MgSO_3.6H_2O$ is prone to turn into $MgSO_3.3H_2O$. Crystal growth lasts 20–25 days, where the temperature is gradually lowered to ambient by a semi-automatic device.

The apparatus allows growth of crystals with maximum length of the basal edge of trigonal pyramid 30–40 mm.

We have obtained single crystals of $MgSO_3.6H_2O$ with included 2–5% Ni^{2+} ions, where nickel is added by $NiCl.6H_2O$. The process starts with mixing the Mg- and Ni-bearing solution with the one containing SO_3^{2-} and $S_2O_5^{2-}$ at 50–55 °C, followed by gradual cooling the joint-solution until it reaches room temperature for a few days.

Polythermic single-crystal growth from low-temperature water-based solutions. In polythermic methods supersaturation is achieved by relying on Van-t-Hoff's equation, which is valid in most cases:

$$\frac{d\ln C}{dT} = \frac{\Delta H}{RT^2}$$

where: C – solubility (in mol parts), T – absolute temperature [°K], ΔH – enthalpy of dissolving, R – gas constant

When $\Delta H > 0$, $\frac{d\ln C}{dT} > 0$, the solubility (C) rises with temperature (T) and vice versa, as it is shown in Figure 2 (with continuous line).
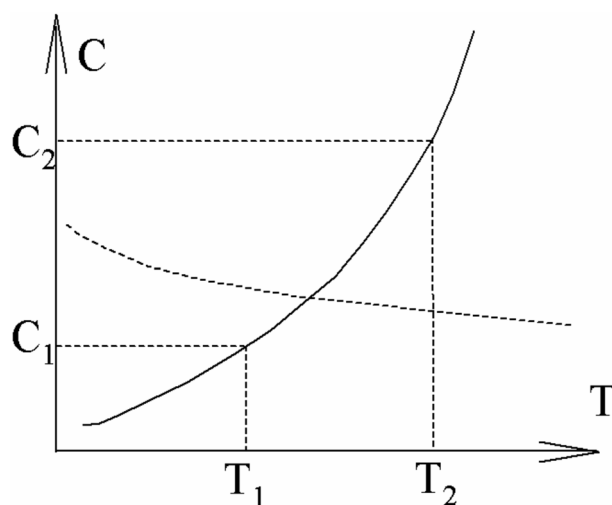
Fig. 2. Trend of solubility in dependence of temperature – ΔH > 0 (continuous line) and ΔH < 0 (broken line)
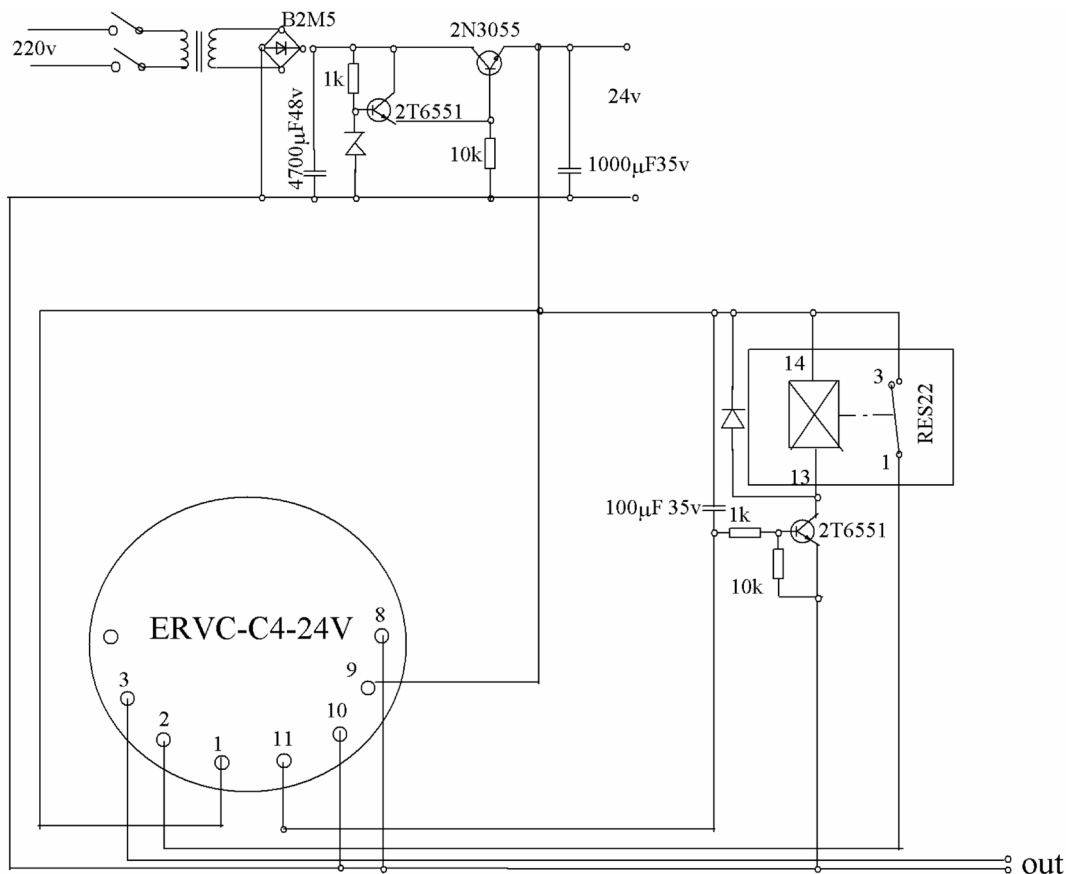
Fig. 3. Power supply and timer blocks

In the opposite case, when $\Delta H < 0$, $\dfrac{d\ln C}{dT} < 0$, the solubility (C) lowers with temperature (T) and vice versa, as it is shown on Figure 1 with broken line.

For a small temperature interval $\Delta T = T_2 - T_1$ (from the true experimental curve), we can determine the absolute saturation $C^0_2 - C^0_1$ and the relative one –

$$\sigma = \frac{C^0_2 - C^0_1}{C^0_1},$$

where C^0 is the corresponding equilibrium concentration for a given temperature T.

At greater temperature intervals of cooling $\Delta T = T_i - T_f$, where, T_i – initial temperature, T_f – final temperature of the process, it is possible to determine (from the true dependency $C^0(T)$), the volume of the solid mass which emanates from one mol solution by result of cooling within the chosen temperature interval. The volume of the solid mass is determined by the difference $C^0_{(T_i)} - C^0_{(T_f)}$. Of course, depending on our practical needs, besides mol-parts, we can choose other units to express the composition. Then, the obtained solid mass will be expressed in the corresponding dimensions.

In the cases where the true dependence $\dfrac{dC^0}{dT} \to 0$ this method is inapplicable .

2.2. Apparatuses

Apparatus consist: water – coated (jacketed) thermostat chamber, hermetic vessels with starting solution mixture and electronic hardware. The latter decreases temperature in the chamber by custom rate.

2.3. Hardware

The power supply block and timer are shown in Figure 3. The power supply block consists of transformer 220/30V, diode-bridge B2M5, Zener diode (24 V) and emitter follower, consisting of the transistors 2T6551 and 2N3055. The stabilization coefficient is not high, but fair enough for the schemes supplied. Capacitors 4700 µF/48V and 1000 µF/35V are meant to filter out the oscillations of the input power after a rectifier bridge and make connecting smoother.

The timer is basically a delaying digital relay ERVC-C4-24V and auxiliary relay RES22/RF4500-125. When the supply is turned on, supply voltage

238
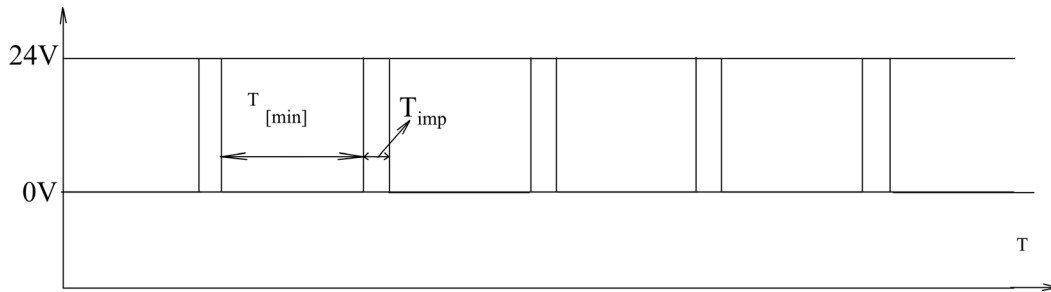
Fig. 4. Output time diagram

reaches ERVC, through the normally closed contact 1–3 of the relay RES22, which is not switched on because the tension on the base of 2T6551 is low. After the delaying relay engages, it switches the contacts from 8–11 to 9–11, at which point tension at the base of 2T6551 becomes high enough (24V) and it is held for a while by the capacitor 100μF/35V. Meanwhile RES22 opens the contacts 1–3, the supply for ERVC is cut off and contacts 9–11 switch to 8–11. Then the base of 2T6551 receives low tension, RES22 is left without supply and the contacts 1–3 close the circuit which powers ERVC. With that the cycle is complete. The pulse made by the contacts 1–3 of the relay ERVC is short-living. Its time span is determined by the elements in the basic circuit of 2T6551 – condenser 100μF/35V, resistors 10kΩ and 1kΩ, basal current of 2T6551 and the transition processes in the relay system. These processes may not be taken into account, because the R-C elements are chosen in such a way so $T_{imp} > 0,5S$. The generator outputs a pulsating tension, whose time-diagram is shown on Figure 4.

As we mentioned above, T_{imp} is firmly determined by the elements incorporated in the base circuit of 2T6551. They are chosen in such a way so the system can restart certainly and provide stable work for the pulse magnet and the counter (Fig. 5).

Elements $C = 3600\,\mu F/35V$ и $R = 5\Omega$ are included in order to provide reliable work for the pulse magnet (PM). This (PM) moves a stepper dialer which rotates the head of the contact thermometer. They mitigate shock pulsations of the electrical current, which appear whenever the pulse magnet is engaged.

In the case about the relative super-saturation σ, defined by the speed of cooling, there is addition caused by deviation of temperature. It is determined by the expression:

$$\Delta\sigma = \frac{dC^0}{dT} * \Delta T * \frac{1}{C^0}$$

where: $\Delta\sigma$ – deviation of the relative supersaturation, caused by ΔT, dC^0/dT; ΔT – deviation from the chosen temperature – T_0.

Apparently, as the dependency $C^0(T)$ goes more sloped and deviation $\Delta T = T - T_0$ becomes greater, so greater will be the fluctuations of super-saturation. Such conditions are unfavorable for crystal-growth
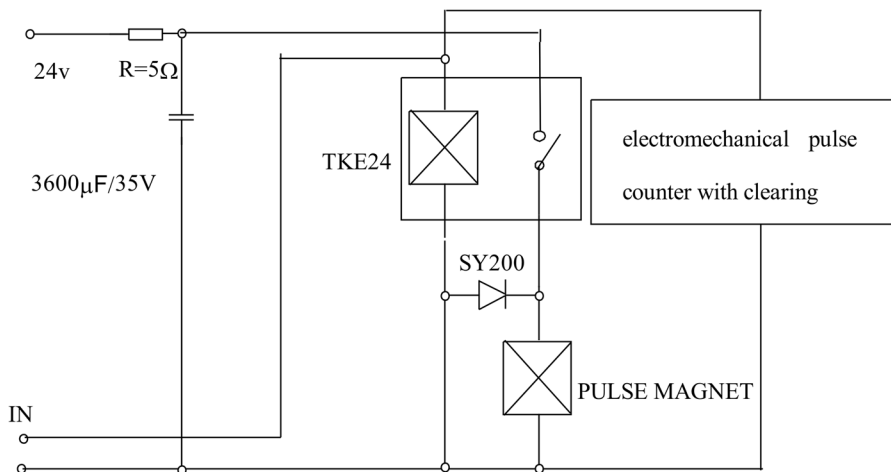
Fig. 5. Scheme of the pulse magnet and counter

from water-based solutions, so measures should be taken to mitigate ΔT. These measures can be as follows:

– Choice of sensor with minimized time for reaction and improvement of the ratio between thermal capacity of thermostatic part and the thermal capacity of the heater.

– Decreasing of the threshold of insensitivity of the sensor (in our case – contact thermometer).

In the case of classic wiring scheme of a contact thermometer when $T > T_{set}$, the electrical current goes through the thermometer and not through the coil of the mercury ampoule. That current $I_{KT} \approx 30$ mA, cannot be lowered in order to keep the circuit safely closed. That circumstance, paired with the induction of the coil and constant temperature, unchanged for long time leads to local soot formation in the capillary tube of the thermometer. That soot formation widens the threshold of insensibility in the contact zone.

In order to avoid that issue, we have developed a simple and reliable scheme (Fig. 6), which worked without breakdown for more than $2.6 \cdot 10^4$ hours.

The scheme consists of relay type TKE56PODG, TKE21PD, MKU48 or D-KD226B and transistor KT801A. The KD226B keeps the transistor safe from voltage surges during relay shut-down process. The value of the resistor R is determined by the following formula:

$$(24 - U_{e\delta}) \cdot \beta / I_R.$$

where: β – Coefficient of amplification (electrical current) of KT801A in a scheme "common emitter" (≈ 50); I_R – current of engagement of the relay (for

MKU48 ≈ 36 mA); $U_{e\delta}$ – potential between the emitter and base, which for the most transistors is $U_{e\delta} \leq 2V$, so:

$$(24 - 2) \cdot 50 / 36 \cdot 10^{-3} \approx 30 \text{ k}\Omega$$

The current through KT can be calculated by the Ohm principle $24V/30 = 0.7$ mA or $7 \cdot 10^{-4}$ A. Voltage over the mercury column is less than 2V. Under these conditions the mercury thermometer is virtually eternal, which is proven by $2.6 \cdot 10^4$ hours of continuous work without any visible change or wear.

2.4. X-ray and SEM apparatuses

For the experiments conducted in Italy, the following apparatuses have been used:

X-ray device and the single-crystal goniometer Siemens P4 four-circle diffractometer with graphite monochromated Mo-*Ka* radiation (l =0.71073Å) and the w/2q scan technique.

The structure was solved by direct methods implemented in the SHELXS-97 program. [G. M. Sheldrick, *SHELXL-97*, Rel. 97-2, Universität Göttingen, 1997]. The refinement was carried out by full-matrix anisotropic least-squares on F² for all reflections for non-H atoms by using the SHELXL-97 program. [G. M. Sheldrick, *SHELXL-97*, Rel. 97-2, Universität Göttingen, 1997].

SEM and the EDX probe Philips-501 scanning-electron microscope equipped with an EDAX 9100/60 energy-dispersive analyzer.

3. EXPERIMENTAL RESULTS AND DISCUSSION

3.1. Structure

It is revealed according to data from X-ray analysis conducted in Italy. Unit cell is shown on Figure 7. Analysis has also shown that nickel can isomorphic displace magnesium.

3.2. Density

Data about the density of various samples of magnesium sulfite hexahydrate are shown in Table 1. Density based on calculations about the size of the unit cell has unusually high value than literature data. As is well-known; there are huge objective difficulties of data processing in such cases [5, 6]. Even small inaccuracies can considerably compromise the final results. Future more precise data processing of difractogramme from X-ray analyses are yet to be done in order to solve these issues.
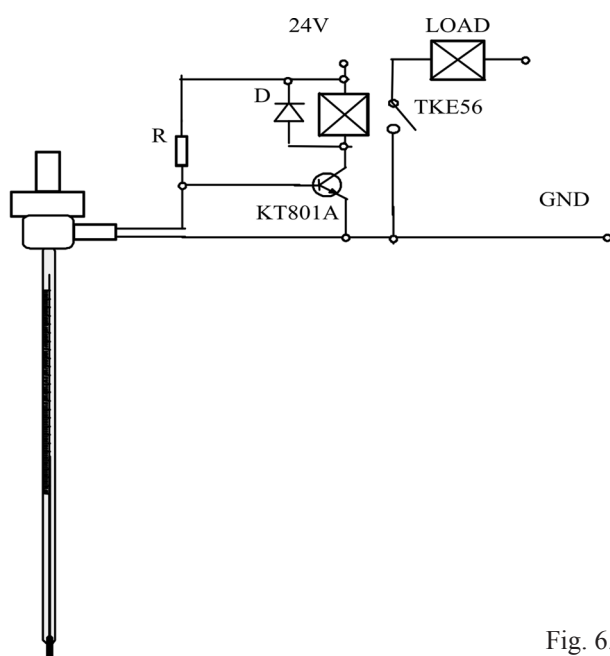
Fig. 6.

Table 1. Density of MgSO$_3$.6H$_2$O

Sample of MgSO$_3$.6H$_2$O	Density [g/cm^3]	Notes, sources
Literature references	1.72	Reference [3]
MgSO$_3$.6H$_2$O (doped with nickel)	2.151	Calculations based on X-ray analysis made in Italy.
MgSO$_3$.6H$_2$O (pure)	1.7138	Picnometric measurement made in Sofia University
MgSO$_3$.6H$_2$O (doped with nickel)	1.7493 (±0,12%)	Picnometric measurement made in Sofia University Crystals doped with nickel show slightly higher density than pure ones.
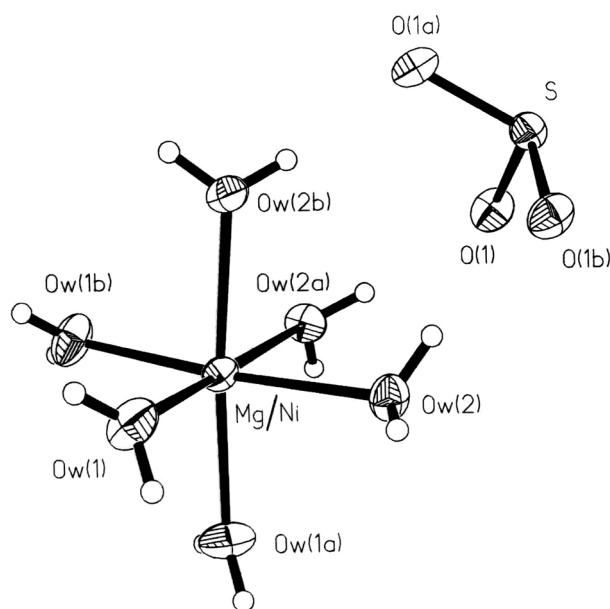
Fig. 7. Unit cell of MgSO$_3$.6H$_2$O: Ni

$$\rho = \frac{P}{(P+P_1-P_2)\cdot\rho^{-1}_{fluid}}$$

where: P – weight of the crystal sample; P_1 – weight of the vial filled with CCl$_4$; P_2 – weight of the vial filled with CCl$_4$ and submerged crystal sample; $P+P_1-P_2$ is the weight of the fluid with volume equal to that of the crystal sample

3.3. Refractive index

It has been measured with refractometer "Pulfrich-PR-2" (made by Carl Zeiss – Jena) and prism (V$_u$ F3). Data for the refractive index measurements are shown in Table 2. MgSO$_3$.6H$_2$O samples doped with nickel show slightly higher refractive indices for a given wavelength than pure samples.

Principal scheme of the refractometer with additional device (polarizer) is shown on Figure 8. The polarizer allows us to measure birefringence of the crystal.

We have conducted additional measurement of the density by picnometric method. For the purpose we have used a picnometric vial with volume of 25 cm^3 class "B" made by JENA^{er} GLASS – DDR. The vial is filled with fluid (in our case CCl$_4$) and then it is weighted on a balance. For the measurement we have used CCl$_4$ instead of water, because MgSO$_3$.6H$_2$O has certain solubility in water, which would compromise the final data. Then a crystal sample with known weight is submerged in the fluid and the vial is weighted again. Then the density is calculated with the following formula:

Fig. 8. Principal optic scheme of refractometer "Pwlfrich-PR-2", where Hg – mercury lamp; K – collimator; F – filters [λ]; P – polarization filter; D – aperture; KR – MgSO$_3$.6H$_2$O crystal (blue); PR – prism (Vu F3); R – angle of refraction; G – precise goniometer

Table 2. Refractive indices of MgSO$_3$.6H$_2$O

Wavelength λ [nm]	n$_o$ MgSO$_3$.6H$_2$O (pure)	n$_o$ MgSO$_3$.6H$_2$O (doped with Ni)	n$_e$ MgSO$_3$.6H$_2$O (pure)	n$_e$ MgSO$_3$.6H$_2$O (doped with Ni)
435.8	1.527	1.529	–	–
546.1	1.517	1.519	1.470	1.474

05-13-1998	16:22:49	KV: 20.0	Tilt: 0.0	TkOff: 35.0	
Fsc: 8022	Cps: 508	LSec: 100	Prst: 100L	Kev: 2.83	Cnt: 110

16:22:32   05-13-98

Elem:	Net	Wt%	At%	Error%	BG	P/B
O K	150.85	47.99	62.28	0.82	2.91	51.84
MgK	428.51	21.04	17.97	0.49	14.54	29.47
SiK	31.93	1.35	1.00	2.15	15.04	2.12
S K	666.74	28.19	18.25	0.39	14.95	44.60
NiK	10.22	1.42	0.50	3.82	5.02	2.04
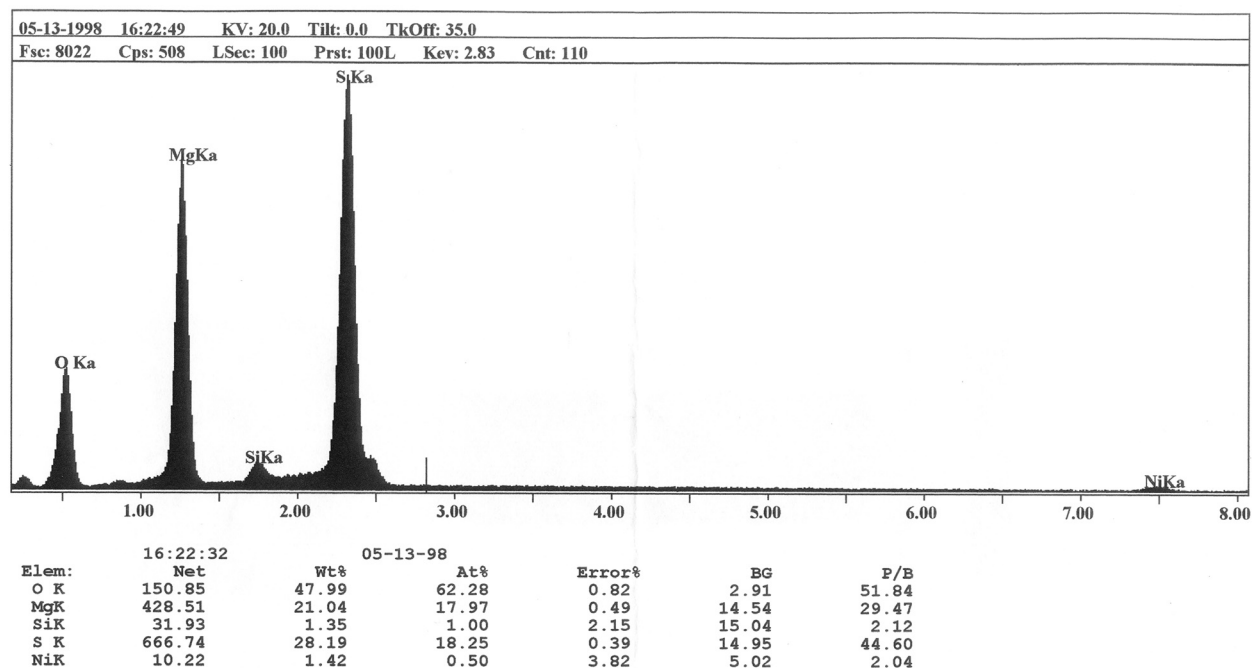
Fig. 9.

These data are in good accordance with the ones obtained previously by us [4] while using indirect method.

Nickel content within the crystals is determined by SEM and X-ray analyses conducted in Italy.

– Mg:Ni ratio results obtained by SEM → Mg: 0,9777; Ni: 0,0223; $\Sigma(Mg+Ni) = 1$

– Mg:Ni ratio results obtained by X-ray analysis → Mg: 09765; Ni: 0,0235; $\Sigma(Mg+Ni) = 1$

Mg:Ni ratio obtained by SEM is shown on Figure 9.

4. CONCLUSION

X-ray analysis has proved that inclusion of Ni is isomorphic on the places of Mg ions and that nickel content is within 2.2% with the latter also being confirmed by SEM analysis. Investigations on density and refractive index have showed that they increase with the presence of nickel.

The difference between density determined by picnometric method – 1.7493 ($\pm 0,12$%) and calculated from X – ray data – 2.151 is caused by the accepted molecular weight for $NiSO_3.6H_2O$, instead proportionally taken between molecular weight of $NiSO_3.6H_2O$ (M=246,865) and $MgSO_3.6H_2O$ (M=212,47). Comparison between the values calculated from X–ray data – 2.151 and picnometric data for $NiSO_3.6H_2O$ – 2.027 and databases: (ICSD #27807, ICSD #24140, ICSD #26149, ICSD #48112, PDF24-0739, PDF 01-0473) suggests such conclusion [7–11]. After recalculations according to considerations above we receive value of 1.858 g.cm^3 – close to real value.

We suppose that $MgSO_3.6H_2O$ possesses certain magneto-optic properties, such as refractive index changing under the influence of magnetic field. We hope to confirm that in our future studies. In the future, we expect to obtain similar data about Co-doppant [12–14]. This would help us to clarify these phenomena.

Unfortunately, $MgSO_3.6H_2O$ is not stable at temperatures exceeding 55–60 °C, and has certain solubility in water. Sources of heat and humidity from the air may limit its application in optical devices.

REFERENCES

1. E. Kirkova, Extremely pure compounds, University press "St Kl Ohridski", Sofia, 1994, 80–102.
2. Ts. Kovachev, *Republic of Bulgaria patent N 34515*.
3. A. I. Efimov, Properties of non-organic compounds, 1983.
4. Zh. Bunzarov, S. Saltiel, Ts. Kovachev, L. Lyutov, D. Russev, in: Proc. SPIE, 1996, vol. 3052, p. 197.

5. H. W. King, E. A. Payzant, *Canadian Metallurgical Quarterly,* **40**(3), 385 (2001).
6. Q. L. Zhang, W. P. Liu, L. H. Ding, *Chinese Sci. Bul.l,* **54**, 3940, doi: 10.1007/s11434-009-0592-6 (2009).
7. H. A. Klasens, W. Perdok, P. Terpstra, *Rec. Trav. Chim. Pays Bas*, **54**, 728 (1935).
8. H. A. Klasens, W. G. Perdok, P. Terpstra, *Z. Krist.*, **94**, 1 (1936).
9. S. Baggio, L. N. Beca, Acta Cryst. B, **25**, 1150 (1969).
10. H. Flack, *Acta Cryst. B*, **29**, 656 (1973).
11. L. Andersen, O. Lindqvist, *Acta Cryst. C* **40**, 584 (1984).
12. Zh. Bunzarov, I. Iliev, T. Dimov, P. Petkova, Ts. Kovachev, L. Lyutov, Y. Tzoukrovski, in: Proc. SPIE, 2009, vol. 7501, 75010X.
13. Zh. Bunzarov, I. Iliev, T. Dimov, P. Petkova, *Bulgarian Journal of Chemical Communications*, in press.
14. L. I. Pavlov, G. B. Hadjichristov, S. T. Lazarov, V. K. Kovachev, Z. Bunzarov, I. Buchvarov, I. Nikolov, M. Iliev, in: Proceedings of SPIE, 2007, vol. 6604, p. 66041P1.

МОНОКРИСТАЛИ ОТ МАГНЕЗИЕВ СУЛФИТ ХЕКСАХИДРАТ, ДОТИРАНИ С НИКЕЛ – СТРУКТУРА, ПЛЪТНОСТ И ОПТИЧЕСКИ СВОЙСТВА

Д. Джорджи[1], Г. Л. Лютов[2], Л. Г. Лютов[2]*

[1] *Университет Сиена, 53100 Сиена, Италия; e-mail: ciads@unisi.it*
[2] *Софийски Университет „Св. Кл. Охридски“, ул. „Джеймс Баучър“ № 1, София, Bulgaria, e-mail: nhll@chem.uni-sofia.bg*

(Резюме)

$MgSO_3.6H_2O$ е кристално вещество със забележителни оптични свойства, които правят възможно приложението му в съвременните висши технологии. Монокристали от веществото се получават по метод, който представлява комбинация на химическа реакция и политермично израстване от нискотемпературни водни разтвори. Химическата реакция е следната:

$$MgCl_2 + Na_2SO_3 \rightarrow MgSO_3 + NaCl$$
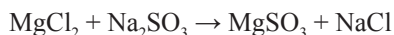
За да не настъпи масова кристализация, в системата се прибавят HSO_3^- йони, които явно разширяват метастабилната зона и инхибират процеса чрез повишаване на разтворимостта (аналогия – калцит). HSO_3^- йони се получават в системата от добавения $Na_2S_2O_5$ по уравненията.

$$Na_2S_2O_5 \rightarrow 2\ Na^+ + S_2O_5^{2-}$$

$$S_2O_5^{2-} + H_2O \rightarrow 2\ HSO_3^-$$
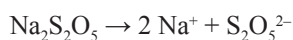
Растежът на кристалите продължава 20–25 дни, като постепенното понижение на температурата се осъществява от автоматизирано устройство.

Апаратурата позволява получаването на кристали с дължина на ръба на основата на тригоналната пирамида 30–40 mm. Получени са кристали от $MgSO_3.6H_2O$ с включени около 2 до 5% Ni^{2+} йони, като никела е добавен под формата на NiCl.6 H_2O.

Проведени са изследвания върху получените за пръв път в световната практика на монокристали от $MgSO_3.6H_2O$ с включени изоморфно Ni^{2+} и Co^{2+} йони. Показано е, че включеният Ni^{2+} повишава коефициента на лъчепречупване и плътността на кристалите, а така също и разликата n_o–n_e. Предполага се, че тези йони биха повлияли и върху магнитооптичните свойства на кристалите.

Theoretical and experimental studies on the coordination ability of 1,4-bis(dimethylphosphinylmethyleneoxy)benzene

P. J. Gorolomova[1], R. P. Nikolova[2], B. L. Shivachev[2], V. I. Ilieva[1], D. Ts. Tsekova[1], T. D. Tosheva[3], E. S. Tashev[3], S. G. Varbanov[4], G. G. Gencheva[1],*

[1] Faculty of Chemistry, University of Sofia, 1164 Sofia, Bulgaria
[2] Institute of Mineralogy and Crystallography, Bulgarian Academy of Sciences, 1113 Sofia, Bulgaria
[3] Institute of Polymers, Bulgarian Academy of Sciences, 1113 Sofia, Bulgaria
[4] Institute of Organic Chemistry with Center of Phytochemistry, Bulgarian Academy of Sciences, 1113 Sofia, Bulgaria

Combined experimental and theoretical study of the crystal, molecular and electronic structure, and coordination ability of 1,4-bis(dimethylphosphinylmethyleneoxy)benzene was performed using X-ray single-crystal analysis, FT-IR spectral characterization and quantum chemical calculations. The title compound crystallizes in the triclinic crystal system, P-1 space group. The asymmetric unit consists of two symmetrically independent molecules. The optimization of the molecular structure of the compound in gas phase at different levels of theory (ab initio, RHF/6-311G(d), MP2/6-311G(d) and DFT B3LYP/6-311G(2df,2p)) shows existence of several conformers. In the description of the conformers, a torsion angle C_{Ar}-C_{Ar}-O-C was used. The results from the optimized molecular structures are compared with the X-ray single crystal data. The electronic structure of the most important for the coordination ability molecular fragments, was described in terms of Natural Bond Orbitals (NBO) analysis and Mulliken charges.

Key words: X-ray diffraction, conformation analysis, chemical reactivity, tertiary phosphine oxides.

INTRODUCTION

Dimethyl(methyleneoxyaryl)phosphine oxides [1] are a relatively small group of organophosphorous compounds that belongs to the family of the tertiary phosphine oxides. The tertiary phosphine oxides are used widely in generation of Wittig-Horner reagents [2], as building blocks in organic synthesis [3] and intermediates for the design of nano-electronic and supramolecular materials [4]. In recent years, there has been considerable interest in the studying their coordination behavior to transition and lanthanide ions [5], because those of them having bulky and branched substituents are very suitable for extraction of rare-earth and transuranic elements [6]. Therefore, the current research on the coordination ability and reactivity of a series of bis(dimethylphosphinylme thyleneoxy)benzenes [7], whose representative is the title compound (Fig. 1) is timely and important, in order to evaluate their potential application in separation chemistry as well as for synthesis of

new materials. The presented paper describes the experimental and theoretical studies of the crystal, molecular and electronic structure of one of these isomers, namely 1,4-bis(dimethylphosphinylmethyl eneoxy)benzene (*p*-I) and discusses its coordination ability.
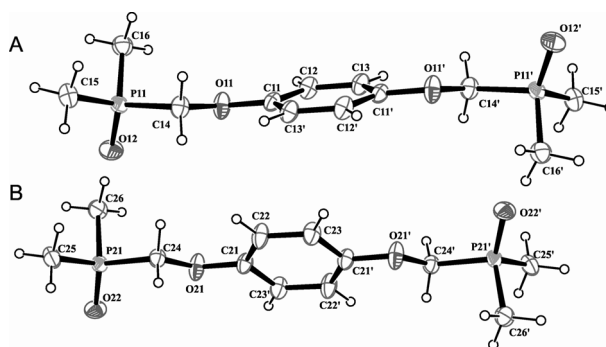
Fig. 1. An ORTEP view (ellipsoids at 50% probability) of 1,4-bis(dimethylphosphinyl-methyleneoxy)benzene with atom labeling scheme. H atoms are shown as small spheres of arbitrary radii

* To whom all correspondence should be sent:
E-mail: ahgg@chem.uni-sofia.bg

EXPERIMENTAL

Crystal growth

Colorless prismatic crystals of 1,4-bis(dimethyl-phosphinylmethyleneoxy)benzene suitable for X-ray diffraction were obtained during the interaction of $CuCl_2$ with a fourfold excess of the title compound in C_2H_5OH (96%). The experimental IR spectrum of p-I was recorded on a ALPHA FT-IR spectrometer – Bruker Optics. IR (cm^{-1}): 1501, 1437, 1416 ν(Ar(C=C)); 1291; 1221 ν(C$_{Ar}$-O); 1163 ν(P=O); 1043 ν(CH$_2$-O); 932, 896, 866, 835 δ(CH$_3$-P-CH$_3$) + δ(CH$_2$-P-CH$_3$); 822; 742; 523; 404.

Single crystal X-ray analysis

A prismatic crystal of the title compound having approximate dimension of 0.28 × 0.24 × 0.24 mm was placed on a glass fiber and mounted on an Enraf-Nonius CAD-4 diffractometer. X-ray data collection was carried out at room temperature with graphite monochromatized Mo-Kα radiation (λ = 0.71073 Å). The unit cell parameters were determined from 15 reflections and refined employing 22 higher-angle reflections, 17<θ< 20°. The $\omega/2\theta$ technique was used for data collection using Nonius Diffractometer Control Software [8]. Lorentz and polarization corrections were applied to intensity data using the WinGX [8]. The structure was solved by direct methods using SHELXS-97 [8] and refined by full-matrix least-squares procedure on F^2 with SHELXL-97 [8]. The hydrogen atoms were placed in idealized positions (C$_{aromatic}$ = 0.93, C$_{methyl}$ = 0.97 and C$_{methylene}$ = 0.96 Å) and were constrained to

Table 1. Crystal data and structure refinement indicators for 1,4-bis(dimethylphosphinylmethyleneoxy)benzene

Empirical formula	$C_{12}H_{20}O_4P_2$
Molecular weight	290.22
Crystal size (mm)	0.28 × 0.24 × 0.24
Crystal system	Triclinic
Space group	$P-1$
T(K)	290
Radiation wavelength (Å)	0.71073 (Mo Ka)
a (Å)	6.202(3)
b (Å)	9.290(6)
c (Å)	13.356(9)
V(Å^3)	728.1(8)
Z	2
α (°)	100.066(12)
β (°)	100.788(12)
γ (°)	99.675(11)
d (mg. m^{-3})	1.324
μ (mm^{-1})	0.302
Reflections collected/unique	5628/2873
$R1$ (I > 2σ (I))	0.056
$wR2$ (all data)	0.164

ride on their parent atoms, with U_{iso}(H) = 1.2U_{eq}(C). The X-ray diffraction data and details concerning data collection and structure refinement are given in Table 1, ORTEP diagram of p-I is shown on Fig. 1

Computational Details

The molecular and electronic structures of 1,4-bis(dimethylphosphinyl-methyleneoxy)benzene were obtained by DFT (Becke's 3-Parameter hybrid functional combined with the Lee-Yang-Parr correlation functional B3LYP [9]) and *Ab initio* (Restricted Hartree-Fock Method (RHF) [10] and second-order Møller-Plesset perturbation theory (MP2) [11]) calculations (full optimization in gas phase) using Gaussian 09 software package [12]. Several basis sets such as triple-ζ Pople type 6-311G(d), 6-311G(2df,2p) and double-ζ 6-31G(d) [13] were employed for the calculations. The Natural Bond Orbitals (NBO) [14] calculations ware performed with the NBO-code included in Gaussian09 [12]. The calculated vibrational frequencies of the compound (program package Gaussian09 [12]) were used to check the structural optimizations and to compare with experimental data.

RESULTS AND DISCUSSION

The title compound crystallizes in the centrosymmetric space group P-1. There are two symmetrically non equivalent p-I molecules (A and B) in the asymmetric unit Fig. 1. The observed bond lengths and angles in A and B are typical for such compounds [3a, 15], Table 2. The phosphorus atoms possess distorted tetrahedral arrangement with bond angles range between 104.07(3) – 114.82(5)° and relatively localized P=O double bonds (1,489 Å for (A) and 1,484 Å for (B)). The two *p*-disposed ether oxygen atoms O11 and O11' as well as O21 and O21' also share the least-squares aromatic plane with an equal deviation of **0.003 Å**. The A and B moieties are arranged in such a matter to minimize the steric hindrance of the bulky methyl groups Fig. 2. The angle between the mean planes of the aromatic rings of A and B is 55.11(4)°. In addition, very weak C-H(methyl)…..O intermolecular interactions are observed. As a consequence of the crystal packing, the dihedral angles C-O-C$_{Ar}$-C$_{Ar}$ in the A and B type molecules differ about 6.5° and these of O12-P11-C14-O11 – about 14.5°.

Geometry optimization of the molecular structure and conformation analysis

Despite of the accuracy of the X-ray data in the determination of the molecular geometry of the

Table 2. Selected geometrical parameters (distances in Å and angles in degrees) of p-I

Parameter	Crystal structure		Optimized structure / Methods		
	A	B	RHF	B3LYP	MP2
Dihedral angles (°)					
O12-P11-C14-O11	−50.22()	−64.76()	+180.00	+180.00	+177.89
P11-C14-O11-C11	−178.77()	+178.37()	+179.99	+180.00	−91.88
C14-O11-C11-C12	−157.91()	+164.77()	+0.02	0.00	−5.61
C14'-O11'-C11'-C13	+157.91()	−164.77()	−179.98	+180.00	175.22
Bond angles (°)					
C12-C11-O11	125.15()	125.04()	115.84	115.74	114.76
C13'-C11-O11	115.64()	115.52()	124.97	124.75	126.20
C11-O11-C14	117.13()	117.21()	119.82	118.36	118.63
O11-C14-P11	108.11()	108.53()	109.33	110.18	115.20
C14-P11-O12	113.77()	114.82()	110.82	110.49	111.75
C14-P11-C15	114.38()	114.39()	104.99	103.87	102.20
C14-P11-C16	105.13()	104.07()	104.99	104.83	106.48
C15-P11-O12	114.38()	114.39()	114.72	115.52	115.93
C15-P11-C16	107.22()	106.54()	105.71	102.72	103.94
C16-P11-O12	112.83()	113.58()	114.71	115.51	115.26
Bond Length ?					
C11-O11	1.377()	1.375()	1.358	1.376	1.376
O11-C14	1.412()	1.423()	1.398	1.420	1.420
C14-P11	1.832()	1.846()	1.832	1.846	1.845
P11-O12	1.489()	1.484()	1.469	1.489	1.498
P11-C15	1.785()	1.777()	1.810	1.818	1.811
P11-C16	1.785()	1.786()	1.800	1.818	1.811
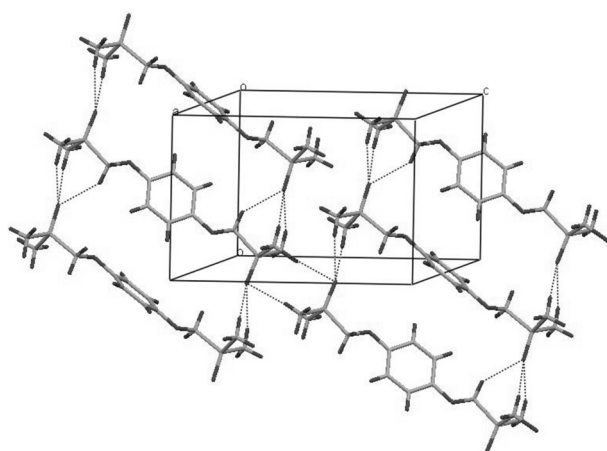
Fig. 2. Packing of the molecules within the unit cell down the b-axis. Intermolecular interactions are marked with dashed lines.

studied compound, to estimate fully its electronic structure and coordination behavior, theoretical analysis was applied. Generally, the molecule possesses two types of coordination centers: the phosphoryl oxygen atoms as well as the ether oxygen atoms. In addition, the bond lengths of the P=O units are indicative for localized double bonds [15] and hence it could be expected relatively limited coordination ability of the phosphoryl oxygen atoms.

The computational modelling of the molecular and electronic structure of 1,4-bis(dimethylphos phinylmethyleneoxy)-benzene was performed in gas phase using different levels of theory: RHF/6-311G(d) and MP2/6-311G(d) and DFT B3LYP/6-311G(2df,2p) (Fig. 3). All theoretical found bond lengths and bond angles are in agreement with X-ray refinements values (Table 2). However, significant differences were observed for the torsion angles. The optimized structures obtained using RHF/6-311G(d) and B3LYP/6-311G(2df,2p) are close but differ significantly of that obtained by MP2/311G(d) (Table 2, Fig. 3). Moreover, each of them differs from the experimental single-crystal data. The differences relate to the positions of the two substituents in respect to the plane of the benzene ring. In addition, if we compare the experimentally determined dihedral angles and these obtained after geometry optimization using the Z-matrix from the X-ray diffraction, torsion relaxations were also observed (Fig. 4.). Thus in gas phase, free from the intermolecular forces, the molecules relax to the nearest local minima in the potential surface. It is evident that the observed large degree of structural mobility is due to the three single bonds C(Ar)-O-C-P in each substituent. In order to characterize the stable conformational states, the potential energy profile for the internal rotation around C_{Ar}-O was calculated. In the description of the conformers, the
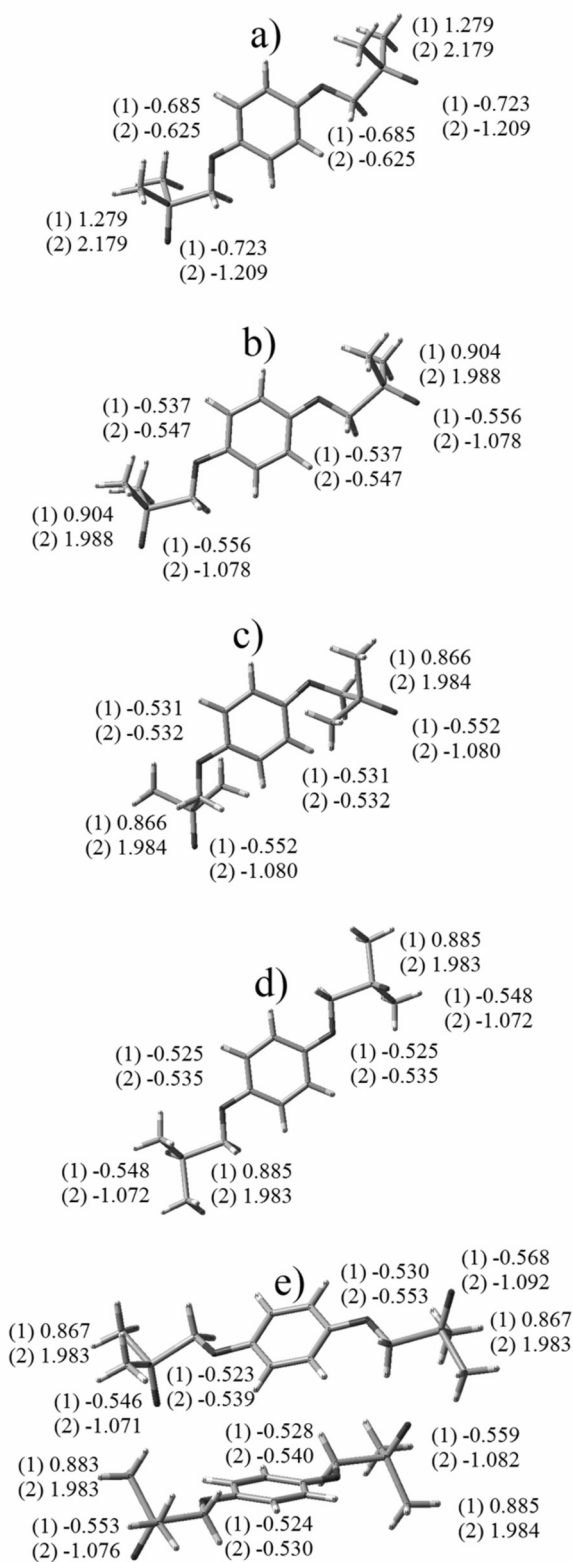
Fig. 3. Optimized structure of 1,4-bis(dimethylphosphinylmethyleneoxy)benzene with depicted values of the Mulliken (1) and NPA (2) charges, obtained using: a) RHF/6-311G(d); b) B3LYP/6-311G(2df,2d); c) MP2/6-311G(d); d) Z-matrix of X-ray data for an isolated A molecule at B3LYP/6-31G(d); e) Z-matrix of X-ray data of the two molecules in the unit cell at B3LYP/6-31G(d)

Fig. 4. Molecular structure of isolated A molecule using X-ray data: a) single point structure, b) after optimization (the optimization was carried out without any restrictions on the symmetry)

torsion angle between the benzene ring and the O11-C14 bond, namely C_{Ar}-C_{Ar}-O-C (ϕ, C12-C11-O11-C14) was used (Fig. 5). The opposite dihedral angle (C12'-C11'-O11'-C14') in the second substituent has values around -179.5° or +179.5°.

B3LYP/6-31G(d) calculations predict the existence of more then five conformations (Fig. 5). The estimated conformational energy differences are very small (<3 kJ/mol) and only between the most stable conformer ($\phi\sim150°$) and the least stable one ($\phi\sim30°$), the energy difference is ~11.5 kJ/mol (Fig. 5). Hence, on the basis of the theoretical results, the existence of several relative stable conformers could be expected.

The minima obtained by the theoretical scan were optimized. The five relevant lowest energy conformers found are depicted on Fig. 6. Their calculated parameters together with these obtained for the optimized molecule structures on the basis of the Z-matrix of the X-ray data for an isolated A molecule as well as for A and B molecules in the unit cell are presented in Tables 3. The calculated data for the minimized energies listed in Table 3 show that the highest symmetric conformer d) with dihedral angles $\phi_1 = C_{14}$-O_{11}-C_{11}-C_{12} and $\phi_2 = C_{14'}$-
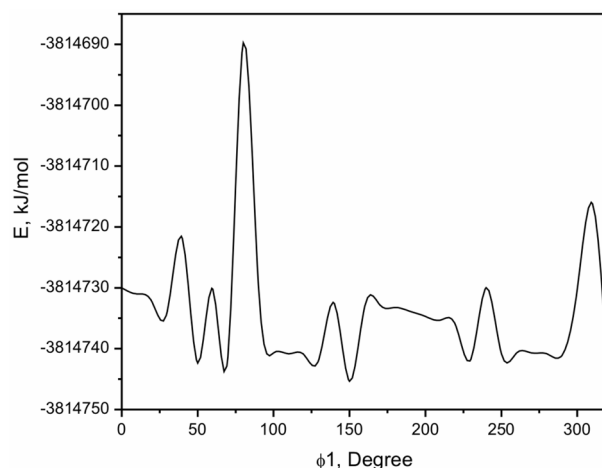
Fig. 5. Calculated potential energy curve for the rotation around the C11-O11 single bond

$O_{11'}$-$C_{11'}$-C_{13} +180° and − 180° is the most stable one among the various conformers. This conformer is with 1.6 kJ/mol more stable, than the optimized molecules, obtained af ter geometric optimization of the Z-matrix of X-ray data (the calculated total

energy is presented per one molecule) and 20.8 kJ/mol more stable than the optimized molecular structure of the isolated A-molecule.

In order to appraise the coordination ability of the compound, its molecular structure was interpreted from the electronic point of view. Selected results from the natural population analysis of the five conformers together with the molecule structures obtained from optimization of the X-ray determined Z-matrix are presented in Tables 3 and 4.

The discussion is focused on the lone pair orbitals (LP) of ether oxygen and phosphoryl oxygen atoms as well as on their principal localization quantitatively estimated through second order perturbation energy stabilization (see Table 3). The one-centre valence lone pairs (LP) orbitals are appropriate for co-ordination to metal ions. One LP orbital on ether oxygens and two LP orbitals of phosphoryl oxygens have mainly p-character and they are practically occupied by two electrons. Natural bond orbital (NBO) analysis provides a description of the molecular structure by a set of localized two-center bond and antibond orbitals as well as one-center core pair, valence lone pair and Rydberg extravalence orbitals. The analysis of the stabilizing interactions between filled and unoccupied as well as destabilizing interactions between filled orbitals based on the data of the Fock matrix in the NBO basis is useful to estimate the hyperconjugation and delocalization in the molecule structure. In this study, DFT level computation was used to investigate the second-order interaction between the oxygen LP orbitals and proper vacant antibonding orbitals as a measure for the lone pair localization (Table 4) and potential coordination ability. The natural orbital interactions were analyzed with the NBO Version 3.1 [14]. Since these interactions lead to donation of occupancy from the localized NBOs of the idealized Lewis structure into the empty non-Lewis orbitals, they refer to the "delocalization" corrections to the zeroth-order natural Lewis structure. For each donor NBO (*i*) and acceptor NBO (*j*), the stabilization energy *E2* as defined in [14e] is associated with the degree of $i \rightarrow j$ intramolecular hyperconjugative interactions and can be used as a measure of the engagement of the lone pairs in the intramolecular delocalization. The larger the *E(2)* values shows the more intensive interaction between electron donors and electron acceptors orbitals. The data about the interactions of $n(O_{11}) \rightarrow \pi(C_{11}$-$C_{12})$* and $n(O_{11'}) \rightarrow \pi(C_{11'}$-$C_{13})$* are related to resonance in the molecules due to electron donation from LP(O) of the ether oxygen atoms to anti-bonding acceptor π(C-C) of the phenyl ring. The large stabilization energy for these interactions (more then 103.8 kJ/mol, Table 4) shows high hyperconjugation between the electron donating ether oxygen and the phenyl ring. These
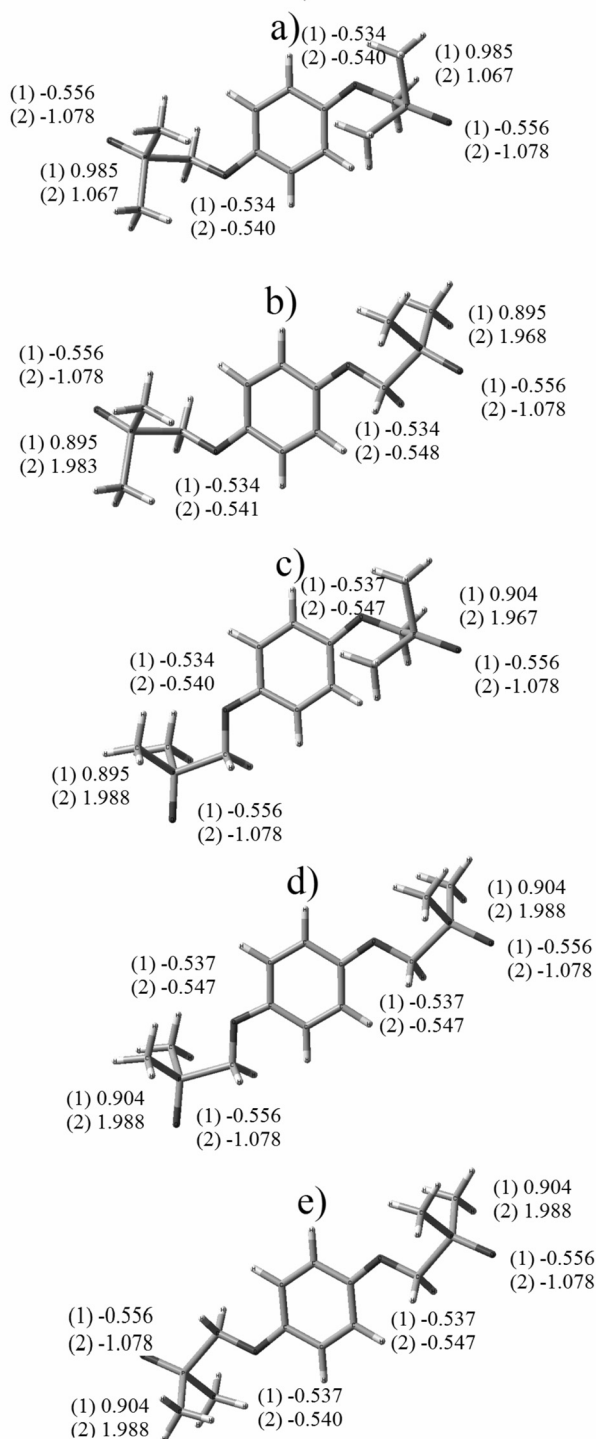
Fig. 6. The lowest energy conformers with depicted values of the Mulliken (1) and NPA (2) charges

Table 3. Theoretical parameters of the selected stabile conformers and the optimized molecules using Z-matrix of X-ray data for the isolated A molecule, and A and B molecules in the crystallographic cell obtained by B3LYP/6-31G(d) level of theory (Dihedral angles $\phi1$= C14-O11-C11-C12 and $\phi2$ = C14'-O11'-C11'-C13; *– HOMO)

Parameter			Dehedral Angles		Lone pair					
Conformation number	Molecular Energy [kJ/mol]		ϕ_1	ϕ_2	LP(O11) Ocupancy % p character Orbital Energy, [kJ/mol]	LP(O11') Ocupancy % p character Orbital Energy, [kJ/mol]	LP1(O12) Ocupancy % p character Orbital Energy, [kJ/mol]	LP2(O12) Ocupancy % p character Orbital Energy, [kJ/mol]	LP1(O12') Ocupancy % p character Orbital Energy, [kJ/mol	LP2(O12') Ocupancy % p character Orbital Energy, [kJ/mol]
a)	−3814739.1		12.33	−170.61	1.85514 99.69 % p −849.9	1.85419 99.78 % p −848.6	1.80991 99.74 % p −619.8	1.79848 99.74 % p −620.0	1.81002 99.74 % p −620.1	*1.79836 99.74 % p −620.0
b)	−3814739.4		11.23	178.69	1.85463 99.73 % p −846.9	1.85974 99.92 % p −845.2	1.80985 99.74 % p −618.1	1.79813 99.74 % p −618.3	1.81097 99.74 % p −618.7	*1.79827 99.73 % p −619.1
c)	−3814740.0		179.74	−172.31	1.85903 99.92 % p −845.6	1.85298 99.84 % p −845.9	1.81094 99.74 % p −618.7	1.79826 99.73 % p −619.1	1.81020 99.74 % p −617.4	*1.79832 99.74 % p −617.5
d)	−3814750.9		180.00	−180.00	1.85904 99.92 % p −843.5	1.85904 99.92% p −843.6	1.81092 99.74 % p −617.3	1.79819 99.73 % p −617.7	1.81092 99.74 % p −617.3	*1.79818 99.73 % p −617.7
e)	−3814750.2		0.03	179.98	1.85974 99.92 % p −842.9	1.85974 99.92% p −842.9	1.91108 99.74 % p −617.3	1.79845 99.75 % p −617.8	1.81107 99.74 % p −617.4	*1.79844 99.74 % p −617.8
X-ray 1mol	−3814730.1		177.38	3.02	1.85689 99.91 % p −821.9	*1.85689 99.91 % p -821.9	1.80764 99.73 % p −609.0	1.79568 99.71 % p −608.5	1.80764 99.73 % p −609.0	1.79568 99.71 % p -608.5
X-ray 2 mol	−7629498.5		−173.56	10.51	1.86100 99.91 % p −841.4	*1.85541 99.91 % p -828.6	1.82171 99.88 % p −675.1	1.80944 99.89 % p −674.3	1.80730 99.73 % p −612.5	1.79523 99.71 % p −612.1
	(−3814749.3 per one molecule)		4.11	177.93	1.84878 99.87 % p −781.0	1.86183 99.79 % p −821.0	1.81071 99.74 % p −553.5	1.79856 99.72 % p −553.0	1.80908 99.73 % p −615.8	*1.79731 99.71 % p −615.3

intramolecular interactions, which are the biggest for calculated molecules of the conformers **c** and **d**, block significantly the possibility of ether oxygens to participate in additional intermolecular interactions as co-ordination to metal ions. The stabilization energy values calculated about the orbital overlap of LP(O) of phosphoryl oxygen atoms and the two antibonding σ(C-P)* orbitals are lower (see Table 4) and the differences between orbital energies are bigger . The mainly p-character of these oxygen lone pair orbitals (Table 3) together with low participation in intramolecular hyperconjugation (Table 4) show behavior close to pure lone pair orbitals. Hence on the basis of the NBO analysis it could be concluded that phosphoryl oxygen atoms are more reactive and capable to coordinate than ether oxygens. Generally, the data presented in Table 4 shows that the two phosphoryl oxygen atoms belonging to one molecule of p-I have different reactivity. The close values for the stabilization energies and the differences of the orbital energies were only observed for the

molecules obtained from the optimization of the Z-matrix of X-ray data. On the basis of the data from the second-order perturbation theory analysis of the orbital donor-acceptor interactions it could be concluded that the more reactive to coordination is one of the two phosphoryl oxygen atoms per molecule and the most reactive molecule is that of the d-conformer, obtained after optimization in gas phase. The coordination through the ether oxygen atoms is less likely because of conjugation with the aromatic π-electrons.

In order to obtain additional chemical interpretation to the charge distribution in the optimized molecular structures and hence complete characterization of the electronic structure, the natural atomic charges and Mulliken charges were analyzed in the ground state. The data for the atomic charges obtained from the Mulliken population analysis [16] and molecular charge distribution in terms of NPA (Natural population analysis) charges (namely – nuclear charge minus summed natural populations

Table 4. Second-order perturbation theory analysis of the of the donor-acceptor interactions based on the NBO basis

Conformation number	Donor NBO (i)	Acceptor NBO (j)	E(2)[a] [KJ/mol]	E(j) – E(i)[b] [a. u.]	F(ij)[c] [a. u.]
a)	LP(O11)	BD*(C11-C12)	100.4	0.35	0.087
	LP(O11')	BD*(C11'-C13)	112.6	0.34	0.092
	LP1(O12)	BD*(P11-C15)	69.2	0.45	0.078
	LP2(O12)	BD*(P11-C14)	94.0	0.43	0.089
	LP1(O12')	BD*(P11'-C15')	68.2	0.45	0.078
	LP2(O12')	BD*(P11'-C14')	94.1	0.43	0.089
b)					
	LP(O11)	BD*(C11-C12)	101.0	0.35	0.087
	LP(O11')	BD*(C11'-C13)	112.7	0.34	0.092
	LP1(O12)	BD*(P11-C15)	67.6	0.45	0.078
	LP2(O12)	BD*(P11-C14)	94.1	0.43	0.089
	LP1(O12')	BD*(P11'-C15')	67.5	0.45	0.078
	LP2(O12')	BD*(P11'-C14')	92.8	0.44	0.089
c)					
	LP(O11)	BD*(C11-C12)	114.5	0.34	0.093
	LP(O11')	BD*(C11'-C13)	115.4	0.34	0.093
	LP1(O12)	BD*(P11-C15)	66.8	0.45	0.077
	LP2(O12)	BD*(P11-C14)	92.8	0.44	0.089
	LP1(O12')	BD*(P11'-C15')	68.5	0.45	0.078
	LP2(O12')	BD*(P11'-C14')	94.1	0.43	0.089
d)					
	LP(O11)	BD*(C11-C12)	114.5	0.34	0.093
	LP(O11')	BD*(C11'-C13)	114.5	0.34	0.093
	LP1(O12)	BD*(P11-C15)	66.8	0.45	0.077
	LP2(O12)	BD*(P11-C14)	92.9	0.44	0.089
	LP1(O12')	BD*(P11'-C15')	66.8	0.45	0.077
	LP2(O12')	BD*(P11'-C14')	92.9	0.44	0.089
e)					
	LP(O11)	BD*(C11-C12)	103.0	0.35	0.088
	LP(O11')	BD*(C11'-C13)	112.6	0.34	0.092
	LP1(O12)	BD*(P11-C15)	66.7	0.45	0.077
	LP2(O12)	BD*(P11-C14)	92.7	0.44	0.089
	LP1(O12')	BD*(P11'-C15')	66.7	0.45	0.077
	LP2(O12')	BD*(P11'-C14')	92.8	0.44	0.089
X-ray 1mol	LP(O11)	BD*(C11-C12)	114.1	0.34	0.092
	LP(O11')	BD*(C11'-C13)	103.8	0.34	0.088
	LP1(O12)	BD*(P11-C15)	80.7	0.45	0.085
	LP2(O12)	BD*(P11-C14)	91.3	0.43	0.088
	LP1(O12')	BD*(P11'-C15')	80.6	0.45	0.085
	LP2(O12')	BD*(P11'-C14')	91.25	0.43	0.088
X-ray 2 mol	LP(O11)	BD*(C11-C12)	100.8	0.35	0.087
	LP(O11')	BD*(C11'-C13)	115.5	0.34	0.093
	LP1(O12)	BD*(P11-C15)	72.0	0.46	0.081
	LP2(O12)	BD*(P11-C14)	83.0	0.45	0.085
	LP1(O12')	BD*(P11'-C15')	80.1	0.45	0.085
	LP2(O12')	BD*(P11'-C14')	92.2	0.43	0.088
	LP(O21)	BD*(C21-C22)	113.3	0.33	0.091
	LP(O21')	BD*(C21'-C23)	107.9	0.34	0.091
	LP1(O22)	BD*(P21-C25)	78.9	0.45	0.084
	LP2(O22)	BD*(P21-C24)	91.7	0.43	0.088
	LP1(O22')	BD*(P21'-C25')	81.4	0.45	0.085
	LP2(O22')	BD*(P21'-C24')	89.0	0.43	0.087

a) E(2) means energy of hyperconjugative interactions;
b) E(j) – E(i) – Energy difference between donor and acceptor i and j NBO orbitals.
c) F(i, j) is the Fock matrix element between i and j NBO orbitals.

of NAOs on the atom) [14d] are presented on Figures 3 and 6. The Mulliken's procedure, the most widely used method for representation of the electron density distribution was performed at each level of theory using variety of basis sets. The analysis of molecular charge distribution supported the description of electron-pair "bonding" unit was done at DFT level of theory using 6-31G(d) basis set. The calculations obtained for the molecule of *p*-I in gas phase and using Z-matrix of the solid state at different level of theory proved the gain of more negative charges from the phosphoryl oxigens and hence higher reactivity. The comparison of the charge distribution in the conformers (Fig. 6) shows that they differ only in respect to the charges on the oxygen and phosphorus atoms.

These differences could be explained with different degree of conjugation in the chain P-CH$_2$-O-Ar-O-CH$_2$-P as a consequence of different spatial location of the substituents in the five conformers. On the basis of the charge distribution, it is worth comparing the reactivity of the phosphoryl O-atoms obtained for the optimized structures in gas phase and solid state using DFT calculations. The most reactive is one of the phosphoryl O-atoms belonging to one of the two molecules obtained after optimization of the X-ray data for the two molecules in the unit cell. It should be emphasized that the electron density distribution on the two molecules obtained after X-ray data optimization differs significantly and the distribution on the molecule A is close to the data obtained from optimization in gas phase.
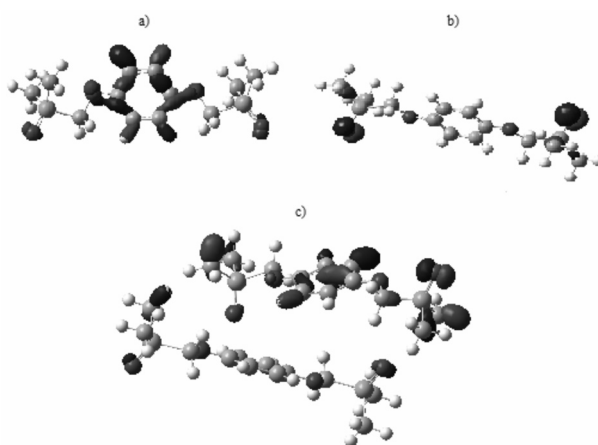
Fig. 7. Frontier molecular orbitals, studied by RHF/6-311G(d) level of theory as the optimization was done in: a) gas phase; b) using the Z-matrix of X-ray data for an isolated A molecule at B3LYP/6-31G(d); e) using the Z-matrix of X-ray data of the two molecules in the unit cell at B3LYP/6-31G(d)

This trend was proved again using RHF/6-311G(d) level of theory, as can be seen from the computed electronic density map presented on Fig. 7.

To clarify the differences in the spatial location of the substituents in the molecule of p-I obtained after optimization in gas phase and that from X-ray single crystal refinement, and their influence on the reactivity, the IR spectrum of the polycrystalline sample of the studied compound was re-

Table 5. Selected experimental and calculated frequencies (B3LYP/6-311G(d) of 1,4-bis(dimethyl phosphinylmethyleneoxy)benzene

Experimental	Calculated			Assignment
	gas phase	X-ray of 1 molecules	X-ray of 2 molecules	
–	1597	–	–	ν(Ar(C=C))
	1566	–	1501	
1501	1485	1499	1499	
1437	–	–	1412	
1416	1403	1411	1411	
1221	1212	1216	1219	ν(C$_{Ar}$-O)
	1196	1204	1217	
			1205	
			1203	
1163	1165	–	1177	ν(P=O)
	1163	1175	1175	
			1173	
1043	1027	1047	1047	ν(CH$_2$-O)
932	1015	932	1044	
896		924		
866	933	875	935	δ(CH$_3$-P-CH$_3$)
835	929	846	876	+ δ(CH$_2$-P-CH$_3$)
	905		868	
	849		847	

corded. The observed experimental IR frequencies were compared with theoretically predicted vibrational spectra (Table 5). The calculated vibrational frequencies proved the correctness of the structural optimizations. The assignments of the bands of the experimental IR spectrum are made in accordance with IR data and NCA published for tertiary phosphine oxides (Table 5) [5b,16]. The comparison of the experimental with the calculated data shows coincidence in different regions. The observed P=O stretching band coincides with calculated frequencies for optimized molecule in gas phase as well as the calculated spectrum using X-ray data is close to experimental spectrum in the range ν H_2C-O and $\delta((CH_3$-P-$CH_3)$ bands. Therefore, it could be assumed that more than one conformer present in real polycrystalline sample.

CONCLUSION

The crystal structure of 1,4-bis(dimethylphosphinylmethyleneoxy)benzene reveals the existence of two symmetrically non equivalent molecules (A and B) in the asymmetric unit. To estimate fully its electronic structure and coordination behavior, theoretical analysis was applied. All theoretical found bond lengths and bond angles are in good agreement with X-ray refinements values and large differences were observed for the dihedral angles related to the location of the two substituents in respect to the plane of the benzene ring. To explain the structural mobility due to the three single bonds C(Ar)-O-C-P in each substituent, the conformational analysis was applied. Five relevant lowest energy conformers were found as the estimated conformational energy differences are very small. The coordination ability of the compound was evaluated in terms of Natural Bond Orbitals, Mulliken charges and analysis of the frontier molecular orbitals. The highest reactivity was proved for the phosphoryl O-atoms. The calculated vibrational frequencies of the compound were used to check the structural optimizations and to compare with experimental data. The most stable conformer was obtained by computation in gas phase, because free from the intermolecular forces, the molecule relaxes to the nearest local minima in the potential surface. The steric hindrance of the bulky methyl groups is an acting force for the arrangement in the crystal structure. In the polycrystalline sample, conformers with different location of the substitutes are possible.

Supplementary Materials

CCDC 805281 contains the supplementary crystallographic data for this paper. This data can be obtained free of charge via www.ccdc.cam.ac.uk/data_request/ cif, by e-mailing data_request@ccdc.cam.ac.uk, or by contacting The Cambridge Crystallographic Data Centre, 12 Union Road, Cambridge CB2 1EZ, UK; fax: +44(0)1223-336033.

REFERENCES

1. S. Varbanov, T. Tosheva, G. Borisov, *Phosphourus, Sulfur & Silicon,* **63**, 397 (1991).
2. a) R. Nassar, B. C. Noll, K. W. Henderson, *Polyhedron,* **23**, 2499 (2004); b) N. M. A. El-Rahman, L. S. Boulos, *Molecules, 7,* 81 (2002).
3. a) B. A. Trofimov, S. F. Malysheva, N. K. Gusarova, V. A. Kuimov, N. A. Belogorlova, B. G. Sukhov*, Tetrahedron Letters, ***49,** 3480 (2008); b) A. R. Daniewski, L. M. Garofalo, S. D. Hutchings, M. M. Kabat, W. Liu, M. Okabe, R. Radinov, G. P. Yiannikouros, *J. Org. Chem.*, **67,** 1580 (2002**)**.
4. R. Lerebours, Ch. Wolf, *Org. Lett,.* **9**, 2737 (2007); b) A. C. Durrell, H. B. Gray, N. Hazari, Ch. D. Incarvito, J. Liu, E. C. Y. Yan, *Cryst. Growth & Des. Communication,* **10**, 1482 (2010).
5. a) G. Borisov, G. Varbanov, L. M. Venanzi, A. Albinati, F. Demartin, *Inorganic Chemistry* **33**, 5430 (1994); b) N. Trendafilova, I. Georgieva, *Vibrational Spectroscopy,* **20**, 133 (1999); c) V. Vassileva, G. Gencheva, E. Russeva, S. Varbanov, R. Scopelliti, E. Tashev, *Inorg. Chim. Acta,* **358**, 2671 (2005); d) L. Le Saulnier, S. Varbanov, R. Scopelliti, M. Elhabiri, J.-Cl. G. Bünzli, *J. Chem. Soc., Dalton Trans.*, 3919 (1999); e) L. N. Puntus, An.-S. Chauvin, S. Varbanov, J.-Cl. G. Bünzli, *Eur. J. Inorg. Chem,.* 2315 (2007).
6. a) F. de M. Ramírez, S. Varbanov, C. Cécile, G. Muller, N. Fatin-Rouge, R. J.-Cl. G. Bünzli, *J. Phys. Chem. B,* **112**, 10976 (2008)**;** c) J. D. Law, K. N. Brewer, R. S. Herbst, T. A. Todd, D. J. Wood, *Waste Managment,* **19**, 27 (1999); d) Z. Chan, Y. Yan-Zhao, Z. Tao, H. Jian, L. Chang-Hong, *J. Radioanal. Nucl. Chem.,* **265**, 419 (2005).
7. a) R. Petrova, B. Shivachev, D. Tsekova, P. Gorolomova, V. Ilieva, S. Varbanov, G. Gencheva, *Ist National Crystallographic Symposium, Sofia*, p. 129 (2009); b) G. Gencheva, D. Tsekova, P. Gorolomova, V. Ilieva, R. Petrova, B. Shivachev, T. Tosheva, E. Tashev and S. Varbanov, *Second Workshop on Size-Dependent Effects in Materials for Enviromental Protection and Energy Application,* p. 51 (2010); c) V. Ilieva, R. Petrova, B. Shivachev, P. Gorolomova, D. Tsekova, T. Tosheva , E. Tashev , S. Varbanov, G. Gencheva, *IInd National Crystallographic Symposium, Sofia*, p. 49 (2010).
8. a) Enraf-Nonius, CAD-4 EXPRESS Software. Enraf-Nonius, Delft, The Netherlands (1994); b) K. Harms and S. Wocadlo, XCAD4. Program for Processing

CAD-4 Diffractometer Data. University of Marburg, Germany (1995); c) G. M. Sheldrick, *Acta Cryst., A64*, 112 (2008).

9. a) A. D. Becke, *J. Chem. Phys.,* **97,** 2155 (1992); b) A. D. Becke, *J. Chem. Phys.,* **98**, 9173 (1992); c) C. T. Lee, W. T. Yang, R. G. Parr, *Phys. Rev., B,* **37**, 785 (1988).

10. a) C. C. Roothan, *Rav. Mod. Phys*., **23**, 69 (1951); b) G. G. Hall, *Proc. Roy. Soc,*. **205**, 541 (1951).

11. C. Møller, M. S. Plesset, *Phys. Rev,*. **46**, 618 (1934).

12. M. J. Frisch; G. W. Trucks; H. B. Schlegel; G. E. Scuseria; M. A. Robb; J. R. Cheeseman; Jr. J. A. Montgomery; T. Vreven; K. N. Kudin; J. C. Burant; J. M. Millam; S. S. Iyengar; J. Tomasi; V. Barone; B. Mennucci; M. Cossi; G. Scalmani; N. Rega; G. A. Petersson; H. Nakatsuji; M. Hada; M. Ehara; K. Toyota; R. Fukuda; J. Hasegawa; M. Ishida; T. Nakajima; Y. Honda; O. Kitao; H. Nakai; M. Klene; X. Li; J. E. Knox; H. P. Hratchian; J. B. Cross; V. Bakken; C. Adamo; J. Jaramillo; R. Gomperts; R. E. Stratmann; O. Yazyev; A. J. Austin; R. Cammi; C. Pomelli; J. W. Ochterski; P. Y. Ayala; K. Morokuma; G. A. Voth; P. Salvador; J. J. Dannenberg; V. G. Zakrzewski; S. Dapprich; A. D. Daniels,; M. C. Strain; O. Farkas; D. K. Malick; A. D. Rabuck; K. Raghavachari; J. B. Foresman; J. V. Ortiz; Q. Cui; A. G. Baboul; S. Clifford; J. Cioslowski; B. B. Stefanov; G. Liu; A. Liashenko; P. Piskorz; I. Komaromi; R. L. Martin; D. J. Fox; T. Keith; M. A. Al-Laham; C. Y. Peng; A. Nanayakkara; M. Challacombe; P. M. W. Gill; B. Johnson; W. Chen; M. W. Wong; C. Gonzalez; and J. A. Pople; Gaussian, Inc., Wallingford CT, Gaussian 09 (Revision-A.01); Gaussian, Inc.: Pittsburgh, PA, 2009.

13. S. F. Boys, F. Bernardi, *Molecular Physics,* **19**, 553 (1970).

14. a) J. P. Foster, F. Weinhold, *J. Am. Chem. Soc.,* **102**, 7211 (1980); b) A. E. Reed, F. Weinhold, *J. Chem. Phys.*, **78**, 4066, (1983); c) A. E. Reed, R. B. Weinstock, F. Weinhold, *J. Chem. Phys.*, **83**, 735, (1985); d) A. E. Reed, F. Weinhold, *J. Chem. Phys.*, **83**, 1736, (1985); e) A. E. Reed, L. A. Curtiss, F. Weinhold, *Chem. Rev.*, **88**, 899, (1988).

15. a) A. C. Durrell, H. B. Gray, N. Hazari, Ch. D. Incarvito, J. Liu, E. C. Y. Yan, *Cryst. Growth & Design*, **10**, 1482 (2010); b) H. K. Wang, *Acta Chem. Scand,*. **19**, 879 (1965); c) V. Chandrasekhar, R. Azhakar, *Cryst. Eng. Comm,*. **7**, 346 (2005).

16. R. S. Mulliken, *J. Chem. Phys.* **23** (1955) 1833.

17. K. Nakamoto, *Infrared and Raman Spectra of Inorganic and Coordination Compounds-Part B,* 5th ed., John Wiley&Sons, New York, NY, USA (1997).

ТЕОРЕТИЧНО И ЕКСПЕРИМЕНТАЛНО ИЗСЛЕДВАНЕ ВЪРХУ КООРДИНАЦИОННАТА СПОСОБНОСТ НА 1,4-БИС(МЕТИЛФОСФИНИЛМЕТИЛЕНОКСИ)БЕНЗЕН

П. Й. Гороломова[1], Р. П. Николова[2], Б. Л. Шивачев[2], В. И. Илиева[1], Д. Ц. Цекова[1], Т. Д. Тошева[3], Е. С. Ташев[3], С. Г. Варбанов[4], Г. Г. Генчева[1]

[1] *Химически факултет, Софийски университет*
[2] *Институт по минералогия и кристалография, Българска академия на науките*
[3] *Институт по полимери, Българска академия на науките*
[4] *Институт по органична химия с Център по фитохимия, Българска академия на науките*

(Резюме)

Молекулната, кристалната структура и координационната способност на 1,4-бис(метилфосфинилмети ленокси)бензен са изучени експериментално, с методите на рентгеновата дифракция и ИЧ- спектроскопия, и теоретично - с *ab initio* RHF/6-311G(d), MP2/6-311G(d) методите, както и с DFT B3LYP/6-311G(2df,2p). Съединението кристализира в триклинна кристална система, с пространствена група на симетрия Р-1. Квантово-химичните пресмятания за газова фаза показаха, че съединението може да съществува в няколко слабо различаващи се по енергия стабилни конформери, описани чрез диедричния ъгъл C_{Ar}-C_{Ar}-O-C. Кординационните свойства бяха характеризирани с помощта на NBO-анализ, оценка на Мъликеновите заряди и разпределението на електронната плътност върху естествените несвързващи LP молекулни орбитали. Получените резултати показаха, че с най-висока координационна способност се отличават фосфорилните О-атоми. Най-стабилният конформер беше получен за газова фаза. Данните от рентгеновата дифракция показаха, че подреждането на молекулите в кристалната опаковка се определя от стеричното отблъскване между обемистите метилови групи от заместителите.

Synthesis of BiBO₃ by crystallization of glasses in the Bi₂O₃–MoO₃–B₂O₃ system

R. S. Iordanova[1], A. D. Bachvarova-Nedelcheva[1]*, L. I. Aleksandrov[1], Y. B. Dimitriev[2]

[1] *Institute of General and Inorganic Chemistry, Bulgarian Academy of Sciences,*
"Acad. G. Bonchev", bld. 11, 1113 Sofia, Bulgaria
[2] *University of Chemical Technology and Metallurgy, 8 Kl. Ohridski blvd., 1756 Sofia, Bulgaria*

The aim of the present work is to verify the synthesis of bismuth borates by crystallization from glasses. Several bismuth boromolybdate glasses were selected and heat treated at 500–530 °C for different exposure times. Obtaining of BiBO₃ polymorphs, Bi₄B₂O₉, Bi₃B₅O₁₂ and Bi₂MoO₆ has been detected by X-ray diffraction (XRD). Additional information for the formation of BiBO₃ crystal phase was obtained by infrared spectroscopy (IR). There is significant difference in the IR spectra of the glass 50Bi₂O₃.50B₂O₃ and crystal BiBO₃ product. The reason is that in the glass sample the content of BO₄ units is higher than in the crystallized one.

Keywords: crystallization, glasses, X-ray diffraction.

INTRODUCTION

There is significant interest in the preparation and characterization of bismuth borate glasses, glass ceramics and single crystals for their application in non-linear optics [1–5]. An early comprehensive study of several oxide glasses containing Bi₂O₃ as a network former was reported by Dumbaugh [6]. A recent article discussed the effects of melting conditions and crucible materials on the optical properties of oxide glasses containing bismuth [7]. Crystalline bismuth borates, also have received increased attention in recent years due to their outstanding properties like high density, refractive index and very high coefficients of second and third harmonic generation. The phase diagram of Bi₂O₃–B₂O₃ system was first determined by Levin and Daniel [8] and a variety of stable phases are known to exist: Bi₂₄B₁₂O₃₉ (boron sillenite), Bi₄B₂O₉, Bi₃B₅O₁₂, BiB₃O₆ (bismuth triborate), Bi₂B₈O₁₅ (bismuth octaborate). The metastable BiBO₃ phase (bismuth orthoborate) that is missing in the original phase diagram possesses two polymorph modifications (BiBO₃-I and BiBO₃-II) [9–11]. It can be prepared by cooling of a melt with composition of 50B₂O₃.50Bi₂O₃ [9, 10], and it was found that it decomposes into a mixture of the stable Bi₄B₂O₉ and

Bi₃B₅O₁₂ phases at 600 °C [9]. Recently, Egorysheva et al. [12] published a review on the vibrational spectra of bismuth borate crystals. Among several inorganic borate crystals for applications in non-linear optical devices, bismuth triborate (BiB₃O₆) phase is known to have the highest coefficient for second harmonic generation (2.5–7) and numerous studies on its single crystal growth and optical properties have been carried out [10, 13]. Ihara et al. [11] demonstrated for first time that the BiBO₃ phase is also a nonlinear optical crystal with second harmonic intensity about 110 times as large as α-quartz.

Although various studies have been published for obtaining of bismuth borate phases from supercooled melts and glasses some questions still remain open concerning the use of different crucible materials and the influence of preparation conditions [4]. In our previous studies [14–17] it was established that MoO₃ is a suitable component to decrease the melting temperatures in the MoO₃–La₂O₃–B₂O₃, MoO₃–Nd₂O₃–B₂O₃ and MoO₃–ZnO–B₂O₃ systems [15] and the possibility to modify the crystallization processes. That is the reason the ternary system MoO₃-Bi₂O₃-B₂O₃ has been chosen as a subject of this study. The present paper is a continuation of our previous investigations on the ternary Bi₂O₃–MoO₃–B₂O₃ system. The location of the glass formation region was determined, the structure of glasses and optical properties of the glasses and

---

* To whom all correspondence should be sent:
E-mail: albenadb@svr.igic.bas.bg

glass-crystalline materials were investigated as well [18]. The aim of the present work is to verify the synthesis of $BiBO_3$ by crystallization from glasses in the presence of MoO_3 as an additional flux agent in the ternary Bi_2O_3–MoO_3–B_2O_3 system.

EXPERIMENTAL

All compositions (10 g) were prepared using reagent grade oxides MoO_3 (Merck, p.a.), Bi_2O_3 (Merck, p.a.) and H_3BO_3 (Reachim, chem. pure) as starting materials. The homogenized batches were melted for 15 min in air in alumina crucibles. The melting temperature was limited to 1000 °C in order to decrease the volatility and reduction of the components. The glasses were obtained by press quenching between two copper plates (cooling rate ~10^2 K/s). Several glass compositions, situated in different part of the glass formation region were selected: $50Bi_2O_3.50B_2O_3$, $50Bi_2O_3.10MoO_3.40B_2O_3$, $60Bi_2O_3.5MoO_3.35B_2O_3$, $49Bi_2O_3.2MoO_3.49B_2O_3$ and $63Bi_2O_3.2MoO_3.35B_2O_3$ and additional heat-treatment at 500–530 °C for different exposure times (2–9 h) was performed. The phase transformations of the samples were detected by X-ray diffraction (Bruker D8 Advance diffractometer, Cu Kα radiation). The microstructure and the size of the crystals were determined by Scanning Electron Microscopy (SEM 525M). Microprobe analysis (analyze EDAX 9900) were performed on polished samples. The thermal stability of the selected glasses was verified by differential thermal analysis (LABSYS™ EVO apparatus) with Pt-Pt/Rh thermocouple at a heating rate of 10 K/min in argon flow, using Al_2O_3 as a reference material. The accuracy of the temperature maintenance was determined ± 5 °C. The optical absorption spectra of the glass and crystalline samples were recorded at room temperature using UV-Vis spectrophotometer (Evolution 300) in the wavelength range 300–1000 nm. The IR spectra were measured using the KBr pellet technique on a Nicolet-320 FTIR spectrometer with a resolution of ±1 cm⁻¹, by collecting 16 scans in the range 1600–400 cm⁻¹.

RESULTS AND DISCUSSION

Transparent and homogeneous glass compositions $50Bi_2O_3.50B_2O_3$, $50Bi_2O_3.10MoO_3.40B_2O_3$, $60Bi_2O_3.5MoO_3.35B_2O_3$, $49Bi_2O_3.2MoO_3.49B_2O_3$ and $63Bi_2O_3.2MoO_3.35B_2O_3$ having a pale yellow to dark yellow color were obtained. The DTA patterns of selected glasses are shown in Fig. 1. It is visible that the increase of MoO_3 content (above 40 mol%) results in the decrease of glass transition tempera-
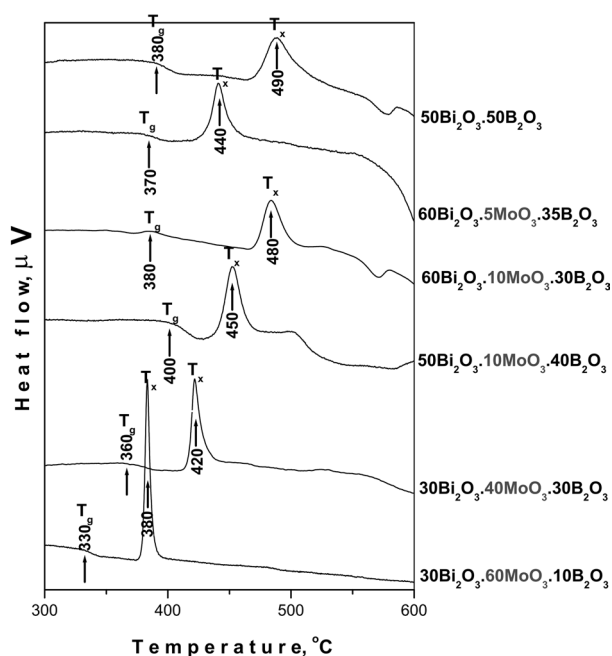
Fig. 1. DTA curves of selected glasses

ture (T_g) and crystallization temperature (T_x) from 370 to 330 °C and from 440 to 380 °C, respectively. The heat treatment regime of the glasses was made having in mind the obtained DTA results and previous reports by Pottier [9], Becker [10] and Ihara [11] as well. In the XRD pattern (Fig. 2) of the binary $50Bi_2O_3.50B_2O_3$ composition only the diffraction lines of $BiBO_3$-II phase, are visible. The addition of 2 mol% MoO_3 leds to the appearance of both $BiBO_3$ polymorphs: $BiBO_3$-I (JCPDS 28-0169) and $BiBO_3$-II (JCPDS 27-0320). Unfortunately, the crystal structures of these two phases have not been determined until now. The increase in MoO_3 content (5 mol%) also leds to the appearance of two phases $Bi_4B_2O_9$ (JCPDS 70-1458) and Bi_2MoO_6 (koechlinite) (JCPDS 82-2067). Further increase in MoO_3 content (10 mol%) shows only the presence of Bi_2MoO_6 (koechlinite). Another experiment at constant MoO_3 content (2 mol%) was made with varying the ratio of the other two components (Bi_2O_3 and B_2O_3). After heat treatment at 500 °C for 9h in the sample with composition $49Bi_2O_3.2MoO_3.49B_2O_3$ both $BiBO_3$ polymorphs were detected (Fig. 3), while in the other sample with composition $63Bi_2O_3.2MoO_3.35B_2O_3$, diffraction lines of several crystal phases were found: $BiBO_3$-I, $BiBO_3$-II, $Bi_4B_2O_9$ and $Bi_3B_5O_{12}$ (JCPDS 15-0372). According to Pottier [9] the $BiBO_3$ phase decomposes into a mixture of the stable $Bi_4B_2O_9$ and $Bi_3B_5O_{12}$ phases at 600 °C. More experiments are needed in order to elucidate this interesting problem.
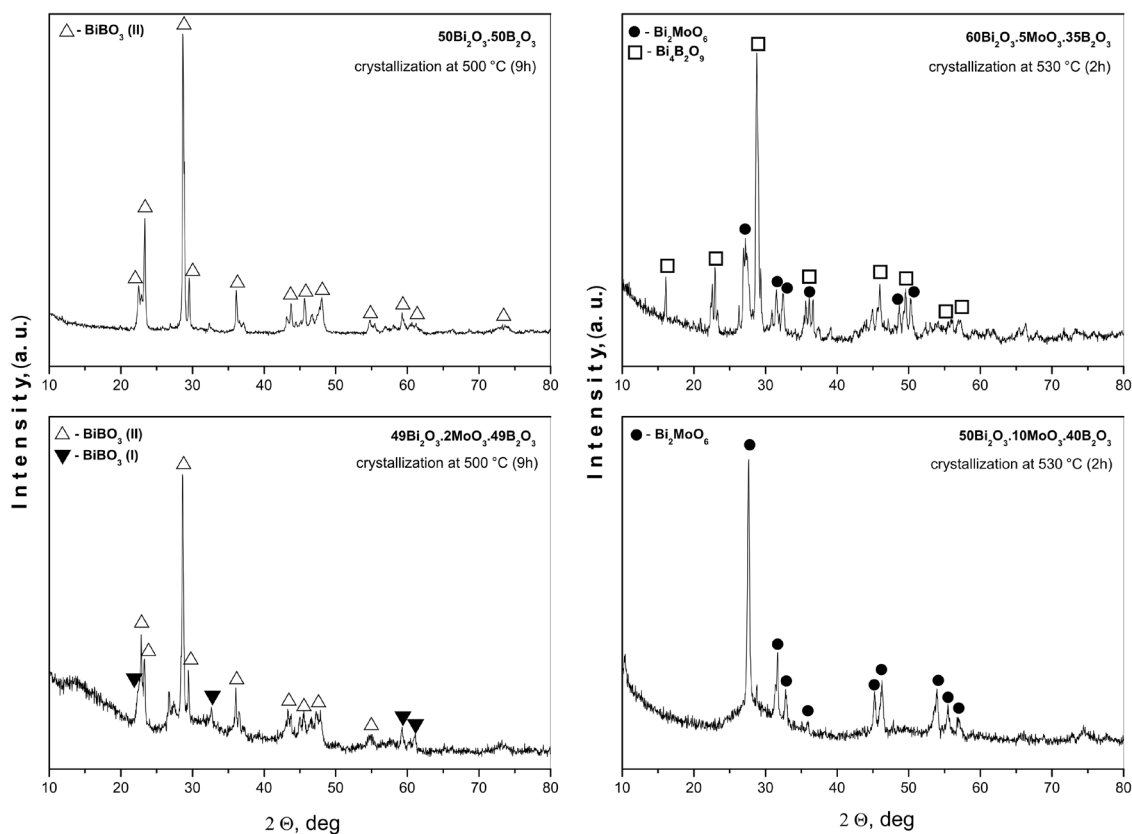
Fig. 2. X-ray diffraction patterns of selected glass compositions after heat treatment

The microstructure of the crystallized sample $50Bi_2O_3.50B_2O_3$ was examined by SEM analysis (Fig. 4). Partial surface crystallization was observed, while the sample volume is still amorphous. The preliminary microprobe chemical composition analysis showed the presence of $BiBO_3$ phase that is in agreement with the XRD results (Fig. 2). The UV-Vis spectra of the glass $50Bi_2O_3.50B_2O_3$ and crystalline $BiBO_3$ are shown in Fig. 5. The absorption of both samples decreases after 400 nm, but the crystallized sample possesses better transparency than the glass. Besides, a band at 480 nm was observed in the spectrum of the glass sample that could be related to the formation of nanoparticles of elementary bismuth (Bi^0) and their influence on the coloration of the glass. This problem was discussed in details by Sanz et al. for bismuth-silicate glasses [7].

There is significant difference in the IR spectra (Fig. 6) of both samples. The amorphous network contains BO_4 (930–880 and 1040 cm^{-1}), BO_3 (1270, 1200 cm^{-1}) and BiO_6 (band centered at 470 cm^{-1})
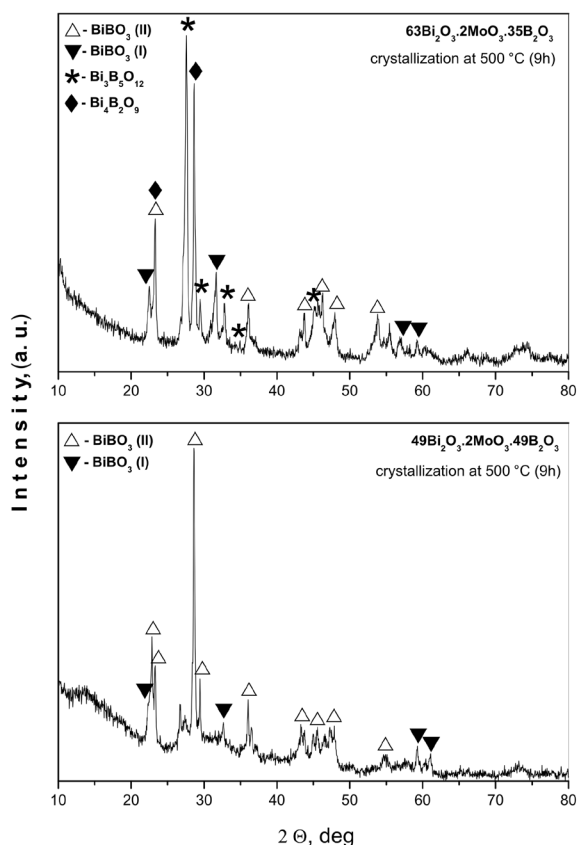
Fig. 3. X-ray diffraction patterns of samples $49Bi_2O_3.2MoO_3.49B_2O_3$ and $63Bi_2O_3.2MoO_3.35B_2O_3$
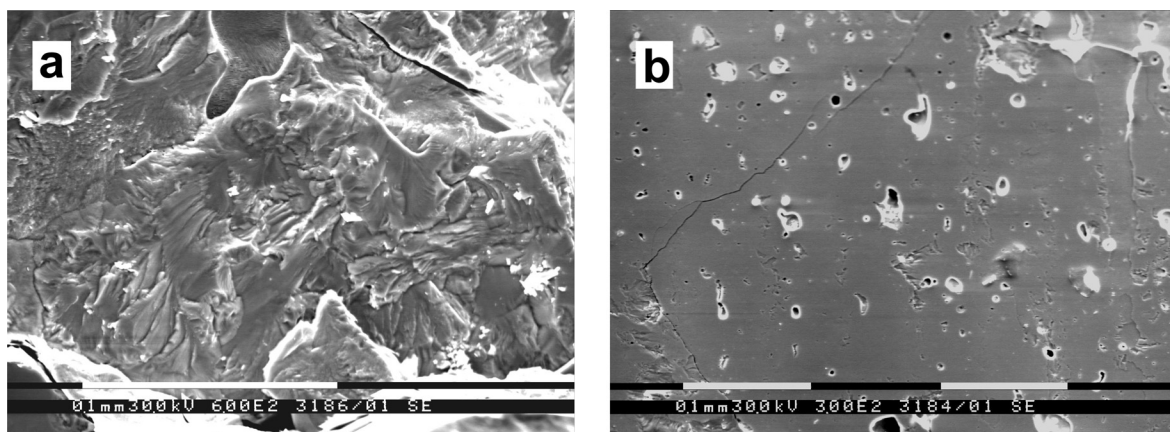
Fig. 4. SEM micrographs of the crystalline BiBO$_3$: a) unpolished surface and b) sample volume
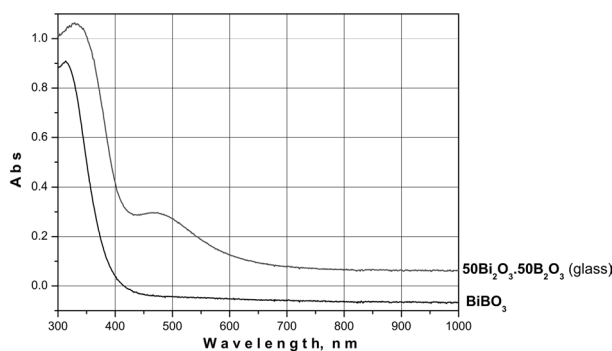
Fig. 5. UV-Vis spectra of the glass and crystalline BiBO$_3$
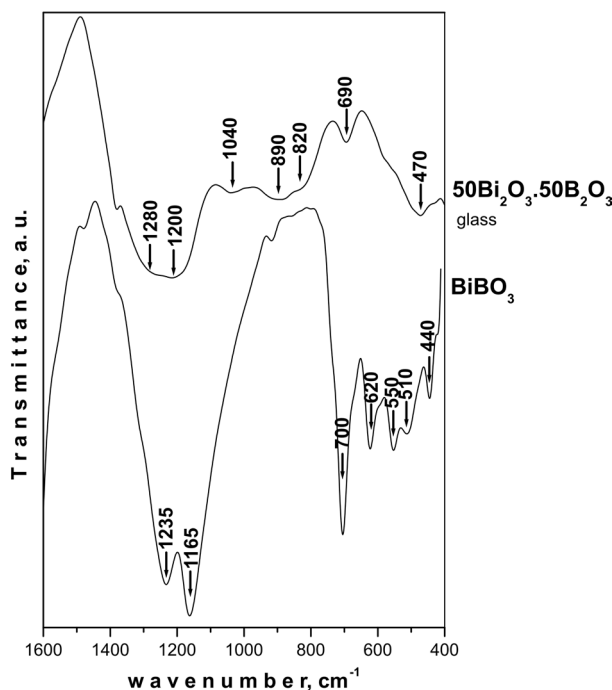
Fig. 6. IR spectra of the glass 50Bi$_2$O$_3$.50B$_2$O$_3$ and crystalline BiBO$_3$

units. In the IR spectrum of crystalline sample the bands which are related to the BO$_4$ vibrations are missing and overall it is similar to the results obtained by Egorysheva et al. [12] for the IR spectra of BiBO$_3$ phase. The obtained results are an additional confirmation that Bi$_2$O$_3$ favors the transformation of BO$_3$ to BO$_4$ units in the amorphous network [4, 18–21].

CONCLUSIONS

Bismuth borate (BiBO$_3$) phase was synthesized by crystallization of binary and ternary glass compositions in the Bi$_2$O$_3$-MoO$_3$-B$_2$O$_3$ system. It was established that the addition of 2 mol % MoO$_3$ leads to the obtaining of BiBO$_3$-I and BiBO$_3$-II bismuth borate polymorphs. The increase in MoO$_3$ content (2–5 mol%) stimulates the simultaneous crystallization of several phases – BiBO$_3$, Bi$_4$B$_2$O$_9$ and Bi$_3$B$_5$O$_{12}$. Further increase in MoO$_3$ content (10 mol%) leads to the obtaining of Bi$_2$MoO$_6$ (koechlinite) phase, only. IR results established that in the glasses the content of BO$_4$ units is higher than in the crystallized sample.

REFERENCES

1. P. Becker, *Cryst. Res. Technol.*, **38,** 74 (2003).
2. I. Kityk, A. Majchrowski, *Opt. Mater.*, **25**, 33 (2004).
3. L. Li, G. Li, Y. Wang, F. Liao, *Chem. Mater.*, **17**, 4174 (2005).
4. A. Bajaj, A. Khanna, B. Chen, J. G. Longstaffe, U. W. Zwanziger, J. W. Zwanziger, Y. Gomez, F. Gonzalez, *J. Non-Cryst Sol.*, **355**, 45 (2009).

5. A. Bajaj, A. Khanna, N. Kulkarni, S. Aggarwal, *J. Amer. Ceram. Soc.*, **92**(5), 1036 (2009).
6. W. Dumbaugh, *Phys Chem Glasses*, **27**, 119 (1986).
7. O. Sanz, E. Haro-Poniatowski, J. Gonzalo, J. M. Fernadez Navarro, J. *Non-Cryst. Sol.*, **352**, 761 (2006).
8. E. Levin, C. McDaniel, *J. Amer. Ceram. Soc.*, **45**, 355 (1962).
9. M. J. Pottier, *Bull. Soc. Chim. Belg.*, **83**, 235 (1974).
10. P. Becker, R. Frohlich, *Z. Naturforcsh.*, **59b**, 256 (2004).
11. R. Ihara, T. Honma, Y. Benino, T. Fujiwara, T. Komatsu, *Opt. Mater.* **27**, 403 (2004).
12. A. V. Egorysheva, V. Burkov, Yu. Kargin, V. Plotnichenko, V. Koltashev, *Crystallogr. Rep.,* **50**(1) 127 (2005).
13. H. Hellwig, J. Lieberz, L. Bohaty, J. *Appl. Phys.*, **88**, 240 (2000).
14. L. Aleksandrov, R. Iordanova, Y. Dimitriev, *J. Non-Cryst Sol.*, **355**, 2023 (2009).
15. Y. Dimitriev, R. Iordanova, L. Aleksandrov, K. Kostov, *Phys. Chem. Glasses Eur. J. Glass Sci. Technol B*, **50**(3), 212 (2009).
16. Y. Dimitriev, R. Iordanova, *Phys. Chem. Glasses Eur. J. Glass. Sci. B*, **50**(2), 123 (2009).
17. M. Krapchanska, R. Iordanova, Y. Dimitriev, A. Bachvarova-Nedelcheva, *J. Optoel. Adv. Mater.*, **12**(8), 1692 (2010).
18. R. Iordanova, L. Aleksandrov, A. Bachvarova-Nedelcheva, M. AtaaLa, Y. Dimitriev, in: Proc 11-th Internat Conf on the Structure of Non-Cryst. Mater., 2011, in press.
19. E. Gateff, V. Dimitrov, Y. Dimitriev, A. Wright, in: Borate glasses, crystals and melts, A. Wright, S. Feller, A. Hannon (eds.), Society of Glass Technology, Sheffield, 1997, p. 112.
20. Y. Cheng, H. Xiao, W. Guo, *Ceram. Intern.*, **34**, 1335 (2008).
21. C. E. Stone, A. C. Wright, R. N. Sinclair, S. A. Feller, M. Affatigato, D. L. Hogan, C. Vira, Y. Dimitriev, E. Gateff, D. Earth, *Phys. Chem. Glasses*, **41**(6), 409 (2000).

СИНТЕЗ НА BiBO₃ ЧРЕЗ КРИСТАЛИЗАЦИЯ НА СТЪКЛА В СИСТЕМАТА MoO₃–Bi₂O₃–B₂O₃

Р. С. Йорданова[1], А. Д. Бъчварова-Неделчева[1]*, Л. И. Александров[1], Я. Б. Димитриев[2]

[1] *Институт по Обща и Неорганична Химия, Българска Академия на Науките, ул. „Акад. Г. Бончев“, бл. 11, 1113 София, България*
[2] *Химикотехнологичен и Металургичен Университет, бул. „Кл. Охридски“ 8, 1756 София, България*

(Резюме)

Целта на настоящата работа е да се провери възможността за синтез на BiBO₃ чрез кристализация на стъкла. Няколко трикомпонентни аморфни състава от изследваната система бяха избрани и термично третирани при 500–530 °C с различно време на задръжка. Чрез рентгено-фазов анализ (РФА) бе установено получаването на полиморфните модификации на BiBO₃, както и на Bi₄B₂O₉, Bi₃B₅O₁₂ и Bi₂MoO₆ кристални фази. Допълнителна информация за синтезирания BiBO₃ бе получена и от инфрачервената спектроскопия (ИЧ). Има съществена разлика в ИЧ спектрите на стъклото със състав 50Bi₂O₃.50B₂O₃ и кристалния BiBO₃ продукт. Причината за това е, че в стъклото съдържанието на BO₄ групите е по-високо отколкото в кристалния образец.

Preparation of nanocrystalline thin films of ZnO by sol-gel dip coating

N. V. Kaneva, C. D. Dushkin*

Laboratory of Nanoparticle Science and Technology, Department of General and Inorganic Chemistry, Faculty of Chemistry, University of Sofia, 1 James Bourchier Blvd.,1164 Sofia, Bulgaria

Nanocrystalline ZnO thin films are deposited from sol-gel of zinc acetateand using dip coating onto two different substrates: glass and aluminium foil. (i) Films on glass substrates. Nanostructured ZnO thin films with different concentrations of Ni^{2+} doping (0, 1, 5, 10 and 15 wt%) are prepared for the first time by the sol gel method. The film surface is with a ganglia-like structure as observed by Scanning Electron Microscopy (SEM). The films comprise of ZnO nanocrystallites with hexagonal crystal structure, as revealed by means of X-ray diffraction (XRD). (ii) Films on aluminium foil substrates. The ZnO films are annealed at different temperatures (100 °C, 300 °C and 500 °C) and characterized by means of SEM and XRD. The film surface is with the characteristic ganglia-like patterns. The crystalline structure is hexagonal with the crystallite sizes increasing with the annealing temperature.

Key words: zinc oxide, thin films, crystallites, aluminium substrate, dip coating.

1. INTRODUCTION

In recent years, zinc oxide has become a particularly interesting metal oxide material because of its unique properties. ZnO is a semiconductor with a wide band gap (3.3 eV), large exciton binding energy, abundant in nature and environmentally friendly. These characteristics make this material attractive for many applications such as solar cells, optical coatings, photocatalysts, antibacterial activities, electrical devices, active medium in UV semiconductor lasers and in gas sensors [1].

Nanocrystalline ZnO is of special interest, because of the possibilities for modification and control of various ZnO-based nanostructures [2–4]. ZnO thin films are prepared by different techniques such as metal organic chemical vapor deposition [5], sol–gel [6–8], thermal evaporation, oxidation and anodizing [9–11]. The sol-gel process with utilization of dip coating is one of the versatile and low-cost techniques strategies to prepare thin films of particles. The recent research demonstrates the possibilities for utilization of homogeneous ZnO thin films, prepared by the sol-gel method [12, 13], which are attractive with desired thickness and nanostructure. The classical sol-gel method using complexing agent monoethanolamine (MEA) [14]

is also applied for the deposition of ZnO films in order to compare them with the films obtained by polymeric formulations.

The aim of this paper is to compare the structural and crystallite features of ZnO thin films obtained onto two different substrates (glass and aluminium foil) in dependence on the doping with Ni^{2+} and on the annealing temperature.

2. EXPERIMENTAL

The compounds used to manufacture ZnO thin films were as follows: zinc acetate dihydrate ($\geq$99.5%), 2-methoxyethanol ($\geq$99.5%), monoethanolamine ($\geq$99.0%) and nickel acetate tetrahydrate ($\geq$99.0%); all of them from Fluka. Malachite green (MG) oxalate was from Croma-Gesellschaft mbH & Co. The microscope glass slides (ca. 76×26 mm) were from ISO-LAB (Germany). Aluminium foil (ca. 76×26 mm) was also used for the respective substrates of ZnO films. The aluminium plates were cleaned successively in hot ethanol and acetone.

Nanocrystalline ZnO thin films were deposited from sol-gel of zinc acetate, 2-methoxyethanol and monoethanolamine (Fig. 1) using dip coating apparatus onto two different substrates: glass and aluminium foil. The following samples systems were prepared:

(i) Zinc oxide thin films on glass substrates. Different concentrations of Ni^{2+} doping (0, 1, 5, 10 and

---

* To whom all correspondence should be sent:
E-mail: nhtd@wmail.chem.uni-sofia.bg
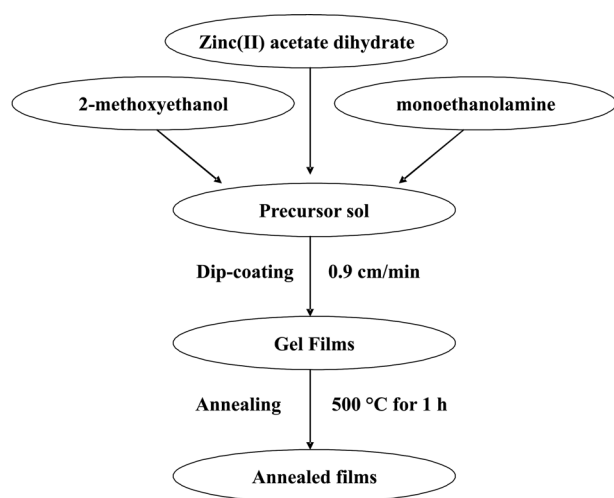
Fig. 1. Scheme of the experimental procedure for deposition of thin ZnO films by sol-gel dip coating

15 wt%) were achieved by nickel acetate tetrahydrate ($Ni(CH_3COO)_2.4H_2O$) dissolved in a mixture of zinc acetate ($Zn(CH_3COO)_2.2H_2O$), 2-methoxyethanol and then monoethanolamine (MEA) added finally as a stabilizer. The substances are mixed together in a round-bottomed flask and stirred at room temperature for 15 min. The obtained clear solution was heated up at 60 °C upon magnetic stirring for 60 min and let overnight.

(ii) ZnO films on aluminium substrates. The sol was obtained using zinc acetate dihydrate ($Zn(CH_3COO)_2.2H_2O$), 2-methoxyethanol and monoethanolamine, mixed together in a round-bottomed flask and stirred at room temperature for 15 min. The obtained clear solution was heated up at 60 °C upon magnetic stirring for 60 min and let overnight.

The final sol was clear and homogenous, to serve as the coating substance for film preparation. No visible changes were observed upon standing of the precursor sol at room temperature for at least 2 months.

Dipping the glass or aluminium foil substrate in the sol and withdrawing it at a rate of 0.9 cm/min at room temperature prepared the gel films. It was found that a higher withdrawal rate results in films of lower quality. The films were deposited with 5 coatings and dried at 80 °C for 15 min after each successive coating. The final gel films onto glass substrate were annealed at 500 °C for 60 min in order to obtain the ZnO films. The films on aluminium foil were annealed for 60 min at different temperatures: 100, 300 and 500 °C

The as-obtained ZnO thin films on glass (undoped and doped with different per cent Ni^{2+}) and aluminium foil substrate were first imaged by a

Scanning Electron Microscope (SEM) model JSM-5510 (JEOL), operated at 10 kV of acceleration voltage. The investigated samples were coated with gold by JFC-1200 fine coater (JEOL) before observation.

The X-Ray diffraction (XRD) spectra were recorded at room temperature on a powder diffractometer (Siemens D500 with CuKα radiation within 2θ range 30–70 deg at a step of 0.05 deg 2θ and counting time 2 s/step). The average crystallite size was estimated according to the Scherrer's equation [15]:

$$d_{hkl} = k\lambda / \beta \cos(2\theta)$$

where d_{hkl} is the average crystallite size (nm), λ is the wavelength of CuKα radiation applied ($\lambda = 0.154056$ nm), θ is the Bragg's angle of diffraction, β is the full-width at half maximum intensity of the peak observed at $2\theta = 25.20$ (converted to radian) and k is a constant usually chosen ~0.9.

3. RESULTS AND DISCUSSION

3.1. Structure characterization of Ni-doped ZnO films on glass substrate

The dip coating is a simple and cheap technique for deposition of thin oxide films, but it requires soluble reagents. It is possible to control precisely the immersion and withdrawal speed, number of dipping cycles and solution viscosity for the purpose of deposition of a layer of oxide material. The plane view of SEM micrograph of annealed ZnO film shows smooth ganglia-like hills (Fig. 2a). The morphology is homogenous with the wrinkles of a width 0.5–1 μm, length ~5 μm and height about 1 μm. The Ni-doped ZnO films display also that peculiar pattern, as seen from the surface micrographs of samples with 1 to 15 wt.% Ni^{2+} (Fig. 2b-e). In the case of Ni-containing films, the ganglia are looking more distorted and branched at their ends. The ganglia-like hills are of typical width 0.1–0.5 μm, length from 1 μm to 5 μm and height about 2.5–3 μm. The increase of Ni^{2+} content decreases the volume and size of ganglia-like hills. The wrinkles are smaller and the morphology is not homogenous.

X-ray diffraction patterns of ZnO and Ni-doped ZnO films are presented in Fig. 3. These patterns correspond to the three main diffraction peaks of crystallized ZnO. This result shows that the as-prepared films, annealed at 500 °C for 1 h, have a polycrystalline hexagonal wurtzite structure. It seems that the doping with Ni^{2+} ions has no appreciable effect on the crystal structure of ZnO. These diffractograms show, however, that the intensities of diffraction peaks decline as the Ni^{2+} ion concentration
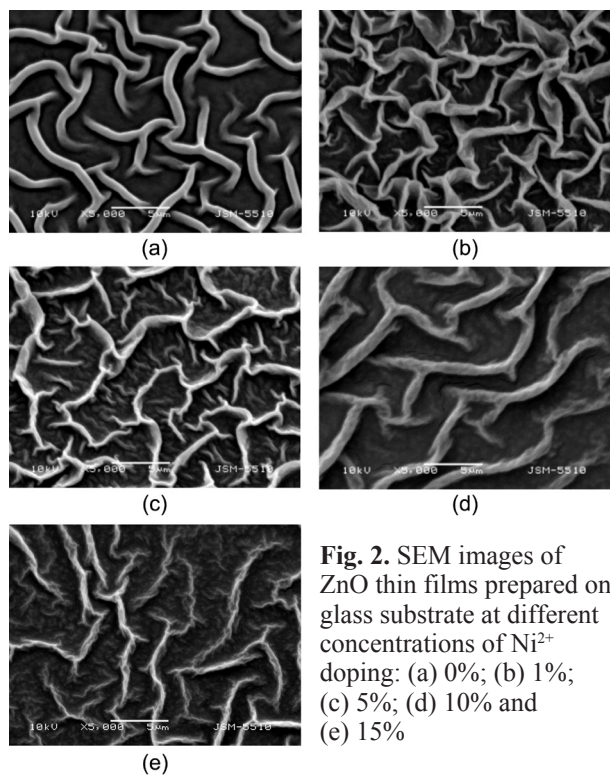
Fig. 2. SEM images of ZnO thin films prepared on glass substrate at different concentrations of Ni^{2+} doping: (a) 0%; (b) 1%; (c) 5%; (d) 10% and (e) 15%

Fig. 3. XRD spectra of ZnO films prepared by sol-gel and doped with Ni^{2+} at (a) 0%; (b) 1%; (c) 5%; (d) 10% and (e) 15%. The respective shown in Fig. 4.

increases, i.e. the nickel doping within ZnO films causes the crystallinity to degenerate. Since the intensity of diffraction peaks becomes weaker and the half-peak width becomes wider with the increase of Ni^{2+} doping concentration, the Ni^{2+} ions inhibit the aggregating growth of ZnO nanocrystals and affect the crystallization of ZnO. The average crystallite size of samples is estimated using the Scherrer's equation. When the Ni concentration increases, the average crystallite size decreases (Fig. 4), which implies on the role of Ni to destabilize the respective sol thus making smaller the zinc hydroxide making species.

3.2. Structure characterization of ZnO films on aluminium foil substrate

The of ZnO films, shown on the SEM images in Fig. 5, exhibit a different surface morphlogy depending on the annealing temperature. The ZnO films annealed at 100 °C (Fig. 5a) have different ganglia-like hills of width of 0.2–0.5 μm, length ~5 μm and height about 1–2 μm. Ganglia-like hills of typical width 0.5–1 μm, length from 5 μm to 10 μm and height about 2.5–3 μm are seen on the surface of films annealed at 300 °C (Fig. 5b). The thin films, obtained after heating at 500 °C (Fig. 5c), have different ganglia-like hills of width 1–2 μm, length ~15 μm and height about 3 μm. The ganglia-like structure seems reproducible irrespective on the conditions of film deposition and annealing.

Fig. 4. Relationship between the crystallite size of ZnO and the percent of Ni^{2+} doping
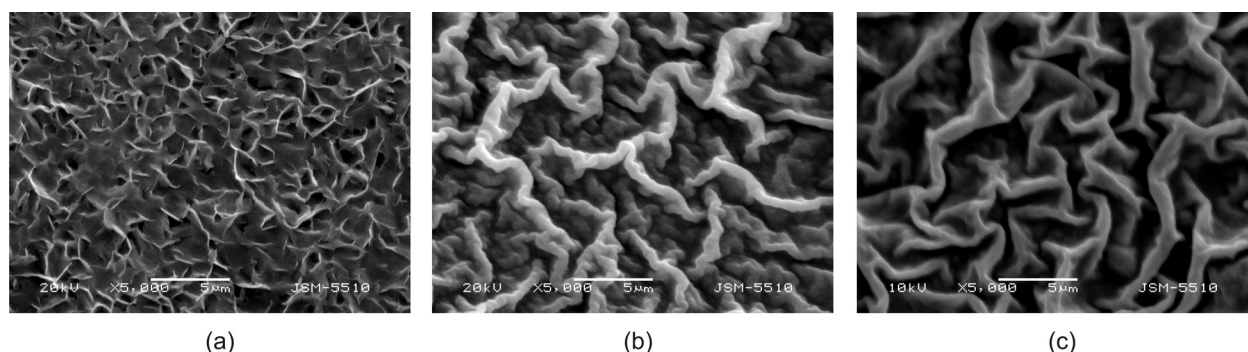
Fig. 5. SEM images of ZnO films prepared on aluminium foil at different annealing temperatures: (a) 100 °C; (b) 300 °C; (c) 500 °C. Increasing the temperature increases the scale of surface pattern of the film surface

Figure 6a shows the XRD data of ZnO films annealed at 100 °C. The lack of three characteristic peaks of ZnO (see below) shows that at this temperature the material is still in its hydroxide form
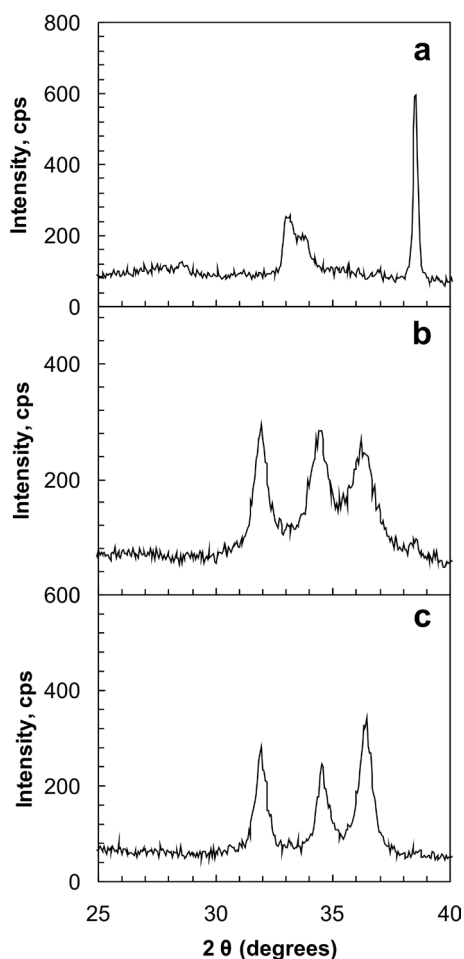
Fig. 6. XRD spectra of ZnO films prepared on aluminium foil by sol-gel and annealed at (a) 100 °C; (b) 300 °C; (c) 500 °C. The crystallite sizes are about 30.0 nm, 70.5 nm and 88.1 nm, respectively (see Fig. 7)
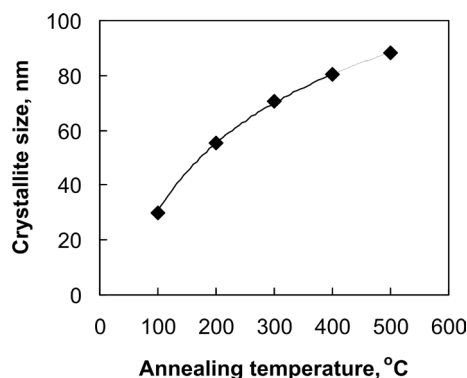
Fig. 7. Relationship between the crystallite size of ZnO and the annealing temperature for the thin films on aluminium foil

of rather amorphous state. Nevertheless, the mean crystallite sizes estimated by the Sherrer's formula are about 30.0 nm. The XRD data from Fig. 6a are compared with literature data, which prove the presence of one characteristic peak of $Zn(OH)_2$, which can be indexed as the orthogonal structure. Increasing the annealing temperature causes a transition from orthogonal in to hexagonal structure, respectively from $Zn(OH)_2$ toward ZnO. The (100), (002), (101) diffraction peaks of ZnO films appear clearly at a higher annealing temperature, which can be indexed as the hexagonal wurtzite structure of ZnO. The thin films consist in this case of polycrystalline grains with no preferential growth observed. The average sizes of crystallites are about 70.5 nm (for the films annealed at 300 °C) and 88.2 nm (at 500 °C) (Fig. 6b, c). Increasing the annealing temperature makes the diffraction peaks better pronounced and increases the size of crystallites. The relationship between annealing temperatures and the corresponding ZnO crystallite sizes are summarized and as illustrated in Fig. 7, respectively. The ZnO thin films prepared by us will find applications in the photocatalytic treatment of waters polluted by

organics due to their activity in UV and visible light (especially those doped with Ni ions).

4. CONCLUSIONS

Thin films of nanostructured ZnO are successfully prepared on glass and aluminium foil substrates using dip coating. The films are characterized by means of scanning electron microscopy and X-ray diffraction: The films (pure and nickel doped) comprise ZnO crystallites with a hexagonal wurtzite structure, which demonstrates that doping wit h Ni^{2+} ions has no appreciable effect on the crystal structure. When the Ni concentration increases, the average crystallite size decreases. The addition of 1 to 15 wt% of Ni^{2+} to the start solution modifies the morphology of films the ganglia-like hills and the wrinkles become smaller. Nanostructured ZnO films are prepared also, on aluminium foil at three different thermal treatment temperatures: 100, 300 or 500 °C. The deposited films have different ganglia-like hills with dimensions, which become much larger after treatment at elevated temperature. The crystallite size of as-prepared ZnO films increases with increasing of the film annealing temperature as well.

REFERENCES

1. K. Sato, H. Katayama-Yoshida, *Japanese Journal of Applied Physics*, **39**, L 555 (2000).
2. M. Andres-Verges, A. Mifsud, C. Serna, *Mater. Letters*, **8**, 115 (1989).
3. M. Andres-Verges, M. Martinez-Gallego, *J. Mater. Sci.*, **27**, 375 (1992).
4. S. Haile, D. Jonson, G. Wiesemen, H. Bowen, *J. Amer. Ceram. Soc.*, **72**, 227 (1989).
5. J. L. Yang, S. J. An,W. I. Park, G. Y. Yi, W. Choi, *Adv. Mater.*, **16**, 1661 (2004).
6. B. Pal, M. Sharon, *Mater. Chem. Phys.*, 76, 82 (2002).
7. F. Peng, S. H. Chen, L. Zhang, H. J. Huang, Z. Y. Xie, *Acta Phys. Chem. Sin.*, **21**, 944 (2005).
8. N. V. Kaneva, G. G. Yordanov, C. D. Dushkin, *Reac. Kin. Catal. Lett.*, **98**, 259 (2009).
9. O. A. Fouad, A. A. Ismail, Z. I. Zaki, R. M. Mohamed, *Appl. Catal. B: Environ.*, **62**, 144 (2006).
10. Ya. I. Alivov, A. V. Chernykh, M. V. Chukichev, R. Y. Korotkov, *Thin Solid Films*, **473**, 241 (2005).
11. Y. Yamaguchi, M. Yamazaki, S. Yoshihara, T. Shirakashi, *J. Electroanal. Chem.*, **442**, 1 (1998).
12. F. Peng, H. Wang, H. Yu, S. Chen, *Mater. Res. Bull.*, **41**, 2123 (2006).
13. G. Delgado, C. I. Romero, S. A. Hernandez, R. Perez, O. Angel, *Solar Energy Materials & Solar Cells*, doi:10.1016/j.solmat.2008.03.020.
14. N. Kaneva, I. Stambolova, V. Blaskov, Y. Dimitriev, S. Vassilev, C. Dushkin, *Journal Alloys Compounds*, **500**, 252 (2010).
15. B. D. Cullity, S. R. Stock, Elements of X-ray Diffraction, 2nd ed., Prentice-Hall, Inc, New Jersey, 2001, p. 388.

ПОДГОТОВКА НА НАНОКРИСТАЛНИ ТЪНКИ СЛОЕВЕ ОТ ZnO СЪС ЗОЛ-ГЕЛНО ПОКРИВАНЕ

Н. Канева, Ц. Душкин

Лаборатория по нанонауки и технологии, Химически факултет, Софийски университет, бул. „Дж. Баучер“ № 1, 1164 София

(Резюме)

Нанокристалните тънки слоеве от ZnO са депозирани по зол-гелна методика с употреба на цинков ацетат. Методът е използван за покриване на два различни видове материали: стъкло и алуминиево фолио. (I) Слоеве върху стъклени повърхности. Нано-структурирани тънки слоеве на ZnO с различни концентрации на легиране с Ni^{2+} (0, 1, 5, 10 и 15 тегловни %) са получени за първи път по зол-гел методът. Повърхността на слоя е пипаловидно-омрежена (гагнгливево подобна) както е видно от сканиращата електрона микроскопия (СЕМ). Слоят се състои от нанокристали на ZnO с хексагонална кристална структура, по данни от рентгенова дифракция (XRD). (II) Филми с основа алуминиево фолио. Слоевете ZnO са отрети при различни температури (100 °C, 300 °C и 500 °C) и са изследвани със СЕМ и XRD. Повърхността на слоя също е гагнгливево подобна. Кристалната структура на ZnO отново е хексагонална като размерите на кристалите нарастват с температурата на отгряване.

Potential of neutron diffraction for disclosure of structural details after chemical substitution

K. A. Krezhov*

Institute for Nuclear Research and Nuclear Energy, Bulgarian academy of sciences,
72 Tzarigradsko chaussee, 1784 Sofia, Bulgaria

Neutron diffraction is nowadays a well established non destructive technique with proven high efficiency in solving complex structural problems in condensed matter. The technique exploits the unique properties of the neutron that make it an especially versatile probe in crystallographic research. Neutrons penetrate through many engineering materials and can be used in complex sample environments, feel hydrogen and light atoms in presence of heavy atoms in general, can detect isotope substitutions and distinguish adjacent elements in the periodic table, and are highly sensitive to magnetism. We give examples of recent applications of neutron diffraction with an emphasis on experiments in nanoscience and magnetism.

Key words: Transition metal oxides; Neutron scattering; Crystal structure; Magnetic structure.

INTRODUCTION

Among the ways the science has learned to produce new materials the chemical substitution is one of the most popular ones. Lately, multifunctional materials fell in the focus of intensive investigations because of possibility to combine multiple functions including mechanical, electronic, photonic, optical, biological, and magnetic functions, and to be capable of exhibiting diverse controllable, and predictable physical responses when subjected to various external conditions.

This paper is motivated by the recent resurgence of interest in complex oxides owing to their coupling of electrical, magnetic, thermal, mechanical, and optical properties, which make them suitable for a wide variety of applications. With many advantages over other forms of radiation, neutrons have made significant contributions towards a detailed understanding of structure-property relationships. In contrast to other probes utilized in structural investigations such as electrons and X-rays, the neutrons have the ability to reveal nuclear positions and mean displacements without bias from the effects of electron distribution.

After a brief presentation of the basic concepts of neutron scattering we will give examples of neutron diffraction and emphasis on the use of thermodiffractometry to follow magnetic phase transitions will be also commented.

THE NEUTRON

More than half of all "visible" matter in the universe is made of neutrons. Except for the neutron component of cosmic rays reaching the Earth, they are bound deep inside the atomic nucleus and it is not easy to free them out. Free neutron is a subatomic particle of mass $m_n = 1.175 \times 10^{-27}$ kg, which according to the quark theory, is constituted by two down (d) and one up (u) quarks giving it a neutral charge.

Within the limits of the very small uncertainty of advanced experiments the neutron has a "zero" electric charge ($q_n/e \leq (-0.4 \pm 1.1)10^{-21}$, e – charge of electron) and "zero" electrical dipole moment ($d_n < 6.3 \, 10^{-26} \, ecm$), but the internal quark structure tolerates an electric charge distribution measured as mean quadratic radius of charge. The charge distribution entails a magnetic moment $\mu_n = -1.913042 \, \mu_N$ (μ_N is the nuclear magneton) and an electric polarisability α_n $\left(\alpha_n = \left(0.98^{+0.19}_{-0.23}\right)10^{-3} \, \text{fm}^3\right)$, 1 fm $= 10^{-13}$ cm.

Expressed via the Pauli matrices $\hat{\sigma}$ (spin operator $\left(\frac{1}{2}\hat{\sigma}\right)$), the neutron magnetic moment is $\hat{\mu}_n = -\gamma\mu_N \, \hat{\sigma}$, where the minus sign reflects the experimental fact that the directions of neutron magnetic moment and neutron spin are opposite, the coefficient $\gamma = 1.91304273(45)$ is determined experimentally with high accuracy [1].

---

* To whom all correspondence should be sent:
E-mail: krezhov@inrne.bas.bg

Because the neutron bears a magnetic moment this gives the possibility with far reaching consequences: why not to make the neutron to become polarized; i.e. to probe the details of matter with well oriented in space "magnetic needles".

The free neutron is unstable in time and decays in proton, electron and antineutrino. The short neutron life time (mean time $\tau = 886.9 \pm 0.9$ s, half-time $T_{1/2} = 614.1 \pm 0.6$ s [2]) is not essential for experiments in condensed matter; neutrons of velocities of the order of $250 \div 5000$ m/s are used so that the decrease in neutron number due to neutron β-decay at distances of the order of several meters up to some hundred meters is negligible.

The *production of neutrons* on a large scale is based on nuclear reactions (Figure 1).

The *nuclear reactor* is using a controlled nuclear fission reaction. The most common source of neutrons is the fission process of nuclei such as ^{235}U in most reactors designed for research experiments or ^{239}Pu being the case of the pulsed reactor IBR-2 of the Joint Institute for Nuclear Research (JINR) in Dubna, Russia.

In another case of using nuclear reactions, different accelerator based neutron sources were developed; neutrons are generated from the bombardment of a target with high energetic particles such as electrons, protons or deuterium. The so-called "*spallation neutron sources*" proved to combine high safety and high neutron generation efficiency.

When a fast particle with λ shorter than the linear dimensions of the nucleus, for instance a high-energy proton ($E_p \approx 0.60 - 1$ GeV), strikes a heavy atomic nucleus (Pb, Hg, W, Ta, ^{238}U) some of its neutrons are "spalled" or knocked out from the nucleus in a nuclear reaction called *spallation*. Other neutrons are "*evaporate*d" as the bombarded nucleus heats up. In principle, the spallation is a stochastic process where particles as protons, muons, neutrinos as well as neutrons are spalled from the nucleus. Presently, the most intense neutron sources use proton accelerators. For every proton bombarding the target nucleus 15 up to 30 neutrons could be emitted depending on the target.

Because of the neutron mass the neutrons generated by fission or spallation can be slowed down (*moderated*) by collisions with light atoms such as hydrogen (H) or deuterium (D) to energies that are favourable for particular studies. The energy ranges roughly correspond to the temperature of the moderator material (Table 1). From the energy range (E<1 keV) of "slow neutrons" in nuclear physics one uses "*hot*" (E ≈ 100–500 meV; $\lambda \approx 0.5$–1 Å) produced by heated (T > 2000 K) bloc of graphite, "*thermal*" (E ≈ 10–100 meV; $\lambda \approx 1$–3 Å) moderated by a vessel containing water at room temperature and "*cold*" (E ≈ 0.1–10 meV; $\lambda \approx 3$–30 Å) – by liquid hydrogen or deuterium (T< 30K).

These energy ranges are corresponding to those of lattice vibrations (phonons) or spin excitations (magnons) and thus creation or annihilation of a lattice wave produces a measurable shift in neutron energy (inelastic scattering). Also, the energies are comparable to vibrational and diffusional energies of molecular systems and are appropriate for detection of molecular motion in the frequency range of 10^7–10^{14} Hz. This dynamic range covers the slow dynamics of polymer reptation up to high frequency diatomic oscillations. The wavelengths are in the range of typical atomic distances so interference
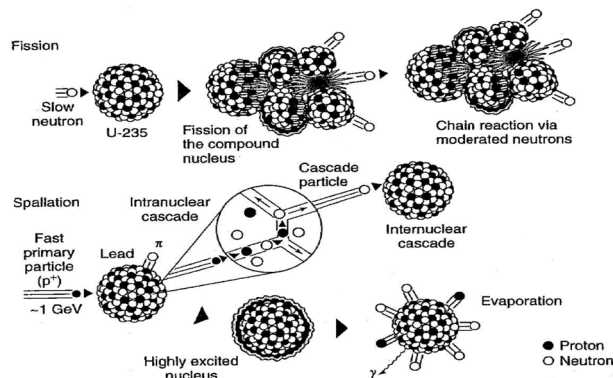
Fig. 1. Schematic drawing of neutron production by fission of 235U nucleus (upper part) and spallation on the example of a heavy target (lower part)

Table 1. Classification of neutrons by energy in condensed matter research

Neutrons		Wavelength (nm), typical	Velocity (m/s)	Temperature (K)	Energy (eV)
epithermal or hot		0.07	5700	2000	0.170
thermal		0.18	2200	300	0.025
cold	cold	0.4	1000	58	0.005
	very cold	6.6	60	0.2	2×10^{-5}
	ultra cold	58.2	6.8	3×10^{-3}	2×10^{-7}

occurs between waves scattered by neighboring atoms (diffraction) [3].

Independently of the way of production, *neutron guides* are used to channel beams of the moderated to lower energies "spalled" or "fission" neutrons that probe material structure and properties to the *neutron spectrometers*. The moderated neutron beams are "white" with a Maxwellian distribution of neutron velocity and neutrons with a broad range of energies can be used for "*time-of-flight*" and "*time-resolved*" (in case of a sufficiently intense neutron flux) measurements [4] but a given wavelength can be appropriately selected for measurements with monochromatic beams.

A low energy (non-relativistic) neutron has energy E, wavelength λ and wave vector $\vec{k}$ directed along the neutron velocity $\vec{v}$. These quantities are related:

$$| \vec{k} | = 2\pi/\lambda, \lambda = h/(m_n | \vec{v} |), E = m_n v^2/2, \quad (1)$$

where h is Planck's constant and m_n is the mass of the neutron. Approximate conversions are as follows:

$$E \text{ [meV]} \approx 81.8042/ (\lambda[\text{Å}])^2 \approx 2.072 \ k^2 = 5.227 \ v^2 = 0.08617 \ T,$$

where T is temperature in units K (Kelvin) and v[mm/μs] $\approx 4/\lambda$[Å]

The most commonly used units of neutron wavelength and energy are the Ångström (Å) and the millielectron volt (meV) respectively: 1 Å = 0.1 nm and

$$1 \text{ meV} \approx 0{,}242 \times 10^{12} \text{ Hz} \approx 8.07 \text{ cm}^{-1} \approx$$
$$11.6 \text{ K} \approx 17.3 \text{ Tesla} \approx 1.6 \times 10^{-15} \text{ erg.}$$

Hence, 1 kJ/mol $\approx$ 10.4 meV/molecule.

Owing to lack of charge to cause ionization in a medium, the neutrons cannot be directly detected. Thermal neutrons are usually detected by sensing the nuclear reaction products following neutron capture. BF_3 gas counters employ the reaction $^{10}B_5$ + $^1n_0 \rightarrow {}^7Li_3$ + $^4He_2$ + 2.7 MeV, the helium-3 gas counters use $^3He_2$ + $^1n_0 \rightarrow {}^3He_1$ + $^1H_1$ +0.77 MeV and film/scintillators: $^6Li_3$ + $^1n_0 \rightarrow {}^3H_1$ + $^4He_2$ + 4.79 MeV. Fission chambers with ^{235}U are most often used to monitor the neutron beam stability in time.

Fig. 2. The three cases of interaction of a monochromatic neutron beam with matter when propagating through a given medium $|\vec{k}_0| = |\vec{k}_i| = 2\pi/\lambda \Rightarrow |\vec{k}| = |\vec{k}_f| = 2\pi/\lambda'$.
Absorption: the transmitted beam preserves the initial direction of propagation but its intensity is lower than incident beam intensity.
Refraction: the intensity is preserved but the direction of propagation slightly changes. The refraction coefficient $n \approx 1$ (the deviation is of the order of $\pm 10^{-5}$) and the angle of deflection α is of the order of one degree)
Scattering: the beam changes both intensity and propagation direction (scattering angle 2Θ).

SCATTERING, REFRACTION AND ABSORPTION: CROSS-SECTION FORMALISM

Figure 2 schematically outlines the outcomes when a beam of neutrons hits a material. The fraction of neutrons propagating along a new direction is named "scattered" neutrons, and the investigation of materials by measuring how they scatter neutrons is known as *neutron scattering*.

The registered quantity in scattering experiments is the intensity I_s of the particles (neutrons), which after interacting with the scatterers are propagating along a certain direction in space and eventually one measures the change in their energy.

The geometry of the scattering event is illustrated schematically in Figure 3.

The incident neutron with wave vector $\vec{k}_0$ (momentum $\hbar \vec{k}_0$) and energy $E_0 = (\hbar \vec{k}_0)^2/2m_n$ is registered by a detector, positioned under an angle 2θ with respect to $\vec{k}_0$, as a neutron with wave vector $\vec{k}$ and energy $E = (\hbar \vec{k})^2/2m_n$. The "wave vector transfer," or "*scattering vector,*" is. The cosine rule $\vec{Q} = \vec{k}_0 - \vec{k}$, applied to the (Q, k_0, k) scattering triangle in Figure 3, gives $Q^2 = k_0^2 + k^2 - 2k_0 k \cos(2\theta)$, where 2θ is the "*scattering angle*" (the angle between the incident and scattered neutron beam directions). For the special case of *elastic scattering* holds $E_0 = E$, $\hbar\omega = 0$, $k_0 = k$, and $Q = 2k_0 \sin\theta = 4\pi \sin\theta/\lambda_0$, where λ_0 is the incident wavelength.
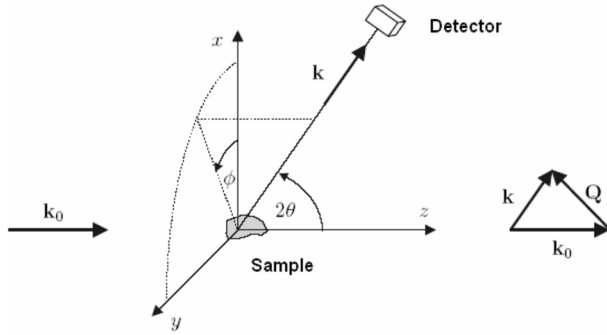
Fig. 3. Geometry of a scattering experiment. The detector collects the neutrons scattered in a solid angle $d\Omega = \sin 2\theta\, d(2\theta)d\varphi$. In elastic scattering studies the vectors $\vec{k}$ и $\vec{k}$ are of equal length $2\pi/\lambda$. The scattering vector $\vec{Q}$ is measured in reciprocal angstroms [Å^{-1}].

The physics in the scattering problem is to disclose what has happened with the momentum $\hbar\vec{Q}$ and energy ΔE transferred to the scatterers:

$$\vec{Q} = \vec{\kappa} = \vec{k}_0 - \vec{k}, \quad \Delta E = \hbar\omega = E_0 - E = \frac{\hbar^2}{2m_n}(k_0^2 - k^2). \quad (2)$$

Expressed through the wavelength the expressions (2) have the form:

$$Q = \kappa = 2\theta \left[\frac{1}{\lambda_0^2} + \frac{1}{\lambda^2} - \frac{2}{\lambda_0\lambda}\cos 2\theta \right]^{1/2}, \quad \hbar\omega = \frac{h^2}{2m}\left[\frac{1}{\lambda_0^2} - \frac{1}{\lambda^2}\right] \quad (3)$$

The "*double differential cross-section*", $(d^2\sigma/d\Omega dE)d\Omega dE$, measures the probability that the neutron is scattered within an elementary solid angle $d\Omega = \sin 2\theta d(2\theta)d\varphi$ with a transferred energy ΔE in the interval E_0, E_0+dE. The full neutron cross section is:

$$\sigma = \int d\Omega \left(\frac{d\sigma}{d\Omega}\right) = \int d\Omega \int dE \left(\frac{d^2\sigma}{d\Omega dE}\right). \quad (4)$$

The basic assumption in using the cross-section formalism is that the probability for neutron scattering in a uniformly irradiated homogeneous sample is proportional to the sample volume. For a given substance the cross-sections are presented per effective chemical unit (formula unit), an atom of a monoatomic substance or a molecule, if the notion is applicable. Thus, the cross section σ or the differential cross-section $d\sigma/d\Omega$ is expressed through the full intensity of the scattered beam I or with the infinitesimal intensity dI under different scattering angles within the solid angle $d\Omega$: I [n/s] $= \varphi\, N\, \sigma$ and dI [n/s] $= \varphi\, N\, d\sigma/d\Omega$. Here, N is the number of formula units in the sample, and the neutron flux (number of incident neutrons per unit time on unit area perpendicular to the direction of neutron propagation) is:

$$\Phi = \Phi(E)\, \eta\, d\Omega\, dE/4\pi, \quad (5)$$

where $\Phi(E)$ is the energy distribution of the neutron source flux in the energy interval E, $E+dE$ and $\eta < 1$ reflects the intensity loss owing to the finite effectiveness of the scattering setup.

The theory of neutron scattering in first Born approximation gives "*the master formula*":

$$\frac{d^2\sigma}{d\Omega dE} = \frac{k}{k_0}\left(\frac{m}{2\pi\hbar^2}\right)^2 \sum_{v_0,s_0} p_{v_0} p_{s_0} \sum_{v,s} \left|\langle ksv|\hat{V}|k_0 s_0 v_0\rangle\right|^2 \delta\left(\Delta E + E_v - E_{v_0}\right), \quad (6)$$

where $p_{s_0} = e^{-\frac{E_{\lambda_0}}{kT}} / \sum_v e^{-\frac{E_{\lambda}}{kT}}$ are the population factor of initial states (for unpolarized beam the polarization states $p_{s_0} = \frac{1}{2}$ for $s_0 = \pm\frac{1}{2}$. It describes that a neutron wave with wave vector $\vec{k}_0$ and spin s_0, after interacting with matter is registered at a distance r with wave vector $\vec{k}$ and spin s. The quantum state of the target (scatterers) changes from $|v_0\rangle$ to $|v\rangle$, accompanied with change in energy state from E_{v_0} to E_v. In (6) v stands for the set of quantum number describing spin and orbital electronic states, phonons, isotope distribution, orientation of nuclear spins etc in the target.

The interaction potential $\hat{V}$ is a sum of two components. The first one is arising from the strong neutron-nucleus interaction. It causes "*nuclear scattering*" and can be described by the so-called Fermi's pseudo potential depicted schematically in Figure 4:

$$\hat{V}(\vec{r}) = \sum_i \frac{2\pi\hbar^2}{m} b_i \delta\left(\vec{r} - \vec{R}\right), \quad (7)$$

Where δ is the Dirac delta function and the quantity b is the asymptotic scattering amplitude: $\lim_{\kappa \to 0} |f(\vec{\kappa})| = -b$. In principle, it is a complex quantity: $b = b' - ib''$. The real part b' is positive for most
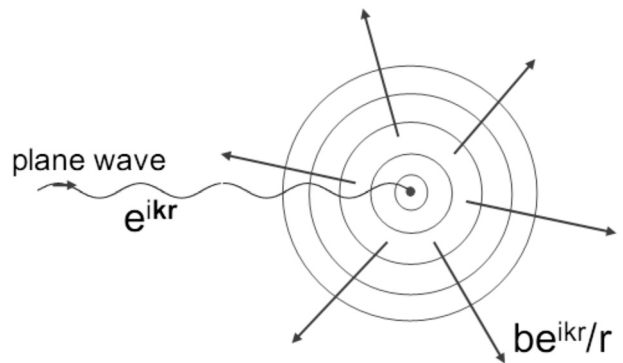
Fig. 4. Nuclear scattering described by the pseudopotential of Fermi: The neutron represented by a plane wave is scattered on the nucleus, which is a point-like object, as spherical waves. The amplitude of the spherical wave is governed by a parameter b known as the scattering length.
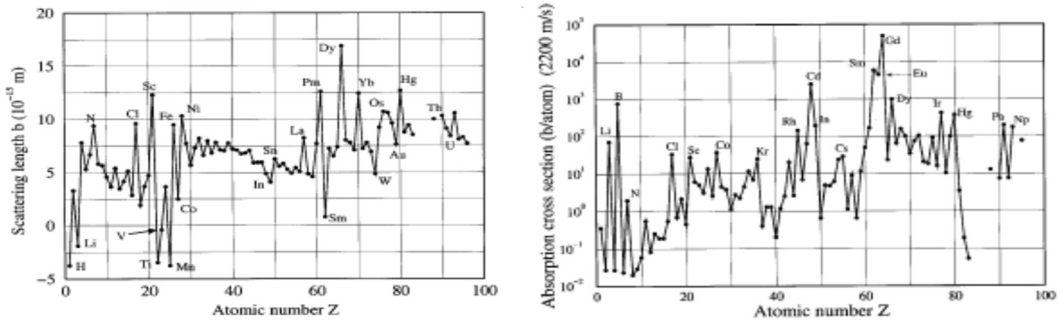
Fig. 5. Left) The real part of the neutron scattering length b; Right) the absorption cross-section for velocity of neutrons 2200 m/s

elements and is in the range $0.3\ 10^{-12} \div 1.1\ 10^{-12}$ cm. For ^{1}H (proton), ^{7}Li, ^{48}Ti, ^{51}V, ^{55}Mn, ^{62}Ni, ^{152}Sm and some others it is negative (Fig. 5, Left panel). For most nuclides the imaginary part $b'' = (k/4\pi)\sigma_a(k)$, which gives rise to the absorption of neutrons, is very small. Here $\sigma_a(k)$ is the absorption cross-section, which is a quantity that covers roughly six orders of magnitude. The values $\sigma_{abs} = \sigma_a(k)$ also vary, occasionally significantly, from one isotope to another. For example σ_{abs} = 940 b/atom for ^{6}Li but only 0.045 b/atom for ^{7}Li.

For a given nucleus b is a fundamental constant; it has dimension of length (10^{-12} cm) and is known as the *Fermi scattering length*. The values of b are accurately measured and tabulated for all elements and nearly all their isotopes [5]. The isotopic differences allow the use of *isotope substitution* and *contrast variation*, which permits highlighting of parts or whole molecules to distinguish them in complex or multicomponent systems. Widely used is the deuterium labelling because b_D = $+6.67\ 10^{-12}$ cm, $b_H = -3.74\ 10^{-12}$ cm.

In early days of neutron scattering the microscopic cross section σ was evaluated from the macroscopic cross section Σ measured from neutron transmission experiments with pure chemical substances (Fig. 6).

The mean potential $\langle \hat{V}(\vec{r}) \rangle$ has the periodicity of the crystal lattice and can be expanded in Fourier series in the reciprocal space.

$$\langle \hat{V}(\vec{r}) \rangle = \frac{1}{N\vartheta_0} \sum_{\vec{\tau}} \exp(-i\vec{\tau}\vec{r}) V_{\vec{\tau}} \qquad (8)$$

where $\vartheta_0 = \vec{a}(\vec{b} \times \vec{c})$ and N are correspondingly the volume of the unit cell and the number of unit cells in the volume of the crystal, and the Fourier components are determined by:

$$V_{\vec{\tau}} = \int d\vec{r} \exp(i\vec{\tau}\vec{r})\langle \hat{V}(\vec{r}) \rangle = N\frac{2\pi\hbar^2}{m} F(\vec{\tau}), \qquad (9)$$

where $\vec{\tau} = h\vec{a}^* + k\vec{b}^* + l\vec{c}^* = \vec{\tau}_{hkl}$ is the reciprocal lattice vector. In (9) it is introduced the quantity $F(\vec{\tau})$ − structure factor of the unit cell:

$$F(\vec{\tau}) = \frac{m}{2\pi\hbar^2} \int_{\vartheta_0} d\vec{\tau} \exp(i\vec{\tau}\vec{r})\langle \hat{V}(\vec{r}) \rangle. \qquad (10)$$

By substituting (10) in (6), for the general form of the differential cross section of coherent elastic scattering of thermal neutrons by a potential with the period of the crystal lattice we get:

$$\left(\frac{d\sigma}{d\Omega}\right)_{coh} = \frac{\gamma e^2}{m_e c^2} \frac{(2\pi)^3}{\vartheta_0} N \sum_{\vec{\tau}} \delta(\vec{\kappa} - \vec{\tau})|F(\vec{\tau})|^2 \qquad (11)$$

The expression (11) is general; it does not depend on the interaction potential and is valid for both nuclear and magnetic interaction. One should have in mind that generally the crystalline and the magnetic lattices do not have the same periodicity. The delta-function tells us that the scattering occurs only for $\vec{Q} = \vec{k}_i - \vec{\kappa}_f = \vec{\tau}$. Going back to the real space one easily derives the familiar form of Bragg's law: $n\lambda = 2d\sin\theta$.

$$I = I_0\, e^{-\Sigma d}$$

$$\Sigma = \Sigma_a + \Sigma_s$$
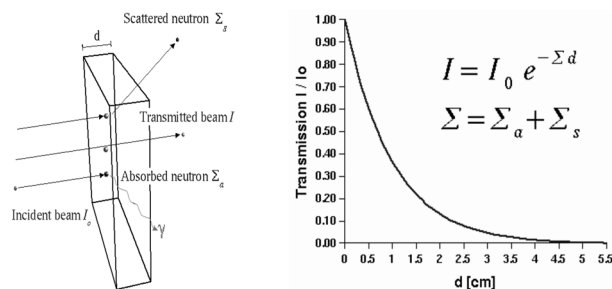
Fig. 6. The attenuation of a narrow neutron monochromatic beam passing a material layer of thickness d [cm] obeys exponential law: Σ − total macroscopic cross section [cm^{-1}], σ − total microscopic cross section, ρ − density [gcm^{-3}], A −atomic weight [gmol^{-1}], Σ = Nσ [cm^{-1}], the number of nuclei per unit volume N = (ρ/A)N$_A$ [cm^{-3}], N$_A$ − Avogadro number

MAGNETIC SCATTERING

In (6) the second component in $\hat{V}$ causes *"magnetic scattering"* and arises from the interaction of neutron with the magnetic induction **B = M + H** within the sample. Generally, **B** is connected with presence in the sample of atoms that have electron shells with unpaired electrons. The potential of magnetic interaction between the neutron magnetic moment operator $\hat{\mu}_n = -\gamma\mu_N\hat{\sigma}$ and the magnetic field $\vec{H}$, created in point $\vec{R}$ by an electron with a magnetic moment $\hat{\mu}_e = -2\mu_B\hat{s}$ moving with velocity $\vec{V}_e = \hat{p}_e/m_e$ is [6]:

$$\hat{V}_\mu(\vec{R}) = -\frac{\gamma\hbar e}{mc}\hat{\sigma}\vec{H} = -\frac{\gamma\hbar e}{mc}\hat{\sigma}\left\{rot\left[\frac{\hat{\mu}_e\times\vec{R}}{|\vec{R}|^3} + \frac{(-e)}{c}\frac{\vec{V}_e\times\vec{R}}{|\vec{R}|^3}\right]\right\}. \quad (12)$$

The first term in (12) arises from the spin of the electron and the second term comes from its orbital motion.

The evaluation of the transition matrix elements in (6) has been carried out for the scattering of both unpolarized and of polarized neutron beams for many classes of magnetic media: paramagnets, ferromagnets, antiferromagnets. The Fourier transform of the atomic magnetization density at the site of every magnetic ion is called *magnetic form factor*. The calculations are rather complicated.

In a magnetically ordered state of the compounds, the computations of magnetic scattering have revealed presence of different kinds of long-range magnetic order, collinear and noncollinear arrangements of spins (atomic magnetic moments) as well as a number of hellical spin structures (magnetic spiral structures). Figure 7 illustrates the geometry of magnetic scattering. For unpolarized neutrons the magnetic cross section has the form [7]:

$$\left(\frac{d\sigma}{d\Omega}\right)coh = \frac{\gamma e^2}{m_e c^2}\frac{(2\pi)^3}{\vartheta_0}N\sum_{\vec{\tau}}\delta(\vec{\kappa}-\vec{\tau})\left|\vec{e}\times\left(\vec{F}(\vec{\tau})\times\vec{e}\right)\right|^2. \quad (13)$$

The constant $p = r_e\gamma/2 = 0.2695$ allows converting the Fourier components of atomic magnetic moments in magnetic scattering amplitudes given in units 10^{-12} cm. The magnetic scattering amplitudes and nuclear scattering lengths are of the same order of magnitude. In favourable cases one can introduce the quantity "magnetic unit-cell structure factor", which is a vector

$$\vec{F}_M(\vec{\tau}) = \sum_{\vec{\tau}}f_\tau(\vec{\tau})\mu_\tau\exp(i\vec{\tau}.\vec{R}_t), \quad (14)$$

where the sum runs over all magnetic atoms, $f_\tau(\vec{\tau})$ is the magnetic form-factor of the atom with localized moment μ_τ and the elastic magnetic scattering cross-section from an ordered magnetic structure is proportional to $\sum_{\vec{\tau}}\delta(\vec{\kappa}-\vec{\tau}_M)\left|\vec{F}_{M\perp}(\vec{\tau})\right|^2$ with $\vec{F}_{M\perp}(\vec{\tau}) = \vec{\tau}\times\vec{F}_M\times\vec{\tau}$.
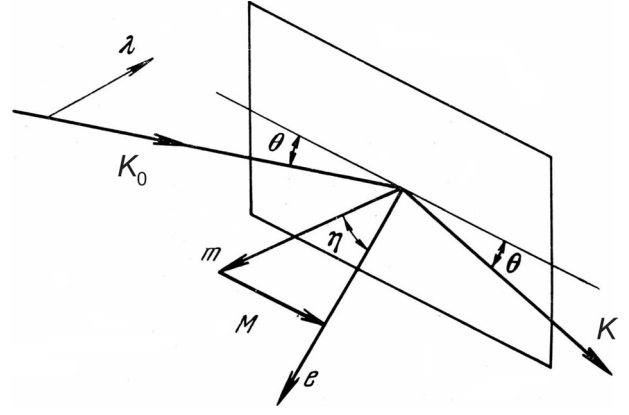
Fig. 7. Schematic drawing of the magnetic scattering of neurons [7] from a medium with magnetization $\vec{M}$ and relation between vector $\vec{q} = \vec{M}$, unit vector $\vec{e}$ and unit vector $\vec{m}$ (in direction of an atomic magnetic moment). Vector $\vec{q} = \vec{M}$ lies always in the scattering plane. For a beam of polarized neutrons the direction of the vector of neutron polarization $\vec{\lambda}$ is also important for the scattering cross-section

If the magnetic and nuclear unit cells do not coincide, then magnetic Bragg scattering is observed at different reciprocal lattice vectors $\vec{\tau}_M$. In paramagnetic state these magnetic peaks are not present and this could be a further advantage for the structure determination.

DISORDER

The interaction potential $\hat{V}(\vec{r})$ between neutron and crystal, strictly speaking, does not possess the crystal lattice periodicity. The reasons are of two kinds: *statistical deviations* due to isotope disorder, magnetic impurities, orientation of nuclear spins and *dynamic deviations* due to atomic and electronic motion [8]. Even so, the crystal as a whole has a periodic structure. It can be defined that the neutron "sees" a mean potential $\langle\hat{V}(\vec{r})\rangle = \sum_{v_0}p_{v_0}\langle v_0|\hat{V}(\vec{r})|v_0\rangle$, the local deviation from which is $\delta\hat{V}(\vec{r})$ such that $\sum_{v_0}p_{v_0}\langle v_0|\hat{V}(\vec{r})|v\rangle = 0$:

$$\hat{V}(r) = \langle\hat{V}(\vec{r})\rangle + \delta\hat{V}(\vec{r}). \quad (15)$$

Substitution of (15) in (6) gives:

$$\frac{d^2\sigma}{d\Omega dE} = \left(\frac{d^2\sigma}{d\Omega dE}\right)_{incoh} + \left(\frac{d^2\sigma}{d\Omega dE}\right)_{coh} \quad (16)$$

The first term in (16) reflects the mechanisms that lead to incoherent scattering and depends weakly on the scattering angle via the Debye-Waller factor $\exp\left(-W_{\vec{d}}(\vec{\tau})\right)$ describing thermal vibration of atoms

about their mean positions. The second term in (16) contributes to the interference Bragg scattering. Beyond the so-called Bragg "cutoff wavelength" λ_c, which is such that the Bragg equation $\lambda_i = 2d_{hkl} \sin\theta$ cannot be satisfied for $\lambda_i > \lambda_c$, there is no coherent scattering whatsoever (neglecting atomic disorder).

THE PAIR CORRELATION CONCEPT

This concept was worked out by van Hove in 1950-ies with the aim to describe the distribution of momentum and energy transfers in a scattering process in terms of the correlation between scattering centres in space and time. It is valid for the case of slow neutron scattering by liquids, gases, and crystals when the Born approximation holds. As it was shown by Van Hove (6) could be expressed in the form [9]:

$$\frac{d^2\sigma}{d\Omega dE} = \frac{k_f}{k_0} N \frac{\sigma_t}{4\pi} S(\vec{Q}, \omega), \qquad (17)$$

where $\sigma_t \equiv 4\pi \left\langle \overline{b^2} \right\rangle = 4\pi N^{-1} \sum \overline{b_i^2}$ is the mean full neutron cross-section and the function $S(\vec{Q}, \omega)$, known as "scattering function" or else "scattering law", is given by:

$$S(\vec{Q}, \omega) = \frac{2}{2\pi \hbar N \left\langle \overline{b^2} \right\rangle} \int_{-\infty}^{\infty} dt e^{-i\omega t} \sum_{k,l} \overline{b_k b_l} \langle e^{-i\vec{Q}\vec{r}_k(t)} e^{i\vec{Q}\vec{r}_l(t)} \rangle. \quad (18)$$

The $S(\vec{Q}, \omega)$ scattering function has dimension of reciprocal energy $[E^{-1}]$ and does not contain variables related with the wave functions of the incident and scattered neutrons, expressed in other words, it does not depend on the velocities **v** and $\mathbf{v}_0$. The only valid quantities are the momentum transfer $\vec{Q} = \vec{k}_0 - \vec{k}_f$ and the energy transfer $\Delta E \equiv \hbar\omega = E_0 - E_f$, i.e. the combination of only 4 parameters. From the point of view of theory the way of realizing the acts of transfer is not of importance. Therefore, equation (6) and correspondingly (9) specify that the probe and the target system are decoupled. This is a very important characteristic of neutron scattering; the neutrons being a very weakly interacting probe just monitor an unperturbed state of the target. Often $S(\vec{Q}, \text{w})$ is called dynamic structure factor.

Hence, in the scattering experiment one measures the summary intensity, where beside interference maxima there is always present incoherent background. The difference between the coherent and incoherent scattering is important because it gives different information for the system. Incoherent scattering gives information for the single particle correlation function, which determines the probability to find a particle at the point with radius vector

$\vec{r}$ at time t, if the same particle was located at point $\vec{r}$ =0 at time t=0. The coherent scattering gives information for the pair correlation function, i.e. the probability to find an atom at origin at $\vec{r}$ =0 at time t=0 and another atom at $\vec{r}$ at time t. The coherent scattering probes the general properties of a large assembly of atoms: the spatial order or the lattice dynamics. Incoherent scattering allows studying the behaviour of a single scatterer (atom), such as the diffusion of given atomic species in the crystal lattice.

The main uses of beams of neutrons in condensed matter research are summarised in Figure 8 and Table 2. Eight cross sections are matter of importance.

The standard method of analyzing the neutron powder diffraction patterns, known as *Rietveld method* or else *full profile refinement*, is to fit the parameters of a model of the crystal and magnetic structure to the measured profile, which is the scattered neutron intensity measured as a function of scattering angle 2θ. The Rietveld method is a structure refinement method, not a structure solution method. It must always be remembered that although neutron diffraction is an extremely powerful technique, it should be used in conjunction with other techniques to fully exploit its potential.

Figure 9 illustrates structure refinement for nanocrystalline goethite [10] with average particle size $D \approx 10 \times 80$ nm as determined from scanning electron microscopy images.

The figure illustrates the extensive incoherent scattering of hydrogen from the hydroxyl group of goethite most probably enhanced additionally by crystalline water, i.e. actually FeO(OH).nH(OH). This is reflected by the steadily rising contribution to instrumental background with decreasing to zero scattering angles. We found our nanomaterial to preserve orthorhombic Pnma symmetry of microc-
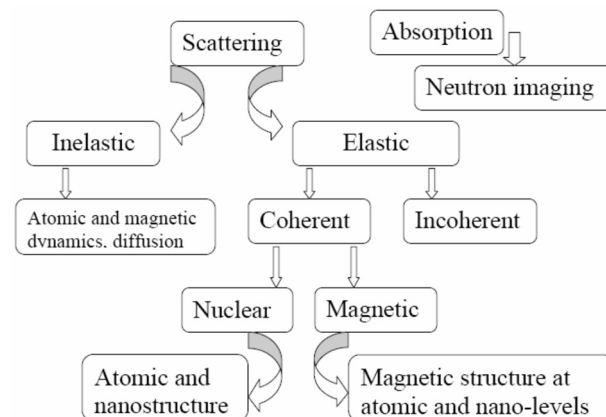
Fig. 8. Interaction of low energy neutrons and condensed matter fields of investigations

Table 2. The neutron as a probe in condensed matter research

1. No electric charge. Weak interaction characterized by a small cross section and hence high penetration capability	The scattering can be treated on the basis of the first Born approximation
	Voluminous samples can be investigated
	Specialized environment is easily used: thick-walled sample cans, high pressure chambers, high and low temperature furnaces
2. Scattering on nucleus known as "nuclear scattering"	One can distinguish: elements, isotopes, e.g. "hydrogen from deuterium" $\Rightarrow$ the contrast variation method
3. Magnetic moment. Scattering on the magnetic field generated by the unpaired electrons of atomic shells	The magnetic properties can be investigated on microscopic level and to analyze the magnetic structure $\Rightarrow$ antiferromagnetism, spiral spin order and other arrangements
4. The wavelength of thermal neutrons is comparable with inter-atomic distances	One can determine both the crystalline structure (symmetry, atomic positions) and the magnetic structure (magnetic symmetry, location, mutual orientation and magnitude of magnetic moments)
5. The thermal neutron kinetic energy falls in the range of elementary excitations	The dynamic properties and excitation energies can be investigated
6. Coherent and incoherent scattering processes can be distinguished	Both collective phenomena and single atom effects (for instance diffusion) can be studied

rystalline material and to order in antiferromagnetic spin arrangement with coinciding crystalline and magnetic unit cells with parameters a=4.6049(9) Å, b=9.958(3), c = 3.022(1) Å. The magnetic structure we determined as canted antiferromagnetic with a slightly reduced effective magnetic moment of cation Fe^{3+}: 2.78(12) μ_B instead 2.98(4) μ_B known for the bulk material.

Nanomaterials are receiving increasing attention in the technical and scientific communities. The reason that size matters is that the properties of materials can have some unexpected differences from their behaviour in larger bulk forms that opens up new application opportunities. Two reasons

for this change in behaviour are the increased relative surface area (producing increased chemical reactivity) and the increasing dominance of quantum effects with impact on the material's optical, magnetic, or electrical properties.

Figure 10 represents the thermal evolution of the NPD pattern of $La_{0.5}Pb_{0.5}FeO_3$ material with average particle size *D = 80 ± 15* nm obtained by combustion route [11].

The appearance of additional diffraction lines of magnetic origin below T_N = 558 ± 5 K is in good correspondence with the phase transition at T = 554.2 ± 0.2 K analyzed by DTA/TG measurements. Symmetry analysis gave the magnetic mode
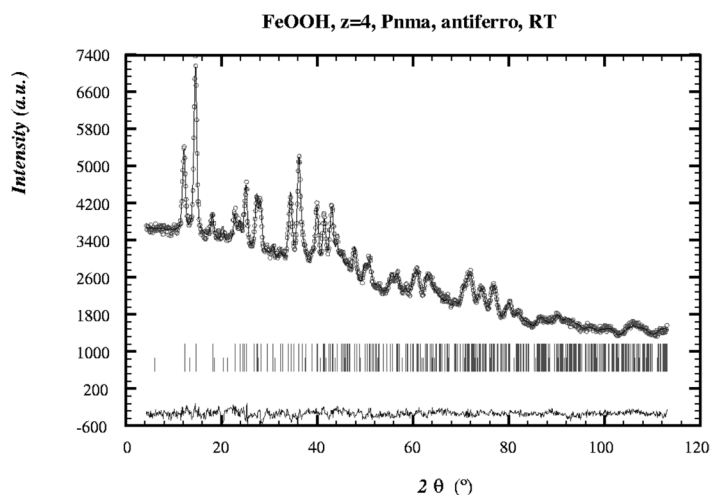
Fig. 9. Rietveld refinement (continuous line) of neutron diffraction data (circles) measured at room temperature on powder material of nanocrystalline FeO(OH). The neutron wavelength is 1.0571 Å. The difference curve between experiment and calculation is shown at the bottom. The background curve is smoothly approximated by a polynomial of 5-th order.
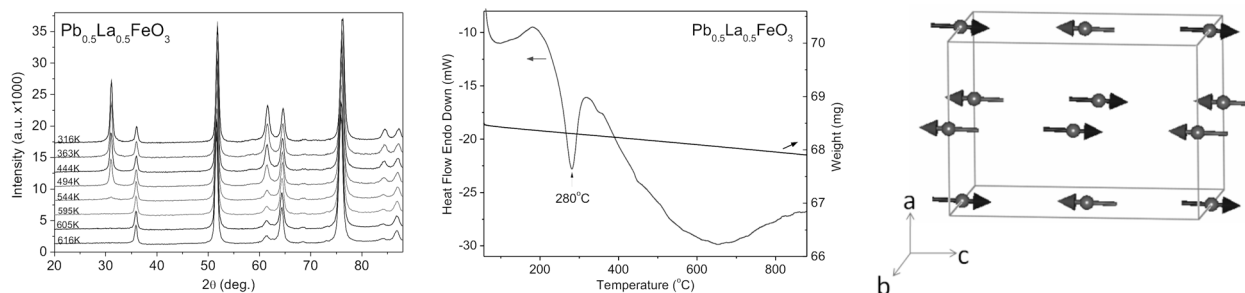
Fig. 10. a) Thermal evolution of neutron scattering upon heating; b) DTA/TGA: no mass loss → evidence for magnetic transition, c) G-type magnetic structure.

Γ_4 (G_x, A_y, F_z; f_z) with $f_z = 0$ (La is non-magnetic), $A_y \approx 0$, $F_z \approx 0$, and $S_x \approx (3.6 \pm 0.2)$ μ_B.

Today to attain better understanding of the magnetism and the magnetic behaviour of systems with reduced dimensions is of utmost importance. Figure11 illustrates on the example of substituted barium hexaferrites [12] that neutron diffraction allows seeing details in both the magnetic and the atomic ordering that were affected due to grain size reduction and cation substitution. Concerning microwave applications as absorbing media, the substitution by non-magnetic Sc ions is known to reduce substantially the ferrimagnetic resonance frequency of $BaFe_{12}O_{19}$. On the other hand, substitution of Fe^{3+} by the Co^{2+}/Ti^{4+} pair is among the most often used ways to enhance magneto-optic effects in the range of wavelengths appropriate for recording technologies.

There is a reasonable understanding of the physics of simple systems without competing magnetic interactions. Many systems, however, exhibit com-peting interactions, that is, interactions that do not all favour the same magnetic ordered state. In this case not all interactions can be minimised simultaneously, best example is the antiferromagnetic exchange interactions on a triangular lattice, and the system is said to be magnetically frustrated [13]. Also, cases when ordered magnetic moments systematically involve 3d or 4f unpaired electrons lead to unexpected results. Sufficiently strong competition (a high degree of frustration) leads to new physics that is manifested by the appearance of noncolinear ordering, novel critical exponents, rich phase diagrams, or an absence of long-range magnetic order at low temperatures, leading to magnetic analogues of liquids and ice.

Magnetism and ferroelectricity form the backbone of many fields of science and technology. Multiferroics have become an object of growing interest due to the coexistence of magnetic order (FM or AFM) and ferroelectric polarization in a single-phase material. Beside important implications for
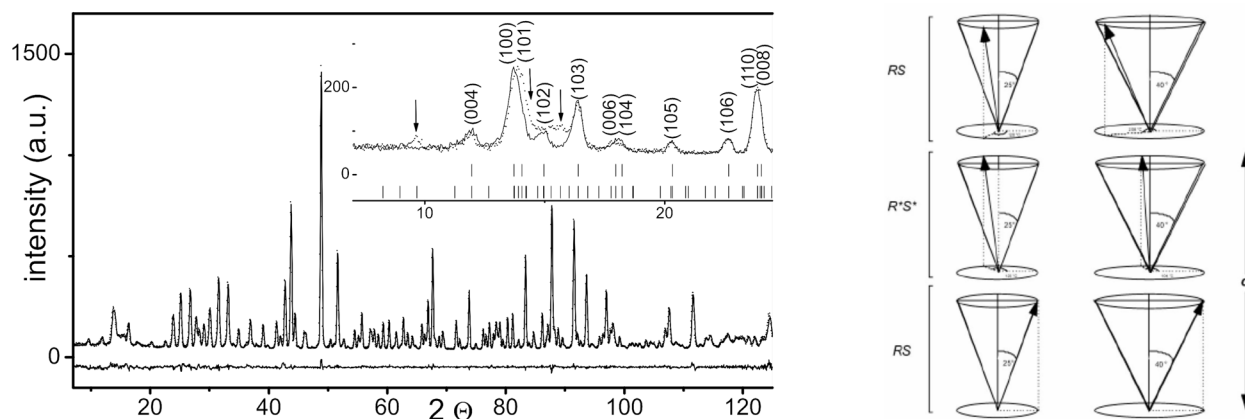
Fig. 11. a) Neutron diffraction pattern (l=1.2251 Å) of $BaFe_{10.4}Sc_{1.6}O_{19}$ at 10K and its Rietveld-refinement in the conical block-type magnetic structure in space group P63/mmc (a=5.9240 Å c=23.5395 Å). The inset shows the low angle part both at 10K (dots) and 300K (solid line), the arrows indicate the extra magnetic reflections at 10K; b) Block-conical magnetic structure. The phase of spin rotation is dependent on substitution; for $BaFe_{12-2x}Co_xF_{ex}O_{19}$ – phase 120° (x=0.8) and 104° (x=1.1). Incommensurate magnetic structure with cone angle ≈ 40o and propagation vector k ≈ 0.24 was found for $BaFe_{10.4}Sc_{1.6}O_{19}$.
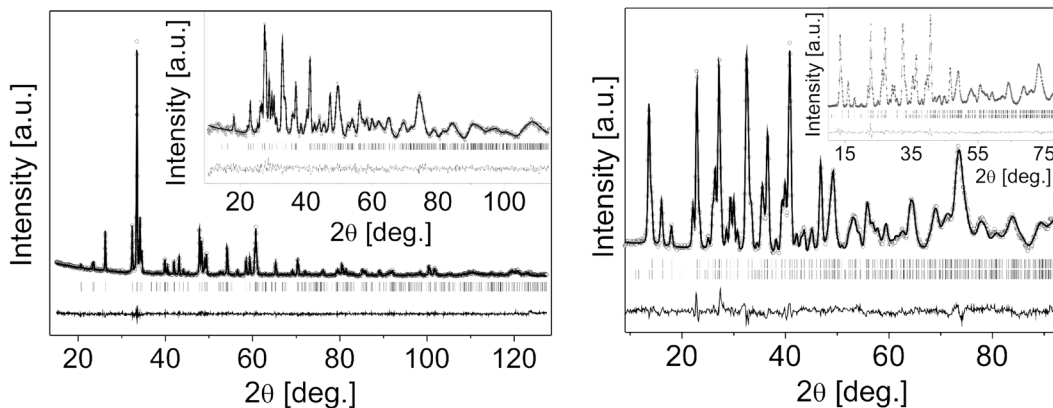
Fig. 12. NPD Rietveld plots of $YFe_{0.875}Cr_{0.125}O_3$ and $YFeO_3$ (inset) b) Simultaneous multipattern XRD and NPD (inset) refinement of $YCrO_3$ in paramagnetic weak ferroelectric state, T = 295 K

novel electronic devices such as electric-field controlled spintronic devices, electric and magnetic field sensors, electric power generators and new four-state logic memory, the physics behind the expected complex magnetoelectric phenomena is among the hot topics in condensed matter [13–16].

We investigated the solid solubility between $YFeO_3$ and $CrFeO_3$ known as weak antiferromagnets and the spin arrangements in the system $YCr_{1-x}–Fe_xO_3$ synthesized by combustion route [14]. The magnetic order occurs below a concentration dependent Néel temperature T_N between 648 K (x=1) and 141 K (x=0). In view of the weak biferroicity of $YCrO_3$ with transition at T_E =400 K to weak ferroelectric state much above the magnetic phase transition to weak AFM state, the evidence helps in improving our understanding of perovskite-like systems with noncollinear spin ordering. Figure 12 shows the Rietveld-

refined diffraction patterns of some members of this solid solution system, demonstrating single phases with centrosymmetric average crystal structure of orthorhombic Pnma symmetry. The XRD structural data alone did not allow accurate determination of TO_6 (T=Fe,Cr) distortions and we carried out a multipattern (X ray + neutron) profile analyses. The compounds with x≥0.60 displayed AFM ordering of type G_yF_x at 295 K and with growing Fe content the weak ferromagnetic component F was found increased.

In the restricted class of multiferroic materials the mixed valence oxides with general formula RMn_2O_5 (R = rare earth metal, Y or Bi) crystallizing in perovskite-like structure are well known for the relatively strong correlations between magnetic order and ferroelectricity. Perovskites represent one of the most important classes of functional materials and also play a leading role in multiferroic research.
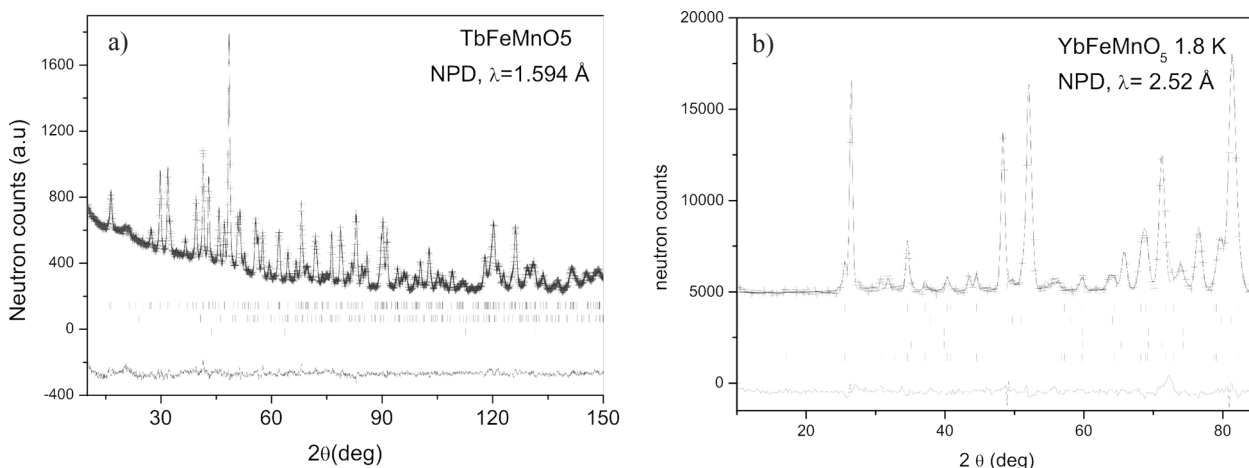
Fig. 13. a) Comparison of the observed (circles), calculated (solid line) and difference (at the bottom) NPD patterns for $TbFeMnO_5$ at T = 295 K. The second series of tick marks correspond to $TbFeO_3$ and the third series to vanadium; **b)** Rietveld plot for $YbFeMnO_5$ at T=1.8 K
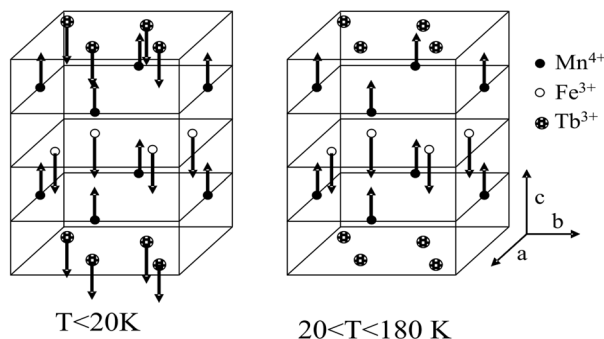
Fig. 14. Magnetic structures in $TbFeMnO_5$. The magnetic cell coincides with the chemical cell ($\mathbf{k} = 0$)

The substitution effects we illustrate with the derivative compounds $YbFeMnO_5$ and $TbFeMnO_5$ where half of manganese is replaced by iron [15,16]. The samples were prepared in polycrystalline form by a soft chemistry route followed by thermal treatments under high-oxygen pressure. The Rietveld analysis of diffraction data showed that the crystal structure is orthorhombic, *Pbam* (SG), formed by chains of edge-linked $Mn^{4+}O_6$ octahedra linked together by dimer groups of square pyramids $Fe^{3+}O_5$ and units $R^{3+}O_8$ ($R= Yb^{3+}$, Tb^{3+}, respectively) (Figure 13).

The thermal evolution of the NPD patterns evidenced that below a transition temperature of $T_c\approx160$ K for $YbFeMnO_5$ and $T_c\approx175$ K it is developed a long-range magnetic order resolved as a ferrimagnetic arrangement of Fe^{3+} ions ($4h$ site) and Mn^{4+} ions ($4f$ site) spins with propagation vector $\mathbf{k}$=0. At lower temperatures, the magnetic moment of the Yb^{3+} (Tb^{3+}) cation also participates in the magnetic structure (see Figure 14), adopting a parallel arrangement with the Mn^{4+} spins; at T = 1.8 K the magnitudes of the magnetic moments of the effective scatterers are 2.00(8), −3.04(17) and 0.35(14) μ_B, over the sites $4f$, $4h$ and $4g$ sites respectively for $YbFeMnO_5$ whereas in the case of $TbFeMnO_5$ we evaluated 1.5(3)μ_B for the Mn^{4+} cations, −2.0(1)μ_B for the Fe^{3+} cations and 3.9(2)μ_B for the Tb^{3+} cations.

The relatively weak magnetic moments with respect to the expected values may be related to the antisite disordering in both sublattices, promoting AFM interactions that partially hinder the FM coupling in the chains of MnO_6 octahedra and in the Fe_2O_{10} dimmers. The lack of evidence for a crystallographic phase transition to a polar space group ruled out the expectations of a spontaneous electric polarization. In addition, the observed collinear ferrimagnetic structure with k = 0 does not allow spin polarization and the magnetic symmetry group excludes a linear magnetoelectric effect.

CONCLUSIONS

As has been discussed above, neutron scattering is a powerful and versatile tool in many research fields and with the advances in neutron sources and equipment many previously dreamed experiments such as *in situ* and time-resolved experiments, even in adverse environment, have been done nowadays. It is believed that the few examples presented will motivate the readers to speculate on the many capabilities of the neutron scattering techniques and to realize how the neutron diffraction in particular could be useful for their own investigations.

REFERENCES

1. http:/www.neutron.anl.gov.
2. http:/www.codata.org/ The Committee for Data in Science and Technology, 2006CODATA.
3. G. E. Bacon, Neutron Diffraction, 3-rd Edition, Clarendon Press, Oxford, 1975.
4. C.G. Windsor, Pulsed neutron scattering, Taylor and Francis, London, 1981.
5. V. F. Sears, Neutron Optics, Oxford University Press, New York, 1989.
6. S.W. Lovesey, Theory of Neutron Scattering from Condensed Matter, Vol. 1 and 2, Oxford University Press, Oxford, 1987.
7. Y.A. Izyumov, R. P. Ozerov, Magnetic neutron diffraction, Plenum Press, New York, 1970.
8. G L. Squires, Introduction to the Theory of Thermal Neutron Scattering, Dover Publications, Inc, Mineola, New York, 1996.
9. L. van Hove, *Physical Review*, **95**, 249 (1954).
10. K. Krezhov, in: 5th Congress of Balkan Geophysical Society, Belgrade, Serbia, 10–16 May, 2009, 4 pages, EAGE article 122, http://www.earthdoc.org/detail.php?pubid=21100.
11. K. Krezhov, S. Kovachev, D. Kovacheva, E. Svab, G. Andre, F. Porcher, in: AIP Conference Proceedings, 2009, vol. 1203, p. 205.
12. K. Krezhov, *Solid State Phenomena*, **159**, 175 (2010).
13. R. Ramesh, N. Spaldin, *Nature Materials*, **6**, 21 (2007).
14. S. Kovachev, D. Kovacheva, S. Aleksovska, E. Svab, K. Krezhov, *Journal of Optoelectronics and Advanced Materials*, **11 (**10), 1549 (2009).
15. M. J. Martínez-Lope, M. Retuerto, J. A. Alonso, M. García-Hernández, K. Krezhov, I. Spirov, T. Ruskov, M. T. Fernández-Díaz, *Solid State Communications*, **149** (13–14), 540 (2009).
16. M. Retuerto, M. J. Martínez-Lope, A. Muñoz, T. Ruskov, I. Spirov, K. Krezhov, M. T. Fernández-Díaz, M. García-Hernández, J. A. Alonso, *Solid State Communications*, **150** (37–38), 1831 (2010).

ВЪЗМОЖНОСТИ НА НЕУТРОННАТА ДИФРАКЦИЯ ЗА УТОЧНЯВАНЕ НА СТРУКТУРНИ ДЕТАЙЛИ ПРИ ХИМИЧНО ЗАМЕСТВАНЕ

К. Крежов*

Институт за ядрени изследвания и ядрена енергетика, Българска академия на науките,
бул. „Цариградско шосе" № 72, 1784 София, България

(Резюме)

Между начините, по които науката се е научила да произвежда нови материали, химичното заместване е сред най-популярните. В последно време, многофункционалните материали станаха в центъра на интензивни изследвания поради възможността да се съчетават няколко функции, включително механични, електронни, фотонни, оптични, биологични и магнитни функции, както и да са способни да проявяват различни контролируеми и предсказуеми физични отговори, когато са подложени на различни външни условия. Тази статия е мотивирана от възраждането напоследък на интереса към сложни оксиди поради взаимодействието на електрическите, магнитните, топлинните, механичните и оптични свойства, което ги прави подходящи за широк спектър от приложения. От времето на пионерските експерименти на Шал и Уолан преди повече от 50 години, неутронната дифракция се прилага за справяне със сложни структурни проблеми във физиката и химията на твърдото тяло. Методиката се възползва от уникалните свойства на неутрона, които го правят особено подходяща сонда в кристалографските изследвания. Неутроните са чувствителни към водород и леки атоми в общия случай и са силно чувствителни към магнетизма. За разлика от други сонди, използвани в структурните изследвания като електрони и рентгеново лъчение, неутроните са в състояние да разкрият положенията на ядрата и средните отмествания без да се повлияват от ефектите на електронното разпределение. Ние илюстрираме тази област с изследвания на ефектите от химично заместване в различни материали. Примерите включват семейството на перовскитите и експерименти, насочени към подобряване на разбирането на някои от основните аспекти на механизмите допринасящи към вътрешно присъщи ефекти, като например подреждането на орбитали и заряди и мултифероизма, които са израз на силно взаимодействие между степените на свобода по орбитала, заряд и спин в тези системи. Структурните заключения се съчетават с резултатите от магнитни и електрически измервания и Мьосбауерова спектроскопия.

Spectroscopy of optical waveguiding layers

M. Kuneva*, S. Tonchev

Institute of Solid State Physics, Bulgarian Academy of Sciences,72 Tzarigradsko Chaussee Blvd., 1784 Sofia, Bulgaria

The authors have shared a 20-years experience on spectroscopy of proton-exchanged waveguide layers in $LiNbO_3$ and $LiTaO_3$. The methods include infrared absorption and reflection spectrometry, X-ray photoelectron spectroscopy (XPS), mode spectroscopy and micro & waveguide Raman spectroscopy. Mode spectra were used for the determination of phases in $Li_{1-x}H_xNbO_3$ and $Li_{1-x}H_xTaO_3$. Vibration spectra allow some comparative and semi-quantitative estimations of the thickness of phase sub-layers to be made, as well as conclusions about the positions of diffused H-ions in the crystal lattice. XPS provides information about the composition at the waveguide surface.

The structural and compositional information delivered by each of these methods helps to create a more complete description of the structure and the properties of such layers. The interpretation of the results emphasizes on the phase content of waveguides obtained at different technological conditions. Such combined analysis can contribute to adjustment of fabrication conditions for obtaining of defined phase compositions needed for waveguide devices with improved stability and characteristics.

Key words: optical waveguides, spectroscopy, phase composition, proton exchange.

INTRODUCTION

Being ferroelectric crystals with very attractive properties for integrated optics, $LiNbO_3$ (LN) and $LiTaO_3$ (LT) are widely used in this field. The electro-optical coefficients of both crystals are high: $r_{33} = 30.5$ pm/V; their Curie temperature (T_c) is 1090÷1210 °C for LN and 540÷700 °C for LT (depending on stoichiometry). LN has much stronger birefringence $\Delta n_{o,e}$ and about three orders of magnitude lower treshold power (10 J/cm²) for optical damage in the visible region.

LN and LT belong to the trigonal crystal system. The unit cell of LN consists of planar sheets of oxygen ions, situated perpendicularly to the optical axis c. Oxygen ions from neighbouring sheets form octahedral interstices which are one-third filled by niobium ions and one-third vacant (V), ordered in the +c direction in the sequence: Li-Nb/Ta-V. The crystal structure of LT is similar. The large number of vacancies favors the penetration of other ions and their high mobility together with the high mobility of the crystal's own metal ions.

An optical waveguide is a light-guiding transparent layer of high refractive index surrounded by regions of lower index. The confinement of the light and the spatial distribution of optical energy inside the guiding layer depend on the refractive index profile.

Proton exchange (PE) [1, 2] is a technology for waveguide fabrication in $LiNbO_3$ and $LiTaO_3$. Going by the scheme:

$$LiMO_3 + xH^+ \Rightarrow Li_{1-x}H_xMO_3 + xLi^+ \ (M=Nb, Ta)$$

it modifies the crystal surface by Li-H ion exchange forming a layer of several μm in depth with a large extraordinary index increase Δn_e ($\Delta n_e \sim 0.12$ at 633 nm) and then with strong waveguiding and polarizing effect.

Development of devices in optoelectronics requires reproducible methods for obtaining of effective low-loss waveguides on or in the substrate material. The easy and fast obtaining of optical waveguides in the electro-optical crystal $LiNbO_3$ by proton exchange (PE) has motivated the attempts to adjust the technology for producing high-quality waveguides. The $Li_{1-x}H_xMO_3$ layer formed by Li-H ion exchange shows complex phase behavior (up to seven different crystallographic phases in $LiNbO_3$ $-\alpha$, κ_1, κ_2, β_1, β_2, β_3 and β_4 and up to 6 ones in $LiTaO_3$ $- \alpha$, κ, β_1, β_2, β_3 and δ) depending on the hydrogen concentration (value of x) [3, 4, 5]. The number and the type of different phase modifications in crystal

---

* To whom all correspondence should be sent:
E-mail: kuneva@issp.bas.bg

solid solutions $Li_{1-x}H_xNbO_3$, what actually is the proton-exchanged lithium niobate, are determined by the crystallographic orientation and the rate of substitution of Li^+ by H^+ (x). Each phase originates as an individual sub-layer undergoing phase jumps with gradual change of x. In every single one of them Δn_e is a linear function of proton concentration. Within a phase transition, the value of Δn_e and/or of the deformations perpendicular to the surface change by leap. As in all cases of generation of new materials and devices, there is a requirement for materials characterization and analysis in all stages of development.

MODE (M-LINE) SPECTROSCOPY

The obtaining of the mode spectrum is the main point of waveguide characterization. It implies measurement of the angles of different modes at the waveguide output and calculation of the effective refractive index n_{eff} for each propagating mode with resolution of $\sim 10^{-4}$.

Mode spectroscopy study was performed by using the two-prism coupling [6] of He-Ne laser ($\lambda = 632.8$ nm) and the distribution of the refractive index Δn in the depth d of the waveguide layer (optical profile) was reconstructed from the set of effective mode indices by using the inverse Wentzel-Kramers-Brillouin method (IWKB) [7]. In the case of single-mode waveguides the mode spectra measurements were performed in two media (air and water) and the optical profile was reconstructed solving the two mode propagation equations for a step-like optical profile. The recognition of that function means to define the waveguide parameters – thickness, maximal value of refractive index and profile shape. The profile shape and the maximal value of the index change allow a preliminary

evaluation of the phase composition according to the phase model to be made for a definite substrate orientation (X, Y or Z).

Exemplary optical profiles are presented in Fig. 1. The preliminary evaluation of the phase composition could be made as follows:

The values of the extraordinary refractive index change $\Delta n_e = 0.15$ for Z-1 and ZN-1 and its gradual change to 0.12 on the optical profiles of the waveguide lead to the suggestion that these waveguides should contain the β_4-phase which is characterized by a higher level of proton doping compared to mono-crystalline $H_xLi_{1-x}NbO_3$ ($0.65 \leq x \leq 0.7$) [8]. The β_4-phase can exist only in Z-cut proton-exchanged lithium niobate and only together with the β_3- and β_1-phases of lower value of x: $0.53 \leq x \leq 0.65$ for the β_3-phase and $0.44 \leq x \leq 052$ for the β_1-phase. Thus, the waveguides Z-1 and ZN-1 consist of at least three β_i-phases: β_1, β_3 and β_4. The other Z-cut single-mode waveguide ZN-5 should be in β_1, ($\beta_1+\beta_2$) or ($\beta_1+\beta_3+\beta_4$) – phase since the value of Δn_e exceeds 0.12, indicating that β_i-phase or phases have been formed during the PE process [4].

The same considerations applied to the X- and Y-cut samples lead to the conclusion that X-3 contains a β_3-phase [4], which can be found only together with a β_1-phase. The β_4-phase could not be formed in X-cut $LiNbO_3$ [9]. As in the case of ZN-5, the shape of the optical profile could not be followed since the waveguides are single-mode. The optical parameters of Y-2 correspond to the coexistence of β_1 and κ_1/κ_2 phases. Y-2 has a step-like optical profile with a maximal index change of $\Delta n_e = 0.11$. Thus, that waveguide should contain the β_1-phase - the only one which could be obtained by low-temperature direct proton exchange in Y-cut $LiNbO_3$ [9].

VIBRATION SPECTROSCOPY

It is widely accepted that the waveguide effect and the increased photorefractive resistance of PE-layers are due to OH group formation when protons interact with oxygen atoms of the crystal lattice [12]. OH groups exist not only in protonated, but also in as-grown crystals due to residual water, and their O-H bonds lie in the oxygen planes, perpendicular to the optical (Z) axis [13]. PE leads to the formation of OH groups which are oriented mainly in the oxygen (X-Y) planes of the $LiNbO_3$ crystal ("in-plane" OH), as it is confirmed by IR spectroscopy [14]. In principle, OH-stretching vibrations investigations allow statements on the proton concentration in the crystal and on the positions of OH defects in the crystal lattice to be made.

A powerful method for studying structural phase transitions in solids is Raman spectroscopy. Raman
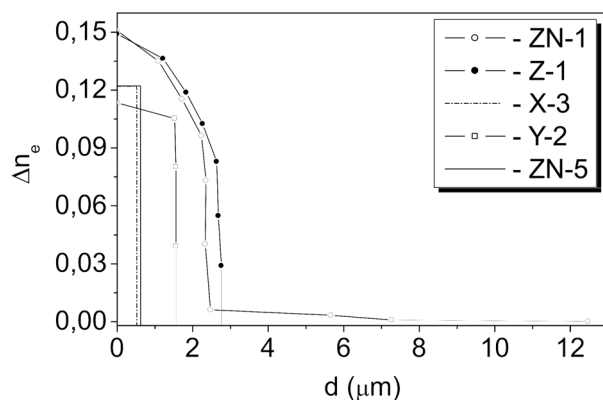
Fig. 1. Optical profiles of different PE waveguides in $LiNbO_3$ [10, 11].

scattering is among the few experimental techniques that can answer questions concerning the phase state and phase transformations, deformations of the crystal lattice, and changes in the atomic configurations. With the development of integrated optics, it has become clear that the waveguide Raman technique is unique in studying the properties of thin waveguide layers [15].

Since the physical processes which determine the phonons active in Raman and infrared spectra also determine the electrooptical and the non-linear dielectric properties of materials, Raman and infrared (IR) spectra provide information for the characterization of the proton-exchanged layers.

Infrared (absorption and reflection) spectroscopy

IR absorption or transmission is very sensitive to H concentration in the crystal and hence offers a measure of the proton content before and after a partial or total doping. IR spectra of protonated and as-grown samples were recorded in the frequency range of 270–700 cm^{-1} of OH-stretching modes with a Brucker LFS-113 V FTIR spectrometer and a Gaussian-Lorentzian decomposition procedure was performed. It was found that Gaussian deconvolution is better for highly protonated samples, but Lorentzian is better for virgin substrates. We have found also that the OH bands of protonated samples are better fitted by Gaussian profiles. Theoretically this different behavior is not surprising since the vibration spectrum of a disordered state – as the protonated crystal – is closely related to a Gaussian form.

After the decomposition, the frequencies and integrated intensities of the bands could be compared.

IR spectra were used for:

– Determining the crystal stoichiometry.

– Establishment of the OH bond orientation in the proton-exchanged layer (in or out of the oxygen planes) and therefore of the positions of the diffused hydrogen (in or out).

– Determining the thickness of the sub-layer which contains interstitial hydrogen (by stepwise polishing of the surface and recording the spectrum after each step).

– Following the changes in the phase composition and H$^+$ presence during annealing procedures.

– Establishment of the phase composition of waveguides obtained by using different sources of protons (melts or vapors of different acidic compounds) or by modifying the PE technological conditions.

The structural studies of LiNbO$_3$ single crystals [16] show that the oxygen anions are situated in the oxygen planes at three different distances from each other: 2.72, 2.88 and 3.36 Å, causing three compo-

nents in the IR absorption spectrum of the vibrations of OH groups in both LiNbO$_3$ and H:LiNbO$_3$. The central peak is attributed to the O–O distance of 2.88 Å. It should be noted that the ratio of the band component intensities depends strongly on the crystal stoichiometry as far as the differences in crystal stoichiometry determine different surrounding.

While the modes of IR spectra of virgin and protonated LiNbO$_3$ were well known from the literature, in the case of LiTaO$_3$ such data were incomplete and this fact directed our efforts to the detailed investigation of the spectra before and after PE and to the determination of their dependence on stoichiometry.

The formula expressing the difference between the real crystal composition and the stoichiometric one can be written as:

$$Li_{1-y}Ta_{1+y/5}O_3$$

The samples were selected to range through the whole interval of y = 0.012÷0.038 (y = 0.033 for congruent composition) which corresponds to Li mole fraction from 0.481 to 0.494.

Absorption IR spectra of three Z-cut samples LiTaO$_3$ with different values of y are shown in Fig. 2, together with a schematic representation of the values of peak frequencies and intensities of the spectral components resulting from the Lorentzian decomposition procedure. The analysis of the results shows that three distinct closely spaced components at 3460, 3474 and 3484 cm^{-1} exist and they can be assigned to O…O bonds of a length about 2.84÷2.87 Å. When y increases (Li depletion), the components shift towards higher frequencies, the halfwidths of the components increase, the intensity of the higher frequency component (dominating in the case of stoichiometry composition) strongly decreases and the spectral structure becomes less pronounced. Optical measurements showed that Li depletion leads to lower values of Δn_e. This fact underlines the importance of crystal composition homogeneity for obtaining reproducible results and high performance of the waveguiding devices. For example, only a few percent changes in n_{eff} in the channels of a directional coupler can break down its action.

The dependence of IR spectra on stoichiometry could be used for approximated estimation of Li/Nb or Li/Ta ratio in virgin LiNbO$_3$ and LiTaO$_3$ or at least for quick identification of crystals of the same stoichiometry which is very important for reproducible technological results.

Infrared spectroscopy has proved its ability to characterize PE layers in LiNbO$_3$ since the Li-H substitution dramatically increases the presence of OH groups in the exchanged layer. IR absorption in the range of OH stretching vibrations (2700–
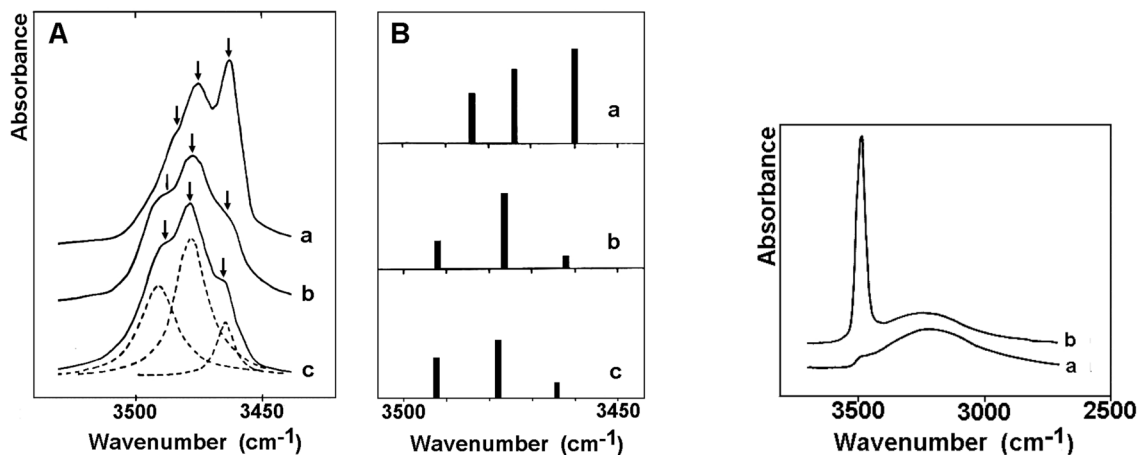
Fig. 2. OH absorption of virgin LT samples with different stoichiometry: a) y = 0.012; b) y = 0.023; c) y = 0.038, and scheme of frequency positions and intensities of the components; polarized OH spectra of a X-cut LT sample: E∥Z (a); E⊥Z (b)

3700 cm^{-1}) has been widely used for estimation of the phase composition [10, 17, 18, 19]. The spectra show several bands (at 3488 cm^{-1}, 3500 cm^{-1}, 3512 cm^{-1}, 3250–3280 cm^{-1}) which could be attributed to different phases forming the PE layers [3]. It should also be noted that all the peaks except of a large shoulder at 3280 cm^{-1} are polarized, showing that OH bonds lay in the oxygen planes of the crystal. The unpolarized band indicates the presence of hydrogen in interstitial positions out of the oxygen planes, which usually means a higher level of doping.

As it is known, a band centered at 3488 cm^{-1} in the IR spectrum of proton-exchanged LiNbO$_3$ is attributed to the α-phase [4, 20]. All other bands could be assigned to the phases formed by PE: the broad band centered at 3250–3280 cm^{-1} – to the β$_2$, β$_3$ and β$_4$ phases, the band at 3500 cm^{-1} – to the β$_i$ (i = 1–3), κ$_1$ and κ$_2$ produce peaks between 3488 and 3500 cm^{-1} (intermediate values between α-phase and β$_1$-phase) and are spectroscopically indistinguishable. For the strongly protonated samples, a fourth additional component emerges at about 3512 cm^{-1} which could be attributed to the β$_4$ only. Since the component due to the substrate α-phase was extracted from the spectra after the deconvolution, only the components of the layers' spectra are present in the histograms (Fig. 3). Thereby the evolution of the bands assigned to different phases versus the variations in the technological parameters could be followed.

Thus, the histograms show not only the presence of definite phases, but also how the technological
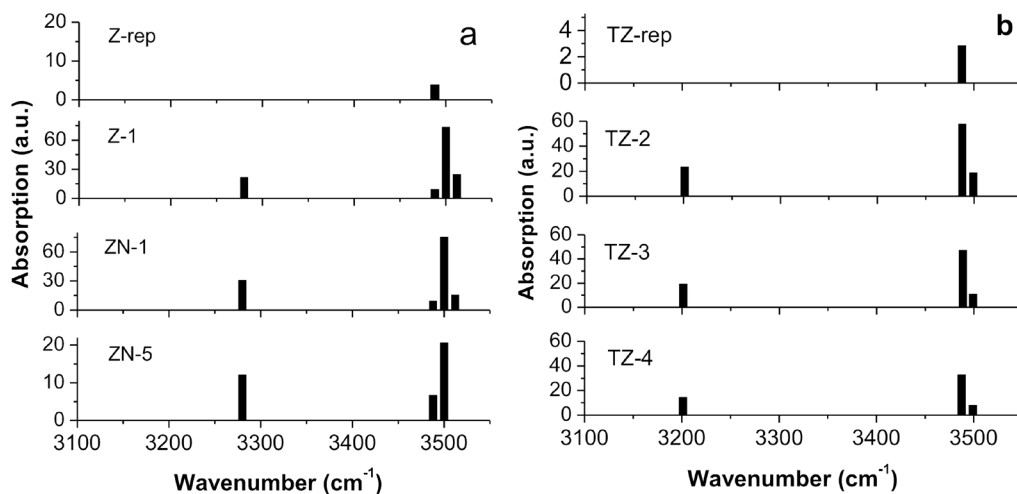
Fig. 3. Relative intensities of the IR-spectra components (after Gaussian decomposition) for PE layers in LiNbO$_3$ (a) and LiTaO$_3$ (b) obtained at different technological conditions [19]. Since the component due to the substrate α-phase was extracted from the spectra after the deconvolution, only the components of the layers' spectra are present in the histograms

condition chosen reflects on the thickness of sublayers formed by these phases. It was established this way that the contribution of the β_4-phase is stronger in samples with higher Δn_e, i.e. higher level of proton doping. The contribution of $\alpha/\kappa_1/\kappa_2$ is stronger in samples obtained at a condition including annealing or an annealing-like step. The contribution of β_1 is stronger for samples obtained by direct proton exchange. We have found that the integrated intensity of OH spectra of PE waveguides does not change during annealing procedures, i.e. no loss but only redistribution of hydrogen ions takes place.

The polarization study (Fig. 2) showed that in PE layers the narrow bands lie in the plane perpendicular to the optical axis (Z) while the OH-bonds corresponding to the wide band are distributed both in and out of this plane. As in the case of H:LiNbO$_3$, the main peak is connected with OH-bonds arranged in the oxygen planes ("in-plane" OH) and the shoulder – with OH bonds situated in the oxygen planes as well as out of them (hydrogen-bonded OH).

In order to shed some light on the proton distribution in our samples we have polished off the sample surface slightly and then, after each polishing step, we have measured the OH absorption. When a layer of $0.1 \div 0.2$ μm thickness was removed, the shoulder in the spectra also disappeared, the central peak remaining almost unchanged.

On the basis of investigations on the polarized spectra, the following conclusions could be made:

1. The absorption band centered at 3240 cm^{-1} is due to a very thin surface layer while the 3496 cm^{-1} band is connected with the proton-exchanged layer extended much deeper in the crystal. The broad absorption band at 3280 cm^{-1} results from a very thin surface layer (about 0.1–0.2 μm); the strong band (peak at 3496 cm^{-1}) is due to the protonated layer extending deeper.

2. The presence of the top film depends on the orientation of the sample, the X- and Y-cut plates being preferable.

3. The H concentration in the upper layer grows much more quickly in time, i.e. the $Li^+ - H^+$ substitution there is more complete.

4. The layers have different crystal symmetries. The OH groups at the surface are randomly oriented and are connected with a variety of short hydrogen bonds. The OH groups in the depth of the basic layer are localized in the plane perpendicular to the Z-axis and are connected with moderate H bonds.

5. After annealing, the intensity of the unpolarized shoulder decreases since protons penetrating deeply in the crystal from out-plane bonds form new in-plane ones.

6. The evolution of IR spectra at different annealing stages indicates phase transitions from highly protonated phases to the original crystal structure (α-phase).

7. Optical measurements and the study of IR absorption show that the H content in the waveguides is not influenced by the annealing procedures and the stoichiometry of the crystal, but only by the parameters of the exchange process.

8. It is difficult to observe any dependence on stoichiometry in the spectra of protonated LiNbO$_3$ or LiTaO$_3$ even if it really exists: the intensity of the band of PE crystals is about ten times higher than that of the virgin samples and slight variations in the spectra of untreated samples due to different stoichiometry cannot affect notably the final form of the spectra.

9. The intensities of the two bands depend on the PE process duration, demonstrating behavior usual for diffusion processes (Fig. 4). Proton concentration in the very surface layer increases much faster in time, i.e. there is a more complete replacement of Li ions by protons.
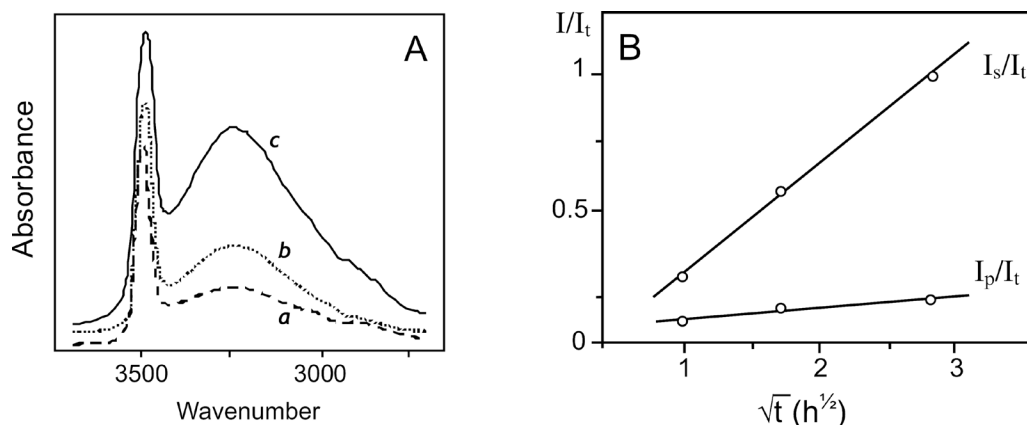
Fig. 4. A) OH absorption of X-cut LiTaO$_3$ (240 °C, pure benzoic acid) at PE duration of 1h (**a**), 3h (**b**) and 8h (**c**); **B)** Dependence of I_p/I_t and I_s/I_t on $\sqrt{t}$ for X-cut LiTaO$_3$ (240 °C, pure benzoic acid); I_p and I_s are the integrated intensities of the bands at 3496 cm^{-1} and at 3240 cm^{-1} respectively, $I_t = I_p + I_s$, t – exchange time.

10. The structures of the surface layer and that of the underlying protonated region are different. OH groups near the surface are chaotically oriented, indicating a great degree of disorder (amorphous state). The OH groups of the basic protonated layer are situated in the planes perpendicular to the optical axis. Lower frequency of the first kind of bonds implies higher mobility of their protons which could deteriorate the waveguide properties. So, the presence or the absence of a shoulder in IR spectra can serve as a criterion for the optical properties of waveguides fabricated by PE.

The PE waveguide stability in time can be followed by IR spectra and optical measurements. It was established that the behavior of integrated intensity in time is the same as this of Δn_e and IR spectra and can be used for studying the stability of waveguide parameters [21].

IR reflection spectra (Fig. 5) were recorded with the same spectrometer as for the absorption ones at angle of incidence 70° (measured from the normal to the surface). Since the penetration depth depends on the angle of incidence, at smaller angles (closer to the normal incidence) deeper penetration takes place and the spectra measurement is affected by the presence of the various phases forming the waveguiding layer. It was established [22] that at 70° the spectrum of the surface layer is separated from those of deeper situated layers in multiphase guides. This way, only the surface phase could contribute to the reflection spectra of multiphase waveguides. The IR reflection spectra contain new bands within the range 890–1010 cm⁻¹ and each phase has its own reflection spectrum [22, 23].

The IR reflection spectroscopy allows the surface phase of multiphase waveguides to be recognized. So, the information given by the analysis of the IR reflection spectra helps us to be much more specific when determining which phases build the waveguide layers investigated. According to [22], the presence

of β_i-phases significantly affects the spectra in the range of 800 – 1000 cm⁻¹ where new bands appear which are absent in the cases of virgin or α-phase PE LiNbO$_3$. The characteristic changes are at 975 cm⁻¹ for β_1-phase, at 980 cm⁻¹ for β_2 and β_3 and at 970 cm⁻¹ for β_4 [22]. Thus, looking at the spectra of Fig. 5a, we could conclude that β_1-phase is present on the top of the sample ZN-5 while β_4-phase forms the top of the waveguide layers of samples ZN-1 and Z-1, which are really strongly protonated. Also, it is seen that the spectrum of ZN-5 is closest to the shape of the spectrum of virgin sample (Z-rep), which suggests that the contribution of the α-phase is larger than in the case of the other two samples. This confirms the result of IR absorption spectra deconvolution, showing the same result (Fig. 3a). It could be seen that Z-1 and ZN-1 have almost the same spectra, confirming their equal phase content, as it could be seen also in Fig. 3a.

The main changes in the reflection spectra introduced by proton exchange in Z-cut LiTaO$_3$ occur in the range of 850–1050 cm⁻¹ (Fig. 5b). They were compared to the spectra of X-cut PE LiTaO$_3$ given in [23] and some correlations with lattice deformations and reflection minimums were made in order to assign the spectral changes to a definite phase. According to [23], the changes observed at 899, 952 and 985 cm⁻¹ in IR reflection spectra of all samples could be assigned to the β-phase, and the change at about 1000 cm⁻¹ to the δ-phase, correspondingly. Since the second perturbation is much stronger, we should conclude that the surface phase of the waveguides investigated is δ.

Micro-Raman and waveguide
Raman spectroscopy

Proton exchange influences both vibration modes in Ra spectra A1(TO) and E(LO) causing intensity reduction of some of the bulk lines, appearance
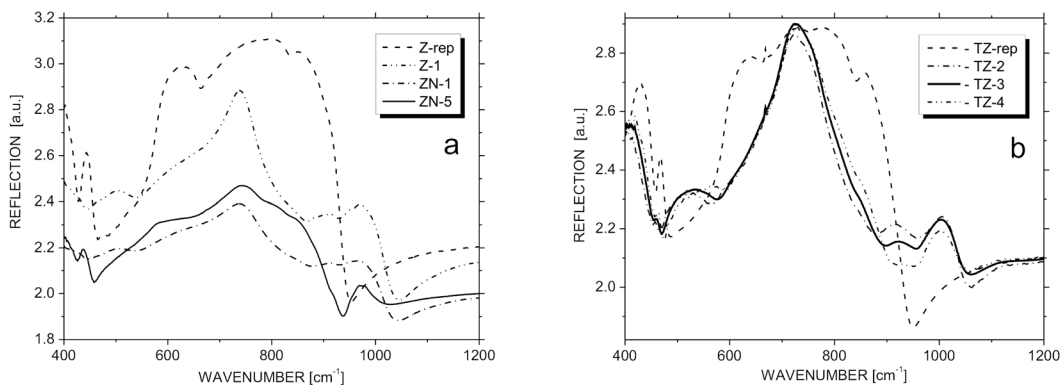
Fig. 5. Infrared reflection spectra for PE waveguides in H:LiNbO$_3$ (**a**) and H:LiTaO$_3$ (**b**) obtained under different technological conditions [19].

of new ones and appearance of lattice disorder-induced broad bands. A1(TO) type Ra spectra are more expressive.

In the Raman scattering geometries used, the phonon spectrum of pure $LiNbO_3$ consists of four A1(TO)-phonons (at 254, 275, 332 and 632 cm^{-1}), polarized along the Z-axis, and seven E(TO)-phonons (at 152, 236, 263, 332, 370, 431 and 578 cm^{-1}), polarized along the X- or Y-axis [24]. It could be seen in Fig. 6 that the main changes introduced by PE concern the intensity of the main spectral lines, the appearance of new ones and the spectra intensity attenuation compared to those of the surface. The strong attenuation occurs in samples with the maximal disorder degree [25]. The disorder in crystals causes violation of the selection rules which determine Raman scattering and can also activate new modes forbidden for the regular lattice. Moreover, as vibrations with $k{\neq}0$ of the material can take part into the light scattering, the Raman bands are broadened. On the other hand, the characteristic phonons of the pure crystal still exist in the spectrum, although they are considerably reduced in intensity.

According to [26], the most notable changes after PE are in band intensities in the 200–500 cm^{-1} region and, most importantly, the appearance of a broad band in the 520–750 cm^{-1} is observed, originating from a paraelectric-like phase, as well as the A1(TO)-peak at 690 cm^{-1} and the bulk spectra intensity attenuation. [27]. The new band present in all spectra of our PE layers could be due to second-order Raman scattering [28] which is a combined Ra scattering from coexisting ferroelectric (α) and paraelectric (β_i) $LiNbO_3$. That way the Ra spectra give some evidence for the presence of α-phase in the PE layer as the IR absorption spectra do (Fig. 3). The peak appearing

at 878 cm^{-1} comes from E(LO) mode, excited due to the strained lattice, and confirms the high level of H^+-doping. The set of narrow peaks in the Ra spectra also indicates high value of x and the presence of β_i-phases (i = 1–3) [29].

The new peak which appears at 690 cm^{-1} is attributed to highly protonated phases having almost paraelectric properties since it is characteristic for the paraelectric phase of $LiNbO_3$. Its relative intensity allows some estimation of the phase contribution to the PE layers to be made. For our samples we can see this peak even in E(TO) spectra. As it is known, in strained crystal some coupling between E(TO) and A1(TO) modes is possible. Thus we could consider the presence of such large band as an evidence for the existence of phases having highest value of x as β_4 for Z-cut samples, β_3 for X-cut or β_1 for Y-cut samples. For quantitative estimates it is important to obtain Raman scattering by guided modes in order to be sure that the optical power is confined completely into the waveguiding layer. If higher order modes are excited, part of the optical field penetrates more or less into the unprotonated substrate and this should be taken into account.

Raman scattering has also been used to determine the kinetics of phase transitions in proton-exchanged LN waveguide layers subjected to thermal treatment [30]. Results of fundamental importance have been obtained for intermediate phase states including the β_i- and ($\alpha+\beta_i$)-phases, as well as room-temperature equilibrium and quenched states in the high H^+ concentration phase. The presence and absence of some Raman lines at 127, 194 and 214 cm^{-1} and the intensity dependence of a proton-induced phonon band at 69 cm^{-1} have enabled the degree of Li-H substitution in PE layers to be determined, the results indicating that at least for z-cut H:LN waveguides, the phase diagram presented for proton-exchanged powders may also be applicable.

Besides waveguide Raman spectroscopy, micro-Raman spectra were also registered allowing some comparative and semi-quantitative estimations of the thickness of phase sub-layers to be made. The micro-Raman spectra were collected by triple Jobin Yvon T64000 spectrometer. Depth profiling of the proton-exchanged layer by Ra spectra was performed by moving the focused laser beam from the substrate to the surface of the layer at approximately 0.5 micrometer steps. An example is shown in Fig. 7.

An exemplary analysis of the spectra shown in Fig. 7 demonstrates that:

Since the spectrum of C1 contains the peaks characteristic for bulk $LiNbO_3$ in positions as well as in relative intensities, the α-phase has a strong contribution to the layer composition. The intensity increase of the band centered at 632 cm^{-1} could be

Fig. 6. Raman spectra of bulk $LiNbO_3$ in ferroelectric state at room temperature (**a**); H:$LiNbO_3$ waveguide (**b**) and bulk $LiNbO_3$ in paraelectric phase at 1130 °C (**c**); laser line at 647.1 nm, A1(TO) geometry
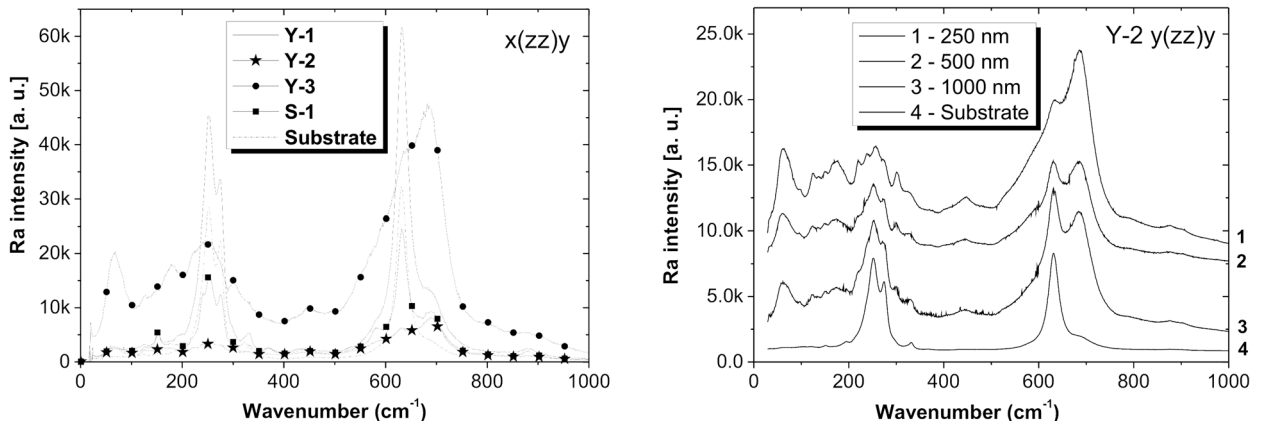
Fig. 7. Raman spectra of proton-exchanged Y-cut LiNbO₃ layers and micro-Raman depth profiling [21]

due to the presence of α and κ_i-phases. The peak at 70 cm⁻¹ is present only in PE LN and usually is used as an indicator for Li-H exchange [27]. The new peak which appears at 690 cm⁻¹ is assigned to highly protonated phases having almost paraelectric properties (β_i phases, i = 1–3). It suggests strong distortion of the niobium octahedra towards non-polar states. The broad band at 690 cm⁻¹ is characteristic for the paraelectric phase of LiNbO₃ [29]. Since the relative intensity of this band is not high, it could be concluded that the paraelectric layer is thin and is present at the top of the waveguiding layer, which is also confirmed by the optical profile shape. The peak appearing at 878 cm⁻¹ comes from E(LO) mode, excited due to the strained lattice, and also confirms the high level of H⁺ doping. It could be assigned to the β_4-phase, since it is well defined only for samples C1 and S1 whose index change indicates the presence of that phase, leading to strong strains in the lattice.

The band centered at 690 cm⁻¹ is the highest and largest band in the spectra of C2. This fact, together with the disappearance of the bands at 245 cm⁻¹ and 275 cm⁻¹, show that mainly phases having a high level of proton doping are present in the layer, i.e. β_i phases. In that case i = 1, since only the β_1 phase could be obtained by direct PE [9].

The set of narrow peaks in the Ra spectrum of C3 and the new one which appears at 70 cm⁻¹ also indicate high value of x and the presence of β_i phases (i=1–3) [29]. A broad band in the range of 520–780 cm⁻¹ is observed, originating from a paraelectric-like phase, as well as the A1(TO) peak at 690 cm⁻¹ and the bulk spectra intensity attenuation. Since C2 and C3 are obtained by direct proton exchange, the layer should consist of β_1 phase but close to its higher concentration value of x = 0.6. That way the peak which appears at 690 cm⁻¹ is attributed to the β_1 phase.

The spectrum of S1 confirms the presence of β_4 on the top (peaks at 878 cm⁻¹ and 578 cm⁻¹ come from E(LO) modes, excited because of strong lattice perturbation introduced by PE). The spectra of C1 and S1 are quite similar, so we could conclude that S1 contains also some of the β_i phases, i = 1–3, κ_i phases (i = 1–2) and α phase.

The most convenient way to determine the exchange ratio x/1–x in protonated layers is to decompose suitable parts of the Raman spectrum into ferroelectric and paraelctric components. In the case of the spectrum in Fig. 7 we have used the ferroelectric components 151 and 234 cm⁻¹ and their paraelectric counterparts – the broad bands at about 136 and 214 cm⁻¹ respectively. The ratio of their integrated intensities I(136)/I(151)=I(214)/I(234) should be equal to x/1–x.

The depth profiling of Y-2 (Fig.7) shows some intensity transfer between A1(TO) mode at 690 cm⁻¹ and E(TO) mode at 630 cm⁻¹, which are excited in the same geometry because of the crystal lattice perturbation introduced by PE. The changes of E(TO) Ra spectra originate from the internal strains in the sample as a result of order-disorder distribution of protons, whereas the changes of A1(TO) Ra spectra are due to the displacement of the positive and negative ions [29]. Thus, in strongly protonated samples, the E(TO) intensities should be stronger and at the same time the A1(TO) intensities should be weaker. Since the intensity of the 690 cm⁻¹ band (A1) increases toward the substrate and that at 630 cm⁻¹ (E) decreases, we could conclude that the layer contains sub-layers, having different value of x (decreasing towards the substrate), i.e. presenting different phases in addition to α- and β_1-phase, which was commented above. They should be k_1/k_2 phases which are also indistinguishable spectroscopically.

X-RAY PHOTOELECTRON
SPECTROSCOPY (XPS)

X-ray photoelectron spectroscopy (XPS) is ideally suited to the determination of the surface chemistry and the way in which that chemistry changes in the surface and near-surface region. The technique provides quantitative elemental and chemical information with extremely high surface sensitivity and is ideal for comprehensively characterizing the elemental composition and chemical bonding states at surfaces and interfaces. It was shown how X-ray photoelectron spectroscopy (XPS) can be used for compositional analysis of the several uppermost atomic layers of the wafer apart from the waveguide/air interface in the case of proton-exchanged waveguides in lithium niobate [31, 32].

The XPS analysis of the samples was carried out with an ESCALAB Mk II (VG Scientific) electron spectrometer. The C1s, O1s, Nb3d and Li1s photoelectron peaks were recorded. A comparative analysis has been performed between virgin sample and layers obtained by PE in melts of pure benzoic acid and of benzoic acid buffered by 1% and 2% lithium benzoate. The goal was to clarify the dependence of crystal composition, Li1s, O1s and Nb3d spectra shape, binding energies (BE) and full width at half maximum (FWHM) in the near surface region (between 0 and 10 nm) on depth and on buffering of the benzoic acid melt with lithium benzoate. Using C1s as a reference at the surface, we determine the O1s position at 530.3 eV. In our investigation of the depth profile we use this binding energy as the reference since it is stable due to the fact that oxygen is a basic part of the $LiNbO_3$ lattice. The intensities were determined as the integrated peak

areas assuming that the background is linear. The element concentrations were calculated by the SSI (surface science instruments) approach according to which the transmission function of the analyzer is taken into account [33]. To avoid formation of a crater, the ion beam was defocused. A sputtering rate of 1 nm/min is established.

The most informative XPS spectra are those of LiO1s, and O1s which allow following of the binding energy change in the depth from the very surface to 500 nm of the exchanged layers versus the sputtering time (Fig. 8). The concentration of Li at the crystal surface could be estimated from XPS records and a correlation between x and Δn_e could be established when the optical profile is built up. It is seen that the Li content decreases and the Nb content increases with depth from the surface (d = 0 nm, t = 0 min.) to the first few atomic layers, lying close to the surface (d = 1–2 nm), i.e. in a nearly two-dimensional region at the surface of the $LiNbO_3$ crystal. Enrichment of Nb with depth along with reduction of Li corresponds to reduction of the molar ratio of Li_2O to Nb_2O_5. The composition remains nearly unchanged between 2 and 10 nm depth in the protonated layer.

The binding energy values are found to be almost equal when unbuffered benzoic acid melt is used instead of buffered melt (Fig. 9). It can be seen that the Li1s BE is lower at d=1–10 nm than at d=0 nm for unbuffered (0%) as well as for 1% and 2% buffered benzoic acid. For the virgin crystal, in contrast, BE increases at d = 1 nm (compared to d = 0 nm) and remains almost the same at 5 and 10 nm. The higher BE value obtained for 1% [34] than for 2% and 0% buffered melt at 1 nm depth is probably due to
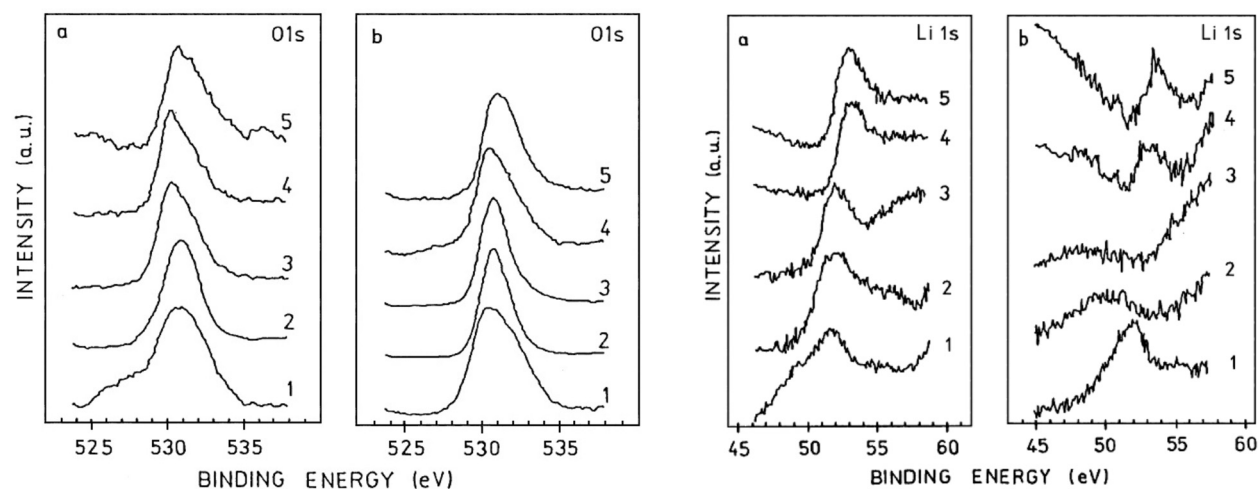
Fig. 8. The XPS spectra of a virgin (**a**) and PE (**b**) $LiNbO_3$ sample after sputtering to the following depths: 1) 0 nm (surface); 2) 10 nm; 3) 100 nm: 4) 200 nm; 5) 500 nm [34].
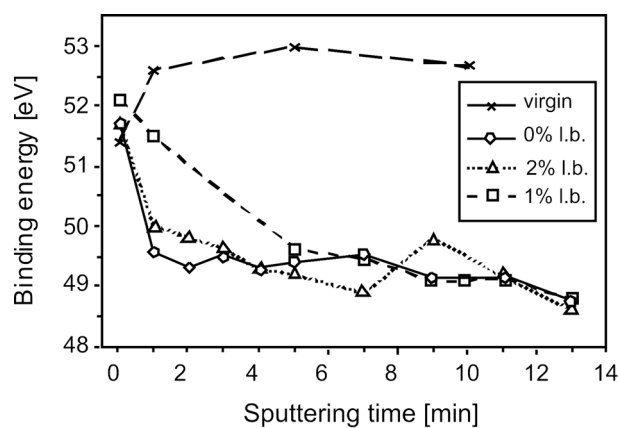
Fig. 9. Li1s binding energy of LiNbO$_3$ versus depth (sputtering time) for unbuffered and for lithium benzoate (l.b.) buffered melts of benzoic acid, as well as for virgin LiNbO$_3$

the fact that another LiNbO$_3$ crystal with different stoichiometry was investigated in [34]. The XPS spectra show that besides the main BE peaks lying between 49 and 53 eV for both treated and untreated samples, a weak peak appears at 54.8 eV for the sample protonated in buffered melt. This peak occurs only at $d \leq 3$ nm and disappears at higher depths. Its BE value is close to the values obtained by Kaufherr et al. [35] where a non-destructive method was used. In comparison to the Li1s, the BE depth dependence for O1s is much less pronounced, especially when PE is performed in an unbuffered melt (Fig. 10). It may be explained with lower BE sensitivity to the changes in the surrounding due to the screening of the oxygen 1s electron from its 2s and 2p electrons. Regarding the change of the band's full width at half maximum (FWHM) with depth, it must be noted that the most evident decrease in comparison to $d = 0$ nm appears at $d=1$ nm in the case of treatment with an unbuffered melt. In that case, some asymmetry of the peak at $d=1$ nm is also
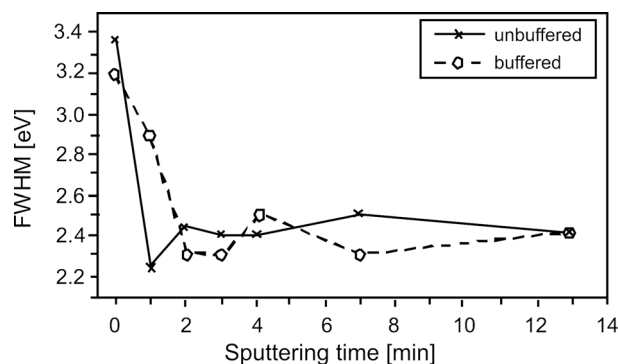
Fig. 10. Narrowing of the O1s band of LiNbO$_3$ protonated in unbuffered benzoic acid melt

seen when normalized XPS spectra are compared. The FWHM changes described are probably due to superimposing of energetically close O1s bands with different halfwidth and relative intensities. Such bands might correspond to weakly differing positions of the OH groups formed depending on depth and degree of protonation. Here it is worth mentioning that LiNbO$_3$ has two O1s peaks with different relative intensities for the crystalline and amorphous state of the material as was already reported in Kaufherr et al. [35]. The experimental data for Nb XPS show that the peaks of the Nb^{5+} doublet 3d$_{3/2}$ and 3d$_{5/2}$ at 207 and 210 eV respectively, are better resolved for $d = 0$ nm than for the atomic layers in depth $d = 1$nm. This is also valid for the virgin LiNbO$_3$ [34], and could be related to a specific structure of the matrix surface layers which we supposed above to be responsible for the lower degree of protonation, i.e. the Li enrichment on the surface. Another explanation may be offered with the assumption that the surface structure is destroyed due to the sputtering and this is the reason for poorer peak resolution. Benzoic acid buffering has some influence on the BE values for the 207 and 210 eV peaks at depths of 1 nm which may be caused by differences in position and orientation of the OH groups toward the Nb atoms, depending on the degree of protonation. The intensity redistribution for the 207 and 210 eV peaks and the appearance of a new peak at 205 eV with increased sputtering time may be understood considering the results obtained in Courts et al. [36] on the reduction of Nb^{5+} to Nb^{4+} and Nb^{3+}, when electron-beam heating of LiNbO$_3$ takes place. Before sputtering, the 205 eV peak is not observed because only Nb^{5+} is present in our sample. The sputtering procedure of 1–2 min leads to the creation of some Nb^{4+} and to superimposing of the low energy peak of the Nb^{4+} doublet (i.e. Nb^{4+} 3d$_{5/2}$) at 205 eV. The higher energy peak Nb^{4+} 3d$_{3/2}$ lies close to the 207 eV peak of Nb^{5+} 3d$_{3/2}$ and is therefore not seen. Further accumulation of Nb^{4+} on the crystal boundary takes place with increasing sputtering time and results at $t>4$–5 min in strong domination of the Nb^{4+} 3d peaks at 205 and 207 eV. So, the Nb^{5+} 3d$_{3/2}$ peak at 210 eV disappears and Nb^{5+} 3d$_{5/2}$ at 207 eV is replaced by the Nb^{4+} 3d$_{3/2}$ peak with almost the same BE. It has been established that the rate of intensity redistribution (increase for the 205 eV peak and decrease for the 210 eV peak) is higher in the case of the sample treatment with unbuffered benzoic acid melt. Probably NbO$_2$ or another Nb^{4+} cluster compound with direct Nb-Nb bonding is formed on the surface due to the sputtering:

$$\begin{array}{ccc} \text{-Nb} & & \text{-Nb} \\ & \diagdown & \quad | \\ & \text{O} \Rightarrow & \quad \oplus \text{O} \\ & \diagup & \quad | \\ \text{-Nb} & & \text{-Nb} \end{array}$$
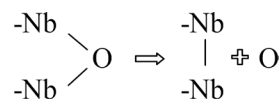
In summary, the study of proton exchanged (PE) $LiNbO_3$ performed using XPS after gradual removing of the surface atomic layers by Ar ion bombardment in depth (d) between 0 and 10 nm shows that:

– Noticeable differences regarding Li_2O and Nb_2O_5 molar ratio, Li1s binding energy values, O1s band width and Nb3d spectra shape are manifested at a depth of d = 1 nm as compared to d = 0 nm. Upon moving from d = 0 nm to d ≥ 1 nm, a decrease of Li content and Li1s BE lowering within 2 eV is revealed in the protonated sample, while for the virgin crystal Li1s BE increases with about 1 eV.

– In the depth range from 1 to 10 nm, only weak changes in Li and Nb content and in Li1s BE take place compared to d = 0-1 nm.

– These results allow us to conclude that a very thin layer on the $LiNbO_3$ crystal surface (about 3–4 atomic layers for X-cut samples) differs in structure and/or composition from the layers located deeper in the bulk. This layer has, as it is observed, a lower degree of H^+ for Li^+ substitution, i.e. a relative Li enrichment on the surface after the PE procedure.

– For PE being performed with unbuffered and buffered (containing 2% Li-benzoate) melts of benzoic acid, closely similar values of Li1s BE are obtained. This result shows that the Li content in the melt does not considerably affect the Li enrichment of the surface. Some influence of benzoic acid buffering is found for the O1s band width at d = 1 nm and for the BE of the Nb3d doublet which may be related to changes in position and orientation of the OH groups formed by the PE process.

CONCLUSIONS

Combined analysis based on mode, IR absorption/reflection, Ra spectroscopy and XPS was performed which allows identification of phases, of the phase in-depth distribution, and of the relative contribution of each of them to the composition of the waveguide layer of multiphase proton-exchanged waveguides in lithium niobate and lithium tantalate.

The main results include:

– establishment of the effect of crystal stoichiometry on the parameters and vibration spectra of PE waveguides in $LiNbO_3$ and $LiTaO_3$;

– improvement of the methods for investigation of phase composition of PE waveguides in lithium niobate and lithium tantalate by combination of several spectroscopic techniques (mode, Raman, infrared (absorption and reflection) spectroscopy, as well as XPS); application of this combined approach for characterization of the waveguide layers;

– following of the phase formation after proton exchange, phase evolution in time (short-term and long-term) and phase transformations after thermal treatment (annealing);

– collection of information about the positions and concentration of the diffusant (H^+).

The methods used could contribute to the improvement of the PE technology towards a strict control of the phase composition, i.e. of the waveguide characteristics and quality.

The results lead to the accumulation of new knowledge on material science regarding the properties of modified waveguiding layers on substrates of ferroelectric crystals.

REFERENCES

1. J. L. Jackel, C. E. Rice, *Appl. Phys. Lett.*, **41**, 607 (1982).
2. W. B. Spillman, N. A. Sanford, R. A. Soref, *Opt. Lett.*, **8**, 497 (1983).
3. Yu. N.Korkishko, V. A. Fedorov, in: Proc. SPIE, 2700**,** 1996, 186.
4. Yu. N. Korkishko, V. A. Fedorov, *IEEE J. Select. Top. Quant. El*. 1 (1996).
5. K. El. Hadi, P. Baldi, S. Nouh, M. P. De MicheliI, A. Leycuras, V. A. Fedorov, Yu. N. Korkishko, *Opt. Lett.*, **20**, 1698 (1995).
6. R. Ulrich, *J. Opt. Soc. Am.*, **60**, 1337 (1970).
7. J. M. White, P. E. Heidrich, *Appl. Opt.*, **15,** 151 (1976)
8. Yu .N. Korkishko, V. A. Fedorov, V. V. Nosikov, S. M. Kostritskii, M. P. De Micheli, in: Proc. SPIE, 2997, 1997, 188.
9. Yu. N. Korkishko, V. Fedorov, M. De Micheli, in: Proceedings of ECIO'97, April 2–4, Stokholm, 1997, 56.
10. M. K. Kuneva, S. Tonchev, M. Sendova-Vasileva, D. Dimova-Malinovska, P. Atanasov, *Sensors and Actuators A*, 99 (2002).
11. M. K. Kuneva, S. Tonchev, M. Pashtrapanska, I. Nedkov, *Materials Science in Semiconductor Processing*, **3**, 581 (2001).
12. C. E. Rice, *J. Sol. St. Chem.*, **64**, 188 (1986).
13. L. Kovacs, V. Szalary, R. Caprlletti, *Solid State Communications*, **52**, 1029 (1984).
14. K. K. Wong, A. C. G. Nutt, D. F. Clark, P. J. R. Layborn, R. M. De La Rue, in: IEE Proc. Part I 133, 1986, 113.
15. I. T. Savatinova, S. Tonchev, E. Popov, E. Liarokapis, C. Raptis, *J. Phys. D: Appl. Phys.*, **25**, 106 (1992.)
16. J. R. Herrington, B. Dischker, A. Rauber, J. Schneider, *Solid State Communications*, **12**, 351 (1973).
17. M. K. Kuneva, S. Tonchev, E. Thatsi, D. Lampakis, *JOAM*, **7**, 549 (2005).
18. M. K. Kuneva, S. Tonchev, P. Dimitrova, *J. Mater. Sci.: Materials in Electronics*, **14**, 859 (2003).
19. M. K. Kuneva, S. Tonchev, P. Atanasov, *Mat. Sci. Eng. B*, **118**, 301 (2005).
20. J. Rams, M. Cabrera, *J. Opt. Soc. Am. B*, **16**, 401 (1999).

21. M. Kuneva, S. Tonchev, B. Bozhkov, *JOAM*, **11**, 1529 (2009).
22. Yu. N. Korkishko, V. A. Fedorov, S. M. Kostritskii, *J. Appl. Phys.*, **84**, 2411 (1998).
23. S. M. Kostritskii, Yu. N. Korkishko, V.A. Fedorov, D. B. Maring, R. F. Tavlykaev, R. V. Ramaswamy, *J. Appl. Phys.*, **91**, 930 (2002).
24. X. Yang, G. Lan, B. Li, H. Wang, *phys. stat. sol. (b)*, **141**, 287 (1987).
25. X. Wu, M.-S. Zhang, D. Feng, *Appl. Phys. Lett.*, **65**, 2916 (1994).
26. G. R. Paz-Pujalt, D. D. Tuschel, *Appl. Phys. Lett.*, **62**, 3411 (1993).
27. Yu. Voron'ko, A. Kudryavtsev, V. Osiko, A. Sobo, E. Sorokin, *Sov. Phys. Solid State*, **29**, 771 (1987).
28. R. Claus, G. Borstel, E. Wiesendanger, L. Stefan, *Z. Naturf.*, **27a**, 1187 (1972).
29. X.-L. Wu, M.-S. Zhang, D. Feng, *phys. stat. sol.* (a), **153**, 233 (1996).
30. I. Savatinova, S. Tonchev, M. Kuneva, E. Liarokapis, *Appl. Phys. A*, **58**, 481 (1994).
31. M. K. Kuneva, V. Krastev, *J. Mater. Sci.: Materials in Electronic*, **11**, 629 (2000).
32. M. K. Kuneva, V. Krastev, *Cryst. Res. & Technol.*, **30**, K61 (1995).
33. L. T. Weng, *Surf. Interface Anal.*, **20**, 179 (1993).
34. M. Kuneva, V. Krastev, *Appl. Phys. A*, **63**, 391 (1996).
35. N. Kaufherr, D. J. Eichorst, D. A. Payne, *J. Vac. Sci. Technol. A*, **14**, 299 (1996).
36. R. Courths, P. Steiner, H. Höchst, S. Hüfner, *Appl. Phys.*, **21**, 345 (1980).

СПЕКТРОСКОПИЯ НА СЛОЕВЕ ОПТИЧНИ ВЪЛНОВОДИ

М. Кънева, С. Тончев

Институт по физика на твърдото тяло „Акад. Г. Наджаков",
бул. Цариградско шосе 72, 1784 София

(Резюме)

Авторите споделят своя 20-годишен опит за спектроскопията на протонно-обменени вълноводни от $LiNbO_3$ и $LiTaO_3$. Методите включват инфрачервена спектроскопия на абсорбция и отражение, микро-Раман и Раман спектроскопия и рентгенова фотоелектронна спектроскопия (XPS).

Информацията (структурна, фазова и химичен състав) получена от всеки от тези методи помага за създаване на по-пълно описание на структурата и свойствата на тези слоеве. Интерпретацията на резултатите набляга на фазите и химичния състав на вълноводите, получена при различни технологични условия. Такъв „комбиниран" анализ допринася за регулиране на производството условията за получаване на определени състави и фази, технологично необходими за вълноводни устройства с подобрена стабилност и характеристики.

Amorphization and solid solution formation in Sn modified Cu-Ag alloys produced by mall milling

L. Lyubenova, T. Spassov*, M. Spassova

Faculty of Chemistry, University of Sofia "St.Kl.Ohridski", 1 James Bourchier str.
1164 Sofia, Bulgaria

The present work aims at studying the influence of Sn on the microstructure of Cu-Ag-based supersaturated solid solutions with potential application for fabrication of nanoporous structures. Nanocrystalline $Cu_{50}Ag_{50-x}Sn_x$ (x=3, 6, 10) fcc solid solutions are synthesized by high-energy ball milling under protective Ar atmosphere and liquid heptane as antisticking agent. Milling for 8h leads to formation of solid solution with fine nanocrystalline microstructure (<10–15 nm) in $Cu_{50}Ag_{40}Sn_{10}$. On the contrary, for the ternary systems with lower Sn concentration (x=3 and 6) only 5h of milling are necessary for complete alloying. Partial amorphization is also detected for all Sn containing alloys. The lattice constant of the fcc solid solution in the ternary systems is larger than that of $Cu_{50}Ag_{50}$, but slightly depends on the Sn concentration in the composition range of 3–10 at.% Sn.

Keywords: Cu-Ag alloys, solid solution, nanocrystalline, ball milling.

INTRODUCTION

Cu–Ag alloys are considered to be attractive for fabrication of nanoporous Ag structures for practical applications [1, 2]. A controlled thickness nanoporous Ag with desired pore and ligament size could be obtained easily after selective electrochemical dissolution of well-mixed and homogenized Cu–Ag solid solutions with proper composition.

Although Cu and Ag satisfy two of the Hume-Rothery rules for common solid-state solubility, equilibrium solid solutions in the Cu–Ag system are practically non-existing and the size factor is apparently not enough to contribute for easy amorphization in this system. However, formation of non-equilibrium supersaturated fcc Cu–Ag solid solutions by applying a variety of preparation methods has been reported: rapid quenching from a melt [3], splat quenching [3, 4] vapor deposition [5], mechanical alloying [1, 6, 7], cold rolling [8]. The microstructure of the Cu–Ag solid solutions with different composition prepared by these methods is most often nanocrystalline or composite, consisting of a mixture of nanocrystalline solid solution and amorphous phases [3, 8, 9]. Formation of entirely amorphous Cu–Ag alloys exclusively by a vapor deposition technique has been reported only in a few papers [10, 11]. Repeatedly cold-rolled Cu–Ag alloys reveal also some local amorphous regions [8]. Mechanical alloying followed by annealing at 200ºC was reported also to result in an amorphous phase formation [9]. Mechanical alloying of Ag-Cu-Sn powders, containing 10–20 wt.% Sn, caused a drastic decrease of their grain sizes. The formation of compounds like Ag_3Sn, Cu_6Sn_5 and $Cu_{10}Sn_3$ occurs after 1 hour of milling, but no amorphization up to 8 hours of milling was reported [12]. Nanocrystalline Ag_3Sn phase (~ 20 nm) was formed by ball milling for 1–2 h of Sn rich Sn-Cu-Ag alloys [13].

The present study aims at investigating the effect of Sn on the amorphization and formation of Cu-Ag-based solid solutions by mechanical alloying. The morphology and microstructure of the prepared solid solutions were also characterized. Due to the improved glass-forming ability of the ternary alloy containing Sn in comparison to the binary Cu-Ag, and the suitability of Sn for preparing nanoporous Ag by selective electrochemical dissolution of Cu-Ag-Sn, in the present study its concentration was varied in the range of 3–10 at.% (3, 6 and 10 at.% Sn).

---

* To whom all correspondence should be sent:
E-mail: tspassov@chem.uni-sofia.bg

EXPERIMENTAL PART

$Cu_{50}Ag_{50-x}Sn_x$ (x=3, 6 and 10) alloys were produced by milling Ag (99.99%), Cu (99.9%) and Sn (99.9%) using a planetary ball mill (Fritsch P6) with rotation velocity of 400 rpm, hardened Cr-steel vials and ball-to powder mass ratio of 9:1. Protective Ar atmosphere and liquid n-heptane were applied for the milling process. The regime of milling was: 30 min of continuous milling and 10 min relaxation time. The milling time was varied with the goal to produce powders with different morphology and microstructure.

The microstructure and morphology of the alloys were investigated by x-ray diffraction using Bruker D8 Advance diffractometer with Cu-Kα radiation and Scanning electron microscopy (SEM, JEOL-5510). Thermal stability of the ball-milled samples was analyzed with a Perkin-Elmer DTA.

RESULT AND DISCUSSION

Electron microscopy analysis (Fig. 1) of the ball-milled powders showed similar particle size for all investigated materials. The average particle size of the alloy with lowest Sn content (~ 10 μm) is only slightly larger than that of the Sn richer compositions (about 7.0 μm) milled for the same time of 10 h. Extending the milling time up to 20 hours results in additional particle decrease: 6 μm for $Cu_{50}Ag_{40}Sn_{10}$. Similar particle size distribution was observed for all compositions.

X-ray diffraction of the two hours milled $Cu_{50}Ag_{40}Sn_{10}$ and $Cu_{50}Ag_{44}Sn_6$ (Fig. 2a) revealed the formation of Ag_3Sn and Cu_4Sn_5 phases, which were not observed at longer than 8 hours of milling. For $Cu_{50}Ag_{47}Sn_3$ formation of these phases was not detected by any duration of milling. Milling for a longer time shows obvious development of the phase composition and microstructure in the systems studied. After 8 hours of milling (Fig. 2 c,d) only the

solid solution formation was observed. In general, the diffraction peaks become slightly sharper (narrower), meaning that a process of nanograin growth takes place during the milling, Fig. 2. The position of the maximum of the main diffraction peak also does not change with milling time, revealing that the terminal solid solutions are already formed at 8 h of milling. It is seen that solid solution formation is faster for the alloy with 3 at.% Sn, i.e. this composition is close to the optimal for $Cu_{50}Ag_{50-x}Sn_x$ with respect to the solid solution formation ability. Furthermore, milling for 8 hours leads also to formation of amorphous phase in $Cu_{50}Ag_{40}Sn_{10}$, proved by DTA analyses of an as-milled alloy. Diffraction peaks of pure Cu and Ag at the longer milling times (> 8 h) were not detected, indicating a process of complete alloying.

The lattice parameters for the formed solid solutions are comparable with the data from our previous investigations on the Cu-Ag binary system (Fig. 3), [8]. It should be noted that unlike the binary Cu-Ag, the longer time of mechanical alloying does not lead to significant changes in the lattice parameter, **a**, of the three-component solid solutions, studied in this work. Generally, the increase of the Sn content in the alloy results in lattice parameter, **a**, enlargement, but for milling durations t≥12 h the alloys with 3 and 6 at.% Sn reveal almost the same **a**.

The three $Cu_{50}Ag_{50-x}Sn_x$ alloys studied show rather different development of the average grain size of the metastable fcc solid solutions with milling time. Whereas for $Cu_{50}Ag_{50-x}Sn_x$ (x=3 and 6) the grain size is more or less constant (4–5 nm) in the range of 5–15 h milling, for $Cu_{50}Ag_{40}Sn_{10}$ it initially decreases with milling time, reaching a value of 6 nm after 12 h of milling, Fig. 4, and then increases again to about 9 nm at t=15 h. The increase of the grain size at longer milling durations can be associated with a nanograin growth process.

DTA analysis reveals broad overlapped exothermic peaks starting at about 100 °C for the ball milled
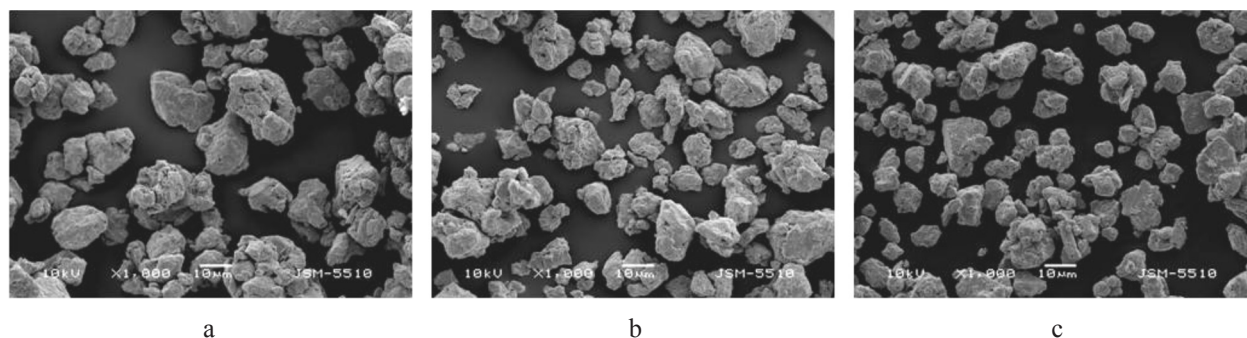
Fig. 1. SEM micrographs of: $Cu_{50}Ag_{47}Sn_3$ (**a**), $Cu_{50}Ag_{44}Sn_6$ (**b**) and $Cu_{50}Ag_{40}Sn_{10}$ (**c**) alloy powders ball-milled for 10 h

alloys, associated with the solid solution decomposition to terminal elemental Ag and Cu, as shown in our previous study [1]. XRD analysis of milled for 20 h and then annealed at 400 °C CuAgSn confirms the alloy decomposition, Fig. 2d (inset). As mentioned earlier [1] ball milled Cu-Ag-based solid solutions show somehow different thermal behavior compared to the cold-rolled and rapidly quenched Cu-Ag alloys

[8], expressed in the presence of exothermic peaks at lower temperatures, which could be associated with relaxation of microstresses created by milling. The thermal behavior of the ball milled Cu-Ag-Sn is different compared to the binary alloys. Generally, the major thermal peaks are shifted to higher temperatures (250–400 °C), implying higher thermal stability of the ternary solid solutions.
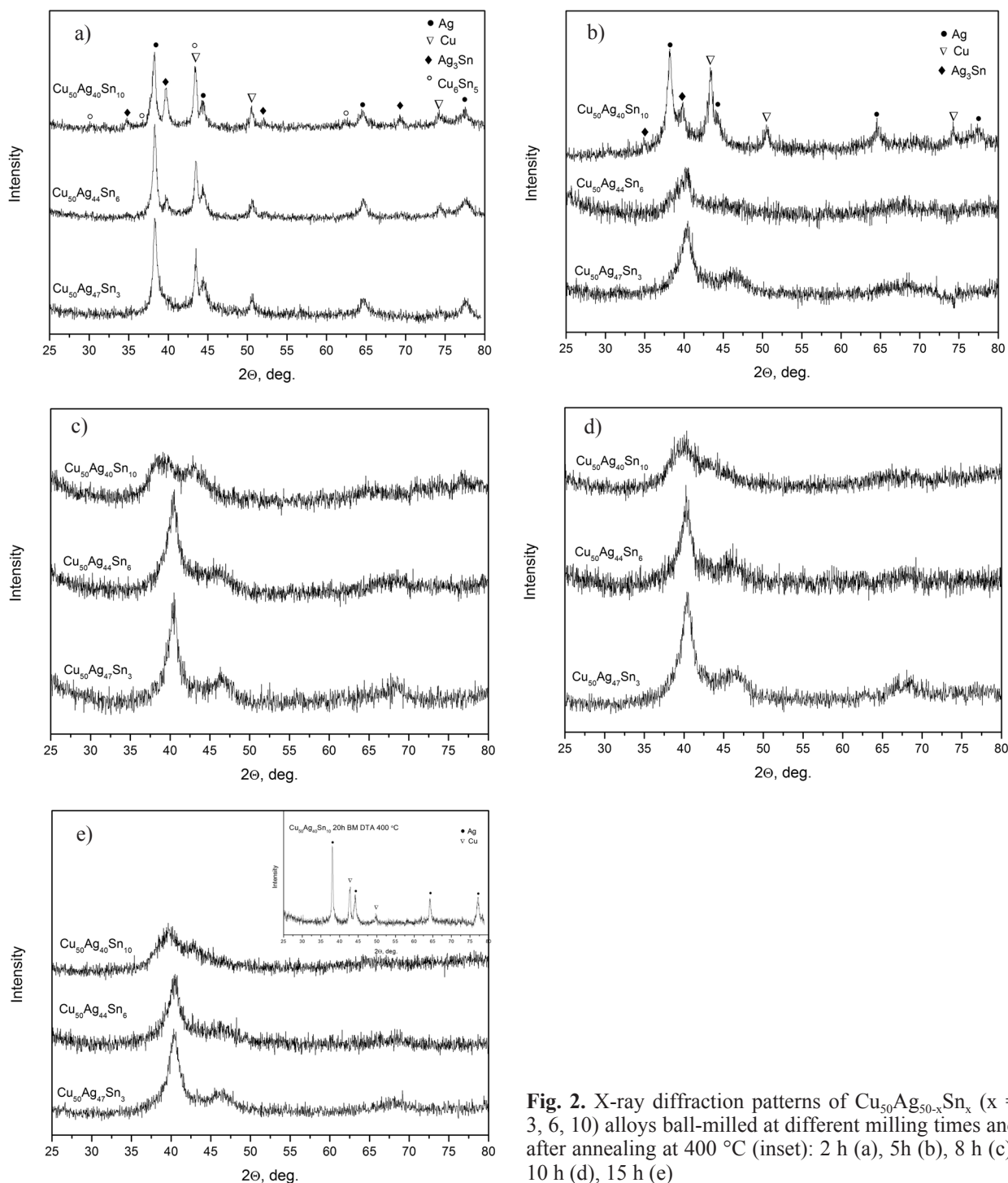
Fig. 2. X-ray diffraction patterns of $Cu_{50}Ag_{50-x}Sn_x$ (x = 3, 6, 10) alloys ball-milled at different milling times and after annealing at 400 °C (inset): 2 h (a), 5h (b), 8 h (c), 10 h (d), 15 h (e)
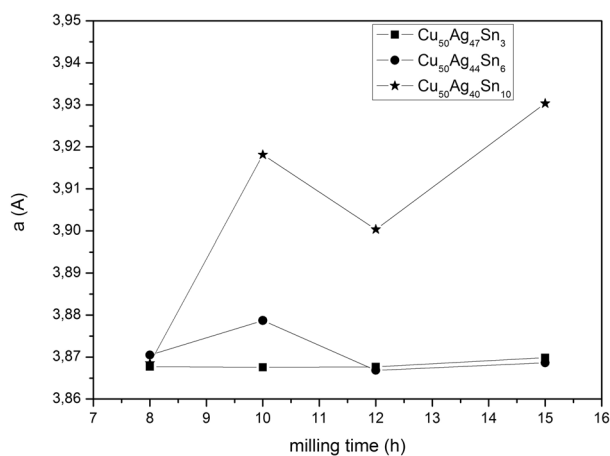
Fig. 3. Lattice parameters, **a**, for the alloys studied at various milling times
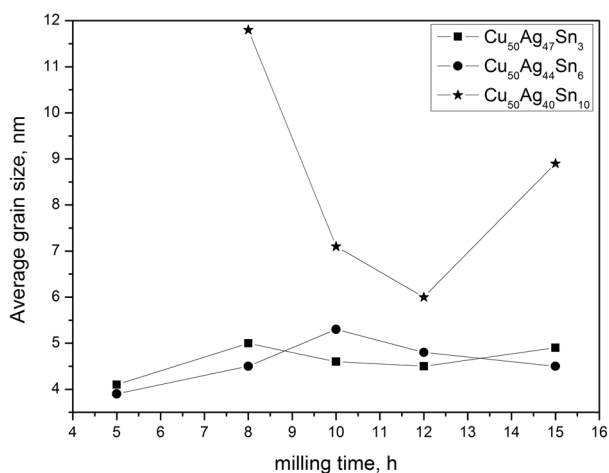
Fig. 4. Average grain size for the alloys studied as a function of milling time

In summary, the present study reveals an improved ability for metastable solid solution formation by ball milling of ternary Cu-Ag-Sn, compared to binary Cu-Ag alloys. The microstructure of the tin containing Cu-Ag fcc solid solutions is fine nanocrystalline (5-10 nm) with a presence of some amorphous phase and as a whole its thermal stability is higher than that of binary Cu-Ag alloys. It is expected that solid solutions with this microstructure would be attractive for preparing nanoporous Ag structures by selective electrochemical dissolution.

CONCLUSIONS

Supersaturated $Cu_{50}Ag_{50-x}Sn_x$ (x=3, 6, 10) solid solutions were prepared by mechanical alloying for different milling times. For $Cu_{50}Ag_{40}Sn_{10}$ 8h of milling were enough to form homogeneous Cu-Ag-based fcc solid solutions, whereas for the ternary systems with lower Sn content even 5h were sufficient for complete alloying. The microstructure of the fcc solid solutions is fine nanocrystalline (< 10 nm) for the ternary system, as ball-milling results also in a better pronounced amorphous phase formation. The lattice constant of the fcc solid solution in the ternary systems is larger than that of $Cu_{50}Ag_{50}$, but slightly depends on the Sn concentration in the composition range of 3–6 at.% Sn. The alloy with 10 at.% Sn shows distinct increase of the lattice constant compared to the Sn deficient alloys at milling times larger than 8 h. Solid solution decomposition, grain growth process and crystallization of the amorphous phase formed during milling have been detected by DTA.

REFERENCES

1. T. Spassov, L. Lyubenova, Y. Liu, S. Bliznakov, M. Spassova, N. Dimitrov, *J. Alloys Compd.*, **478**, 232 (2009).
2. F. Yeh, C. Tai, J. Huang, I. Sun, *J. Phys. Chem. B*, **110**, 5215 (2006).
3. P. Duwez, R. H. Willens, W. Klement, *J. Appl. Phys.*, **31**, 1136 (1960).
4. R. K. Linde, J. Appl. Phys., **37**, 934 (1966).
5. B. Cantor, R. W. Cahn, *Acta Mettal.*, **24**, 845 (1976).
6. T. Klassen, U. Herr, R. S. Averback, *Acta Mater.*, **45**, 2921 (1997).
7. F. Wu, P. Bellon, A. Melmed, T. Lusby, *Acta Mater.*, **49**, 453 (2001).
8. H. W. Sheng, G. Wilde, E. Ma, *Acta Mater.*, **50**, 475 (2002).
9. Y. Qin, L. Chen, H. Shen, *J. Alloys Compd.*, **256**, 230 (1997).
10. S. Mader, A. S. Nowick, *Acta Metall.*, **15**, 215 (1967).
11. C. N. J. Wagner, *J. Vac. Sci. Technol.*, **6**, 650 (1969).
12. J. Dutkiewicz, L. Litynska, R. Swiatek, *J. Mater. Processing Technol.*, **53**, 131 (1995).
13. B. Reddy, P. Bhattacharya, B. Singh, K. Chattopadhyay, *J. Mater. Sci.*, **44**, 2257 (2009).

АМОРФИЗАЦИЯ И ОБРАЗУВАНЕ НА ТВЪРДИ РАЗТВОРИ В ЛЕГИРАНИ С Sn Cu-Ag СПЛАВИ, ПОЛУЧЕНИ ПОСРЕДСТВОМ МЕХАНИЧНО СМИЛАНЕ

Л. Любенова, Т. Спасов, М. Спасова

Химически факултет, СУ „Св. Климент Охридски", бул. „Дж. Баучър" 1, 1164 София, България

(Резюме)

Настоящата работа е насочена към изучаване влиянието на добавки от Sn върху микроструктурата на метастабилни твърди разтвори на основата на Cu-Ag с потенциално приложение за получаването на нанопорьозни структури. Нанокристални твърди разтвори със състав $Cu_{50}Ag_{50-x}Sn_x$ (x = 3, 6, 10) са получени посредством механохимично сплавяване във високо енергетична планетарна мелница в Ar-атмосфера и течен n-хептан. Образуването на фина нанокристална микроструктура (<10–15 nm) в проби от $Cu_{50}Ag_{40}Sn_{10}$ бе наблюдавано след смилане в продължение на 8 часа. Пълното сплавяване на компонентите в системите с по-малки количества Sn (x = 3 и 6) бе постигнато само за 5 часа синтез. Частична аморфизация бе наблюдавана при всички изследвани сплави, съдържащи Sn. Решетъчната константа на твърдия разтвор за трикомпонентните системи е по-голяма, отколкото тази на $Cu_{50}Ag_{50}$, но зависи слабо от концентрацията на Sn в интервала от 3–10 at.% Sn.

The effect of the composition on the crystallization behavior
of sintered glass-ceramics from blast furnace slag

I. K. Mihailova[1,*], P. R. Djambazki[1], D. Mehandjiev[2]

[1] *University of Chemical Technology and Metallurgy, 8 Kl. Ohridski, Sofia 1756, Bulgaria*
[2] *Institute of Catalysis, Bulgarian Academy of Sciences, Acad. G. Bonchev St., Bldg. 11, Sofia 1113, Bulgaria*

Glass-ceramics manufacturing has been considered as a very effective method for recycling and utilizing different types of industrial wastes. The purpose of this paper was to investigate the crystallization process of sintered glass-ceramics prepared from vitrified mixtures which were composed on blast furnace slag (68–80 %$_{mass}$), kaolin, Al_2O_3 and TiO_2. First the parent glasses were prepared. Then the glass-ceramics were obtained by one-step heat treating at 1000 °C from pressed glass powders. The crystallization behavior was studied by X-ray diffraction (XRD) and scanning electron microscopy (SEM). The crystalline phases were identified to be melilite, anorthite and pyroxene. The ratio between crystalline phases depends on chemical composition of the parent glasses. The examined microstructures were in accordance with the surface mechanism for crystal nucleation. The enhanced nucleation activity of fine glass powders caused crystallization, which led to good mechanical properties of glass-ceramics.

Key words: blast furnace slag, glass-ceramics, crystallization, structure.

INTRODUCTION

Although the exploitation of industrial wastes is not a new problem, it is still very actual and relevant one. Large part of solid wastes is formed by slags as by-products of metallurgical industry. The issue of slag application is still not resolved, not only for the metallurgical slags produced annually, but also for the large quantities of slags accumulated over the decades. One of the alternative options is to use slags as a raw material for the production of glass-ceramics [1–10] known as "slagsitall" and "slagceram". Glass-ceramics manufacturing is a well established process [3]. The glass-ceramic is a fine-grained crystalline material obtained by controlled crystallization of glass. There are two main production techniques. The first one usually involves a two-step thermal treatment of nucleation and crystal growth performed on monolithic glass. In most cases so-called nucleation agents are added to the base composition of the glass-ceramic. These nucleation agents aid and control the crystallization process. The second approach is based on the viscous flow sintering of fine glass powders, with concurrent

crystallization, known as "sinter-crystallization". The use of sinter-crystallization technology gives many advantages. The high specific surface of fine powders enhances the surface nucleation and thus crystallization may occur without the use of any nucleating agent. This technology gives the possibility to obtain materials with diverse and complicated shapes and good mechanical properties [10]. Glass-ceramics with not frequently encountered crystal phases [11], or processed with rapid heating [12], have been successfully prepared.

Although there are many studies of glass-ceramics obtained from metallurgical slag [1–10], some of the problems remain unresolved. Even slags ensuing from one type of production process have specific composition, depending on the type of ores used. For example, blast furnace slags are usually considered with regard to the systems $CaO–Al_2O_3–SiO_2$ or $CaO–Al_2O_3–MgO–SiO_2$. In addition to these major components sometimes they also include BaO, MnO, FeO, K_2O, Na_2O and other components [13], i.e., the actual processes take place in a far more complex multi-component system. Another typical problem in the production of glass-ceramic materials based on metallurgical slag is the non-uniform (variable) chemical composition of slags. On the other hand, the phase composition and microstructure of slag glass-ceramics, and respectively their

---

* To whom all correspondence should be sent:
E-mail: irena66@mail.bg

Table 1. Composition of the batches

Sample, № Materials, % mass	1	2	3	4	5	6	7
Blast furnace slag	73.6	67.8	68.2	74.3	80.2	79.9	74.0
Kaolin	20.7	24.8	20.5	12.0	7.9	12.2	16.4
Al_2O_3	–	1.7	5.7	8.0	6.2	2.2	3.9
TiO_2	5.7	5.7	5.7	5.7	5.7	5.7	5.7

properties, are dependent on the slag composition and the used additive agents. The purpose of this study is to determine the effects of the change in the chemical composition on the phase composition and microstructure of glass-ceramics. This was the reason to select seven batch compositions with different proportions of the main oxides CaO, Al_2O_3 and SiO_2. Blast furnace slag from Kremikovtsi plant, as a main component and inexpensive additives (kaoline, Al_2O_3 and TiO_2) were used for the synthesis of glass ceramics materials via sinter-crystallization technology. The choice of particular compositions and additives was based on our previous experimental data [14–16], which showed that glass-ceramics with good mechanical properties can be obtained from such compositions.

MATERIALS AND METHODS

Synthesis of glass ceramics

The investigations performed have shown the blast furnace slag to be suitable for the production of melilite containing glass ceramics material without substantially changing the chemical composition of slag. Blast furnace slag, kaolinite, Al_2O_3 and TiO_2 were used for the synthesis of glass ceramics

Table 2. Chemical composition of the used blast furnace slag

Oxides	Content,% mass
SiO_2	35.16
Al_2O_3	9.29
FeO	0.97
MgO	5.15
MnO	2.61
BaO	3.24
CaO	40.46
Na_2O	0.28
K_2O	0.97
S^2	1.17
Fe	0.70

materials by sintering of the samples obtained by semidry pressing. In the experiments, TiO_2 was chosen as nucleating agent. TiO_2 is the most common nucleating agent in the glass-ceramics. TiO_2 is soluble in wide range of molten glasses. But during cooling or subsequent reheating large number of submicroscopic particles are precipitated and these assist the development of major crystalline phases [17]. Data is also available for the role played by TiO_2, which is usually considered to induce amorphous separation and volume crystallization during ceramming. The heat treatment of amorphous glasses leading to nucleation would cause a disruption of silica network which followed phase separation. The phase separation followed the generation of crystal [18]. Taking into account our previous studies [14–16] the compositions were chosen in the upper boundary region of the crystallization field of gehlenite in the $CaO–Al_2O_3–SiO_2$ system. The batches for the seven experimental compositions are given in Table 1.

The chemical composition of the used blast furnace slag from Kremikovtsi is reported in Table 2.

The synthesis of the seven experimental samples was carried out under identical conditions. First the parent glasses were prepared. The batches were melted in a laboratory box furnace at 1450–1470 °C for 60–90 minutes. The melt were fritted and the resulting frit was ground in a porcelain ball mill to a grain size below 0.1 mm. A 3% aqueous polyvinyl alcohol solution was added. Then the mixture was homogenized, granulated and pressed with an automatic press (pressure 300 kg/cm²). Cylindrical briquettes (with a diameter 30 mm and a height of 14 mm) were obtained. The sintering and crystallization proceeded in a muffle furnace at 1000 °C, with retention time of 3 hours. Thus glass-ceramics were obtained from pressed glass powders by one-step heat treatment. The obtained glass ceramic samples are presented in Fig. 1. They were labeled as № 1, 2, 3, 4, 5, 6 and 7. According our previous studies [14–16] data on some of the properties of glass-ceramics, such as: density 2.88–3.00 g/cm³; water absorption 0.01–0.05 %; Vikers microhardness 5.5–8.3 GPa, chemical resistance in NaOH 35% w/w aqueous solution above 99.9%, temperature of the onset of

Fig. 1. Glass-ceramics samples

deformation ~1150 °C, thermal stability ~700 °C, linear thermal expansion coefficient (x10^{-7}/°C) ~90, agrees with literature data for similar materials [3] and proves to be promising and feasible.

Experimental methods

The X-ray diffraction (XRD) was performed using a D2 Phaser (Bruker) X-ray diffractometer with Cu Kα radiation (λ=1.5418 Å). The measurements were carried out on powder samples in the 5º to 70º 2θ (30kV, 10 mA, step 0.05 º/sec). The crystalline phases were identified using the International Centre for Diffraction Data (ICDD) database. PowderCell 2.4 software [19] was applied to determining the unit cell parameters on the basis of experimental X-ray data.

The microstructure of the glass ceramic materials was investigated by SEM. Microscope JEOL JSM 5510 is used. The samples were coated with gold in an auto fine coater JEOL JFC-12200.

RESULTS AND DISCUSSION

XRD data is given in Fig. 2. Three main crystal phases in varying proportions were present in the samples: melilite, anorthite and pyroxene. Experimental XRD data were compared with
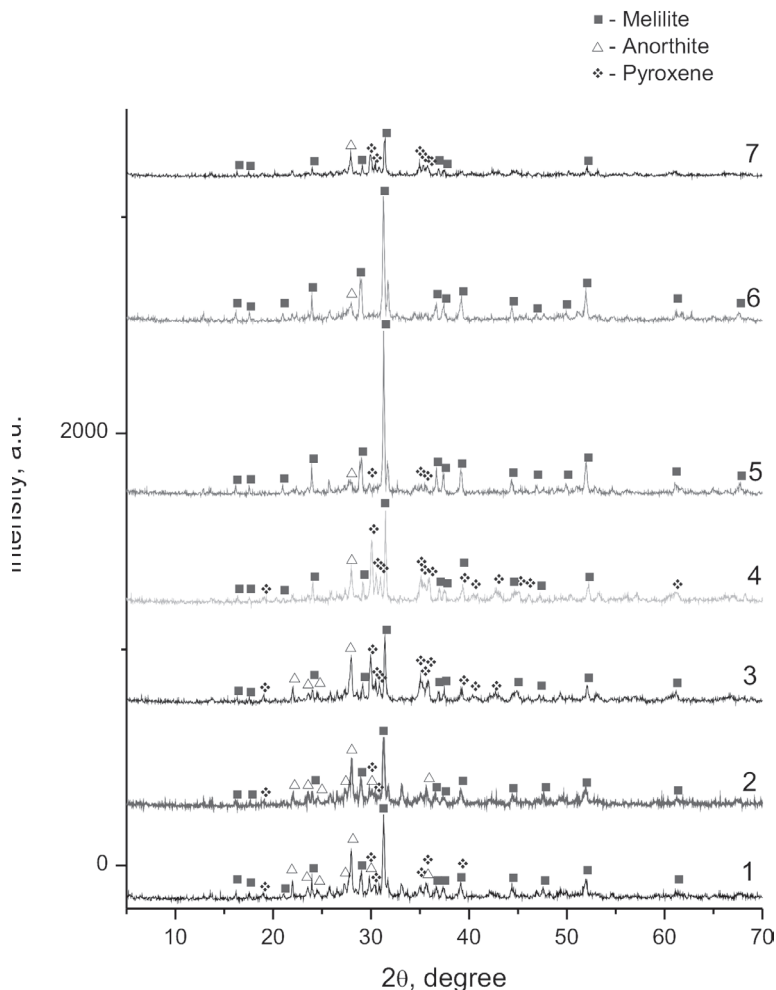
Fig. 2. XRD patterns of glass-ceramics samples

Table 3. Phase composition of glass-ceramics – crystalline phases identified in glass-ceramics

Sample № / Crystalline phases	1	2	3	4	5	6	7
Melilite, vol.%	32	33	20	26	60	66	25
Anorthite, vol.%	51	55	40	23	25	34	33
Pyroxene, vol.%	17	12	40	51	15	–	42

Powder diffraction file cards № 35-0755, 41-1486 and 31-0249. The phase compositions of the glass-ceramic samples determined through the XRD analysis are presented in Table 3. The quantitative phase analysis of the samples was performed with the PowderCell 2.4 software. The amorphous mass (glass) quantity was not taken into consideration. No amorphous hallo is visible in Fig. 2. but SEM analysis clearly indicates the presence of glass.

XRD data show maximum intensity of the diffraction peak (211) of melilite in all X-ray diffraction patterns. However, melilite was the predominant crystal phase only in samples 5 and 6. These were the compositions with the highest CaO content (e.g. highest blast furnace slag content), and it is logical that the compositions that are the closest to the gehlenite stoichiometry show the highest melilite content.

The phase content of samples 1 and 2 was nearly identical, with anorthite accounting for slightly more than 50% of the crystalline phases. These were the compositions containing the smallest quantity of blast-furnace slag and the largest quantity of kaolin,

i.e., relatively less CaO and more SiO_2. Composition 2, in which the largest amount of anorthite was observed, corresponds to the minimum content of CaO and the maximum content of SiO_2.

Compositions 3, 4 and 7 are characterized by a more significant participation of pyroxene in the phase content: 40–50% of the crystalline phases. Their chemical composition differs by the relatively high content of Al_2O_3, composition 4 having the highest Al_2O_3 content and the highest pyroxene content. Judging by the intensity of the diffraction peaks of the crystalline phases when compared with other samples, composition 7 exhibited the lowest degree of crystallization and the lowest content of the melilite phase.

The observed dependencies are presented graphically in Fig. 3 and 4. Fig. 3 shows the dependencies of phase composition of the glass-ceramics on the amount of additives while Fig. 4 illustrates the effect of chemical composition. The calcium, silicon and aluminum contents in parent glasses are presented in oxide form. Note that the dependence between the content of anorthite and SiO_2 (Fig. 4a) is more
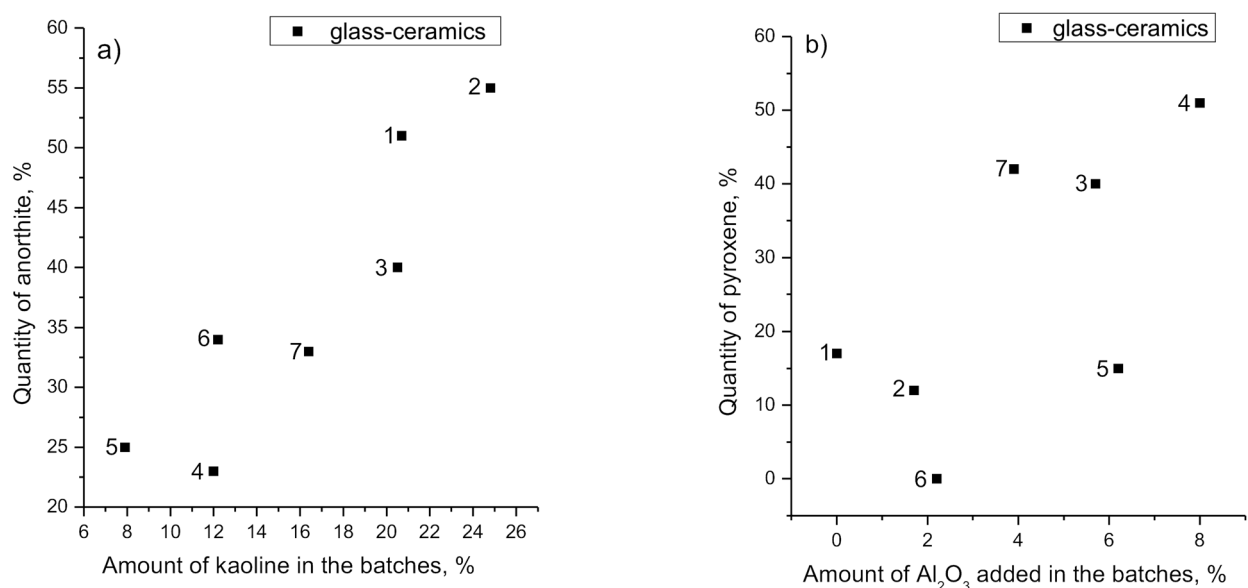
Fig. 3. Dependence of phase composition of the glass-ceramics on the amount of additives
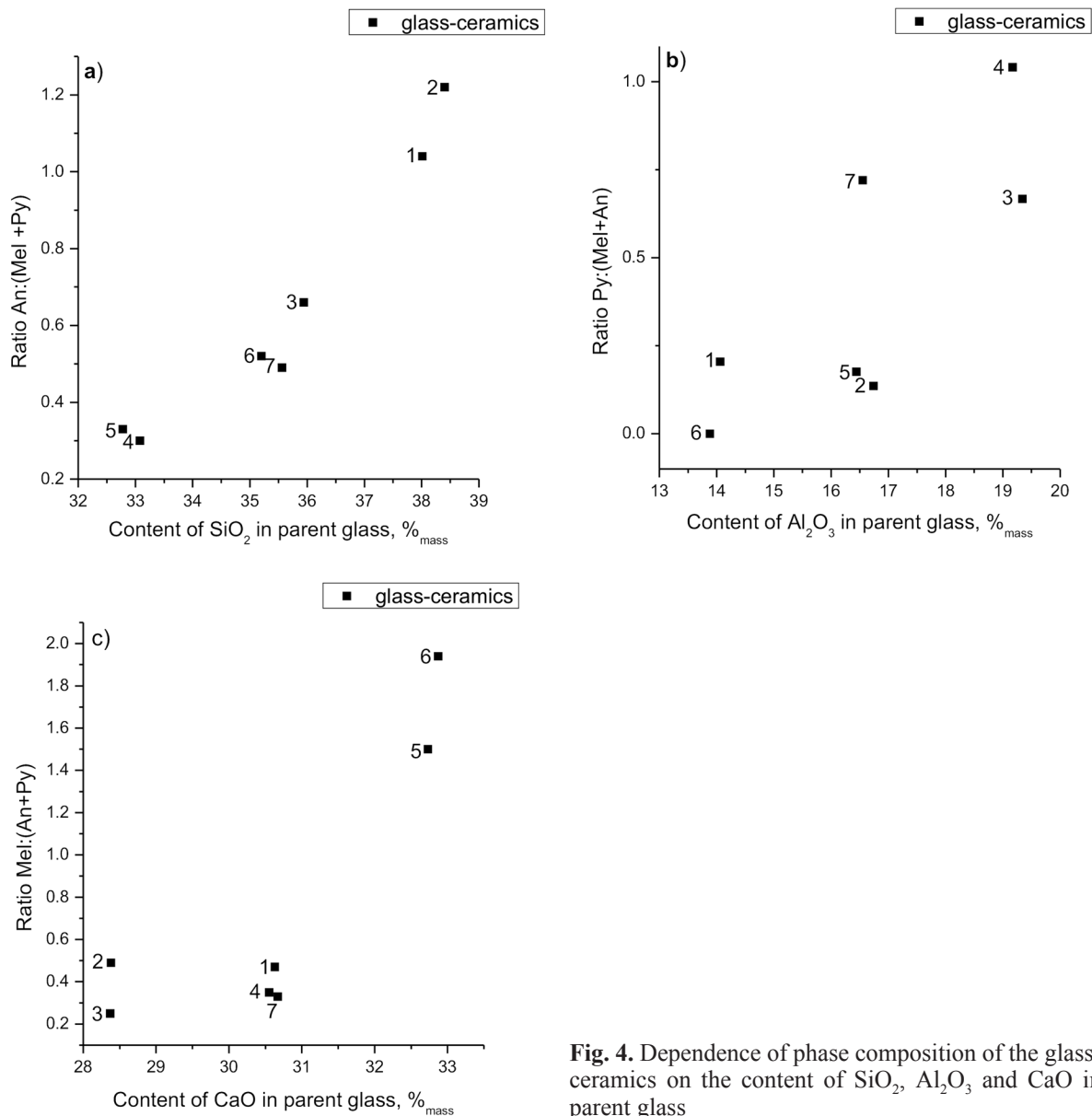
Fig. 4. Dependence of phase composition of the glass-ceramics on the content of SiO_2, Al_2O_3 and CaO in parent glass

clearly expressed than the dependency between melilite and CaO content (Fig. 4c). The replacement of SiO_2 with Al_2O_3 leads to an increase of pyroxene for compositions with the same content of CaO: 1, 7 and 4, 6 and 5, 2 and 3 (Fig. 4b).

It is known that the three crystalline phases identified in glass-ceramics can form solid solutions. Melilites, usually regarded as solid solutions between gehlenite ($Ca_2Al_2SiO_7$) and akermanite ($Ca_2MgSi_2O_7$), may include a number of isomorphic impurities: Ba, Na, Mn, Fe and others. This has an impact on the unit cell parameters of the formed melilite phases (Table 4). The unit cell parameters of the melilite phase are closer to those of gehlenite in compositions 3 and 4, i.e., closer to those in compositions with a high Al_2O_3 content. The unit cell parameters in compositions 1 and 6 that have a lower Al_2O_3 content deviate from those of gehlenite and tend to approximate the akermanite unit cell parameters. The unit cell parameters of the anorthite phase in compositions 1, 2 and 3, which have the highest anorthite content, correspond most closely to literature data [20]. Pyroxenes also tend to have isomorphic substitutions; however, the unit cell parameters of the formed pyroxene phases in the glass-ceramic samples did not differ significantly. It cannot be therefore expected that the phase compositions of pyroxene in the samples differ.

Common micro-structural features were observed in slag glass-ceramics № 1, 2, 3, 4, 5 and 6, which are represented in Fig. 5. A common structural feature of the samples was the presence of an

Table 4. Cell parameters of crystalline phases in glass-ceramics

Sample №	1	2	3	4	5	6	7
	Cell parameters of melilite, Å						
a	7.748	7.759	7.696	7.702	7.728	7.752	7.701
c	5.042	5.046	5.065	5.047	5.038	5.037	5.074
	Cell parameters of anorthite, Å						
a	8.182	8.178	8.185	8.212	8.109	8.128	8.199
b	12.885	12.895	12.879	12.956	12.953	12.959	12.911
c	14.147	14.155	14.165	14.238	14.236	14.211	14.188
α	93.315	93.527	93.328	94.300	93.601	93.434	93.215
β	115.577	115.606	115.586	115.641	115.545	115.649	115.710
γ	90.985	90.866	90.983	90.881	92.027	92.120	91.097
	Cell parameters of pyroxene, Å						
a	9.676	9.709	9.709	9.709	9.509	–	9.709
b	8.752	8.752	8.752	8.752	8.752	–	8.752
c	5.368	5.350	5.335	5.335	5.354	–	5.351
β	105.060	106.517	106.299	106.299	105.060	–	106.263

amorphous phase densely enveloping the crystals. The obtained glass-ceramic materials had a finely dispersed crystalline structure showing microcrystals of ~3–4 μm. Idiomorphic crystals with a characteristic morphology that corresponds respectively to anorthite, melilite and pyroxene were identified in large rounded pores measuring up to 10–20 μm. The diversity in size and morphology of the crystalline phases illustrates the complex phase composition of the samples. The typical orientation of melilite and anorthite crystal slabs was perpendicular (transverse) to the boundary surface of pores. SEM observations confirmed the view that the inter-phase surface is a factor favorable for crystallization. The observed intensive crystallization in the above mentioned pores, where even amorphous mass linkage was missing, proves this. In addition to the larger, rounded pores, smaller pores of irregular shape were observed. There was a good sintering of the input powders. Different-sized pores were closed and did not lead to increase in the water absorption of samples, which was in the range 0.01–0.05%. Usually the dense microstructure without any pores is considered to be characteristic of glass-ceramics. On the other hand, the presence of pores is not without a precedent and has an explanation. For example, two types of closed porosity are well distinguished in diopside glass-ceramics [21, 22]: intergranular residual pores have an irregular shape and are characterized by a smooth surface, while intragranular induced crystallization pores have a semi-spherical shape and an indented polycrystalline surface. It is shown by Karamanov and Pelino [21, 22] that, due to the volume variation related to crystallization,

spherical intragranular pores are formed in sintered glass-ceramics. The amount of the induced porosity is a function of the crystallization. In spite of the increase in porosity, the mechanical properties are improved with the rise in crystallinity. The pores observed in our study (Fig. 5) were typical intragranular induced crystallization pores.

Previous experiments have shown [14-16] that the thermal treatment of similar in composition monolithic slag glasses does not incur bulk crystallization. On the other hand, when thermally treated, pressed powders transform into strong and relatively dense materials with several crystalline phases. Therefore, in ceramic technology (sintering of glass powders) the process of crystallization proceeds much more intensively. The interphase surface stimulates the crystallization, which starts from the surface of the glass particles. Larger pores, in which the highest degree of crystallization was observed, also support the idea of the role of the surface. We consider that probably these pores were formed as a consequence of the glass crystallization The crystals formed in the amorphous matrix had a higher density than the density of the amorphous mass, which led to shrinking of the sample and the formation of induced porosity.

CONCLUSIONS

Glass-ceramics with good properties have been successfully synthesized from blast furnace slag (between 68 and 80%$_{mass}$), kaolin, Al_2O_3 and TiO_2 additives via sinter-crystallization technology. The
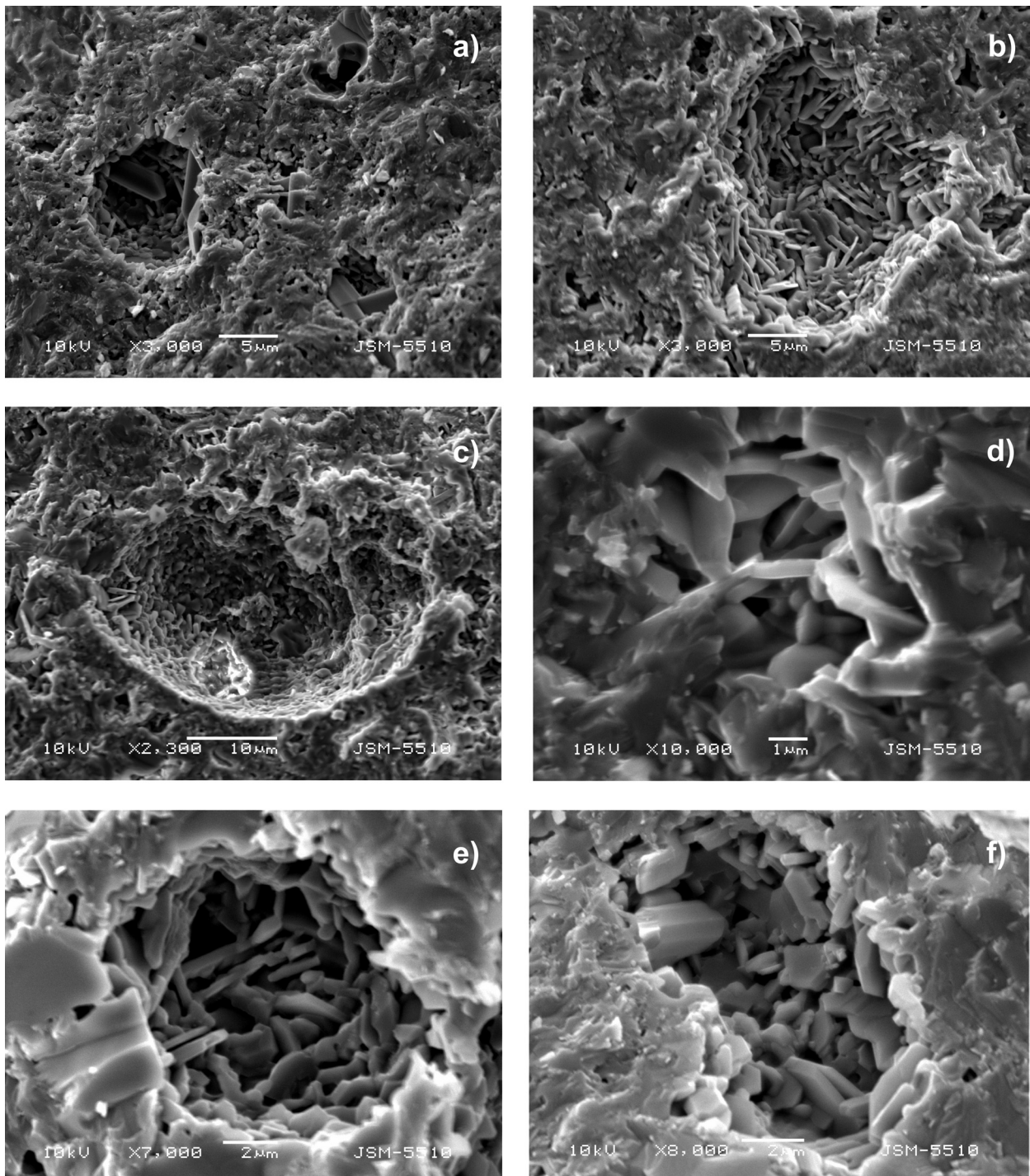
Fig. 5. SEM images of glass-ceramics samples: a) – 2; b) – 3; c) and d) – 4; e) – 5; f) – 6

final crystalline phases of glass-ceramics were melilite, anorthite and pyroxene. The batch compositions affected the phase composition of glass-ceramics. Glass-ceramic materials with a main phase in the form of melilite were obtained from the compositions with higher slag content (~ 80%).

Kaolin additive led to an increase of anorthite and the increase of Al_2O_3 content facilitated the crystallization of pyroxene. Therefore the use of additives could be applied to control phase composition. However, it is more important that glass-ceramic materials with a similar microstructure and promis-

ing properties were obtained within the scope delineated by the seven batches. Therefore, the unavoidable variations in the chemical composition of the used slag could change the phase composition of the obtained glass-ceramics, without having any significant impact on its structural characteristics and properties.

REFERENCES

1. I. T. Ivanov, V. V. Lapin, *Stroitelni materiali i silikatna promishlenost*, **11**, 18 (1971).
2. V. V. Lapin, I. T. Ivanov, *Izv. AN SSSR, Ser. Neorg. Mat.*, **9**, 683 (1973).
3. Z. Strnad, Glass–ceramic materials, Elsevier Science Publishers, Amsterdam, 1986.
4. D. D. Sun, J. H. Tay, H. K. Cheong, D. L. K. Leung, G. R. Qian, *J. Hazard. Mat.*, **87**, 213 (2001).
5. A. A. Francis, *J. Eur. Ceram. Soc.*, **24**, 2819 (2004).
6. C. Liu, P. Shi, D. Zhang, M. Jiang, *J. Iron Steel Res. Int.*, **14**, 73 (2007).
7. A. Karamanov, M. Aloisi, M. Pelino, *J. Hazard. Mat.*, **140**, 333 (2007).
8. H. Liu, H. Lu, D. Chen, H. Wang, H. Xu, R. Zhang, *Ceram. Int.*, **35**, 3181 (2009).
9. Z. Wang, W. Ni, Y. Jia, L. Zhu, X. Huang, *J. Non-Cryst. Solids*, **356**, 1554 (2010).
10. A. Karamanov, G. Taglieri, M. Pelino, *J. Am. Ceram. Soc.*, **87**, 1354 (2004).
11. E. Bernardo, R. Castellan, S. Hreglich, *Ceram. Int.*, **33**, 27 (2007).
12. E. Bernardo, L. Esposito, E. Rambaldi, A. Tucci, Y. Pontikes, G. N. Angelopoulos, *J. Eur. Ceram. Soc.*, **29**, 2921 (2009).
13. T. Ivanov, V. V. Lapin, *Rudodobiv i metalurgia*, **7**, 3 (1971).
14. I. T. Ivanov, I. Georgieva, F. Dipchikov, in: Proc. 11th Int. Conf. Glass and Ceramic, Varna, 1993, B. Samuneva. I. Gutzow, Y. Dimitriev, S. Bachvarov (eds.), Acad. Publ. House Marin Drinov, Sofia, 1994, p. 240.
15. I. Ivanov, I. Georgieva, F. Dipchikov, C. Ionchev, in: Proc. 12th Int. Conf. Glass Ceramics, Varna, 1996, B. Samuneva et al. (eds.), Acad. Publ. House Marin Drinov, Sofia, 1997, p. 200.
16. I. Georgieva - Mihailova, PhD Thesis, UCTM, Sofia, 1997.
17. P. W. McMillan, Glass-Ceramics, 2nd ed., Academic Press, London, 1979.
18. M. Ma, W. Nia, Y. Wanga, Z. Wanga, F. Liua, *J. Non-Cryst. Solids*, **354**, 5395 (2008).
19. Kraus, W., Nolze, G., Powdercell2.4, Federal Institute for materials Research and Testing Rudower Chaussee 512485 Berlin, Germany.
20. P. Benna, G. Zanini, E. Bruno, *Contrib Mineral Petrol* **90**, 381(1985).
21. A. Karamanov, M. Pelino, *J. Eur. Ceram. Soc.*, **26**, 2511 (2006).
22. A. Karamanov, M. Pelino, *J. Eur. Ceram. Soc.*, **28**, 555 (2008).

ВЛИЯНИЕ НА СЪСТАВА ВЪРХУ КРИСТАЛИЗАЦИЯТА НА СИТАЛИ НА ОСНОВАТА НА ДОМЕННА ШЛАКА

И. К. Михайлова[1,*], П. Р. Джамбазки[1], Д. Механджиев[2]

[1] *Химико-технологичен и металургичен университет, бул. „Кл. Охридски" № 8, София 1756, България*
[2] *Институт по катализа, Българска академия на науките, бул. „Акад. Г. Бончев", бл. 11, София 1113, България*

(Резюме)

Производството на ситали е считано като много ефективен метод за рециклиране и използване на различни типове промишлени отпадъци. Целта на настоящата работа е да изследва процеса на кристализация на ситали, получени по керамична технология чрез спичане на стъклени прахове. Първоначално са получени изходни стъкла от шихти, съставени от доменна шлака (68–80%$_{mass}$), каолин, Al_2O_3 и TiO_2. Ситалите са получени чрез едно-стъпална термообработка при 1000 °C на пресованите стъклени прахове. Кристализацията е изследвана с рентгено-фазов анализ и сканираща електронна микроскопия. Кристалните фази са определени като мелилит, пироксен и анортит. Съотношението между кристалните фази зависи от химичния състав на изходните стъкла. Установените различия в параметрите на елементарната клетка са във връзка с изоморфни замествания в кристалните фази и респективно променливия им състав. Микроструктурата на ситалите е в съгласие с повърхностен механизъм на зародишообразуване. Засилената склонност към зародишообразуване на финните стъклени прахове води до получаване на ситали с добри механични свойства.

Structural changes in the system natural apatite – NH$_4$ clinoptilolite during triboactivation

N. Petrova*, V. Petkova

Institute of Mineralogy and Crystallography, Bulgarian Academy of Sciences, Sofia, Bulgaria

The tribochemical activation of natural phosphate-clinoptilolite mixtures facilitates the transitions of hardly assimilated by plants P$_2$O$_5$ forms into readily assimilated ones. Thus this approach is a solution of ecological and stuff problems, aiming to increase the transition of P$_2$O$_5$ into assimilated by plants form. Mixtures of Tunisian phosphorite and NH$_4$-exchanged clinoptilolite from Beli plast deposit (Bulgaria) (in different ratio) were activated in a planetary mill.

Structural changes in the mixtures during activation result in increasing of P$_2$O$_5$ solubility. These changes were studied by XRD and IR spectroscopy. The obtained results show ion-exchange reactions between natural apatite and NH$_4$-clinoptilolite and deformation or rapture of Si-O-Si and Si-O-Al bonds in the clinoptilolite structure on one hand, and defectiveness and isomorphism in the apatite structure on the other.

Key words: Apatite, NH$_4$-clinoptiolite, tribochemical activation, XRD, IR spectroscopy.

INTRODUCTION

Production of phosphorus fertilizers from natural apatite through conventional acid-treatment technologies leads to environmental problems, such as contamination with solid and gaseous waste. This is the reason to look for new non-conventional methods for obtaining of useful products from low-quality row materials [1]. The assimilation degree of phosphorus fertilizers by plants is determined by the solubility of their main useful component – P$_2$O$_5$.

Natural zeolites improve the soil texture and increase the soil fertility due to their high ion-exchange capacity. Because of the alkali reaction of suspended zeolite they improve acidic soil and adsorb selectively heavy metals and radioactive isotopes. These factors determine the use of zeolite in a system with natural phosphates [2]. A controlled and renewable release fertilization system has been proposed, that employs NH$_4$ exchanged clinoptilolite to aid in dissolution of apatite and thereby in release of soluble N, P, and exchangeable Ca for uptake by plants [3].

The tribochemical activation (TCA) of natural phosphate-clinoptilolite mixtures is an alternative solution of ecological and stuff problems, aiming to increase the transition of P$_2$O$_5$ into assimilated by plants form (P$_2$O$_5$^{ass}). The applicability of TCA on phosphate and clinoptilolite minerals, their reactivity and interaction [4–6], thermal behaviour and solid phase reactions [7] have been studied.

The application of infrared spectroscopy and X-ray diffraction analysis allows the study of structural and phase transformations in the system apatite (Ap) – NH$_4$-exchanged clinoptilolite (NH$_4$-Cpt), with a focus on the changes that occur during TCA.

The aim of this study is to clarify how the structural changes during TCA and ion-exchange reactions in the system Ap–NH$_4$-Cpt affect the solubility of P$_2$O$_5$.

EXPERIMENTAL

Natural Cpt from Beli Plast deposit, Bulgaria and natural Ap from a Tunisian deposit were used in this work [6, 7, 8].

The clinoptilolite tuff contains about 80% clinoptilolite and impurities of montmorilonite, biotite, seladonite, low-crystobalite, quartz and feldspars. The chemical composition of isolated clinoptilolite (wt. %) is: SiO$_2$ – 66.15; Al$_2$O$_3$ – 11.31; Fe$_2$O$_3$ – 0.67; MgO – 0.46; CaO – 4.20; Na$_2$O – 0.34; K$_2$O – 3.13; H$_2$O – 13.92. The tuff sample was treated with 1M solution of

* To whom all correspondence should be sent:
E-mail: nadia5@mail.bg

NH_4NO_3 by shaking for three days at 60 °C changing the solution every day and finally washed and dried at room temperature The total cation exchange capacity with respect to Al content is 2.2 meq/g as the degree of ion exchange with NH_4^+ is higher than 98%. An evidence for NH_4^+ presence in the Cpt is the vibration doublet at 1446 and 1404 cm⁻¹ [7].

The natural Ap consists mainly of francolite (about 94%) and impurities of calcite, dolomite, feldspar, and quartz. The chemical composition of the Ap (wt. %) is: total P_2O_5 – 29.00; R_2O_3 – 1.07; SO_3 – 3.58, CaO – 48.40; MgO – 0.47; SiO_2 – 1.88; Na_2O – 1.38; K_2O – 0.07; F – 2.74; Cl – 0.056; CO_2 – 6.48. The initial Ap contains structural associated water and CO_3^{2-} ions, substituting PO_4^{3-} group (CO_3^{2-} – B-type Ap). These data determine the used in this work sample as hydroxy-CO_3-F-Ap [7].

Initial samples and three mixtures with different mass ratio of Ap to NH_4-Cpt, namely 80:20, 50:50 and 20:80 were treated by tribochemical activation. The TCA was carried out in a planetary mill (Pulverisette–5, Fritsch Co, Germany) with agate milling bodies during 240 min and rotating speed of 280 min⁻¹. Obtained samples were blended in 2% citric-acid solution since the variation of phosphate solubility was estimated by the phosphorus content in the solution. A standardized method for determination of $P_2O_5^{ass}$ was used following Bulgarian National Standard 14131-88.

The X-ray diffraction (XRD) measurements of the samples were performed on D2 Phaser Bruker AXS, using a Ni-filtered Cu-$K_α$ radiation ($λ$ = 0.15418 nm). A step-scan technique was applied with a step size of 0.05° $2θ$ and 3 s per step in the range 8–70° $2θ$. Phase identification was performed using the index file PDF (Powder Diffraction File, ICDD, 2001).
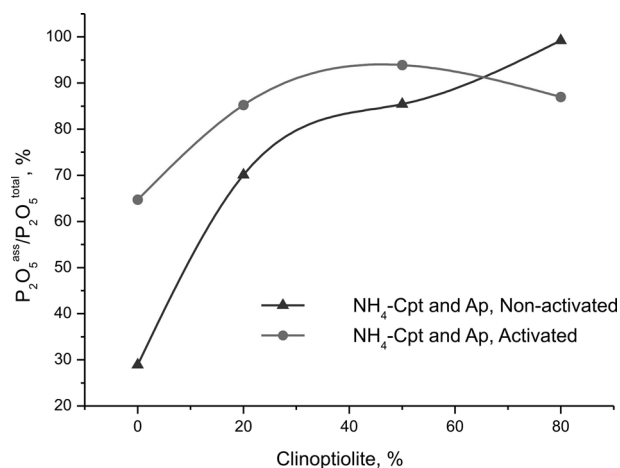
The Fourier transform infrared (FTIR) spectra were taken on a Bruker Tensor 37 spectrometer, using KBr pellet technique. A resolution of 2 cm⁻¹ was used collecting 120 scans for each sample.

RESULTS AND DISCUSSION

Chemical results

Dependences of $P_2O_5^{ass}/P_2O_5^{total}$ on NH_4-clinoptilolite content in the mixture are presented on Fig. 1. The presented results show high degree of transition of P_2O_5 into assimilated by plants form [7].

TCA improves the apatite reaction ability and solubility when the phosphate part dominates in the mixture.

The effect of ion-exchange reaction is manifested significantly when NH_4-Cpt dominates in the non-activated system:

Soil solution
Ap+ NH_4-Cpt   ↔   Ca-Cpt + $(NH_4^+)_{solution}$ + $(H_2PO_4^-)_{solution}$
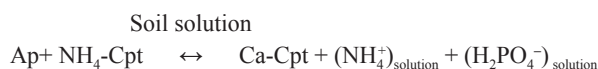
The combination of dissolution and ion-exchange reaction is more advantageous than applying each of the methods separately because both reactions drive each other [2, 3].

Chemical analyses give ground to suggest that some structural changes have occurred during the TCA in both components. The latter needs further evidences, provided by other structural methods.

XRD data

XRD data of Ap and NH_4-Cpt: initial samples (a) and activated (b) are presented on Fig. 2 while that of their mixtures on Fig. 3. The identified phases by XRD obtained during TCA are summarized in Table 1.

In the case of TCA, a tendency of amorphization for both samples and their mixtures is observed. Besides the expected decrease in intensity and widening of the peaks, peak splitting and appearance of new peaks are also recorded when Ap dominates in the mixture (Figs. 2 and 3a). Both reducing the intensity and peak widening are explained by crystallite size decrease. It has been shown [10, 11, 12], that under similar conditions of TCA of apatite samples, nano-sized particles of around 10-20 nm have been obtained. The result of the treatment is decreasing of the apatite structure stability and formation of nano-sized metastable phase with high chemical reactivity (Table 1). The appearance of new peaks in the main patterns of apatite (d = 2.79 Å) suggests the formation of new phase or the appearance of defects and isomorphic substitution.

Fig. 1. $P_2O_5^{ass}/P_2O_5^{total}$ relations vs. clinoptilolite content in the mixtures
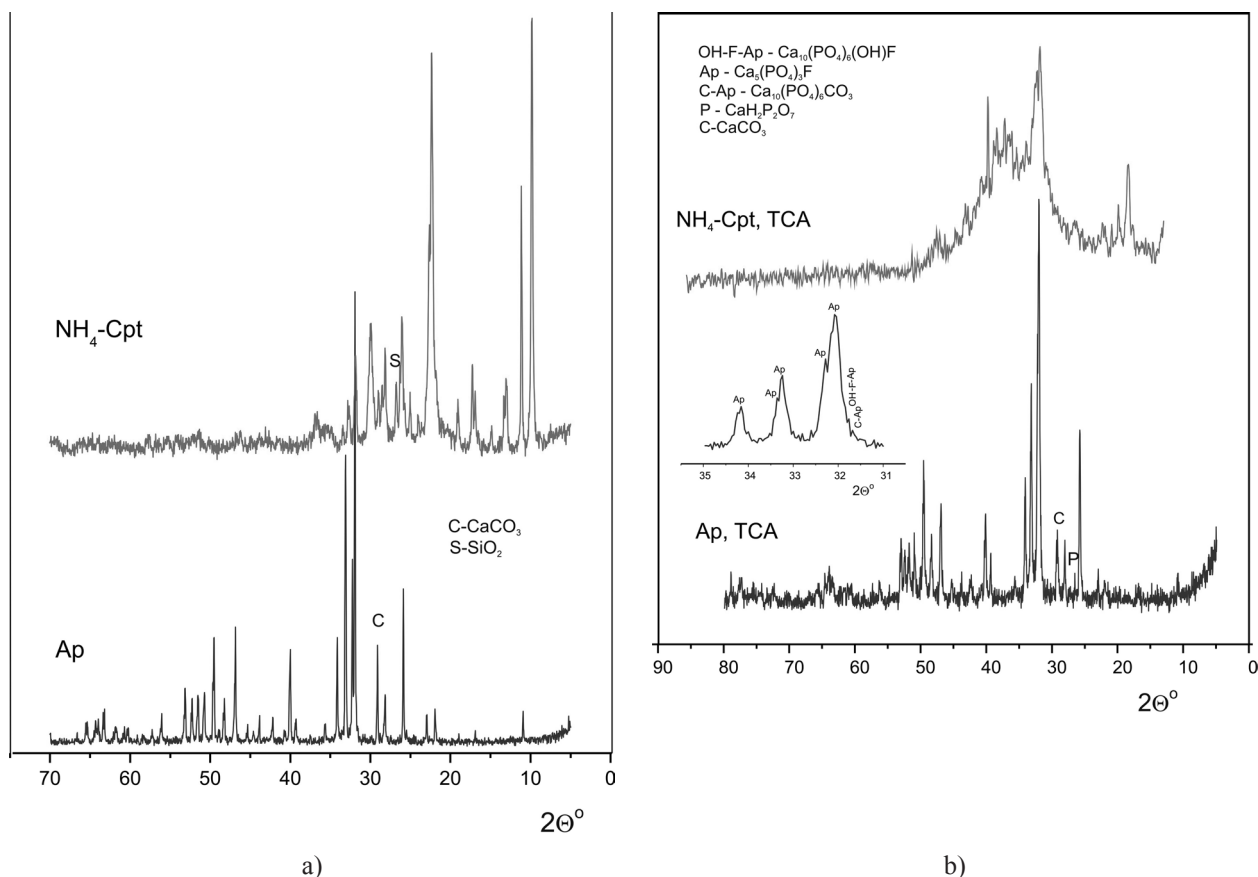
Fig 2. XRD data of initial (a) and tribo-activated (b) Ap and NH$_4$-Cpt
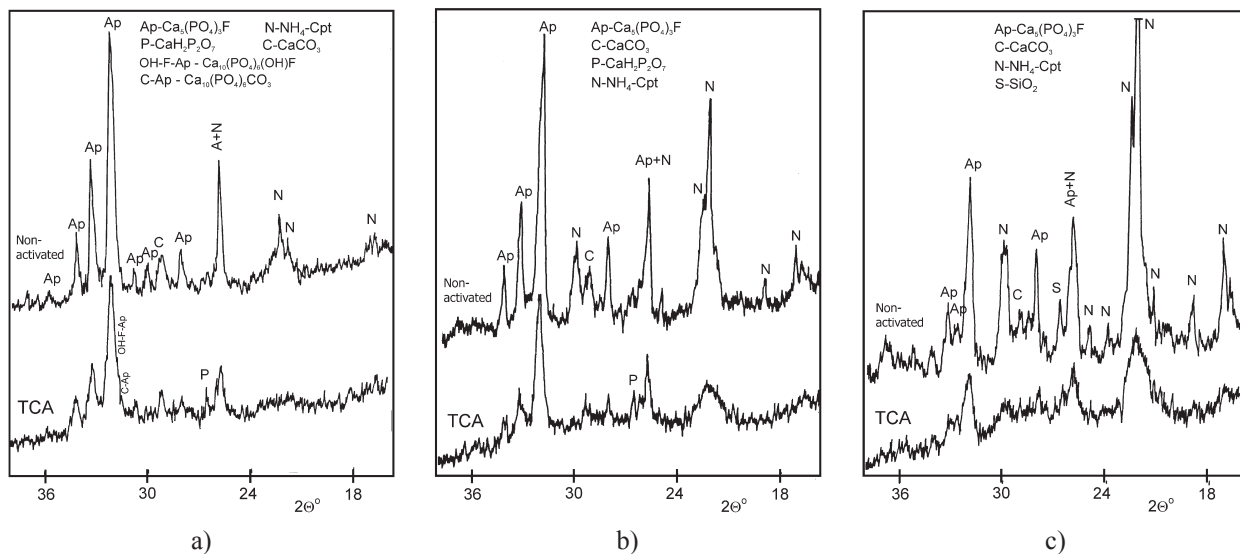
Fig. 3. XRD data of mixtures with Ap:NH$_4$-Cpt ratio 80:20 (a); 50:50 (b); 20:80 (c)

The established phase composition suggests that the new peaks in Fig. 2b (small picture) should probably be attributed to the mixed type apatite: carbonate-apatite (C-Ap) and hydroxyl-carbonate apatite-fluorine (C-OH-F-Ap). Their solid phase synthesis is associated with partial substitution of phosphate group by carbonate and fluorine ion by hydroxyl and/or carbonate. This substitution seems

303

Table 1. XRD data of Ap and NH_4-Cpt and their mixtures

Sample	Identified phases
Nonactivated Ap	$Ca_5F(PO_4)_3$, $CaCO_3$
Ap, TCA	$Ca_5F(PO_4)_3$, $CaCO_3$, $Ca_{10}(PO_4)_6(OH)F$ [9], $Ca_{10}(PO_4)_6CO_3$, $CaH_2P_2O_7$
Ap+NH_4-Cpt, 80:20, TCA	$Ca_5F(PO_4)_3$, $CaCO_3$, $Ca_{10}(PO_4)_6(OH)F$ [9], $Ca_{10}(PO_4)_6CO_3$, $CaH_2P_2O_7$, NH_4-Cpt,
Ap+NH_4-Cpt, 50:50, TCA	$Ca_5F(PO_4)_3$, $CaCO_3$, NH_4-Cpt, $CaH_2P_2O_7$
Ap+NH_4-Cpt, 20:80, TCA	$Ca_5F(PO_4)_3$, $CaCO_3$, NH_4-Cpt, SiO_2
Nonactivated NH_4-Cpt	NH_4-Cpt, SiO_2
NH_4-Cpt, TCA	NH_4-Cpt, SiO_2

to be facilitated by local temperature increase, due to both impact and friction effects. The resulting isomorphic phase is probably non-stoichiometric.

IR spectra

IR spectra of TCA samples with different mixing ratio are presented on Fig. 4, while their band positions and types of fundamental vibrational modes are listed in Table 2.

In the case of NH_4-Cpt domination (Figs. 4 and 5a) a new vibration band at 900 cm^{-1} appears (v_3, asymmetric stretching mode T-O-T, T=Si, Al). This band misses in nonactivated samples, while in activated samples it is related to the processes of deformation and rupture of intertetrahedral bonds – Si-O-Si or Si-O-Al [5, 13]. According to the theory of tribochemical activation, as a result of deformation and rupture of individual bonds in Si-O-Al groups, active centres are formed in the zeolite structure, which then interact with the phosphate.

In the case of Ap domination (Figs. 4 and 5b and c): Spectra of Fig. 5b focus on changes in the positions of the carbonate ion in the activated samples. Under the influence of TCA, changes of absorption bands of carbonate group incorporated in the apatite structure occur ($v_3 = 1400$–1470 cm^{-1}). In studied samples an irregular widening of the left slope of the band are recorded, due to the appearance of a low-intensity band at about 1503 cm^{-1}. A peak fitting procedure via Gaussian function was applied to determine this position. (Fig. 5b small picture). The presence of this bend is probably due to the incorporation of carbonate ions in the apatite structure during tribochemical activation, which is an evidence for the formation of $Ca_{10}(PO_4)_6CO_3$ and $Ca_{10}(PO_4)_5CO_3(OH)F$ (Table 1).

Given the results of both XRD analysis and IR spectroscopy a conversion of inactive phosphate – $Ca_5(PO_4)_3F$, type B into $Ca_{10}(PO_4)_5CO_3(OH)F$ and $Ca_{10}(PO_4)_6CO_3$ is assumed, as the carbonate
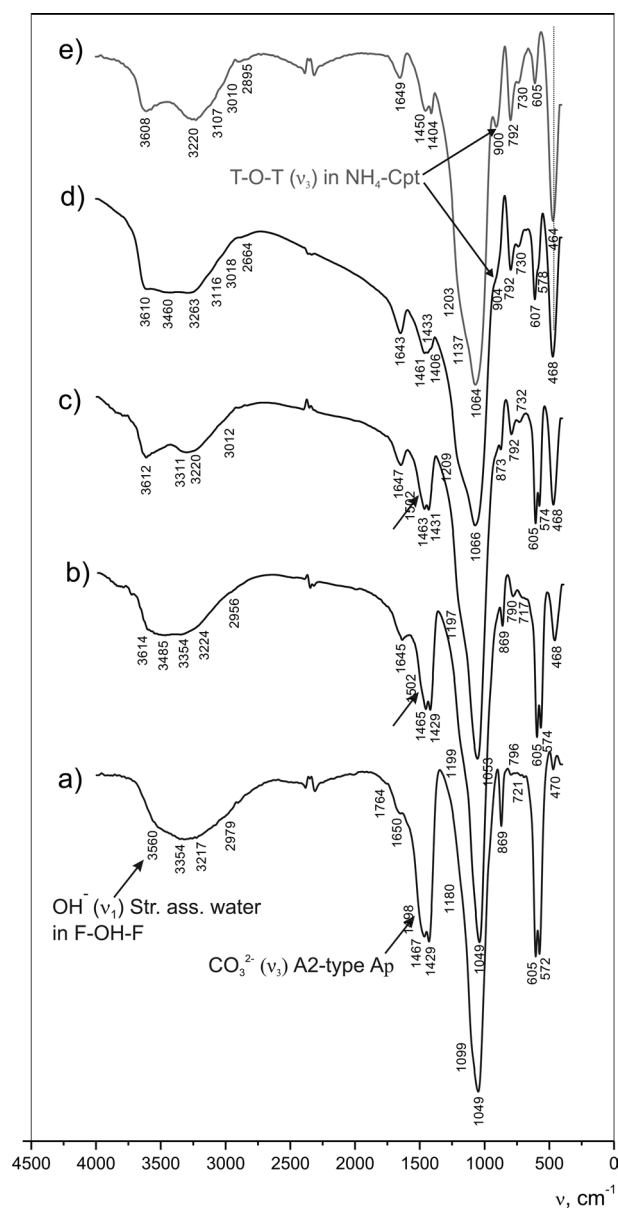
Fig. 4. IR spectra of TCA samples: a) Ap; b) 80:20; c) 50:50; d) 20:80 and e) NH_4-Cpt

Table 2. IR data of Ap and NH$_4$-Cpt and their mixtures in mode of TCA

No	Band position, cm^{-1}					Vibrational Mode
	Ap	20:80	50:50	80:20	NH$_4$-Cpt	
1.	470	468	468	468	464	Symmetric O-P-O (v_2) bending mode in C-F-Ap Symmetric T-O-T (T=Si, Al) (v_2) bending mode in NH$_4$-Cpt and Symmetric (v_1) stretching mode Me-O (Me= Si, Al)
2.	572 605	574 605	574 605	578 607	– 605	Asymmetric O-P-O (v_4) bending mode in B-type C-F-Ap Asymmetric O-T-O (T=Si, Al) (v_4) bending mode in NH$_4$-Cpt
3.	721	717	–	–	–	Asymmetric O-C-O (v_4) bending mode of CO$_3^{2-}$ in B-type C-F-Ap
4.		790	732 792	730 792	730 792	Symmetric (v_1) stretching mode O-T-O (T= Si, Al) in NH$_4$-Cpt [20]
5.	869	869	873	–	–	Symmetric O-C-O (v_2) bending mode in CaCO$_3$ and B-type CO$_3^{2-}$ in C-F-Ap
6.	–	–	–	904	900	Asymmetric T-O-T (T=Si, Al) (v_3) stretching mode in NH$_4$-Cpt [5]
7.	1049 1099 – 1180	1049 – – 1199	1053 – – 1197	1066 – – 1209	1064 1137 1203	Asymmetric P-O-P (v_3) stretching mode of PO$_4^{3-}$ in C-F-Ap
8.	–	–	–	1406	1404	Asymmetric N-H (v_4) bending mode of NH$_4^+$ in NH$_4$-Cpt
9.	1429 – 1467	1429 – 1465	1431 – 1463	1433 – 1461	1450 –	Asymmetric C-O (v_3) stretching mode of CO$_3^{2-}$ in B-type CFAp and CaCO$_3$
10.	1498	1502	1502	–	–	Asymmetric C-O (v_3) stretching mode A2-type CO$_3^{2-}$ in C-OH-F-Ap [1, 15]
11.	1650 1764	1645 –	1647 –	1643 –	1649 –	Symmetric OH$^-$ (v_2) bending mode in zeolitic water
12.	–	–	3012	3018	3010	Symmetric N-H (v_1) stretching mode of NH$_4^+$ in NH$_4$-Cpt
13.	–	–	–	3116	3107	Asymmetric N-H (v_3) stretching mode of NH$_4^+$ in NH$_4$-Cpt
14.	3200–3430	3230–3485	3240–3440	3220–3440	3230–3430	Symmetric OH$^-$ (v_1) stretching mode in zeolitic water
15.	3560	–	–	–	–	Symmetric OH$^-$ (v_1) stretching mode in structure associate water [21]
16.	–	3614	3612	3610	3608	Symmetric (v_1) stretching mode of OH$^-$ directly bonded to Si [22]

ion occupies A (A2) type position [14–17]. Such carbonate ion substitutions in the apatite structure result in samples with violated stoichiometry (Ca/P > 1.667). This carbonate-containing, non-stoichiometric apatite is thermally less stable and exhibits higher citrate and citric solubility [7, 18].

Similar changes occur in the positions of the hydroxyl ion as a result of TCA (Fig. 5c). Both decrease of band intensity and appearance of new low intensity bands in the range 3535–3540 cm^{-1}, indicating increased amount of OH$^-$ in fluorine chains (F-OH-F) have been observed.(Fig. 5c small picture). This leads to a band shift [19] towards the higher frequency, illustrated by the spectra on Figs. 4–5c. Observed effects are in correlation with the concept of formation of nano-sized phase with low degree of crystallinity and increased solubility of the activated samples in 2% citric acid.

The XRD and IR spectroscopy data in this work are confirmed by results, concerning the thermal behaviour of TCA Tunisian apatite and its mixture with Cpt [7]. It has been considered that changes
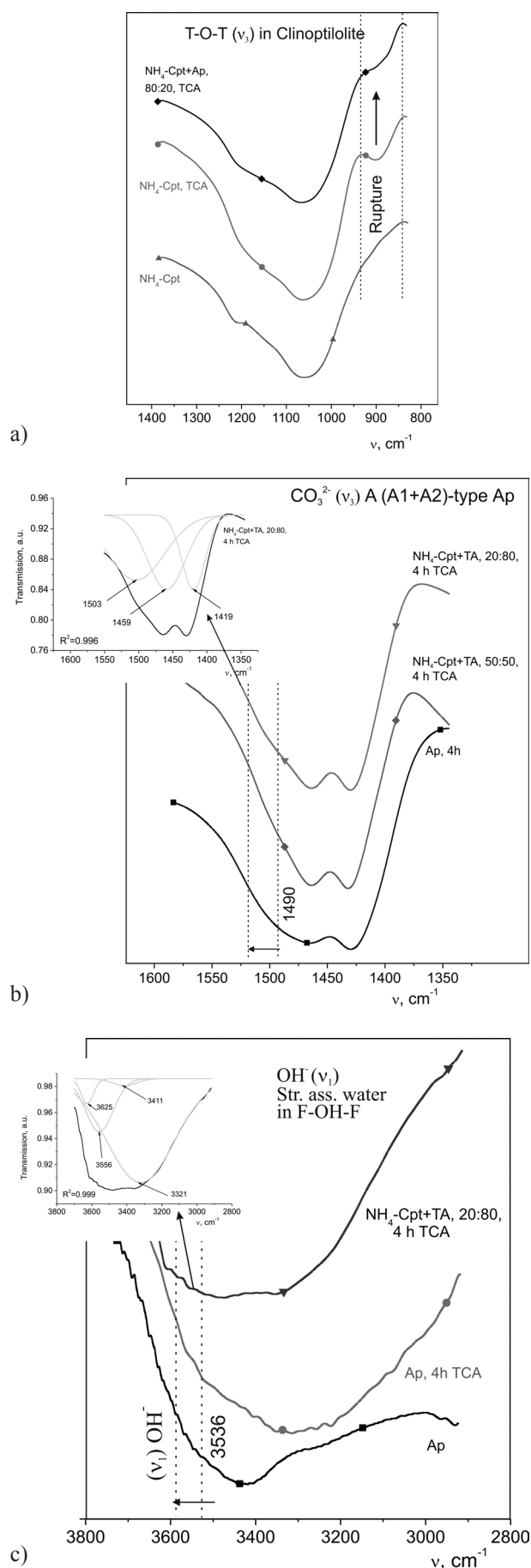
Fig. 5. Structural changes observed in IR spectra of: a) samples with NH_4-Cpt domination; b) and c) samples with Ap domination

in the temperature range 520–840 °C are related to isomorphic substitutions in the apatite structure.

CONCLUSIONS

– The TCA leads to deformation and rupture of Si-O-Si and Si-O-Al bonds and decreasing of ion-exchange capacity in the clinoptilolite sample;

– The activation provokes amorphization and structural defects in apatite structure, which leads to increased reactivity, especially in the case of apatite domination;

– The results of the applied methods provide the opportunity to explore the structural and phase transformations, reactions of solid phase synthesis and degradation in natural samples and their mixtures, as well as to select the most appropriate conditions for tribochemical treatment.

REFERENCES

1. M. V. Chaikina, *Mechanochemistry of natural and synthetic apatites*, Novosibirsk, Publishing house of SB RAS, Branch "GEO", 2002.
2. E. R. Allen, D. W. Ming, in: *Natural Zeolites'93: Occurrence, Properties, Use,* D. W. Ming, F. A. Mumpton (eds.), Int. Comm. Natural Zeolites, New York, Brockport, 1993, p. 477.
3. T-M. Lai, D. Elerl, *Zeolites*, **6**, 129 (1986).
4. T. S. Yusupov, L. G. Shumskaya, E. A. Kirillova, V. V. Boldyrev, *J. of Mining Sci.*, **42**, 2, 189 (2006).
5. T. S. Yusupov, L. G. Shumskaya, *J. of Mining Sci.*, **38**, 2, 177 (2002).
6. A. Toneva, N. Petrova, S. Bakardjieva, in: *Proc. Kontact'97*, N. Manolov (ed.), Sofia, 1997, p. 45.
7. V. Petkova, E. Serafimova, N. Petrova, Y. Pelovski, *J. of Therm. Analysis and Calor.*, in press.
8. N. Petrova, V. Petkova, in: *Book of abstracts of 8th International Conference on the Occurrence, Properties, and Utilization of Natural Zeolites, Zeolites 2010*, O. E. Petrov Y. K. Tzvetanova (eds.), Prof. Marin Drinov Academic Publishing House, Sofia, 2010, p. 212.
9. K. Tonsuadu, K. Rimm, M. Veiderma, *Phosphorus, Sulphur and Silicon*, 84, 73 (1993).

10. V. Yaneva, O. Petrov, V. Petkova, *Mater. Research Bull.*, **44**, 693 (2009).
11. V. Petkova, V. Yaneva, *J. of Balkan Tribolog. Assoc.*, **16** (1), 88 (2010).
12. V. Petkova, Yu. Kalvachev, O. Petrov, in: *Proc. Ist National Crystallographic Symposium*, October 2009, p. 74, (http://www.clmc.bas.bg/symp09/docs/First_Cryst_Symp.pdf).
13. L. G. Shumskaya, E. A. Kirillova, T. S. Yusupov, *J. of Mining Sci.,* **35** (1), 96 (1999).
14. E. F. Michael, *Biomaterials,* **30**, 1473 (2009).
15. M. E. Fleet, X. Liu, *J. Solid State Chem.,* **174**, 412 (2003).
16. M. E. Fleet, X. Liu, P. L. King, *Amer. Mineral.*, **89**, 1422 (2004).
17. M. E. Fleet, X. Liu, *Amer. Mineral.*, **93**, 1460 (2008).
18. N. Senamaud, D. Bernach-Assollant, E. Champion, M. Heughebaert, C. Rey, *Solid State Ionics*, **101-103**, 1357 (1997).
19. G. Penel, G. Leroy, C. Rey, B. Sombret, J. P., Huvenne, E. Bres, *J. of Mater. Sci.: Materials in Medicine,* **8**, 271 (1997).
20. H. Tanaka, N. Yamasaki, M. Muratani, R. Hino, *Mater. Research Bull.*, **38**, 713 (2003).
21. L. Rintou, E. Wentrup-Byrne, Sh. Suzuki, L. Grøndahl, *J Mater Sci: Mater. Med.,* 1701 (2007).
22. M. T. Blanco Varela, S. Martínez Ramírez, I. Ereña, M. Gener, P. Carmona, *Applied Clay Sci.*, **33**, 149 (2006).

СТРУКТУРНИ ПРОМЕНИ В СИСТЕМАТА ПРИРОДЕН АПАТИТ – NH$_4$ КЛИНОПТИЛОЛИТ ПРИ ТРИБОАКТИВАЦИЯ

Н. Петрова*, В. Петкова

Институт по минералогия и кристалография, Българска академия на науките, София, България

(Резюме)

Трибоактивацията на смеси от природен фосфат и клиноптилолит благоприятства преминаването на трудно усвояемите от растенията P$_2$O$_5$ форми в лесноусвояеми. Това е един нетрадиционен метод за решаване на екологични и суровинни проблеми. Смеси от туниски фосфорит и NH$_4$-обменена форма на клиноптилолит от българското находище Бели Пласт (в различно отношение) са активирани в планетарна мелница. Структурните промени в смесите, в резултат на активацията, рефлектират върху повишаване на разтворимостта на P$_2$O$_5$. Тези промени са констатирани с помощта на XRD метод и IR спектроскопия. Получените резултати показват протичането на йонообменни реакции между природния апатит и NH$_4$ клиноптилолит, както и деформация или прекъсване на Si-O-Si и Si-O-Al връзки в клиноптилолита, от една страна и изоморфизъм в структурата на апатита от друга страна.

New phases of K, Eu-silicate in the family of compounds with the orthorhombic pellyite-like unit cell

R. K. Rastsvetaeva*, S. M. Aksenov

Shubnikov Institute of Crystallography, Russian Academy of Sciences, Leninskii pr. 59, Moscow, 119333 Russia

The structures of three phases of the synthesized europium potassium silicate were determined by X-ray diffraction. Two of these phases crystallize in a new structural type. The chemical formulas of the phases were determined. The orthorhombic unit-cell parameters of all three phases are equal: $a = 14.852(1)$ Å, $b = 15.902(1)$ Å, $c = 7.243(1)$ Å, sp. gr. $P2_12_12$ (phase **I**) and sp. gr. *Pbam* (phases **II** and **III**). The structures were solved by direct methods and refined from X-ray diffraction data collected from one crystal to $R = 0.0271$, 0.0479, and 0.0582 based on 4370, 3320, and 2498 reflections, respectively, with $|F| > 3\sigma(F)$. The crystalchemical formulas of the phases ($Z=4$) are $K_3Eu^{3+}[Si_6O_{15}] \cdot 2H_2O$, $K_3Eu^{3+}[Si_6O_{13}(OH)_4] \cdot 2H_2O$, and $K_3Eu^{3+}[Si_4O_{9.5}(OH)](OH)_2 \cdot 5.5H_2O$. The structure of phase **I** consists of silicon–oxygen sheets $[Si_6O_{15}]$ analogous to those found in the isostructural compound $K_3Nd[Si_6O_{15}] \cdot 2H_2O$. In the structures of phases **II** and **III**, the ribbons $[Si_6O_{17}]$ and $[Si_8O_{21}]$ run along the shortest c axis and are linked together by Eu^{3+} octahedra and trigonal prisms to form three-dimensional layered and framework structures containing K atoms between the sheets and in the channels.

Key words: europium potassium silicate, X-ray diffraction, crystal structure, crystal chemistry, endotaxy.

INTRODUCTION

Eu-containing potassium and sodium silicates are of interest because of photoluminescence, ion-exchange and some other properties of these microporous compounds. The crystals were synthesized at the Vinogradov Institute of Geochemistry and Analytical Chemistry, Siberian Division, Russian Academy of Sciences, by a research group headed by V.L. Tauson. The hydrothermal synthesis of Eu-containing phases was carried out from a mixture of silicon, aluminum, and europium oxides under a total pressure of 1000 atm and temperature 500 °C during 45 days in autoclaves [1]. The colorless transparent crystals were synthesized as rhombic prisms up to 1.5 mm in length. The chemical composition of the phases was determined on a JXA-8200 electron probe X-ray microanalyzer and the nonstoichiometrycal formula calculated for six Si atoms is $Eu_{0.84}Al_{0.03}Si_6K_{1.98}O_{14.31}$.

Here we report on study by X-ray diffraction of Eu-containing phases. Two crystals were studied, and three different phases having the pellyite unit cell were found in each crystal. The simultaneous presence of several phases in the same crystal has not been structurally studied previously.

EXPERIMENTAL

The X-ray diffraction data collected from two crystals within a full sphere of reciprocal space on an Oxford Diffraction Xcalibur diffractometer equipped with a CCD detector are presented in Table 1. Data sets contain averaged 4805 and 4477 $|F|>3\sigma(F)$ respectively. An analysis of the systematic absences suggested sp. grs. *Pbam* and $P2_12_12$. It should be noted that five weak reflections $0kl$ with $k \neq 2n$ and $h0l$ with $h \neq 2n$ were inconsistent with sp.gr. *Pbam*.

It was found that the X-ray diffraction patterns of both crystals of europium potassium silicate are superimpositions of three individual phases. Structural investigation of these phases was a challenging task taking into account that it was impossible to separate the contributions of the three components in overlapping reflections, which made it difficult to localize oxygen atoms belonging to water molecules and resulted in high R factors, particularly for the third phase. Inspection of reciprocal diffraction space demonstrated that there were no additional satellite reflections or diffuse streaks be-

---

Table 1. Crystallographic characteristics and X-ray data-collection statistics

Crystal samples	1	2
a, Å	14.852(1)	14.858(1)
b, Å	15.902(1)	15.890(1)
c, Å	7.243(1)	7.245(1)
V, Å^3	1710.60(3)	1710.49(3)
Diffractometer	Xcalibur Oxford Diffraction, CCD detector	
Radiation, λ, Å	MoK$_\alpha$; 0.71073	
Scan mod	ω	
θ_{max}, deg	55.01	54.95
h, k, l ranges	$-34<h<29, -35<k<31, -16<l<16$	$-29<h<32, -34<k<34, -16<l<16$
Crystal dimensions, mm	0.20×0.25×0.27	0.25×0.25×0.5
Number of measured / independent reflections	15038 IFI>3σ(F) / 4805 IFI>3σ(F)	14371 IFI>3σ(F) / 4477 IFI>3σ(F)
R_{int}	0.016	0.020
Computational program	AREN [2,3]	
Program for absorption correction	DIFABS [4]	

tween main reflections which were the evidence of the zonal structure of crystals or modulation nature of cation distribution.

The translation lattices of all phases are described by an orthorhombic unit cell parameters a = 14.852(1) Å, b =15.902(1) Å, c = 7.243(1) Å, sp. gr. $P2_12_12$ (phase **I**) and sp. gr. *Pbam* (phases **II** and **III**). The most reflections (~95%) took part in the indexing in the frame of these cell parameters. The strongest reflections corresponding to fragments of the sublattice formed by europium, potassium, and part of the silicon atoms are common to the three structures. Independent reflections are individual and were included in the least-squares refinement of each component, whereas the remaining reflections were rejected based on the residual. The maximum number of reflections (~90%) belongs to phase **I**, and the minimum number of reflections (~50%) belongs to phase **III**. For phase **II**, ~70% of the total

number of reflections was used. In crystal 2 the ratio of the phases is the same, whereas the intensities of reflections belonging to phases **II** and **III** are redistributed in accordance with their volumes. Thus, the volume of phase **III** in crystal 2 is larger. This allowed us to obtain the structural model of phase **III** by direct methods, whereas the model of phase **II** was found by direct methods only with the use of the experimental data collected from crystal 1.

The crystal structures of all three phases were found by direct methods with following the automatic successive approximation procedure [2, 3]. Some water molecules were found from the difference electron density map. All three structures refined with the use of the same X-ray diffraction data set collected from crystal 1 (Table 2). All calculations were carried out with the use of the AREN program package [2,3]. The absorption correction was applied using the DIFABS program [4].

Table 2. Some crystal-structural data for three phases (all structures were refined with the use of the X-ray diffraction data set collection from crystal 1)

Phases	I	II	III
Chemical formula (Z=4)	K$_3$Eu^{3+}[Si$_6$O$_{15}$]·2H$_2$O	K$_3$Eu^{3+}[Si$_6$O$_{13}$(OH)$_4$]·2H$_2$O	K$_3$Eu^{3+}[Si$_4$O$_{9.5}$(OH)](OH)$_2$·5.5H$_2$O
Sp. gr., Z	$P2_12_12$, 4	*Pbam*, 4	*Pbam*, 4
Number of independent reflections	4370 IFI>3σ(F)	3320 IFI>3σ(F)	2498 IFI>3σ(F)
Density ρ_{calc}, g/cm^3	2.771	2.911	2.654
R factor upon isotropic/ anisotropic refinement	7.06 / 2.71	7.86 / 4.79	12.73 / 5.82

Table 3. Atomic coordinates and equivalent isotropic displacement parameters (B_{eq}) for structure of phase I

Atom	x	y	z	B_{eq}, Å^2
Eu1	0	0	–0.0034(1)	0.59(2)
Eu2	0	0.5	0.0000(1)	0.77(1)
K1	0.0890(1)	0.4295(1)	0.490(1)	3.61(4)
K2	0.3422(1)	0.3445(1)	0.504(1)	4.16(3)
K3	0.1162(1)	0.2132(1)	1.027(1)	4.92(4)
Si1	0.2001(1)	0.0380(1)	0.7199(1)	0.68(5)
Si2	0.3665(1)	0.1452(1)	0.2861(1)	0.51(5)
Si3	0.3729(1)	0.2908(1)	0.002(1)	0.56(4)
Si4	0.3643(1)	0.1440(1)	0.7157(2)	0.88(5)
Si5	0.2182(1)	0.4093(1)	–0.001(1)	0.78(4)
Si6	0.2001(1)	0.0374(1)	0.2829(2)	0.97(5)
O1	0.2666(2)	0.3170(1)	0.002(2)	1.5(2)
O2	0.4404(1)	0.3678(1)	0.001(2)	1.2(2)
O3	0.4323(2)	0.0696(2)	0.243(1)	1.5(2)
O4	0.1124(2)	0.3982(2)	0.002(2)	1.8(2)
O5	0.0999(2)	0.0500(3)	0.221(1)	1.7(2)
O6	0.3885(2)	0.2317(2)	0.177(1)	1.3(2)
O7	0.3882(3)	0.2333(3)	0.814(1)	1.9(2)
O8	0.2555(3)	0.4573(2)	0.180(1)	2.0(2)
O9	0.2105(2)	0.0154(2)	0.505(2)	1.6(2)
O10	0.0984(3)	0.0528(3)	0.781(1)	1.9(2)
O11	0.2592(2)	0.1217(2)	0.759(1)	1.1(2)
O12	0.3692(2)	0.1734(2)	0.502(1)	1.6(2)
O13	0.2614(3)	0.1224(3)	0.238(1)	1.7(2)
O14	0.4315(3)	0.0706(3)	0.757(1)	1.9(2)
O15	0.2518(3)	0.4559(3)	0.812(1)	1.9(2)
W(1)	0.014(1)	0.132(1)	0.496(3)	6.3(2)
W(2)	0.164(1)	0.270(1)	0.417(2)	6.8(1)

Because of the lack of precise chemical data, the atomic positions in the models were identified based on the crystal-chemical criteria. The H_2O molecules and OH-groups were revealed by the bond-valence method according to Brese [5]. Atomic coordinates and equivalent isotropic displacement parameters (B_{eq}) for the structures are given in Tables 3–5.

The Eu atoms are in special positions $00\,z$ and $0\,0.5\,z$ and have an octahedral or trigonal-prismatic coordination with average bond lengths ranging from 2.31 to 2.32 Å (Table 6), which confirm there trivalent state. As a result, we determined the chemical and crystal-chemical formulas of the three individual phases.

STRUCTURES DESCRIPTION

Figure 1 shows the silicon–oxygen groups, which were found in the structures of the three phases and pellyite. The full structures of the phases I-III and pellyite are presented in Figs. 2–5.

Phase I

The structure of phase **I** was solved with the use of the X-ray diffraction data, which were collected from crystal 1 and merged in sp. gr. $P2_12_12$. Atomic coordinates and equivalent isotropic displacement parameters (B_{eq}) for this structure are given in Table 3. The Eu atoms are in special positions $00\,z$ and $0\,0.5\,z$ and have an octahedral coordination with bond lengths ranging from 2.280(2) to 2.340(4) Å (Table 6). The Si atoms are in tetrahedral sites surrounded by O atoms with the following bond lengths: Si1–O = 1.589(5)–1.618(3) Å; Si2–O = 1.580(4)–1.620(4) Å; Si3–O = 1.583(2) –1.656(6) Å; Si4–O = 1.564(5)–1.631(3) Å; Si5–O = 1.581(3)–1.634(3) Å; and Si6–O = 1.566(3)– 1.662(5) Å. The tetrahedra are linked together to form diortho groups, which are arranged perpendicular to each other in a chess-board fashion and are linked together by shared vertices to form corrugated silicon–oxygen sheets containing loops of three types (eight-, six-, and four-membered) (Fig. 1a). The sili-
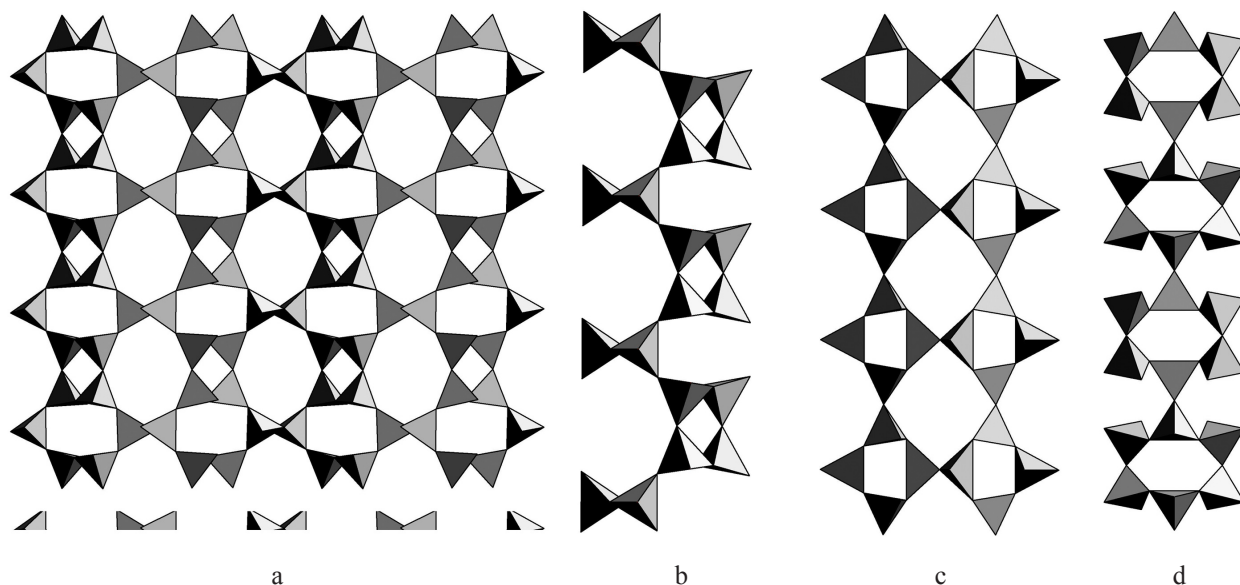
Fig. 1. Silicon–oxygen sheet $[Si_6O_{15}]$ in the structure of phase **I** (a); silicon–oxygen ribbon $[Si_6O_{17}]$ in the structure of phase **II** (b); the ribbon $[Si_8O_{21}]$ in the structure of phase **III** (c) and $[Si_6O_{17}]$ in the structure of pellyite (d)

con sheets are linked together by the europium octahedra to form a mixed framework structure. The latter contains channels running along the shortest period (~7 Å) which are occupied by potassium atoms and water molecules coordinated to potassium (Fig. 2). A similar structural type has been found previously in the compound $K_3Nd[Si_6O_{15}].2H_2O$ [6, 7] with the symmetry described by the sp. gr. *Pbam* in both publications. Although the structural motif of the K,Nd-containing compound is identical to that of the Eu-containing compound, the symmetry of the latter is reduced to $P2_12_12$ due to the displacement of some atoms from the symmetry plane *m*.
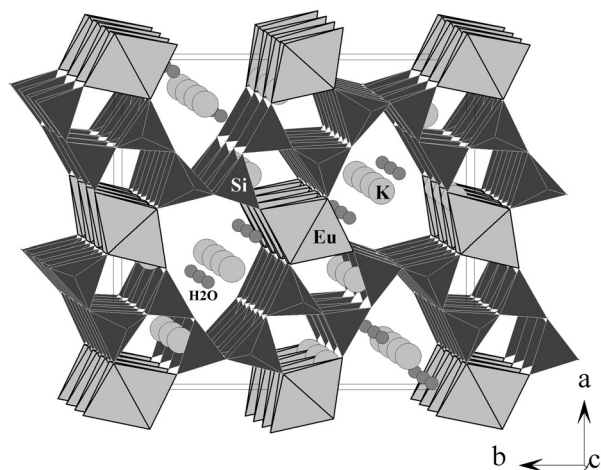
Fig. 2. Crystal structure of phase I

The chemical formula of phase I found from the X-ray diffraction data is (for $Z=4$): $K_3Eu^{3+}[Si_6O_{15}] \cdot 2H_2O$.

Phase II

Atomic coordinates and equivalent isotropic displacement parameters (B_{eq}) for phase II structure are given in Table 4. The principal compositional and structural characteristics of phase **II** are reflected in its crystal chemical formula ($Z = 4$) $Eu^{3+}K_3[Si_6O_{13}(OH)_4] \cdot 2H_2O$. The Eu atoms occupy special positions $xy0$ ($x \sim 0$, $y \sim 0.25$) and are in an octahedral environment with the Eu–O bond lengths ranging from 2.298(7) to 2.322(6) Å (Table 6). Four independent Si atoms are in tetrahedral sites surrounded by O atoms with the following Si–O bond lengths: Si1–O = 1.571(5)–1.77(1) Å; Si2–O = 1.578(5)–1.632(2) Å; Si3–O = 1.587(7)–1.633(6) Å, and Si4–O = 1.560(7)–1.76(1) Å. The Si tetrahedra are linked together to form diortho groups, which form corrugated ribbons of a new type running along the shortest *c* axis. In spite of the fact that the ribbons have a $[Si_6O_{17}]$ composition identical to that found in pellyite, these ribbons are topologically different (Fig. 1b, 1d). The asymmetric ribbons of phase **II** are cutouts of the above-described layer. The ribbons are arranged parallel to each other and are linked together by discrete Eu octahedra to form mixed sheets perpendicular to the longest period (~16 Å). The K atoms and water molecules involved in the coordination environment of K are located between the sheets and in channels

311

Table 4. Atomic coordinates and equivalent isotropic displacement parameters (B_{eq}) for structure of phase II

Atom	x	y	z	B_{eq}, Å^2
Eu	−0.0006(1)	0.2510(1)	0	0.66(1)
K1	0.3711(4)	0.4243(3)	0.5	4.02(3)
K2	0.3441(3)	0.0939(2)	0.5	3.52(3)
K3	0.1463(4)	0.1934(4)	0.5	6.12(3)
Si1	0.1346(1)	0.3947(1)	0.2854(2)	0.70(4)
Si2	0.2999(1)	0.2877(1)	0.2816(2)	0.84(4)
Si3	0.2817(1)	0.1593(1)	0	0.81(6)
Si4	0.1262(1)	0.0411(1)	0	0.45(6)
O1	0.2330(4)	0.0672(3)	0	1.4(3)
O2	0.289(1)	0.264(1)	0.5	1.5(3)
O3	0.388(4)	0.1486(4)	0	1.8(2)
O4	0.252(1)	0.2066(3)	0.185(1)	2.0(1)
O5	0.248(1)	0.3731(3)	0.240(1)	2.4(2)
O6	0.0688(4)	0.3201(3)	0.231(1)	1.7(2)
O7	0.0593(4)	0.1168(4)	0	1.3(2)
O8	0.4006(3)	0.3022(4)	0.219(1)	1.8(2)
O9	0.191(1)	0.405(1)	0.5	9.1(1)
OH1	0.379(1)	0.476(1)	0.198(2)	5.40(8)
OH2	0.1088(4)	0.4819(4)	0.179(1)	1.8(2)
W(1)	0.024(1)	0.104(1)	0.5	4.3(1)
W(2)	0.484(2)	0.173(2)	0.5	6.5(1)
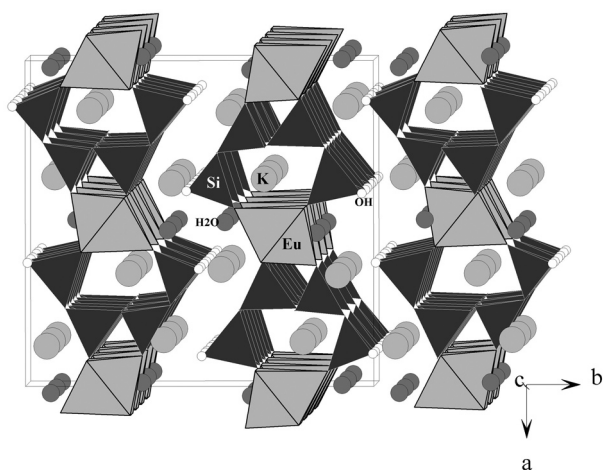
Fig. 3. Crystal structure of phase II

inside the ribbons (Fig. 3). The mixed sheets are also linked by hydrogen bonds between OH groups and water molecules to form a three-dimensional structure.

Phase III

Atomic coordinates and equivalent isotropic displacement parameters (B_{eq}) for the phase III structure are given in Table 5. The principal compositional and structural characteristics of the mineral are reflected in its crystal-chemical formula ($Z = 4$): $K_3Eu^{3+}[Si_4O_{9.5}(OH)](OH)_2 \cdot 5.5H_2O$. The europium atoms in phase **III**, like those in phase **II**, are in special positions $xy0$ ($x \sim 0.25$, $y \sim 0$) with the Eu–O bond lengths ranging from 2.30(1) to 2.32(1) Å (Table 6). This phase differs from the other two phases in that the Eu octahedron is transformed into a trigonal prism. Two vertices of the prism are occupied by OH-groups. The Si atoms are in tetrahedral sites surrounded by O atoms with the following Si–O bond lengths: Si1–O = 1.55(1)–1.68(1) Å; Si2–O =1.569(8)–1.65(1) Å; and Si3–O = 1.523(3)–1.74(1) Å. The tetrahedra are linked together to form strongly corrugated silicon–oxygen ribbons of a new type. It should be noted that the ribbons in phase **II** are exact cutouts of the sheet, whereas the configuration of the ribbon in phase **III** only partially corresponds to the sheet and inherits the fragment of eight-membered rings. The ribbon formed as a result of this transformation is unique (Fig. 1c). The ribbons are parallel to the short c axis and are arranged in a chess-board fashion along the diagonals of the (001) plane. The Eu trigonal prisms are located between the silicon ribbons and link the latter to form a mixed framework structure whose channels are occupied by two types of potassium polyhedra with eight and nine vertices, respectively (Fig. 4).

Table 5. Atomic coordinates and equivalent isotropic displacement parameters (B_{eq}) for structure of phase III

Atom	x	y	z	B_{eq}, Å^2
Eu	0.2490(1)	−0.0002(1)	0	0.79(1)
K1	0.1321(1)	0.2880(1)	0	1.56(4)
K2	0.1663(2)	0.0676(2)	0.5	2.22(4)
K3	0.4051(2)	0.1563(2)	0.5	2.31(4)
Si1	0.3812(2)	0.2062(2)	0	1.17(7)
Si2	0.3842(1)	0.3553(1)	0.2853(3)	0.88(5)
Si3	0.0323(2)	0.0909(2)	0	1.00(1)
O1	0.377(1)	0.325(1)	0.5	1.6(3)
O2	0.139(1)	0.102(1)	0	1.9(3)
O3	0.361(1)	0.267(1)	0.186(1)	1.9(2)
O4	0.317(1)	0.430(1)	0.245(1)	1.7(2)
O5	0.488(1)	0.375(1)	0.230(1)	2.3(2)
O6	0.5	0.5	0	4.8(3)
O7	0.314(1)	0.132(1)	0	1.7(3)
OH1	0.485(1)	0.183(1)	0	1.6(3)
OH2	0.149(1)	0.450(1)	0.217(1)	1.9(28)
*W*1	0.099(1)	0.227(1)	0.5	2.8(3)
*W*2	0.019(1)	0.381(1)	0.259(2)	3.3(2)
*W*3	0	0.5	0.5	5.3(3)
*W*4	0.240(1)	0.206(1)	0.5	4.4(2)
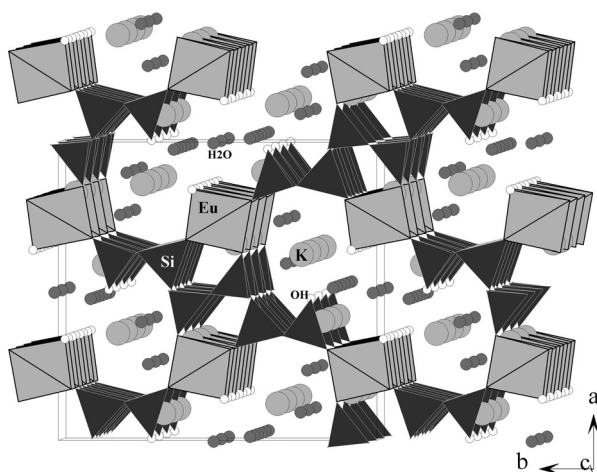
Fig. 4. Crystal structure of phase III

DISCUSSION

The epitaxy, or the oriented growth of one crystal on another, resulting in the coherent intergrowth of two lattices is the most commonly observed process. The topotaxy or syntaxy are also described as intergrowths of phases but within the same crystal. We studied by X-ray diffraction the topotaxy of natural Ba,Mn-titanosilicate [8] because it was possible to separate the reflections belonging to each of two mineral modifications with the axes of their unit cells turned at an angle of 60°.

The phenomenon observed in this study can be assigned to endotaxy, as the oriented growth of one crystal inside another. Endotaxy appears in crystals because all the three phases with equal unit cell parameters, similar symmetry, chemically

Table 6. Selected bond lengths (Å) in the structure of phases I, II, III

Phase-I				Phase-II		Phase-III	
Eu1-O2	2.280(2)x2	Eu2-O3	2.310(4)x2	Eu-O3	2.298(7)	Eu-O2	2.30(1)
Eu1-O10	2.300(5)x2	Eu2-O14	2.322(5)x2	Eu-O6	2.302(6)x2	Eu-O7	2.30(1)
Eu1-O5	2.340(4)x2	Eu2-O4	2.324(5)x2	Eu-O7	2.312(6)	Eu-O4	2.317(7)x2
				Eu-O8	2.322(6)x2	Eu-OH2	2.320(9)x2
average	2.307	average	2.319	average	2.310	average	2.312

Table 7. Crystalstructural data for the family of compounds with the orthorhombic pellyitelike unit cell and related Si,O-radicals

Formula	Si,O-radicals	Unit cell dimensions, Å	Space group	References
$K_3Nd[Si_6O_{15}]\cdot 2H_2O$	$[Si_6O_{15}]_{??}$	$a=16.008(2)$ $b=15.004(2)$ $c=7.2794(7)$	*Pbam*	[6,7,9]
$K_3Nd[Si_6O_{15}]$	$[Si_6O_{15}]_{??}$	$a=14.370(2)$ $b=15.518(2)$ $c=14.265(2)$	*Bb2₁m*	
$Cs_2Th[Si_6O_{15}]$	$[Si_6O_{15}]_{??}$	$a=16.2920(10)$ $b=7.2154(6)$ $c=13.6800(10)$	*Pca2₁*	[10]
$K_3Eu^{3+}[Si_6O_{15}]\cdot 2H_2O$	$[Si_6O_{15}]_{??}$	$a=14.852(1),$ $b=15.902(1),$ $c=7.243(1)$	*P2₁2₁2*	[1, present study]
$K_3Eu^{3+}[Si_6O_{13}(OH)_4]\cdot 2H_2O$	$[Si_6O_{17}]_?$		*Pbam*	
$K_3Eu^{3+}[Si_4O_{9.5}(OH)](OH)_2\cdot 5.5H_2O$	$[Si_8O_{21}]_?$			
$Ba_3CaCu[Si_6O_{17}]$	$[Si_6O_{17}]_?$	$a=14.405(2)$ $b=16.077(2)$ $c=7.088(2)$	*B2mb*	[11]
Pellyite $Ba_2CaFe^{2+}_2[Si_6O_{17}]$	$[Si_6O_{17}]_?$	$a=15.677(4)$ $b=7.15(2)$ $c=14.209(6)$	*Cmcm*	[12]

and structurally related and coherently oriented. As it has been shown previously, these three phases crystallize in sp. gr. *Pbam* and its lower subgroup $P2_12_12$; they have identical europium and potassium sublattices; and both silicon–oxygen ribbons are cutouts of the same silicon–oxygen sheet. The presence of these phases in the crystals under study is, apparently, attributed to the specific crystallization conditions. Thus, nonequilibrium crystal growth for 45 days is accompanied by the fractionation of chemical elements due to the formation of additional compounds. The true volumes of these phases are unknown. However, it can be suggested that phase **I** containing the silicon–oxygen sheet dominates over the other two phases in both crystals; phase **II** containing $[Si_6O_{17}]$ ribbons dominates over phase **III** consisting of $[Si_8O_{21}]$ ribbons in crystal 1; and, on the contrary, phases **I** and **III** are the largest components in crystal 2. The difference in the volumes of the three phases is indirectly confirmed by the fact that these phases are characterized by different intensities of the corresponding reflections in the experimental data collected from two crystals.

Eight synthetic compounds and natural mineral with orthorhombic pellyite-like unit-cell are summarized in Table 7. The base of their structures is formed by cations with close ionic-radii: Ca (1.00 Å), Eu^{3+} (0.95 Å), Nd^{3+} (0.98 Å), Th^{4+} (0.94 Å). Their special positions led to the parameters of orthorhombic unit-cells which vary in the range of $a=15.52–16.29$ (av. 15.9) Å, $b=13.68–15.00$ (av. 14.34) Å, $c=7.1–7.28$ (av. 7.19) Å. These variations
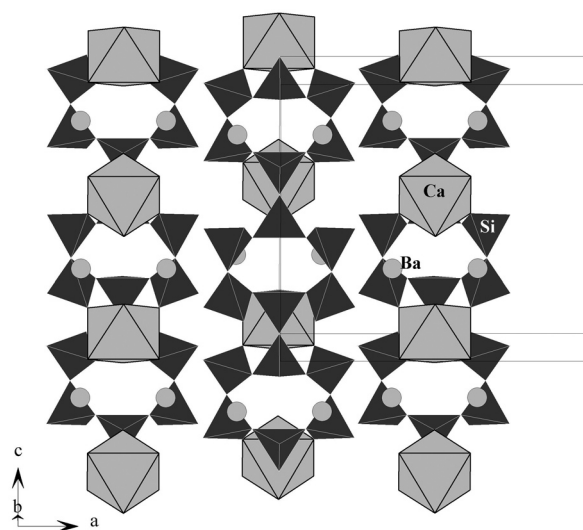
Fig. 5. Crystal structure of pellyite. Fe tetrahedra are not shown

are related to the presence of large cations K, Ba, Cs and water molecules in the channels of the structures, as well as additional small cations Fe^{2+} in pellyite and Cu in its synthetic analog.

These representatives have different Si,O radicals related to the $[Si_6O_{15}]$ sheet which was found in four structures. Among other structures three have $[Si_6O_{17}]$ ribbons (including two pellyitelike bands) and one $[Si_8O_{21}]$ which are cutouts from the sheet and two of them present unknown for to-day Si,O-radicals. The bands $[Si_6O_{17}]$ in the pellyitelike

structures (Fig. 5) are also cutouts from the sheet but in transverse direction.

CONCLUSIONS

To sum up, the structure solution and refinement of three phases showed the presence of endotaxic (or syntaxic) intergrowths in crystals of synthetic europium potassium silicate having a orthorhombic pellyite-like unit cell. The endotaxy, which was found for the first time and characterized by X-ray diffraction, is apparently not a rare phenomenon, but its observation by X-ray diffraction methods presents difficulties as well as high-resolution transmission electron microscopy is inapplicable because of the presence of hydrogen containing complexes of OH and H_2O in the compounds under study.

The presence of three endotaxic phases with the different ratios Eu:Si:O:H_2O = 1:6:15:2; 1 :6:17:2; and 1:4:12.5:5.5 (phases **I**, **II**, and **III**, respectively) in the same single crystal under study explains why attempts to determine the chemical formula of the compound by electron probe microanalysis failed.

REFERENCES

1. R. K. Rastsvetaeva, S. M. Aksenov, V. K. Taroev, *Crystallogr. Reports*, **55** (6), 1041 (2010).
2. V. I. Andrianov, *Sov. Phys. Crystallogr.*, **32** (1), 130 (1987).
3. V. I. Andrianov, *Sov. Phys. Crystallogr.*, **34** (3), 352 (1989).
4. N. Walker, D. Stuart, *Acta Crystallogr. A*, **39** (2), 158 (1983).
5. N. E. Brese, M. O'Keefe, *Acta Crystallogr. B*, **47**, 192 (1991).
6. D. Yu. Pushcharovskii, O. G. Karpov, E. A. Pobedimskaya, N. V. Belov, *Dokl. Akad. Nauk SSSR*, **234**, 1323 (1977).
7. S. M. Haile, B. J. Wuensch, *Acta Crystallogr. B*, **39**, 335 (1983).
8. R. K. Rastsvetaeva, R. A. Tamazyan, E. V. Sokolova, D. I. Belakovskii, *Sov. Phys. Crystallogr.*, **36** (2), 186 (1991).
9. S. M. Haile, B. J. Wuensch, *Acta Cryst. B,* **56**, 335 (2000).
10. J. D. Woodward, P. M. Almond, T. E. Albrecht-Schmitt, *Acta Cryst. E*, **61**, 58 (2005).
11. R. J. Angel, N. L. Ross, L. W. Finger, R. M. Hazen, *Acta Cryst. C*, **46**, 2028 (1990).
12. E. P. Meagher, *Amer. Min.*, **61**, 67 (1976).

НОВИ (K-Eu) СИЛИКАТНИ ФАЗИ ОТ ГРУПАТА СЪЕДИНЕНИЯ С ОРТОРОМБИЧНА ЕЛЕМЕНТАРНА КЛЕТКА, ПОДОБНА НА ПЕЛИИТОВАТА

Л. К. Расцветаева*, С. М. Аксенов

Институт по кристалография „Шубников", Руска академия на науките, Ленински просп. 59, Москва, 119333 Русия

(Резюме)

Чрез рентгенова дифракция са определени структурите на три синтетични фази на (K-Eu) силикати. Две от тези фази кристализират в нов структурен тип. Изчислени са техните кристалохимични формули и параметрите на елементарната им клетка, които са еднакви: a = 14.852(1) Å, b =15.902(1) Å, c = 7.243(1) Å, пр. гр. $P2_12_12$ (фаза I) и пр. гр. $Pbam$ (фази II и III). Структурите са решени с директни методи с използване на рентгенови дифракционни данни, получени от монокристал с фактори на достоверност R = 0.0271, 0.0479, и 0.0582, на базата съответно на 4370, 3320 и 2498 рефлекса ($|F| > 3\sigma(F)$). Кристалохимичните формули на фазите (Z=4) са $K_3Eu^{3+}[Si_6O_{15}]$. $2H_2O$, $K_3Eu^{3+}[Si_6O_{13}(OH)_4]$. $2H_2O$, и $K_3Eu^{3+}[Si_4O_{9.5}(OH)](OH)_2$. $5.5H_2O$. Структурата на фаза I се характеризира с силициево-кислородни слоеве $[Si_6O_{15}]$, аналогични на тези в изоструктурната фаза $K_3Nd[Si_6O_{15}] \cdot 2H_2O$. В структурите на фази II и III лентите $[Si_6O_{17}]$ и $[Si_8O_{21}]$ следват късата ос c и са свързани помежду си с Eu^{3+}-октаедри и тригонални призми, формирайки триизмерни слоисти и скелетни структури, включващи калиеви атоми между слоевете и в каналите.

Crystal structure of 3-oxo-2-(4-hydroxybenzylidene)-butyric acid ethyl ester

S. Stanchev[1], R. P. Nikolova[2], B. L. Shivachev[2], I. Manolov[1]

[1] *Department of Pharmaceutical Chemistry, Faculty of Pharmacy, Medical University, 2, Dunav St, BG-1000 Sofia, Bulgaria*
[2] *Bulgarian Academy of Sciences, Institute of Mineralogy and Crystallography, 1113 Sofia, Acad. Georgi Bonchev Str., Building 107, Bulgaria*

3-Oxo-2-(4-hydroxybenzylidene)-butyric acid ethyl ester (compound **I**), was synthesized and its structure was investigated by X-ray crystallography, IR, ^{1}H-NMR and mass-spectroscopic analyses. The title compound, $C_{13}H_{14}O_4$, crystallizes in the triclinic crystal system in the space group $\bar{P}1$ with cell parameters: $a = 8.7340(14)$ Å, $b = 9.1602(13)$ Å, $c = 9.1640(30)$ Å, $\alpha = 114.964(15)°$, $\beta = 100.197(18)°$, $\gamma = 108.173(11)°$, and $V = 589.5(3)$ Å^3 ($Z = 2$). The molecules are hydrogen-bonded to chains, running parallel to [110]. Additional short contacts stabilize the three dimensional packing in the structure.

Key words: 3-oxo-2-(4-hydroxybenzylidene)-butyric acid ethyl ester, crystal structure.

INTRODUCTION

The investigations on the interaction between 1,3-dicarbonylic compounds (ethyl acetoacetate or 2,4-pentanedione) and aldehydes or ketones began at the end of XIX century and they are continuing until now [1, 2]. It was accepted that one of the factors for obtaining large diversity of condensation products is the molar ratio of the reactants, the temperature and the catalyst. Recently we started a systematical investigation of the synthetic products of aromatic aldehydes and ethyl acetoacetate in the presence of piperidine as a catalyst. Here we present crystal structure of 3-oxo-2-(4-hydroxybenzylidene)-butyric acid ethyl ester (**I**), $C_{13}H_{14}O_4$ – a side product obtained in the studied system.

EXPERIMENTAL

Synthesis and characterization

The title compound (**I**) was obtained according to the reaction scheme
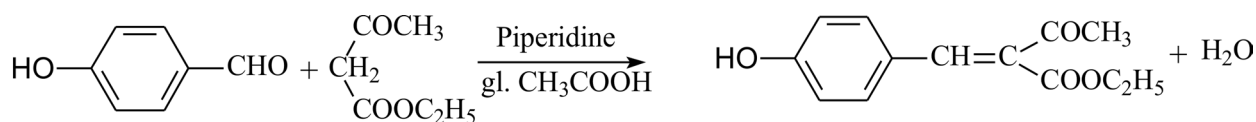
The used materials were 4-Hydroxybenzaldehyde (3.66 g, 0.03 mol), acetoacetic ester (6.5 g, 0.05 mol), piperidine (2.6 g, 0.03 mol), glacial acetic acid (2.4 g, 0.04 mol), and 100 mL distilled water. Yellow rectangular crystals suitable for X-ray diffraction analysis have been obtained after slow evaporation from isopropyl alcohol at room temperature.

Elemental analyses: $C_{13}H_{14}O_4$, (234), (C, H) (calculated/measured): % C 66.66 / 66.50, % H 6.02 / 5.94. UV-VIS spectra: λmax = 206, 224, 286 nm (ethanol);

FTIR (nujol): 3325.7, 1732.3, 1641.6, 1597.3, 1205.7, 819.8 cm^{-1};

^{1}*H NMR* (acetone-d$_6$, 200 MHz): δ = 1.3 (t, J = 7.1 Hz, 3H) (methyl), 2.3 (s, 3H)(methyl), 4.3 (q, J = 7.1 Hz, 2H) (methylene), 6.91–6.85 (m, 2H) (aromatic), 7.44–7.38 (m, 2H) (aromatic), 7.46–7.44 (m, 1H) (methine), 10.5 (s, 1H)(hydroxyl);

^{13}*C NMR* (acetone-d$_6$, 67 MHz): δ = 15, 30, 55, 110, 116, 130, 135, 140, 142, 160, 166, 190, 196;

EIMS: m/z (%) = 234 (100, M$^+$), 233 (57), 220 (10), 219 (69), 217 (17), 205 (15), 191 (25.4), 189 (38.25), 187 (11.3), 175 (8.7), 163 (11.3), 161 (11.3),

160 (28.7), 151 (28.7), 147 (68.7), 146 (11.3), 145 (37.4), 131 (7), 123 (30.4), 120 (9.6), 119 (20), 118

(19.1), 115 (2.6), 107 (6), 91 (20), 89 (19.1), 65 (11.3), 63 (12.1), 53 (5), 45 (0.9).

X-ray single crystal analyses

A crystal of the title compound having approximate dimension 0.22×0.20×0.20 mm was placed on a glass fiber and mounted on an Enraf-Nonius CAD-4 diffractometer. X-ray data collection was carried out at 290 K with graphite monochromatized Mo-Kα radiation ($\lambda = 0.71073$ Å). The unit cell parameters were determined using 15 reflections and refined employing 22 higher-angle reflections, $18 < \theta < 20°$. The $\omega/2\theta$ technique was used for data collection using Nonius Diffractometer Control Software [3].

Lorentz and polarization corrections were applied to intensity data using WinGX [4]. The structure was solved by direct methods using SHELXS-97 [5] and refined by full-matrix least-squares procedure on F^2 with SHELXL-97 [5]. The hydrogen atoms were placed in idealized positions and refined as riding on their parent atoms, with $U_{iso}(H) = 1.2U_{eq}(C$ or $O)$.

RESULTS AND DISCUSSION

The chemical diagram of the studied compound (**I**) is illustrated in Scheme 1 and experimental conditions, crystal data and refinement parameters are summarized in Table 1. Selected

Table 1. Data collection parameters, crystal data and refinement parameters

Data collection parameters	
Enraf Nonius CAD4 diffractometer	$R_{int} = 0.0502$
Radiation source: sealed tube	$\theta_{max} = 29.96°$
Monochromator: graphite	$\theta_{min} = 2.63°$
$T = 290(2)$ K	$h = -12 \quad 12$
non–profiled $\omega/2\theta$ scans	$k = -12 \quad 12$
Absorption correction: none	$l = -12 \quad 12$
6790 measured reflections	3 standard reflections
2436 independent reflections	every 120 min
1933 reflections with $I > 2\sigma(I)$	intensity decay: −1%
Crystal data	
C13 H14 O4	$F_{000} = 248$
$M_r = 234.24$	$D_x = 1.32$ Mg m^{-3}
Triclinic, *P–1*	Melting point: not measured
Hall symbol: −P 1	Mo *K*α radiation
$\lambda = 0.71073$ Å	
$a = 8.734$ (2) Å	Cell parameters from 22 reflections
$b = 9.160$ (3) Å	$\theta = 18.0–28.8°$
$c = 9.163$ (6) Å	$\mu = 0.11$ mm^{-1}
$\alpha = 114.96$ (3)°	$T = 290$ (2) K
$\beta = 100.20$ (3)°	Prism, colorless
$\gamma = 108.17(1)°$	Crystal size:
$V = 589.5(5)$ Å^3	0.22 × 0.20 × 0.20 mm
$Z = 2$	
Refinement parameters	
Refinement on F^2	Primary atom site location: structure-invariant direct methods
Least-squares matrix: full where $P = (F_o^2 + 2F_c^2)/3$	$w = 1/[\sigma^2(F_o^2) + (0.0719P)^2 + 0.0263P]$
$R[F^2 > 2\sigma(F^2)] = 0.052$	$(\Delta/\sigma)_{max} < 0.001$
$wR(F^2) = 0.106$	$\Delta\rho_{max} = 0.20$ e Å^{-3}
$S = 0.99$	$\Delta\rho_{min} = -0.18$ e Å^{-3}
3435 reflections	Extinction correction: none
154 parameters	

bond distances and bond angles are listed in Table 2. Hydrogen bonding geometry is presented in Table 3. A diagram of the molecular structure with 50% probability and the atom numbering scheme is shown in Fig. 1. The data for publication were prepared with WinGX [3], ORTEP [6], and Mercury [7] program packages.

In the asymmetric unit of **I** two symmetrically equivalent molecules are present. The structural parameters of the title compound are comparable with those reported earlier [8, 9] The phenyl ring system is essentially planar with r.m.s. deviations

of 0.021(4) Å. In the three-dimensional arrangement of the molecules of **I** only one classical hydrogen bond could be described (Fig. 2). Additional C-H…O week interactions stabilize the molecular arrangement.
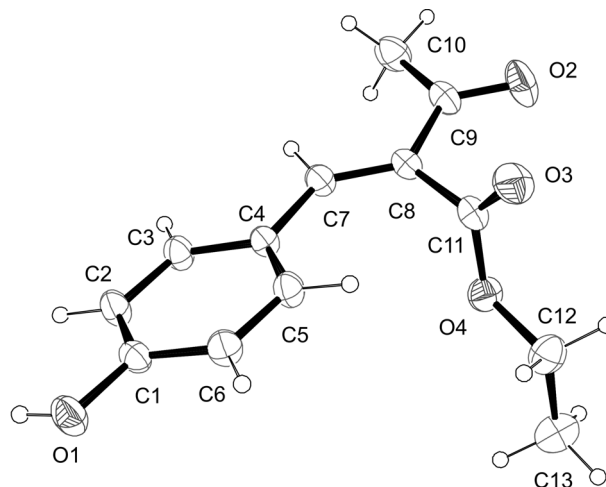
Fig. 1. View of molecule with an atom-numbering scheme. Displacement ellipsoids for the non-H atoms are drawn at the 50% probability level. The H atoms are presented with spheres with arbitrary radii.

Scheme 1. Chemical diagram of the studied compound

Table 2. Selected geometrical parameters for I (Å, °)

O3 – C11	1.335(2)	C6 – C5	1.399(2)
O3 – C12	1.457(2)	C1 – C2	1.376(2)
O1 – C3	1.362(2)	C11 – O4	1.198(2)
C7 – C8	1.347(2)	C11 – C8	1.501(3)
C7 – C6	1.455(2)	C8 – C9	1.476(2)
C6 – C1	1.399(2)	C3 – C2	1.380(3)
C11 – O3 – C12	115.89(15)	C9 – C8 – C11	114.45(15)
C8 – C7 – C6	131.11(17)	O1 – C3 – C2	122.67(15)
C1 – C6 – C5	117.25(15)	O1 – C3 – C4	117.31(16)
C1 – C6 – C7	117.32(15)	C2 – C3 – C4	120.00(15)
C5 – C6 – C7	125.36(15)	C4 – C5 – C6	121.13(15)
C2 – C1 – C6	121.87(16)	C1 – C2 – C3	119.59(16)
O4 – C11 – O3	124.16(17)	C5 – C4 – C3	120.13(16)
O4 – C11 – C8	125.35(17)	O2 – C9 – C8	119.14(18)
O3 – C11 – C8	110.48(15)	O2 – C9 – C10	119.66(18)
C7 – C8 – C9	122.02(17)	C8 – C9 – C10	121.18(16)
C7 – C8 – C11	123.53(16)	O3 – C12 – C13	107.46(17)

Table 3. Hydrogen bond for I (Å, °)

D-H⋯A	D(D-H)	d(H⋯A)	d(D⋯A)	<(DHA)
O(1)-H(1)⋯O(2)[i]	0.820	1.940	2.754(3)	169.2

Symmetry codes: (i) *1–x, 1–y, z*
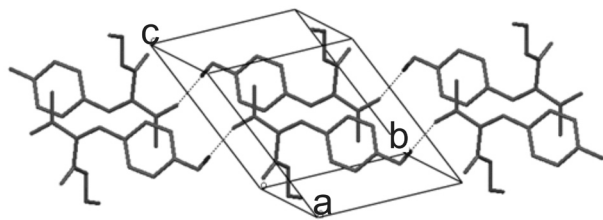
Fig. 2. Three-dimensional packing of the molecules. Only the hydrogen atoms involved in hydrogen bonding are shown.

SUPPLEMENTARY MATERIALS

CCDC 805277 contains the supplementary crystallographic data for this paper. This data can be obtained free of charge via www.ccdc.cam.ac.uk/data_request/cif, by e-mailing data_request@ccdc.cam.ac.uk, or by contacting The Cambridge Crystallographic Data Centre, 12 Union Road, Cambridge CB2 1EZ, UK; fax: +44(0)1223-336033.

REFERENCES

1. Li Wenhong, Lan Jiaming, Li Cheng, Cao Yuntao, Wang Haibo, Wang Lanzhi, Zhang Ping, Wang Yongxiang, Li Yuan, *Нuaxие Xuebao* **67**, 2732 (2009).
2. S. Stanchev, V. Hadjimitova, T. Traykov, T. Boyanov, I. Manolov, *Eur. J. Med. Chem.*, **44**, 3077 (2009).
3. Enraf-Nonius diffractometer control software, Release 5.1, Enraf-Nonius, Delft, The Netherlands, 1993.
4. L. J. Farrugia, *J. Appl. Cryst.*, **32**, 837 (1999).
5. G. M. Sheldrick, *Acta Cryst. A*, **64**, 112 (2008).
6. L. J. Farrugia, *J. Appl. Cryst.*, **30**, 565 (1997).
7. I. J. Bruno, J.C. Cole, P. R. Edgington, M. Kessler, C. F. Macrae, P. McCabe, J. Pearson, R. Taylor, *Acta Cryst. B*, **58**, 389 (2002).
8. W. Wen-juan, Ch. Wen-ping, Sh. Li-li, L. Cai-Hua, Y. Jian-guo, *Kin. Cat.,* **50,** 186 (2009).
9. S. Stanchev S., G. Momekov, F. Jensen, I. Manolov, *J. Med. Chem.*, **43**, 694 (2008).

КРИСТАЛНА СТРУКТУРА НА 3-OXO-2-(4-HYDROXYBENZYLIDENE)-BUTYRIC ACID ETHYL ESTER

С. Станчев[1], Р. П. Николова[2], Б. Л. Шивачев[2], И. Манолов[1]

*[1] Департамент по фармацевтична химия, Фармацевтичен факултет,
Медицински Университет, ул. „Дунав" 2, 1000 София
[2] Институт по минералогия и кристалография „Акад. Иван Костов",
Българска Академия на Науките, ул. „Акад. Г. Бончев" бл. 107, 1113 София*

(Резюме)

3-Oxo-2-(4-hydroxybenzylidene)-butyric acid ethyl ester бе синтезирано и изследвано чрез монокристален рентгеноструктурен, ИЧ, ^{1}H-ЯМР и мас спектроскопски анализи. Съединението, $C_{13}H_{14}O_4$, кристализира в триклинна кристална система и пространствена група $\bar{P}1$ с параметри на елементарна клетка $a = 8.7340(14)$ Å, $b = 9.1602(13)$ Å, $c = 9.1640(30)$ Å, $\alpha = 114.964(15)°$, $\beta = 100.197(18)°$, $\gamma = 108.173(11)°$ и $V = 589.5(3)$ Å^3 ($Z = 2$). Молекулите са свързани с водородни връзки и образуват верижки паралелни на [110]. Тримерната структура е допълнително стабилизирана от слаби електростатични взаимодействия.

Variation of the unit cell parameters of the REBa$_2$Cu$_3$O$_y$ (RE = Gd, Er) ceramics in function of the oxygen content

A. Stoyanova-Ivanova[1]*, St. Georgieva[2], T. Nedeltcheva[2], L. Dimova[3], B. Shivachev[3]

[1] *Georgi Nadjakov Institute of Solid State Physics, Bulgarian Academy of Sciences,*
72 Tzarigradsko Chaussee Blvd., 1784 Sofia, Bulgaria
[2] *University of Chemical Technology and Metallurgy, 8 Kl. Ohridski, 1756 Sofia, Bulgaria*
[3] *Bulgarian Academy of Sciences, Institute of Mineralogy and Crystallography, 1113 Sofia,*
Acad. Georgi Bonchev Str., Bl. 107, Bulgaria

High temperature Gd$_1$Ba$_2$Cu$_3$O$_y$ and Er$_1$Ba$_2$Cu$_3$O$_y$ ($y = 6.5 + \delta$) superconducting ceramics were prepared via solid-state reaction. The amount of oxygen in the synthesized samples was varied as they were kept at 460±5 ºC in flowing argon. The oxygen non-stoichiometry content, δ was determined by measuring the absorption of the blue colored I$_3^-$-starch compound. The unit cell parameters were determined from powder XRD patterns. A correlation between c unit cell parameter and y-oxygen coefficient in Er$_1$Ba$_2$Cu$_3$O$_y$ and Gd$_1$Ba$_2$Cu$_3$O$_y$ ceramics was established. The derived new relations can be used for the rapid semi-quantitative analysis of the oxygen content in the mentioned ceramics.

Key words: superconducting ceramics, oxygen stoichiometry coefficient, I$_3^-$-starch compound, X-ray.

INTRODUCTION

Since the discovery of Y$_1$Ba$_2$Cu$_3$O$_y$ ($y = 6.5+\delta$) high temperature superconducting ceramics (HTSC) many attempts to improve their critical temperature (T_c) and current (J_c) have been made: by optimizing the preparation procedure and conditions, by doping with different atoms, by introduction of pining centers, by replacing Yttrium with rare earths such as Er, Gd, etc. [1]. One of the key moments in the production of rare earth HTSC is the determination of oxygen content as the superconducting properties are correlated with its value. When the oxygen coefficient y is in the range 6.5–7.0, RE$_1$Ba$_2$Cu$_3$O$_y$ (RE = Y, Er, Gd, etc.) ceramics are superconducting and their structure is orthorhombic. An orthorhombic to tetragonal phase transition, occurring around $y \approx$ 6.5 is responsible for the loss of the superconducting properties.

Many wet methods have been developed for the determination of the non-stoichiometric oxygen coefficient δ in RE$_1$Ba$_2$Cu$_3$O$_y$ samples [2–5]. Oxygen content could also be obtained by methods such as Raman spectrometry and X-ray diffraction if appropriate mathematical relations "oxygen content–physical parameter" are preliminary found [6, 7]. Such mathematical relation between c-axis unit cell parameter (determined from Inorganic Crystal Structure database (ICSD) data) and the y-oxygen coefficient (determined by iodometric titrations) has been derived data for Y$_1$Ba$_2$Cu$_3$O$_y$ HTSC [7]. It will be usefully to find the relations "oxygen content–c-unit cell parameter" for other RE$_1$Ba$_2$Cu$_3$O$_y$ HTSC, to verify if the relation can be extrapolated for other RE. We decided to compare the relation with Gd$_1$Ba$_2$Cu$_3$O$_y$ and Er$_1$Ba$_2$Cu$_3$O$_y$ HTSC because the ionic radii of Gd (0.938 nm), Er (0.890 nm) and Y (0.900 nm) are similar [8]. Unfortunately a limited number of orthorhombic Gd$_1$Ba$_2$Cu$_3$O$_y$ [14, 19–23] and Er$_1$Ba$_2$Cu$_3$O$_y$ [9–18] structures have been reported in the ICSD thus no satisfactory correlation between c-unit cell parameter and oxygen content could be derived. Therefore the aim of the present work is to produce RE$_1$Ba$_2$Cu$_3$O$_y$ (RE = Gd, Er) superconducting ceramics with different oxygen content, to determine their oxygen coefficient, y and c-unit cell parameter, and to derive the relations between y-coefficient and c-parameter.

---
* To whom all correspondence should be sent:
E-mail: angelina@issp.bas.bg

EXPERIMENTAL

Samples preparation

A solid-state reaction was used to prepare the $Gd_1Ba_2Cu_3O_y$ and $Er_1Ba_2Cu_3O_y$ HTSC samples. The triple heat treatment regime with intermediate grindings was used. The first step includes mixing and milling of appropriate amounts of Gd_2O_3, Er_2O_3, CuO, $BaCO_3$, and calcination in flowing oxygen at 900 °C for 21h. The second step of the heat treatment was conducted at 930 °C for 21h in the same atmosphere, followed by annealing at 450 °C for 2h. The last step (third) started with grinding and pressing of the powder in pellets, followed by sintering at 940 °C for 23 h, slow cooling to 450 °C and holding at that temperature for 23 h. Pieces of the synthesized superconducting samples were grinded and kept at 460±5 °C in flowing argon for various times (0–120 h) then quenched to room temperature.

Critical temperature measurement (T_c)

The critical temperature T_c was obtained from resistivity measurements by the Four probe contact method. The temperature was stabilized by typical scheme including PID controller with 10mK accuracy [24]. Both synthesized samples $RE_1Ba_2Cu_3O_y$ are superconducting and the values of their critical temperature T_c are as follows: 91.5K for $Gd_1Ba_2Cu_3O_y$ and 90.4 K for $Er_1Ba_2Cu_3O_y$.

Samples analysis by spectrophotometric method

The non-stoichiometric oxygen coefficient, δ was determined by the spectrophotometric method based on the formation of the I_3^--starch compound [2]. The samples are dissolved in HCl and KI solution under inert atmosphere and the iodine liberated is bounded with Starch in a blue colored compound. The absorption is measured by differential mode and the non-stoichiometric oxygen coefficient δ is obtained as a relation of two absorptions.

Samples analysis by X-ray method

Powder X-ray diffraction (XRD) data were recorded at room temperature using Bragg-Brentano geometry with Co $K\alpha$ radiation. Step scans were performed over the angular range $8 < 2\theta < 70$ for $Er_1Ba_2Cu_3O_y$ and $8 < 2\theta < 90$ for $Gd_1Ba_2Cu_3O_y$ with the step size of 0.02 °/sec. The diffractograms were indexed using DICVOL [25] and the obtained unit cell parameters were refined using the X'pert Highscore program [26]. The peak shape was described by a pseudo-Voigt function. The background level was defined by a polynomial function. For each diffraction pattern the scale factor, the peak asymmetry and the unit-cell dimensions were refined while the instrumental zero shifts were kept constant.

RESULTS AND DISCUSSION

The average results for non-stoichiometric coefficient δ for $Gd_1Ba_2Cu_3O_y$ and $Er_1Ba_2Cu_3O_y$ HTSC samples (initially synthesized as well as annealed under argon flow) obtained by the spectrophotometric method are listed in Table 1. Each result is a mean value of at least three parallel determinations. The standard deviation is in the limits of ±0.002. A decrease of the oxygen coefficient y in function of the annealing time is observed (Fig. 1).

From the trends observed in Fig.1a it is visible that for $Gd_1Ba_2Cu_3O_y$ the process of oxygen release is very

Table 1. Non-stoichiometric coefficient δ and unit cell parameter for c-axis

Samples	Annealing time, [h]	non-stoichiometric coefficient δ	c-unit cell parameter
	0	0.420	11.670(2)
	12	0.365	11.682(2)
$Er_1Ba_2Cu_3O_y$	24	0.293	11.686(4)
	48	0.214	11.695(2)
	72	0.183	11.697(2)
	0	0.376	11.692(4)
	12	0.243	11.708(7)
$Gd_1Ba_2Cu_3O_y$	36	0.239	11.710(8)
	96	0.225	11.720(5)
	120	0.206	11.724(2)
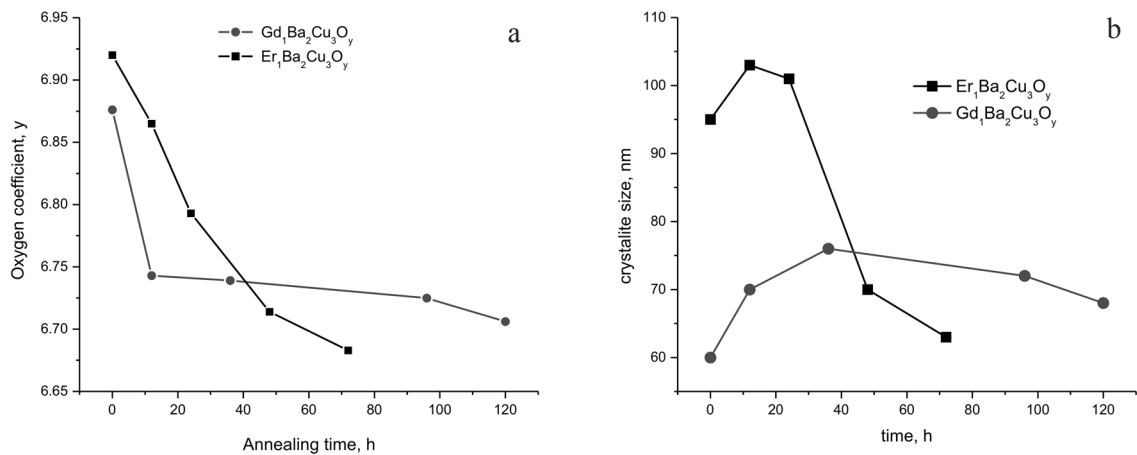
Fig. 1. Decrease of the oxygen coefficient *y* (a) and crystallite size (b) of the studied HTSC in function of the annealing time

rapid during the first 12 h. After the 12th hour the oxygen decrease is time-consuming. For Er$_1$Ba$_2$Cu$_3$O$_y$ the loss of oxygen at the beginning is almost proportional to the annealing time. The plateau in the oxygen content variation starts around the 48 h of the annealing. This difference of oxygen loss may be related to the differences in crystallite size and thus to the specific surface area and porosity.

The results of XRD analyses of the all Er$_1$Ba$_2$Cu$_3$O$_y$ and Gd$_1$Ba$_2$Cu$_3$O$_y$ samples are shown on Figures 2 and 3, respectively. The peak positions and intensities of the obtained phase correspond well to these of the known superconducting erbium and gadolinium 123 HTSC phase. All samples were indexed as orthorhombic with $a \sim 3.82$ $b \sim 3.88$ and $c \sim 11.68$ [1]; the values of the refined *c*-axis unit cell parameter are listed in Table 1. As expected the

c-axis cell parameter increases with the decrease of the non-stoichiometric oxygen coefficient δ.

The variation of crystallite size obtained from the XRD patterns is shown on Fig. 1b. After an initial increase of the size the tendency is reversed and the diminution is somewhat consistent with oxygen content depletion and reaching of a plateau (probably a stage before orthorhombic to tetragonal phase transition).

Based on the spectrophotometric and XRD data the regression equations of the correlation between the non-stoichiometric oxygen coefficients δ and *c* cell parameter for the studied HTSC were obtained (Table 2). The equations $y = f(c)$ were also derived (Table 2) and are shown on Figure 4. One can see that the graphical relation for Er$_1$Ba$_2$Cu$_3$O$_y$ is very close to that of Y$_1$Ba$_2$Cu$_3$O$_y$ HTSC plotted from the
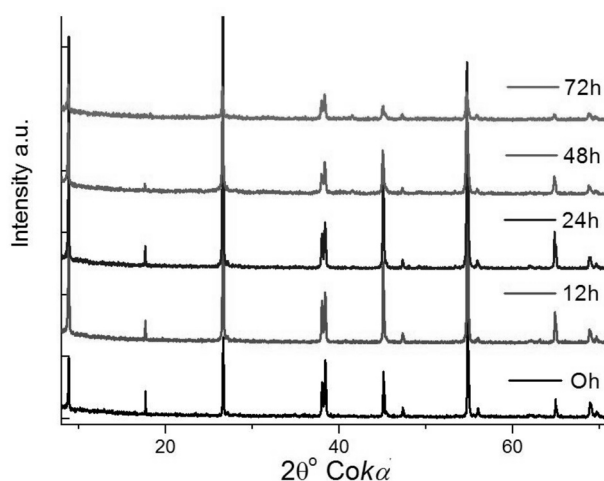
Fig. 2. XRD patterns of the synthesized and annealed in flowing argon Er$_1$Ba$_2$Cu$_3$O$_y$ sample
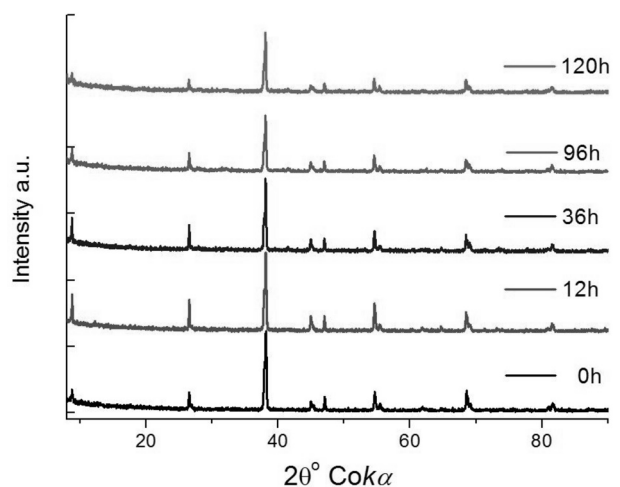
Fig. 3. XRD patterns of the synthesized and annealed in flowing argon Gd$_1$Ba$_2$Cu$_3$O$_y$ sample

Table 2. Results of the correlation

	Regression equation $c = k_0 - k_1\delta$	Error		Equation $y = f(c)$
		k_0	k_1	
$Er_1Ba_2Cu_3O_y$	$c = 11.718 - 0.107\delta$	0.004	0.013	$y = 116.01 - 9.346\,c$
$Gd_1Ba_2Cu_3O_y$	$c = 11.755 - 0.172\,\delta$	0.010	0.038	$y = 74.843 - 5.814\,c$

Table 3. Values of the difference Δy: $\Delta y = yEr/Gd - yY$

c-axis value [Å]	11.675	11.680	11.685	11.690	11.695	11.700	11.705	11.710
$\Delta y = y_{Er} - y_Y$	−0.015	0.003	0.021	0.038	0.055	0.073	0.091	0.108
$\Delta y = y_{Gd} - y_Y$	−0.084	−0.084	−0.084	−0.084	−0.084	−0.084	−0.084	−0.085
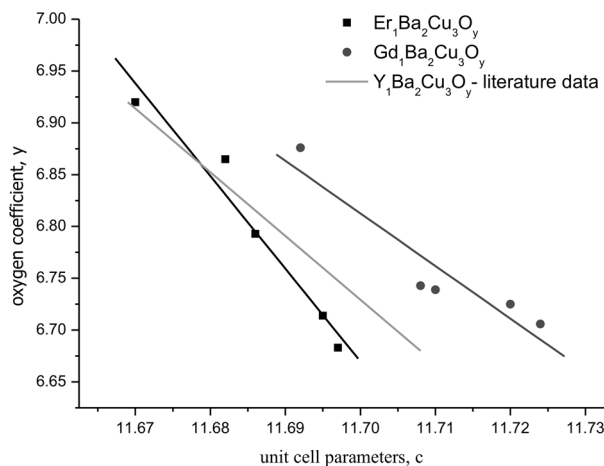
Fig. 4. Variation the oxygen content in function of the c-axis parameter

CONCLUSIONS

The crystallite size of $Er_1Ba_2Cu_3O_y$ and $Gd_1Ba_2Cu_3O_y$ ceramics diminishes with depletion of oxygen. Both the oxygen content, y and crystallite size reach a "plateau", more rapidly for samples with smaller crystallites.

A correlation between c-unit cell parameter and y-oxygen coefficient in $Er_1Ba_2Cu_3O_y$ and $Gd_1Ba_2Cu_3O_y$ ceramics is established. The new derived equation can be used for the rapid semi-quantitative analysis of the oxygen content in the cited HTCS ceramics. The relation "oxygen content–c cell parameter" obtained for $Y_1Ba_2Cu_3O_y$ HTSC could not be employed to calculate precisely the oxygen content value, y for $Er_1Ba_2Cu_3O_y$ and $Gd_1Ba_2Cu_3O_y$ superconducting samples.

equation $y = 75.250 - 5.856c$ [7]. The $Gd_1Ba_2Cu_3O_y$ relation is a little distant from that of $Y_1Ba_2Cu_3O_y$ – almost parallel to it. The differences between y coefficients calculated by the equations for gadolinium/erbium and ref. 7 yttrium ceramics are given in Table 3. In view of the fact that the difference Δy in almost all cases is greater than the errors of the spectrophotometric and XRD methods one can conclude that relation "oxygen content – c cell parameter" is specific for each ReBCO. Interestingly the observed deviations are in accordance with the difference between the ionic radii of Gd-Y and Er-Y and Y, with respective values of 0.04 nm (for Gd) and 0.01 nm (for Er). The development of a more complex relation, taking into account additional physical, chemical, structural etc. parameters may be envisaged with the accumulation of additional data.

REFERENCES

1. S. Kambe, Y. Murakoshi, R. Sekine, M. Kawai, K.Yamada, S. Oshima, K. Okuyama, *Phys. C*, **178,** 71 (1991).
2. T. Nedeltcheva, St. Georgieva, L.Vladimirova, A. Stoyanova-Ivanova, *Talanta*, **77**, 1745 (2009).
3. T. Nedeltcheva, L.Vladimirova, *Anal. Chem. Acta*, **437**, 259 (2001).
4. W. Chen, J. Chen, X. Jin, *Physica C*, **132**, 276 (1997)
5. A. Styanova-Ivanova, St. Gergieva, T. Nedeltcheva, L.Vladimirova, S. Terzieva, *JOAM*, **3**, 476 (2009).
6. S. Degoy, J. Jimenez, P. Martin, O. Martinez, A. Prieto, D. Chambonnet, C. Audry, C. Belouet, J. Perriere, *Physica C*, **256**, 291 (1996).
7. P. Benzi, E. Bottizzo, N. Rizzi, *J. Cryst. Growth*, **269**, 625 (2004).
8. R. D. Shannon, *Acta Cryst. A*, **32**, 751 (1976).
9. T. Ishigaki, H. Asano, K. Takita, *Jap. J. Appl. Phys.*, **26**, 987 (1987).

10. T. Ishigari, H. Asano, K. Takita, H. Katoh, H Akinaga, F. Izumi, N. Watanabe, *Jap. J. Appl. Phys.*, **26**, 1681 (1987).
11. D. Currie, T. Weller, *Physica C*, **214**, 204 (1993).
12. M. Guillaume, P. Allenspach, J. Mesot, B. Roessli, U. Staub, P. Fischer, A. Furrer, *Zeitschrift für Physik B*, **90**, 13 (1993).
13. E. Poerschke, P. Meuffels, B. Rupp, in: Materials Research Society Symposia Proceedings, **166**, 181, 1990.
14. D. G. Chryssikos, I. E. Kamitsos, A. J. Kapoutsis, P. A. Patsis, V. Psycharis, A. Koufoudakis, C. Mitros, G. Kallias, E. Gamari-Seale, D. Niarchos, *Physica C*, **254**, 44 (1995).
15. S. P. V. Awana, K. S. Malik, B. W. Yelon, A. C. Cardoso, F. O de Lima, A. Gupta, A. Sedky, V. A. Narlikar, *Physica C*, **338**, 197 (2000).
16. J. Mesot, P. Allenspach, U. Staub, A. Furrer, H. Mutka, R. Osborn, A. Taylor, *Phys. Rev. B*, **47**, 6027 (1993).
17. B. Rupp, E. Poerschke, P. Meuffels, P. Fischer, P. Allenspach, *Phys. Rev. B*, **40**, 4472 (1989).
18. C. C. Torardi, M. E. McCarron, A. M. Subramanian, S. H. Horowitz, B. J. Michel, W. A. Sleight, E. D. Cox, *American Chemical Society: Symposium Series*, **351**, 152 (1987).
19. A. Fernandes, J. Santamaria, S. Budko, O. Nakamura, J. Guimpel, I. Schuller, *Phys. Rev. B*, **44**, 7601 (1991).
20. H. Shakeripour, M. Akhavan, Superconductivity: *Science and Technology*, **14**, 213 (2001).
21. F. Prado, A. Caneiro, A. Serquis, *Physica C*, **295**, 235 (1998).
22. A. J. Campa, M. J. Gomez de Samar, Gutierrez-Puebla, A. M. E. Monge, I. Rasines, C. Ruiz-Valero, *Phys. Rev. B*, **37**, 529 (1988).
23. H. Asano, K. Takita, H. Katoh, H. Akinaga, T. Ishigaki, M. Nishino, M. Imai, K. Masuda, *Jap. J. Appl. Phys.*, **26**, 1410 (1987).
24. D. Dimitrov, A. Zahariev, J. Georgiev, G. Kolev, J. Petrinski, Tz. Ivanov, *Cryogenics*, **34**, 487 (1994).
25. A. Boultif, D. Louer, *J. Appl. Cryst.*, **24**, 987 (1991).
26. X'pert HighScore, Panalytical.

ИЗМЕНЕНИЯ НА ПАРАМЕТРИТЕ НА ЕЛЕМЕНТАРНА КЛЕТКА НА REBa$_2$Cu$_3$O$_Y$ (RE = Gd, Er) КЕРАМИКИ В ЗАВИСИМОСТ ОТ КИСЛОРОДНОТО СЪДЪРЖАНИЕ

А. Стоянова-Иванова[1], С. Георгиева[2], Ц. Неделчева[2], Л. Димова[3], Б. Шивачев[3]

[1] Институт по физика на твърдото тяло „Акад. Г. Наджаков", бул. Цариградско шосе 72, 1784 София
[2] Химикотехнологичният и металургичен университет – София, бул.
„Св. Климент Охридски" 8, 1756 София
[3] Институт по минералогия и кристалография „Акад. Иван Костов",
Българска Академия на Науките, ул. „Акад. Г. Бончев", бл. 107, 1113 София.

(Резюме)

Високо температурни Gd$_1$Ba$_2$Cu$_3$O$_y$ и Er$_1$Ba$_2$Cu$_3$O$_y$ ($y = 6.5 + \delta$) свръхпроводими керамики бяха получени. Количеството на кислород в образците бе променяно като образците бяха отгрявани на 460±5 ºC в аргонова атмосфера. Нестехиометричното кислородно съдържание, δ, бе определено спектрофотометрично. Параметрите на елементарна клетка бяха определени чрез прахова рентгенова дифракция. Изведена бе зависимостта между c параметъра на елементарната клетка и съдържанието на кислород, y. Получените зависимости могат да се използват за бързо полуколичествено определяне на съдържанието на кислород.

Extinction in textures: Nullifying the extinction effect

I. Tomov*

Acad. J. Malinowski Institute for Optical Materials and Technologies, Bulgarian Academy of Sciences, Sofia 1113, Bulgaria

Accounting for secondary extinction (SE) in a crystallographic direction, a straightforward approach is devised for XRD characterizations of textures by nullifying the extinction effect. To this end, a proper reconsideration of the nature of the extinction coefficients is carried out. It is shown that whereas the SE coefficient g is *proportional* to the product of pole density P and incident-beam intensity I_0, the empirical extinction coefficient k is *independent* of the ratio g/PI_0. Based on the invariability of the k-coefficient with respect to g/PI_0, the extinction effect is nullified by equating two its expressions defined by intensities of a reflection measured at a series a levels interaction whose variation is controlled by P and I_0. Techniques representing extended versions of this approach are developed for (i) reliability-evaluation of the controlled variation of the levels of interaction by using instrumental variable (generator current) and, hence, to test the capability of the XRD apparatus to collect accurate and precise data, and (ii) determination of extinction-free data of the pole density that is a fundamental physical parameter. The experimental results are discussed in terms of the influence of extinction coefficient g on the accuracy in the determination of the pole density in ideal <100> direction of nickel texture.

Key words: extinction, texture, pole density.

1. INTRODUCTION

Extinction was introduced to account for the reflecting power of a real crystal with respect to the power described by kinematical diffraction [1]. Extinction in a mosaic structure is power loss caused by the production of the diffracted beam. Depending on the block size, one has to distinguish between primary extinction, which is extinction within a single crystal block, and secondary extinction, which occurs when a ray reflected by one mosaic block is subsequently reflected by another block with the same orientation.

To overcome the deficiencies in the theoretical estimates of extinction correction factors, based on simplified parameterization of the extinction effect across the scan of reflection, devoted experimental procedures were applied to *decrease* as well as *cancel* the extinction effect. In this respect, Schneider (1976) designed γ-ray diffractometry experiments where extinction is only in the order of 10% or less [2]. Analyzing the process of the X-ray scattering

and the level of interaction between radiation and crystal medium, Mathieson substantiated an approach for derivation experimental structure-factor values, which are free from extinction effects [3]. The approach involves "(i) determination of integrated reflectivity at a series of levels of interaction (attained by controlled variation of a suitable physical parameter) and (ii) extrapolation of an appropriate function of the measurements to zero level of interaction as identified by zero diffracted power". The procedures to experimental realizations of the null-intensity (extinction-free) limit were illustrated in the paper of Mathieson & Mackenzie [4] as well. To attain a true zero-extinction kinematic limit value, the question of extrapolation to zero extinction in case of wavelength in the γ-ray region has been discussed from different point of views in the literature [5–7]. In this connection, the γ-ray data used in each of these investigations have been fitted by using polynomials of different types corresponding to the particular conceptions of the authors for attainment of the true zero-extinction kinematic limit value.

The present study outlines an alternative approach for nullifying the extinction effect. In this respect, careful considerations are carried out of

---

* To whom all correspondence should be sent:
E-mail: iv_tomov@yahoo.co.uk

the process of the scattering of X-rays and the level of interaction between the radiation and the crystal medium. Our concern here is essentially with mutual connection between extinction coefficients and their exact relationship with diffraction at a series of levels of interaction attained by controlled variations of suitable physical parameters.

2. BASIC DEFINITIONS OF EXTINCTION THEORY AND TEXTURE ANALYSIS

The formalism considered here is valid for the symmetrical Bragg geometry with a plane-parallel plate sample appearing infinitely thick to the X-rays. According to theory [1, 8–14] and experiment related with it [2, 5–7], the extinction decreases the measured intensity I_m of a reflection with a factor y, the extinction factor, defined by

$$I_m = yI_{kin} \qquad (1)$$

Here, I_{kin} is the intensity that a Bragg reflection would have if kinematic theory would apply exactly to the system being examined. Therefore, the intensity I_{kin} delimits an imaginary (physically non-attainable) level of interaction of the diffraction process. In the symmetrical Bragg geometry, I_{kin} has to be expressed as

$$I_{kin} = PI_0 QS/2\mu \qquad (2)$$

where I_0 is the intensity of the incident beam, S is the cross section of the beam, Q is the reflectivity per unit crystal volume, μ is the ordinary linear absorption coefficient, and P is the pole density. It is defined by the volume fraction dV/V of crystallites whose $<hkl>$-poles fall into a (infinitely small) space-angle element $d\Omega$ (Bunge [15, 16]):

$$\left(dV/V\right)\!/d\Omega = P . \qquad (3)$$

The factor P connects (2) with the well known formula

$$I_{kin}^r = I_0 QS/2\mu , \qquad (4)$$

which is derived under assumption for *random distribution of crystallites*, i.e. $P=1$. In the case of pure SE, Chandrasekhar gave an expression for the extinction factor y [17]:

$$y = \mu/\mu_\varepsilon , \qquad (5)$$

where μ_ε is an effective absorption coefficient. In the symmetrical Bragg geometry with a plane parallel plate sample one should use the effective absorption coefficient as a first order approximation for the SE correction ε [9]:

$$\mu_\varepsilon = \mu + gQ\left(p_2/p_1^2\right). \qquad (6)$$

Here g is the SE coefficient, which is a dimensionless quantity [1]. The symbol p_n denotes the polarization factor for incident X-ray beam [9]:

$$p_n = \left[1 + \cos^2\left(2\theta_0\right)\cos^{2n}\left(2\theta_B\right)\right]\!\big/\!\left[1 + \cos^2\left(2\theta_0\right)\right] \quad (7)$$

where $n = 1, 2, ...$, θ_B is the Bragg angle of reflection. From (6) a formula follows for the SE correction ε, which has been derived by Darwin [1], and later the polarization p_2/p_1^2 of the incident X-ray beam has been incorporated in ε by Chandrasekhar [17] and Zachariasen [9]:

$$\varepsilon = gQ\left(p_2/p_1^2\right). \qquad (8)$$

3. ANISOTROPY AND BEHAVIOUR OF THE EXTINCTION COEFFICIENTS

Bragg et al. [18] deduced the SE correction empirically, whereas Darwin [1] deduced it theoretically. To this end, the authors have supposed respectively that both the empirical extinction coefficient k and the SE coefficient g are constants for the crystal, that is, parameters independent of crystallographic direction. Moreover, Darwin [1] had assessed that the definition, deduced by Bragg et al. [18], was correct to the first order approximation for the SE correction alone. Consequently, in the discussed frames, the two definitions for the SE correction have to be equivalent. In order to account for the crystal and textural anisotropy, the nature of k and g is reconsidered here. Replacing Q by its corresponding expression from (2) transforms (8) into

$$\varepsilon = kI_{kin}\left(p_2/p_1^2\right), \qquad (9)$$

where the expression

$$k = 2g\mu/PI_0 S \qquad (10)$$

shows that k and g are mutually connected. Reforming (10) yields the expression for

$$g = kPI_0 S/2\mu . \qquad (11)$$

Evidently, (2) and (11) reveals that whereas I_{kin} defines the upper limiting value of the diffraction process, g defines the extinction-induced weakening of the level of interaction of the same process. Depending on P, g and k are anisotropic coefficients. The anisotropy of P comprises the crystallographic, microstructural and textural anisotropies. Acting together for all crystallites contributing to reflection, anisotropy parameters such as *size, shape, dislocation substructure, crystallographic orientation and crystallite arrangement* (Bunge [19]) synthesize

the resulting anisotropy of g and k. The coefficients show different behaviour with respect to the level of interaction of the diffraction process that is controlled simultaneously by P and I_0 under otherwise equal conditions. At lower limiting values of either both $PI_0 \to 0$ or one of them makes it evidently that in the only case of no diffraction ($I_{kin} \to 0$) (2), there is no extinction ($g \to 0$) (11). This is in accord with Mathieson's statement that '*extinction is only zero, in absolute sense, when diffracted power is identically zero* [3]. Moreover, whereas g is proportional to the product PI_0, the coefficient k e is proportional to the ratio g/PI_0. Therefore, by virtue of the interdependence between g and PI_0, any change of either both, P and I_0, or one of them does not cause change of the ratio g/PI_0 and, hence, k is independent of the product of both $P>0$ and $I_0>0$.

3.1. Definitions for k independence of the levels of interaction

Suppose the incident beam changes its intensity from $I_{0,i}$ to $I_{0,i*}$ under P=const. Here i and $i*$ denote the values of the generator current. Then, by analogy of (10), we shell have

$$k_i = 2\mu g_i / P I_{0,i} S , \qquad (12)$$

$$k_{i*} = 2\mu g_{i*} / P I_{0,i*} S , \qquad (12a)$$

where it is accounted that g_i and g_{i*} are proportional to $I_{0,i}$ and $I_{0,i*}$, respectively, i.e.

$$\left(g_i / I_{0,i}\right) / \left(g_{i*} / I_{0,i*}\right) = 1 . \qquad (13)$$

Dividing (12) and (12a) with accounting for (13) yields

$$k_i = k_{i*}, \qquad (14)$$

that k is independent of the level of interaction. Second, suppose the pole density changes from P to P^r=1 under I_0=const. Following (12), k_i is then transformed into k_i^r, i.e.:

$$k_i^r = 2\mu g_i^r / I_0 S . \qquad (15)$$

Here it is accounted that g_i^r is proportional to P^r corresponding to random distribution of crystalline orientations. Dividing (12) and (15) with taking into account for $P=g_i/g_i^r$ yields

$$k_i = k_i^r . \qquad (16)$$

Thus, (14) and (16) constitute conditions for the invariability of k from the level of interaction of the diffraction process. Then, one can utilize k for nullifying the extinction effects by equating two its expressions that are defined by two different couples
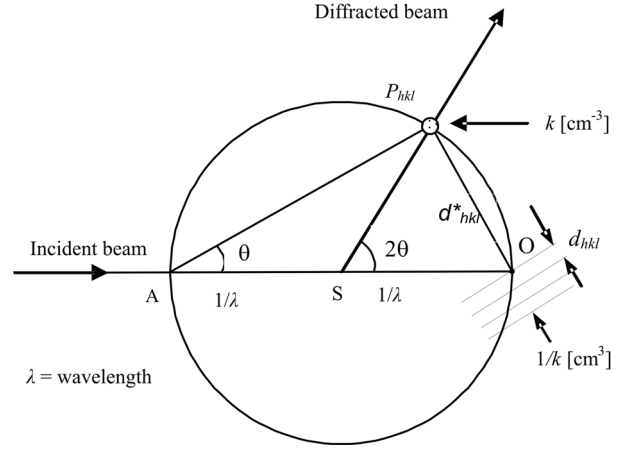
Fig. 1. Diffraction conditions design by means of the reciprocal (scattering) space. The radius $1/\lambda$ of the Ewald's sphere is defined by the wavelength λ of X-rays. O is the origin of the real space and Phkl is a node of the reciprocal space where fall the *<hkl>* poles of the crystallites in Bragg condition. The coefficient k defines the scanned volume inside the node. The distance OP_{hkl} is defined by $d_{hkl}^* = 1/d_{hkl}$, where d_{hkl} is the space between atomic networks (hkl).

of intensities of a reflection measured at a series of levels of interaction.

To analyze what a constant is k, let us throw look at Fig. 1, which designs the diffraction condition in terms of the reciprocal (scattering) space (Ewald [20]). The coefficient k has dimension of reciprocal volume (see (10)). It corresponds to the scattering space. Actually, this is the scanned volume inside the node P_{hkl}. Due to the relationship between real and scattering space, the reciprocal quantity of k $[1/k=(S/2\mu)(PI_0/g)]$ corresponds to the real space. Then, one may consider $1/k$ as consisting of two terms of different range. For an infinitely thick sample, the term, $S/2\mu$, represents the irradiated crystalline volume that is a constant *for all reflections* of the XRD pattern, whereas PI_0/g is a constant inherent *for any particular reflection*. The last is due to the interdependence of these three parameters since I_0 scales g by means of P (see (11)). The quantity $1/k$ defines a volume in the real space where the X-radiation, interacting with crystal medium, produces the measured intensity I_m.

3.2. Expressing the SE coefficient g and SE correction ε in case of polycrystalline materials

Due to fine-crystalline structure and high density of imperfections [21], reflection broadening in textures is about two orders of magnitude larger than that one in single crystals, which amounts to a

few ten of seconds of arc [5, 7]: for the same reason, the textures exhibit pure SE as well [22, 23]. This reflects in the observed reflection broadening recorded by conventional diffractometry. Actually, it is a superposition of physical (microstructural) and instrumental broadening. Since the determination of the SE coefficient $g = 1/2\eta\sqrt{\pi}$ is based on the crystal-mosaic distribution alone [8]), it is not justified to expect that this definition would adequately account for the microstructural properties of polycrystalline materials. (Here η is the standard deviation of the Gaussian function). The only way to account adequately for the anisotropic effects of the pole density P on the SE coefficient is to determine g using quantities corresponding to reflection whose profile synthesizes all microstructural effects. Thus, if k and I_{kin} are known, from (8) and (9) one obtains:

$$g = kI_{kin}/Q. \qquad (17)$$

Replacing I_{kin} with its corresponding expression obtained by reforming (1) in succession with (5), (6) and (9), transforms (17) into

$$g = k\mu I_m \Big/ Q\Big[\mu - kI_m\left(p_2/p_1^2\right)\Big] \qquad (17a)$$

By analogy, for the SE correction ε defined by (9), one writes

$$\varepsilon = \mu kI_m\left(p_2/p_1^2\right)\Big/\Big[\mu - kI_m\left(p_2/p_1^2\right)\Big] \quad (17b)$$

These definitions account implicitly for parameters describing as a whole the crystallographic, textural and microstructural anisotropy in the probing direction of the sample as well as the measurement conditions. Moreover, in the Appendix A is shown that the basic source of the g-coefficient anisotropy

is the loading density (the number of atoms per unit area of $\{hkl\}$ system of net-planes [24]). This constitutes that g is grater for a denser atomic net-plane system. In general, reducing the loading density of net-planes, the lattice imperfections diminish thus the coefficient g.

4. PARAMETERIZATION OF THE RELATIONSHIP BETWEEN LEVELS OF INTERACTION CONTROLLED BY I_0-INTENSITY

The levels of interaction of the diffraction process at a series of measurements of a reflection are defined by respective change of the incident X-ray beam intensity I_0. The controlled variation of the I_0-intensity can be caused by ether transmission factor of a thin foil crossed by the incident beam or stepwise reduction of the generator current of the XRD apparatus [26]. Meanwhile, the last type of the procedures may supply information that is representative for the internal consistency of the XRD apparatus, i.e. for its capability to collect precise and accurate data. Below this idea is depicted.

4.1. Expressing the relationship R between a couple of levels of interaction controlled by generator current

Suppose a reflection is measured in succession at intensities, $I_{0,i}$, $I_{0,i*}$, $I_{0,i**}$, and $I_{0,i***}$, of the incident beam, where the generator tension V is constant, and the reduction of the values of the generator current i is dependent on geometric progression ($i=2i*=4i**=8i***$). In the equations listed inside of Fig. 2, A is a constant, V_K is the critical excitation

$$
\begin{aligned}
&I: \quad I_{kin,i}; g_i; k_i & ----------- \quad & I_{0,i} = Ai\left(V - V_K\right)^n \\
&\qquad k_i = k_{i*} & \updownarrow R_{i,i*} \qquad & i = 2i* \\
\\
&II: \quad I_{kin,i*}; g_{i*}; k_{i*} & ----------- \quad & I_{0,i*} = Ai*\left(V - V_K\right)^n \\
&\qquad k_{i*} = k_{i**} & \updownarrow R_{i*,i**} \qquad & i* = 2i** \\
\\
&III: \quad I_{kin,i**}; g_{i**}; k_{i**} & ----------- \quad & I_{0,i**} = Ai**\left(V - V_K\right)^n \\
&\qquad k_{i**} = k_{i***} & \updownarrow R_{i**,i***} \qquad & i** = 2i*** \\
\\
&IV: \quad I_{kin,i***}; g_{i***}; k_{i***} & ----------- \quad & I_{0,i***} = Ai***\left(V - V_K\right)^n
\end{aligned}
$$

Fig. 2. Parameterization of the relationship between couples of levels of interaction of the diffraction process. Since diffraction and extinction are indissolubly linked (see (2) and (11)), I_{kin} and g define in the same way any level of interaction and, hence, the relationship R between couples of neighbor levels of interaction (18), (22) and (23).

potential of the *Kα* radiation, and n = ≃ 1.5 [27]. The intensity I_0 quantifies any level of interaction of the diffraction process simultaneously by quantities both the kinematical intensity I_{kin} (2) and the SE coefficient g (11). Then, in the frames of the straight proportionality between I_0 and i ($I_0 = Ai(V - V_K)^n$), the parameter $R_{i,i*}$ defines the relationship between the first couple of levels of interaction:

$$I_{0,i}/I_{0,i*} = I_{kin,i}/I_{kin,i*} = g_i/g_{i*} = i/i* = R_{i,i*} \quad (18)$$

The intensities, $I_{kin,i} \leftrightarrow I_{kin,i*}$, defining the first and second levels of interaction (Fig. 2) can be expressed respectively by reforming (1) in succession with (5), (6) and (9), i.e.:

$$I_{kin,i} = \left\{ \mu / \left[\mu - k_i I_{m,i} \left(p_2 / p_1^2 \right) \right] \right\} I_{m,i}, \quad (19)$$

$$I_{kin,i*} = \left\{ \mu / \left[\mu - k_{i*} I_{m,i} \left(p_2 / p_1^2 \right) \right] \right\} I_{m,i*} \quad (20)$$

Solving (19) and (20) for $k_{i,i*} = k_i = k_{i*}$, with taking into account for $R_{i,i*}$ from (18), yields

$$k_{i,i*} = \frac{\mu \left[R_{i,i*} - \left(I_{m,i}/I_{m,i*} \right) \right]}{I_{m,i} \left(p_2 / p_1^2 \right) \left[R_{i,i*} - 1 \right]}. \quad (21)$$

Hereafter any coefficient of the type $k_{i,i*}$ will be denoted with indices i and $i*$ corresponding to the values of the generator current applied to the measurement of the respective couple of intensities, $I_{m,i} \leftrightarrow I_{m,i*}$, used for its expressing. With a view to expressing the parameters $k_{i,i*}$ and $R_{i,i*}$ by using measured intensities alone, one needs additional data. Then, by analogy of (18), the parameters $R_{i*,i**}$ and $R_{i**,i***}$, corresponding to the first-neighbour levels of interaction, are defined respectively with

$$\frac{I_{0,i*}}{I_{0,i**}} = \frac{I_{kin,i*}}{I_{kin,i**}} = \frac{g_{i*}}{g_{i**}} = \frac{i*}{i**} = R_{i*,i**}, \quad (22)$$

$$\frac{I_{0,i**}}{I_{0,i***}} = \frac{I_{kin,i**}}{I_{kin,i***}} = \frac{g_{i**}}{g_{i***}} = \frac{i**}{i***} = R_{i**,i***}, (23)$$

where the value of any of the parameters

$$R_{i,i*} = R_{i*,i**} = R_{i**,i***} \quad (24)$$

has to be equal to any of the respective ratios defined by the values of the generator current

$$i/i* = i*/i** = i**/i*** = 2. \quad (25)$$

By virtue of (14), k is constant for any level of interaction under otherwise equal condition, i.e.

$$k_i = k_{i*} = k_{i**} = k_{i***}. \quad (26)$$

Then, the intensities, $I_{kin,i**} \leftrightarrow I_{kin,i***}$, are expressed by analogy of (19) and (20), respectively:

$$I_{kin,i**} = \left\{ \mu / \left[\mu - k_{i**} I_{m,i} \left(p_2 / p_1^2 \right) \right] \right\} I_{m,i**}, \quad (27)$$

$$I_{kin,i***} = \left\{ \mu / \left[\mu - k_{i***} I_{m,i} \left(p_2 / p_1^2 \right) \right] \right\} I_{m,i***}. (28)$$

Solving (27) and (28) for $k_{i**,i***} = k_{i**} = k_{i***}$ with accounting for $R_{i**,i***}$ from (23) yields

$$k_{i**,i***} = \frac{\mu \left[R_{i**,i***} - \left(I_{m,i**}/I_{m,i***} \right) \right]}{I_{m,i**} \left(p_2 / p_1^2 \right) \left[R_{i**,i***} - 1 \right]}. \quad (29)$$

Now, solving (21) and (29) for $R_{i,i*} = R_{i**,i***}$, under nullifying the extinction effect by equating $k_{i,i*} = k_{i**,i***}$ yields

$$R_{i,i*} = \frac{I_{m,i} I_{m,i**} \left(I_{m,i*} - I_{m,i***} \right)}{I_{m,i*} I_{m,i***} \left(I_{m,i} - I_{m,i**} \right)}. \quad (30)$$

By analogy, one can derive the relationship between the second-neighbor levels of interaction assuming that $R_{i,i**} = R_{i,i*} R_{i*,i**}$ and $R_{i*,i***} = R_{i*,i**} R_{i**,i***}$ (see Figure 2) as well. The coefficients $k_{i,i**}$ and $k_{i*,i***}$ are then expressed with the couple of intensities $I_{kin,i} \leftrightarrow I_{kin,i**}$ and $I_{kin,i*} \leftrightarrow I_{kin,i***}$, (see (19)↔(27) and (20)↔(28)), respectively:

$$k_{i,i**} = \frac{\mu \left[R_{i,i**} - \left(I_{m,i}/I_{m,i**} \right) \right]}{I_{m,i} \left(p_2 / p_1^2 \right) \left[R_{i,i**} - 1 \right]}, \quad (31)$$

$$k_{i*,i***} = \frac{\mu \left[R_{i*,i***} - \left(I_{m,i*}/I_{m,i***} \right) \right]}{I_{m,i*} \left(p_2 / p_1^2 \right) \left[R_{i*,i***} - 1 \right]}. \quad (32)$$

At the end, solving (31) and (32) for $R_{i,i**} = R_{i*,i***}$, under nullifying the extinction effect by equating $k_{i,i**} = k_{i*,i***}$ yields

$$R_{i,i**} = \frac{I_{m,i} I_{m,i*} \left(I_{m,i**} - I_{m,i***} \right)}{I_{m,i**} I_{m,i***} \left(I_{m,i} - I_{m,i*} \right)}. \quad (33)$$

Variation of the levels of interaction, and hence of I_{kin} and g, with control has an additional advantage in that it allows for the capability for internal experimental checks that are based on using of instrumental variables. Actually, the generator current i is incorporated implicitly in this technique as referent parameter. For instance, the capability of the measurement tool to collect accurate and precise

data is controlled by the degree of approximation of R to the ratio $i/i*$.

5. EXPRESSING THE EXTINCTION-FREE POLE DENSITY P

By definition, the extinction-induced systematic error of the pole density is expressed with the difference ΔP_m between P and P_m, i.e.

$$\Delta P_m = P - P_m , \qquad (34)$$

$$P = I_{kin}/I_{kin}^r , \qquad (35)$$

$$P_m = I_m/I_m^r . \qquad (36)$$

Here P and P_m are defined by using the kinematical intensities from (2) and (4) and the measured intensities of the textured sample, I_m, and powder standard, I_m^r, respectively. To express P by measured intensities, a proper procedure is designed to data collection (Fig. 3). In this respect, the same reflection of textured sample and powder standard is measured at a series of the incident beam intensities $I_{0,i}$, $I_{0,i*}$, $I_{0,i**}$ and $I_{0,i***}$ caused by stepwise reduction of the values of the generator current, i.e. i, $i*$, $i**$ and $i***$.

Any of the particular levels of interaction is characterized by respective kinematic, I_{kin}, intensities, the pole densities, P and P^r, and the coefficient k. According to the definitions (14) and (16), k is the same for each of the levels of interaction and P^r is equal to unit. Then, P_i is expressed by the kinematic intensities corresponding to the first couple of levels of interaction measured at the intensity $I_{0,i}$:

$$P_i = I_{kin,i}/I_{kin,i}^r . \qquad (37)$$

where

$$I_{kin,i};k_i;P \quad ------------$$

$$\uparrow \qquad\qquad \updownarrow P$$

$$R_{i,i*} \quad ----- \quad I_{kin,i}^r;k_i^r;P^r=1; \leftarrow I_{0,i}=Ai(V-V_k)^n$$

$$\downarrow$$

$$I_{kin,i*};k_{i*};P \quad ------------$$

$$\uparrow \qquad\qquad \updownarrow P$$

$$R_{i*,i**} \quad ----- \quad I_{kin,i*}^r;k_{i*}^r;P^r=1; \leftarrow I_{0,i*}=Ai*(V-V_K)^n$$

$$\downarrow$$

$$I_{kin,i**};k_{i**};P \quad ------------$$

$$\uparrow \qquad\qquad \updownarrow P$$

$$R_{i**,i***} \quad ----- \quad I_{kin,i**}^r;k_{i**}^r;P^r=1; \leftarrow I_{0,i**}$$

$$\downarrow$$

$$I_{kin,i***};k_{i***};P \quad ------------$$

$$\updownarrow P$$

$$----- \quad I_{kin,i***}^r;k_{i***}^r;P^r=1; \leftarrow I_{0,i**}$$

$$k_i=k_i^r=k_{i*}=k_{i*}^r=k_{i**}=k_{i**}^r=k_{i***}=k_{i***}^r$$
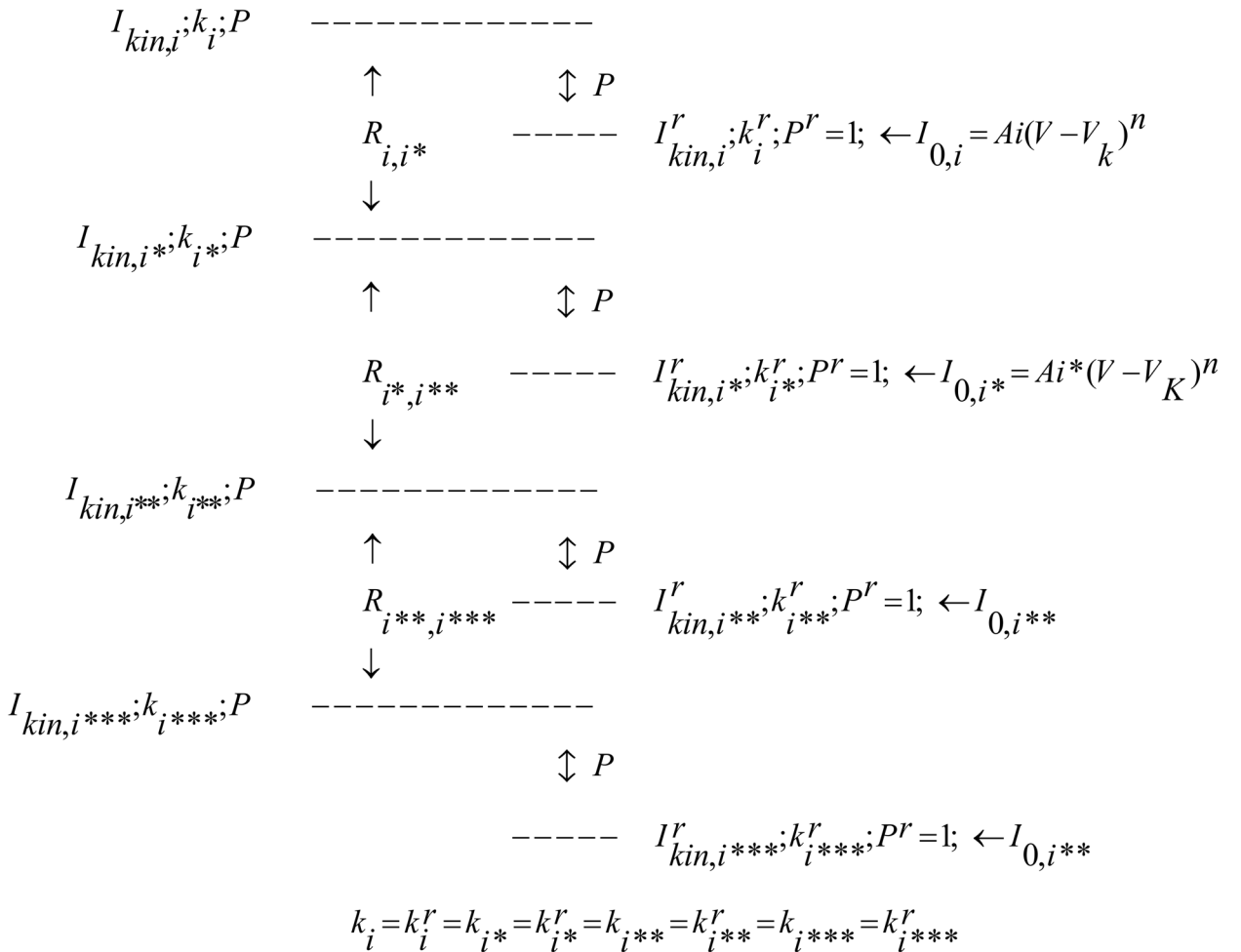
Fig. 3. Data collection procedure that is designed by the levels of interaction of the diffraction process. The same reflection of textured sample and random standard is measured at a series of the incident beam intensities I_0 caused by variation of the generator-current values i.

$$I^r_{kin,i} = \left\{ \mu \Big/ \left[\mu - k^r_i I^r_{m,i} \left(p_2 / p_1^2 \right) \right] \right\} I^r_{m,i}. \quad (38)$$

Solving the system of equations (19) and (38) for $k_i = k^r_i$ (see (16)) yields:

$$k_i = \frac{\mu \left[P_i - \left(I_{m,i} / I^r_{m,i} \right) \right]}{I_{m,i} \left(p_2 / p_1^2 \right) [P_i - 1]} . \quad (39)$$

Further, by analogy of (37), we write for the second couple of levels of interaction measured at the intensity $I_{0,i}$:

$$P_{i*} = I_{kin,i*} / I^r_{kin,i*} , \quad (40)$$

where

$$I^r_{kin,i*} = \left\{ \mu \Big/ \left[\mu - k^r_i I^r_{m,i*} \left(p_2 / p_1^2 \right) \right] \right\} I^r_{m,i*}. \quad (41)$$

Solving the system of equations (20) and (41) for $k_{i*} = k^r_{i*}$ (see (16)) yields:

$$k_{i*} = \frac{\mu \left[P_{i*} - \left(I_{m,i*} / I^r_{m,i*} \right) \right]}{I_{m,i*} \left(p_2 / p_1^2 \right) [P_{i*} - 1]} . \quad (42)$$

At the end, solving (39) and (42) for the unknown parameter $P_{i,i*} = P_i = P_{i*}$ under nullifying the extinction effects $k_i = k_{i*}$ yields an extinction-free value for the pole density corresponding to the first and second couples of levels of interaction:

$$P_{i,i*} = \frac{I_{m,i} I_{m,i*} \left(I^r_{m,i} - I^r_{m,i*} \right)}{I^r_{m,i} I^r_{m,i*} \left(I_{m,i} - I_{m,i*} \right)} . \quad (43)$$

Therefore, starting from kinematic definitions (37) and (40) for the pole density, an operative formula (43) that is in exact accord with the kinematic theory is derived using measured intensities. Following the same procedure, extinction-free data for the pole density $P_{i,i**} P_{i*,i**}, P_{i,i***}$, corresponding to respective combination of the other couples of levels of interaction are achieved as well. Once determined, the empirical extinction coefficient k can be employed for calculation of the kinematic intensities, the SE coefficient g defined by (17a) and the SE correction from (17b).

6. EXPERIMENTAL, RESULTS AND DISCUSSION

As a model, an electrodeposited nickel coating (Ni38) was used. It represents fiber texture with a main <100> component. The 200 reflection was measured with conventional goniometer using CuK$_\alpha$ radiation separated by graphite focusing monochromator. The divergence slit was 1/2°, and receiving one 0.05 mm. The four step measurement procedure, shown in Figure 2, was carried out in such a way to compensate the stepwise decrease of the generator current from i to $i***$ ($i=2i*=4i**=8i***$) by respective increase of the data collection time per scanned step from τ to $\tau***$, i.e. ($i\tau=i*\tau*=i**\tau**=i***\tau***$). The compensative condition ensures the same statistical errors in the respective points of the measured profiles.

Fig. 4 illustrates the proportionality between coefficient g and incident beam intensity I_0. The ordinate axis represents the values of the coefficient g determined at different levels of interaction of the diffraction process. The abscissa axis shows that the I_0-reduction is dependent on geometric progression, i.e. I_0/R^n (n = 0, 1, 2, 3) where R is the ratio between neighbor levels of interaction. Figs. 4a and 4b
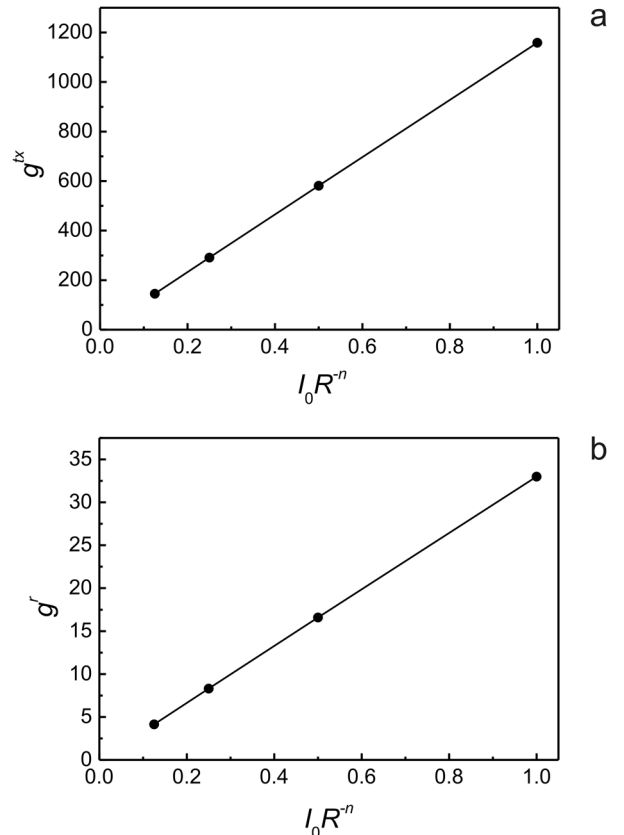
Fig. 4. a) Plot of the SE coefficient g^{tx} *vs.* incident beam intensity I_0 whose stepwise reduction is dependent on geometric progression $I_0 R^{-n}$ (n=0,1,2,3), where R [=2.00213] is the ratio between neighbor levels of interaction. The measurement of the 200 reflection of Ni38 sample representing sharp <100> texture (P=35) is carried out by CuKα-radiation. b) Analogical plot for the SE coefficient g^r of random standard: the conditions of its measurements are the same.

show the degree of extinction effects measured at the textured sample (Fig. 4a) and random standard (Fig. 4b), respectively. The scale between *g* values, corresponding to the textured sample and random standard is equal exactly to $P=g^{tx}/g^{r}$.

In Table 1, results are listed about the pole density. The first column shows that the stepwise reduction of the incident beam intensity is dependent on geometric progression, I_0R^{-n} (n=0,1,2,3), where *R* is the ratio between neighbor levels of interaction caused by the generator current. The second column contains extinction-free data, and third column contains data affected by extinction. While the extinction-free data represent constant values, the extinction-affected data suffer systematic errors ΔP of different values. The systematic error is highest at the highest level of interaction and lowest at the lowest level of interaction. The percentage errors vary from about 6% to less than 1%.

7. CONCLUDING REMARKS

The main advantage of this approach is to gain accuracy and, hence, physical reality of the data. Accuracy can only be gained by care in the design and implementation of an experiment. Actually, this approach offers a possibility for existing methods both to be re-considered and improved for texture characterizations and to develop new ideas. In general, one can state that no problem related to using the integral intensities can be correctly solved if secondary extinction effects are not nullified.

Since diffraction and extinction are indissolubly linked, the formalism developed here is valid for single crystals, textures and crystalline powders. The loading density (number of atoms per unit area of a net-plane) that is the source of the crystal anisotropy unifies the general behaviour of these three structural forms.

APPENDIX A

Source of the coefficient g anisotropy

To find the source of the anisotropic nature of the coefficient *g*, one has to resort to *P*. Since *P* comprises as a whole the crystallographic, textural and microstructural anisotropy, the resulting anisotropy of the coefficient g is synthesized by their contributions to the probing direction. Suppose the space-angle element $d\Omega$ covers the range of the probing direction and the volume element dV contains very many crystallites [16]. Following (3), one can write an extended expression for the factor *P*:

$$(dV/V)/d\Omega = P = \vartheta\, m \,. \qquad (44)$$

Here *m* is all the number of crystallites per unit volume of the sample, and ϑ is the average volume of the crystallites. If the crystallite size *D* is defined as the cube root of the average crystallite volume, $\vartheta^{1/3}$, one can rewrite (44) as

$$P = D\vartheta^{2/3}m \,. \qquad (45)$$

where $\vartheta^{1/3}$ is the area of the crystallographic plane contributing to reflection. Replacing *P* with its corresponding expression from (45) transforms (11) into

$$g = D\vartheta^{2/3}mG \,, \qquad (46)$$

where $G = kI_0S/2\mu$ is a number. Further, one can represent the crystallite size as:

$$D = Nd \,, \qquad (47)$$

where (*N* + 1) is the number of the (*hkl*) atomic planes having net-plane spacing, *d*. Kleber (1970) showed that *d* is directly proportional to loading density *L* (the number of atoms per unit area of a net-plane):

$$d = V_c L \,, \qquad (48)$$

where V_c is the volume of the primitive cell. By virtue of (47) and (48), from (46) an expression follows that connects the coefficient *g* with the loading density *L*:

$$g = LNV_c\vartheta^{2/3}mG \qquad (49)$$

Evidently, the coefficient *g* depends on the crystallographic direction by means of the loading density. This outcome qualifies *L* as the source of the extinction anisotropy and constitutes that the coefficient *g* is grater for a denser atomic net-plane system under otherwise equal conditions. In general, reducing the loading density of net-planes, the lattice imperfections diminish thus the coefficient *g*.

REFERENCES

1. C. G. Darwin, *Phil. Mag.*, **43**, 800 (1922).
2. J. R. Schneider, *Acta Cryst. A*, **33**, 235 (1977).
3. A. McL. Mathieson, *Acta Cryst. A*, **35**, 50 (1979).

4. A. McL. Mathieson, J. K. Mackenzie, *Acta Cryst. A*, **35**, 45 (1979).
5. A. Palmer, Jauch, W. *Acta Cryst. A*, **51**, 662 (1995).
6. A. McL. Mathieson, A. Stevenson, *Acta Cryst. A*, **58**, 185 (2002).
7. W. Jauch, A. Palmer, *Acta Cryst. A*, **58**, 448 (2002).
8. W. H. Zachariasen, *Theory of X-ray Diffraction in Crystals*. New York: Wiley, (1945).
9. W. H. Zachariasen, *Acta Cryst.* **16**, 1139 (1963).
10. W. H. Zachariasen, *Acta Cryst.* **23**, 558 (1967).
11. P. J. Backer, P. Coppens, *Acta Cryst. A*, **30**, 129 (1974).
12. P. J. Backer, P. Coppens, *Acta Cryst. A*, **31**, 417 (1975).
13. T. M. Sabine, *Acta Cryst. A*, **44**, 368 (1988).
14. T. M. Sabine, International Tables for Crystallography, Vol. **C**, Dordrecht, Kluwer Akademik Publishers, pp. 530–533, 1992.
15. H. J. Bunge, Texture Analysis in Materials Science, London, Butterworths, 1982.
16. H. J. Bunge, *Textures and Microstructures*. **29**, 1, (1997).
17. S. Chandrasekhar, *Advances in Physics*, **9**, 363 (1960).
18. W. L. Bragg, R.W. James and C. H. Bosanque, *Phyl. Mag.*, **42**, 1 (1921)
19. H. J. Bunge, in: Directional Properties of Materials, H. J. Bunge (ed.), Oberursel 1, DMG Informationgesellschaft mbH, pp. 1–63, 1988.
20. P. P. Ewald, *Ann. d. Phys.*, **54**, 519 (1917).
21. P. B. Hirsch, *Progress in Metal Physics*, **6**, 275 (1956).
22. I. Tomov, K. Ivanova, *Textures and Microstructures*, **26–27,** 59 (1996).
23. V. Yamakov, I. Tomov, *J. Appl. Cryst.* **32**, 300 (1999).
24. W. Kleber, An Introduction to Crystallography, Berlin, VEB Verlag Technik, 1970.
25. I. Tomov, *Z. Kristallog.* Suppl., **26**, 131 (2007).
26. I. Tomov, S. Vassilev, in: Proceedings of the 1st National Crystallographic Symposium, Sofia, 22–23 Oct. 2009, p. 96.
27. A. Guinier, Theorie et Technique de la Radio-crystallographie. 2nd edition, Paris, Dunod, 1956.

ЕКСТИНКЦИЯ В ТЕКСТУРИ: АНУЛИРАНЕ НА ЕКСТИНКЦИОННИ ЕФЕКТИ

И. Томов

*Институт по оптически материали и технологии „Акад. Й. Малиновски“,
Българска академия на науките*

(Резюме)

Отчитайки вторичната екстинкция (ВЕ) в едно кристалографски направление, аналитичен метод е описан за рентгеново дифракционно характеризиране на текстури чрез анулиране на екстинкционни ефекти. За тази цел е извършено подходящо преразглеждане на природата на екстинкционните коефициенти. Показано е, че докато коефициентът на ВЕ g е пропорционален на произведението от полюсната плътност P и интензитета I_0, то емпиричният екстинкционен коефициент k е независим от отношението g/PI_0. На основата на неизменността на коефициента k по отношение на g/PI_0, екстинкционният ефект се анулира чрез изравняване на два негови израза, дефинирани чрез интензитетите на едно отражение, измерено при серия от нива на взаимодействия, чиято изменение се контролира от P и I_0. Техники, представляващи разширени версии са развити за (i) оценка на достоверността на контролираното изменение на нивата на взаимодействие чрез използване на инструментална променлива (силата на генераторния ток) и, оттук следва да се тества потенциалната възможност на рентгеновия апарат да събира точни и прецизни данни, и (ii) определяне на свободни от екстинкция данни на полюсната плътност, която е основен физичен параметър. Експерименталните резултати са дискутирани посредством влиянието на екстинкционния коефициент g върху точността на определяне на полюсната плътност в идеалното <100> направление на никелови текстури.

An extinction-free technique for pole density measurements of textures by XRD

I. Tomov[1],*, S. Vassilev[2], G. Avdeev[3]

[1] *Acad. J. Malinowski Institute for Optical Materials and Technologies, Bulgarian Academy of Sciences, Sofia 1113, Bulgaria*
[2] *Institute of Electrochemistry and Energy Systems, Bulgarian Academy of Sciences, Sofia 1113, Bulgaria*
[3] *Acad. R. Kaischew Institute of Physical Chemistry, Bulgarian Academy of Sciences, Sofia 1113, Bulgaria*

Pole density is a fundamental parameter of the diffraction pole figures used for calculation of orientation distribution functions that characterize the physical properties of textures. To gain accuracy and, hence, physical reality of the data, an approach is elaborated to derive experimental pole-density values, which are free of extinction effects. The approach is based on the intrinsic invariability of the empirical extinction coefficient k at a series of levels of interaction of the diffraction process. The invariability of k is a precondition for nullifying the extinction effects by equating couple of its expressions defined with the intensities measured at the same series of the levels of interaction. A nickel sample representing <100> texture component is investigated. The resultant derived series of data for the distribution of pole density P of the {200} diffraction pole figure is in exact accord with kinematic theory.

Key words: extinction, texture, diffraction pole figures, texture goniometer.

INTRODUCTION

Characterization of textural anisotropy is based on using pole density P that is defined by relative volume fraction of crystallites contributing with their <hkl> poles to the *hkl* reflection [1]. As diffraction and extinction are indissolubly linked [2], the pole density P_m determined by using the well-known definition $P_m = I_m/I_m^r$ suffers an extinction-induced systematic error caused by the measured intensities I_m and I_m^r of the same reflection of textured sample and powder standard, respectively. To overcome the inherent deficit of precision in the above definition, a pioneer technique is developed for *analytical* nullification of the extinction effects of diffraction pole-figures measured with texture goniometer. The technique is based on the invariability of the empirical extinction coefficient k with respect to the level of interaction of the diffraction process. Practically, the nullification of the extinction effects is attained by equating two expressions of k defined properly by measured intensities. To realize the purposes of this study, our concern here is essentially with exact relationship between diffraction and extinction at a series of levels of interaction attained by controlled variations of suitable physical parameters as in [3].

ANISOTROPY OF EXTINCTION COEFFICIENTS: NULLIFICATION OF THE EXTINCTION EFFECTS

Bragg *et al*. [4] and Darwin [5] have supposed that the empirical extinction coefficient k and the secondary extinction coefficient g, respectively, are constants for the crystal, i.e. they have considered k and g as parameters independent of crystallographic direction. Accounting for the crystal and textural anisotropy, the nature of k and g is reconsidered here. To this end, two definitions given by Darwin-Zachariasen [5, 6] and Bunge [1], respectively, are used:

$$\varepsilon = gQ\left(p_2/p_1^2\right), \qquad (1)$$

$$I_{kin} = PI_0QS/2\mu . \qquad (2)$$

Here ε is the secondary extinction (SE) correction, g is a dimensionless quantity, p_n (n=1,2,...,) is the polarization factor for incident X-ray beam [6, 7], I_0 is the intensity of the incident beam, S is the cross

---

* To whom all correspondence should be sent:
E-mail: iv_tomov@yahoo.co.uk

section of the beam, Q is the reflectivity per unit crystal volume, μ is the ordinary linear absorption coefficient. Combining (1) and (2) yields

$$\varepsilon = k I_{kin}\left(p_2/p_1^2\right)S , \qquad (3)$$

where the expression

$$k = 2g\mu/PI_0S \qquad (4)$$

shows that k and g are mutually connected. Reforming (4) gives an expression for

$$g = kPI_0S/2\mu \qquad (5)$$

illustrating that g depends on reciprocal way of the same parameters. Thus, the coefficients k and g should show different behaviour with respect to the diffraction process, whose level of interaction is controlled for any particular case by both P and I_0. First, at $PI_0 \to 0$, the lower limiting values of $I_{kin} \to 0$ (2) and $g \to 0$ (5) show, respectively, that in the only case of no diffraction, there is no extinction. Second, whereas g is proportional to the product PI_0, the coefficient k e is proportional to the ratio g/PI_0. Therefore, by virtue of the interdependence between g and PI_0, any change of P or I_0 or both does not cause change of the ratio g/PI_0 and, hence, k is constant for any measured point of a pole figure and, hence, independent of the level of interaction of the diffraction process. To prove this deduction suppose the pole density changes from P to $P^r=1$ under $I_0=$const. Following (4), k is transformed respectively into k^r, i.e.

$$k^r = 2\mu g^r/I_0S . \qquad (6)$$

Here, it is accounted that g^r is proportional to P^r which corresponds to random distribution of crystalline orientations. Dividing (4) by (6) and taking into account that $P=g/g^r$ yields

$$k = k^r , \qquad (7)$$

irrespective k and k^r correspond to different crystalline orientation distributions. Whereas k corresponds to $\{hkl\}$ diffraction pole figure (intensity distribution function) of a texture, k^r corresponds to hkl reflection of a sample representing the same substance with random orientation distribution.

The invariability of k constitutes its capability to nullify the extinction effects by equating two its expressions that are defined by the intensities of a pole figure measured at a series of levels of interaction. By virtue of the mathematical logics, the condition (7) has to be in exact accord with the kinematical theory and the resultant derived data will be then extinction-free.

EXPRESSING POLE DENSITY P BY NULLIFICATION OF EXTINCTION EFFECTS

To express P by nullifying extinction effects, a proper procedure is designed to data collection (Figure 1). In this respect, the $\{hkl\}$ diffraction pole figure of textured sample and hkl reflection of a powder standard with random crystalline distribu-

$$I_{kin,i}(\phi);k_i;P(\phi) \quad ----------$$

$$\uparrow \qquad \updownarrow P$$

$$R_{i,i*} \quad ----- \quad I^r_{kin,i};k^r_i;P^r; \leftarrow I_{0,i}=Ai(V-V_k)^n$$

$$\downarrow$$

$$I_{kin,i*}(\phi);k_{i*};P(\phi) \quad ----------$$

$$\updownarrow P$$

$$----- \quad I^r_{kin,i*};k^r_{i*};P^r; \leftarrow I_{0,i*}=Ai*(V-V_K)^n$$

$$k_i = k^r_i = k_{i*} = k^r_{i*}$$

Fig. 1. Data collection procedure that is designed by the levels of interaction of the diffraction process. The $\{hkl\}$ pole figure of textured sample and hkl reflection of powder standard are measured at the incident beam intensities $I_{0,i}$ and $I_{0,i*}$ cased by the generator current i and $i*$. Here ϕ is the angle to the sample normal direction.

tion are measured at the incident beam intensities $I_{0,i}$, $I_{0,i*}$ caused by stepwise reduction of the generator current values i and $i*$ ($i=2i*$).

In the equations listed in Figure 1, A is a constant, V_K is the critical excitation potential of the $K\alpha$ radiation, and $n=1.5$ [8]. As a whole, the measurement procedure is carried out at constant generator tension V. Any of the particular levels of interaction is characterized by kinematic intensities, $I_{kin}(\phi)$ and I_{kin}^r of the texture and power standard, respectively, the pole densities, $P(\phi)$ and P^r, and the coefficient k. Let us focus our attention that k is the same for each of the levels of interaction, and P^r is equal to unit. Then, the pole density $P_i(\phi)$ is express by the kinematic intensities corresponding to the first couple of levels of interaction measured at the intensity $I_{0,i}$:

$$P_i(\phi) = I_{kin,i}(\phi)/I_{kin,i}^r \qquad (8)$$

The relation (8) is valid for the interval $0° < \phi < 70°$ of the pole figure measured at the intensity $I_{0,i}$. As shown in the paper [3], the kinematic intensities are defined by the respective measured intensities I_m:

$$I_{kin,i}(\phi) = \left\{ \mu / \left[\mu - k_i I_{m,i}(\phi)\left(p_2/p_1^2\right) \right] \right\} I_{m,i}(\phi), \quad (9)$$

$$I_{kin,i}^r = \left\{ \mu / \left[\mu - k_i^r I_{m,i}^r \left(p_2/p_1^2\right) \right] \right\} I_{m,i}^r. \quad (10)$$

Solving the system of equations (9) and (10) for $k_i = k_i^r$ (see (7)) yields the expression:

$$k_i = \frac{\mu\left[P_i(\phi) - \left(I_{m,i}(\phi)/I_{m,i}^r \right) \right]}{I_{m,i}(\phi)\left(p_2/p_1^2\right)[P_i(\phi) - 1]}. \qquad (11)$$

By analogy of equations from (8) to (11), the coefficient $k_{i*} = k_{i*}^r$ corresponding to the second couple of levels of interaction is expressed by using the next three definitions:

$$P_{i*}(\phi) = I_{kin,i*}(\phi)/I_{kin,i*}^r. \qquad (12)$$

$$I_{kin,i*}(\phi) = \left\{ \mu / \left[\mu - k_{i*} I_{m,i}(\phi)\left(p_2/p_1^2\right) \right] \right\} I_{m,i*}(\phi), (13)$$

$$I_{kin,i*}^r = \left\{ \mu / \left[\mu - k_{i*}^r I_{m,i*}^r \left(p_2/p_1^2\right) \right] \right\} I_{m,i*}^r \quad (14)$$

$$k_{i*} = \frac{\mu\left[P_{i*}(\phi) - \left(I_{m,i*}(\phi)/I_{m,i*}^r \right) \right]}{I_{m,i*}(\phi)\left(p_2/p_1^2\right)[P_{i*}(\phi) - 1]}. \qquad (15)$$

Solving (11) and (15) for $P_{i,i*}(\phi) = P_i(\phi) = P_{i*}(\phi)$ under nullifying the extinction effect by equating the coefficients $k_i = k_{i*}$ yields an extinction-free

value for the pole density for the ϕ-angle of the diffraction pole figure:

$$P_{i,i*}(\phi) = \frac{I_{m,i}(\phi)I_{m,i*}(\phi)\left(I_{m,i}^r - I_{m,i*}^r\right)}{I_{m,i}^r I_{m,i*}^r \left(I_{m,i}(\phi) - I_{m,i*}(\phi)\right)}. \quad (16)$$

Therefore, starting from kinematic definitions (8) and (12) for the pole density, an operative formula (16) that is in exact accord with the kinematic theory is derived using measured intensities. This procedure has to be repeated for any ϕ-angle of the measured interval $0° < \phi < 70°$.

EXPERIMENTAL, RESULTS AND DISCUSSION

As model samples, an electrodeposited nickel coating (Ni1) and a nickel powder standard with random crystalline distribution were used. The nickel coating represents fiber texture with a main <100> component. The {200} pole figure and 200 reflection corresponding to the respective samples were measured with texture goniometer using Ni filtered CuK$_\alpha$ radiation. The two-step measurement procedure, shown in Figure 1, was carried out in such
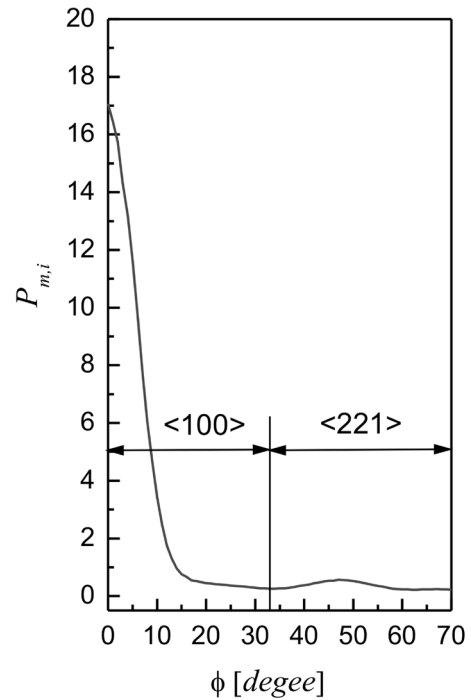
Fig. 2. {200} pole figure of an electrodeposited nickel (Ni1) measured at generator current i. It represents the distribution of strongly extinction-affected pole densities: $P_{m,i}(\phi) = I_{m,i}(\phi)/I_m^r$, ϕ is the angle to the sample normal direction.
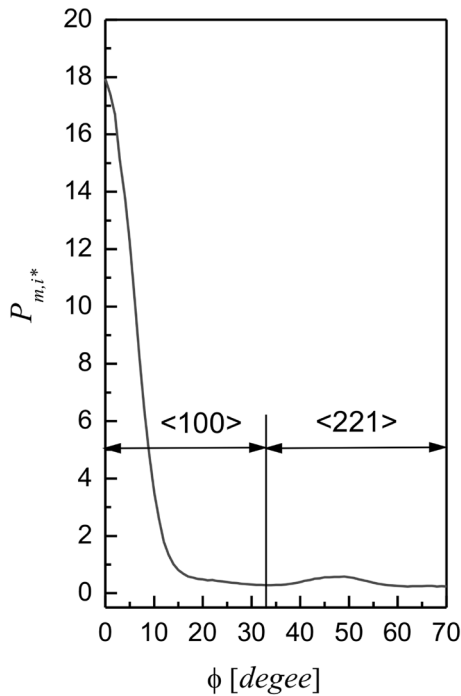
Fig. 3. {200} pole figure of an electrodeposited nickel coating (Ni1) measured at generator current i^*. It represents the distribution of less extinction-affected pole densities: $P_{m,i^*}(\phi) = I_{m,i^*}(\phi)/I_m^r$.
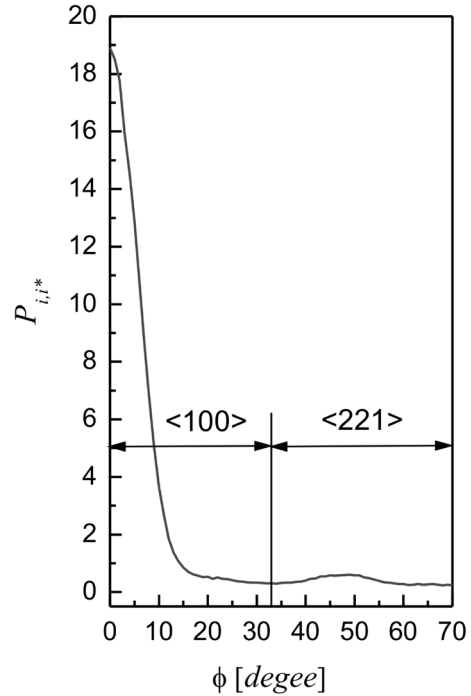
Fig. 4. {200} pole figure of an electrodeposited nickel coating (Ni1) representing extinction-free data calculated by (16).

a way to compensate the stepwise decrease of the generator current from i to i^* ($i = 2i^*$) by respective increase of the data collection time per scanned step from τ to τ^*, i.e. ($i\tau = i^*\tau^*$). The compensative condition ensures the same statistical errors in the respective ϕ-angles of the measured entity.

The pole density $P_m(\phi)$ distributions determined for the first and second measurements are shown in Figure 2 and Figure 3, respectively. Due to lower extinction effects, the $P_{m,i^*}(\phi)$ values (Figure 3) are higher than those of the $P_{m,i}(\phi)$ distribution (Figure 2) that are strongly affected by extinction. The systematic error is higher at the higher level of interaction and lowest at the lowest level of interaction. This error depends on the absolute value P_m of the pole density as well. Figure 4 shows extinction-free data determined by (16). The percentage errors between the respective data listed in Figure 4 and that ones listed in Figure 2 and Figure 3 vary from about 5% to less than 1% for the whole measured interval $0° < \phi < 70°$.

CONCLUDING REMARKS

The main advantage of this approach is to gain accuracy and, hence, physical reality of the data. Accuracy can only be gained by care in the design and implementation of an experiment. Actually, this approach offers a possibility for existing methods both to be re-considered and improved for texture characterizations and to develop new ideas. In general, one can state that no problem related to using the integral intensities can be correctly solved in textures if secondary extinction effects are not nullified.

REFERENCES

1. H. J. Bunge, *Textures and Microstructures*., **29**, 1, (1997).
2. A. McL. Mathieson, *Acta Cryst. A*, **35**, 50 (1979).
3. I. Tomov, in the same issue, submitted.
4. W. L. Bragg, R. W. James, C. H. Bosanque, *Phyl. Mag*., **42**, 1 (1921).
5. C. G. Darwin, *Phil. Mag*., **43**, 800 (1922).
6. W. H. Zachariasen, *Acta Cryst.* **16**, 1139 (1963).
7. S. Chandrasekhar, *Advances in Physics*, **9**, 363 (1960).
8. A. Guinier, Theorie et Techn. de la Radiocryst, 2nd Edition, Paris, Dunod, 1956.

ЕДНА ТЕХНИКА ЗА ИЗМЕРВАНЕ НА СВОБОДНИ ОТ ЕКСТИНКЦИЯ ПОЛЮСНИ ПЛЪТНОСТИ ЧРЕЗ РЕНТГЕНОВА ДИФРАКЦИЯ

И. Томов[1],*, С. Василев[2], Г. Авдеев[3]

[1] Институт по оптически материали и технологии „Акад. Й. Малиновски”,
Българска академия на науките
[2] Институт по електрохимия и енергийни системи, Българска академия на науките
[3] Институт по физикохимия „Акад. R. Каишев“, Българска академия на науките

(Резюме)

Полюсната плътност е фундаментален параметър на дифракционните полюсни фигури, които се използват за изчисляване на ориентационните разпределителни функции, характеризиращи физичните и механични свойства на текстурите. За да се спечели точност, а оттук следва и физична реалност на данните, е разработен един подход за извличане стойностите на експерименталните полюсни плътности, които са свободни от екстинкционни ефекти.

Structure stability towards cation substitutions in $A_2B_2O_5$ perovskites with crystallographic shear planes

P. Tzvetkov[1,*], D. Kovacheva[1], D. Nihtianova[1, 2], T. Ruskov[3]

[1] Institute of General and Inorganic Chemistry, Bulgarian Academy of Sciences
1113 Sofia "Acad. Georgi Bonchev" str. bld.11
[2] Institute of Mineralogy and Crystallography, Bulgarian Academy of Sciences
1113 Sofia "Acad. Georgi Bonchev" str. bld.107
[3] Institute for Nuclear Research and Nuclear Energy, Bulgarian Academy of Sciences
1784 Sofia "Tzarigradsko chaussee" 72 Blvd.

New perovskite-related compounds with general formula $Pb_{2-x}Ba_xFe_{2-y}Co_yO_5$ ($0.67 \leq x \leq 1$, $0 \leq y \leq 1$) were prepared by solution-combustion technique. The compounds were characterized by X-ray powder diffraction, SAED TEM, and ^{57}Fe Mössbauer spectroscopy. The structure is closely related to other perovskite-derived structures such as Ca_2FeAlO_5 and $Ca_2Mn_2O_5$ and can be described as an anion deficient perovskite in which half of the B^{3+} cations are located in the octahedral coordination as in the prototype perovskite structure and the other half are five-coordinated in distorted tetragonal pyramids. The pyramidal coordination is formed by glide of one perovskite block in respect to the previous one at $b/2$ along [010] direction as a result of ordered oxygen vacancies. The pyramids share common edges and form double chains and channels between them along the b-axis. Inside the channels there are Pb^{2+} cations that are located coordinated by six oxygen atoms and one $6s^2$ electron lone pair of the lead atom. The second cation position is situated within the perovskite block and has mixed occupancy by the larger Pb^{2+} and Ba^{2+} ions. The study reveals that substitution of iron by cobalt is possible only at high substitution levels of lead by barium. The influence of the composition on the structural parameters and stability of the structure is discussed.

Key words: perovskites, crystallographic shear planes, cation substitutions.

1. INTRODUCTION

The perovskite structure is typical for compounds with general formula ABX_3, where A^+ is cation with ionic radius close to that of the anion X^- (oxygen or halide anion) and B^+ is a smaller cation usually of a transitional metal. The structure can be described as cubic close packing of A^+ and X^- ions, where B^+ is occupying ¼ of the octahedral interstices. Since perovskite structure is very flexible towards modification of the composition and topological changes perovskite-type materials exhibit great variety of physical and chemical properties. Among the perovskites one can find typical dielectrics, high temperature superconductors, ion conductors, colossal magneto-resistant materials, optical materials, catalysts, etc. Many structures can be derived from that of perovskite by different ways: by mixed occupancy and cation ordering in A and B position; vacancy ordering in the anion sublattice; intergrowth of perovskite and other structure type blocks (e.g. NaCl, CaF_2), and the formation of hexagonal perovskite polytypes, thus, leading to a huge number of compounds. Complex structural phenomena concerning the anion sublattice of the perovskites were observed and studied with regard to their influence on the physical properties of the materials. Among them are the oxygen vacancy distribution, ordering and evolution [1–4] and the formation of crystallographic shear planes [4–6]. The shear operation changes the connectivity scheme of the metal-oxygen polyhedra, replacing corner-sharing BO_6 octahedra by edge-sharing BO_5 distorted tetragonal pyramids. The introduction of periodically ordered translational interfaces into the perovskite structure was performed on the basis of detailed transmission electron microscopy investigations of a new class of Pb and Fe-containing compounds [6–8]. These compounds are closely related to the brownmillerite-type structure and are isostructural with

---

* To whom all correspondence should be sent:
E-mail: p-tzvetkov@gmx.net

$Pb_{1.33}Sr_{0.67}Fe_2O_5$ (*Pnma*, a = 5.687, b = 3.920, c = 21.075 Å) [9]. The structure is complex due to the fragmentation of the perovskite matrix. The corner sharing FeO_6 octahedra alter with double chains of edge sharing mirror-related FeO_5 distorted tetragonal pyramids. The FeO_5 chains running along the *b*-axis and the octahedra of the perovskite blocks delimit six-sided tunnels, where Pb atoms are located. Two configurations of FeO_5 chains occur, arbitrary denoted as L- and R-chains. At room temperature they are fully ordered and alternate along the *c*-axis. A phase transition between an ordered and disordered arrangement of the chains was detected in $PbBaFe_2O_5$ around 270 °C [10]. The Sr(Ba) and Pb atoms occupy mixed positions located in the cuboctahedral cavities inside the perovskite blocks. The accommodation of lone $6s^2$ electron pair (Pb^{2+}, Bi^{3+}) in the A position of the perovskite structure is a condition for ferroelectric properties. In addition, the coordination of Fe^{3+} in the structure with B–O–B angles of 180° and 90° can lead to unusual magnetic behavior [6]. The perovskite structure is flexible and accommodates variety of substitutions.

The purpose of the present work is to study the tolerance toward cation substitutions in A and B positions of the perovskite structure modified by translational interfaces (crystallographic shear planes). We report the synthesis and structural characterization of a new series of polycrystalline compounds with general formula $Pb_{2-x}Ba_xFe_{2-y}Co_yO_5$ ($0.67 \leq x \leq 1$, $0 \leq y \leq 1$).

2. EXPERIMENTAL

Polycrystalline samples with chemical composition $Pb_{2-x}Ba_xFe_{2-y}Co_yO_5$ ($0.67 \leq x \leq 1$, $0 \leq y \leq 1$) were prepared by the solution-combustion technique [11, 12]. The starting compounds used were $Fe(NO_3)_3.9H_2O$, $Pb(NO_3)_2$, $Ba(NO_3)_2$, $Co(NO_3)_2.6H_2O$ and sucrose ($C_{12}H_{22}O_{11}$), all of analytical grade purity. A stoichiometric mixture of the reagents was dissolved in a minimum quantity of distilled water. The dish containing the reaction mixture was placed on an electric heater and evaporated until drying. After drying, the samples were left on the heater to raise the temperature and initialize the combustion reaction. The samples burned quickly, forming light fine powders. The obtained powders were further homogenized in agate mortar and heated at 400ºC for 2 hours in order to burn the organic residue, homogenized again and pressed into pellets (14 mm diameter) at 714 atm [kg/cm²] pressure. The pellets were placed into corundum crucibles and heated for 24 hours at 850 °C in air with one intermediate grinding after the first 12 hours. The samples were grinded and heated again at 930 °C for 1 hour in order to promote the reaction of $BaPbO_3$ detected as a minor impurity phase in the samples.

Mössbauer spectra were taken in the transmission mode at room temperature using a constant acceleration spectrometer. A source of $^{57}Co(Rh)$ was used. $PbBaFe_{2-x}Co_xO_5$ (x = 0, 0.5, 1) powder material was mixed with polyvinyl alcohol powder (glue substance) and then pressed into a disk. The thickness of the disk was chosen to achieve Mössbauer absorber thickness of 50 mg cm^{-2}. The spectra were fitted using an integral Lorentzian line shape approximation [13, 14]. The isomer shifts are referred to the centroid of α-iron foil reference spectrum at room temperature. The geometric effect was taken into account.

The TEM investigations for $PbBaFe_{2-x}Co_xO_5$ (x = 0.5, 1) were performed by TEM JEOL 2100 with 200 kV accelerating voltage. The specimens were grinded and dispersed in ethanol by ultrasonic treatment for 6 min. The suspensions were dripped on standard holey carbon/Cu grids.

Powder X-ray diffraction patterns were collected at room temperature on Bruker D8 Advance diffractometer using CuKα radiation and LynxEye PSD detector within the range 5–140° 2θ, step 0.02° 2θ and 6 sec/strip (total of 1050 sec/step). To improve the statistics, rotating speed of 60 rpm was used. The crystal structure parameters were refined using TOPAS 3 program [15].

3. RESULTS AND DISCUSSION

According to the results of the powder XRD analyses it was found that the substitution of cobalt for iron in the structure of $Pb_{2-x}Ba_xFe_2O_5$ depends strongly on the degree of substitution of lead by barium. For x < 0.9 only small amount of cobalt can be accommodated in the structure. With the increase of the substitution level to x = 1 a solid solution series with composition $PbBaFe_{2-x}Co_xO_5$ (x = 0, 0.25, 0.5, 0.75, 1) was successfully synthesized. Unit cell parameters of the corresponding phases are presented in Table 1. The substitution leads to slight increase of *b* parameter and simultaneous decrease of both *a* and *c* parameters. As a result, the volume of the unit cell decreases with the increase of the substitution level. This fact is consistent with the difference of the ionic radii of Fe^{3+} (0.645Å) and Co^{3+} (0.61Å) [16].

The Rietveld refinement of the compounds within the series $PbBaFe_{2-x}Co_xO_5$ (x = 0, 0.25, 0.5, 0.75, 1) revealed that they all are isostructural with the end member $PbBaFe_2O_5$. Detailed structural parameters for the composition $PbBaFeCoO_5$ are presented in Table 2. Due to the small difference of the atomic scattering factors of Fe^{3+} and Co^{3+}, the distribution of

Table 1. Unit-cell parameters for the $PbBaFe_{1-x}Co_xO_5$ solid solutions calculated from XRD data

x	a (Å)	b (Å)	c (Å)	V (Å^3)
0.00	5.76504(6)	3.99197(4)	21.1376(2)	486.440(9)
0.25	5.76277(6)	3.99414(5)	21.0965(2)	485.62(1)
0.50	5.76075(5)	3.99950(4)	21.0468(2)	484.96(1)
0.75	5.75921(4)	4.00445(3)	20.9975(2)	484.297(7)
1.00	5.75834(4)	4.00866(3)	20.9558(2)	483.745(9)

Table 2. Refined structural parameters for $PbBaFeCoO_5$, space group $Pnma$(62), a = 5.75834(4), b = 4.00866(3), c = 20.9558(2), Z = 4

Atom	Wyck.	x/a	y/b	z/c	SOF	B_{iso}(Å^2)
Pb(1)	4c	0.0051(8)	1/4	0.56867(7)	1.00	0.69(3)
Ba(2)	4c	0.4888(9)	1/4	0.68424(9)	1.00	0.44(5)
Fe(1)	4c	0.521(2)	1/4	0.4463(2)	1.00	0.38(6)
Co(2)	4c	1.000(2)	1/4	0.3155(3)	1.00	0.38(6)
O(1)	4c	0.962(4)	3/4	0.3188(7)	1.00	1.3(2)
O(2)	4c	0.728(4)	1/4	0.235(1)	1.00	1.3(2)
O(3)	4c	0.201(4)	1/4	0.394(2)	1.00	1.3(2)
O(4)	4c	0.747(4)	1/4	0.387(2)	1.00	1.3(2)
O(5)	4c	0.542(4)	3/4	0.4608(6)	1.00	1.3(2)

R_B = 1.46, R_{wp} = 3.52, R_{exp} = 1.09, GOF = 3.23

cobalt over the two possible cation sites could not be determined from the XRD experiments. Therefore, a Mössbauer spectroscopy was performed.

The Mössbauer spectra of the two types of samples $PbBaFe_2O_5$ (Type I) and $PbBaFe_{1.5}Co_{0.5}O_5$ (Type II) are shown in Fig. 1. The fitted parameters corresponding to isomer shift (IS), full width at half maximum (FWHM) of the absorption lines, quadrupole shift (QS), magnetic field at the site of the Fe nucleus (H), and relative spectral area are summarized in Table 3.

Each spectrum was fitted by superposition of two well-resolved magnetic Zeeman sextets, (1) and

(2), corresponding to the two positions of the iron in the crystal lattice of the investigated material. For the first sample (that without Co) we obtained the isomer shift of the sextet (1) as 0.329 mm/s, while for the sextet (2) it is 0.418 mm/s. For the second sample (with Co) the isomer shifts are 0.33 mm/s and 0.42 mm/s, respectively. Therefore, within the experimental error, there is no difference as to the isomer shift for the two samples. In both positions the valence state of the iron is Fe^{3+}. However, in general, taking into account the systematic decrease of the isomer shift on decreasing of the coordination of iron, we should assign, for both types of samples,

Table 3. ^{57}Fe Mossbauer spectral parameters of hyperfine interaction for $PbBaFe_2O_5$ and $PbBaFe_{1.5}Co_{0.5}O_5$

Sample	Site	IS [mm/s]	FWHM [mm/s]	QS [mm/s]	H [kOe]	Relative area [%]
Type I	1	0.329(3)	0.17(1)	0.107(3)	434.6(3)	50.7 ± 1.4
	2	0.418(3)	0.18(1)	−0.106(4)	502.5(2)	49.3 ± 1.4
Type II	1	0.33(1)	0.26(2)	0.128(6)	431.6(4)	46.6 ± 1.8
	2	0.42(1)	0.25(2)	−0.106(5)	496.2(3)	53.4 ± 1.8
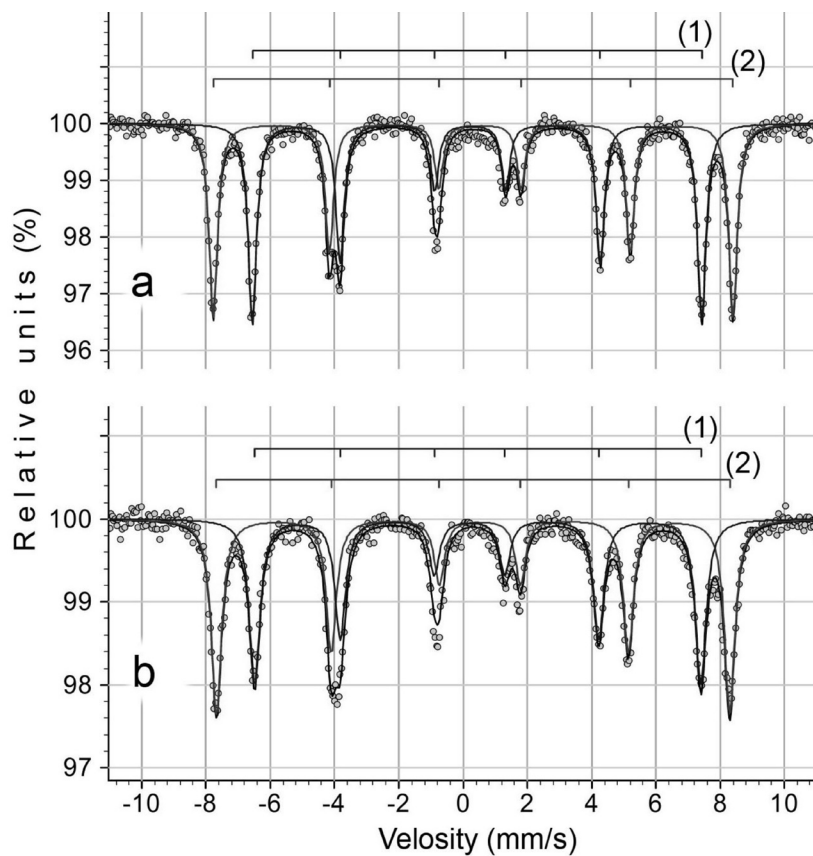
Fig. 1. Mössbauer spectra of $PbBaFe_2O_5$ (a) and $PbBaFe_{1.5}Co_{0.5}O_5$ (b)
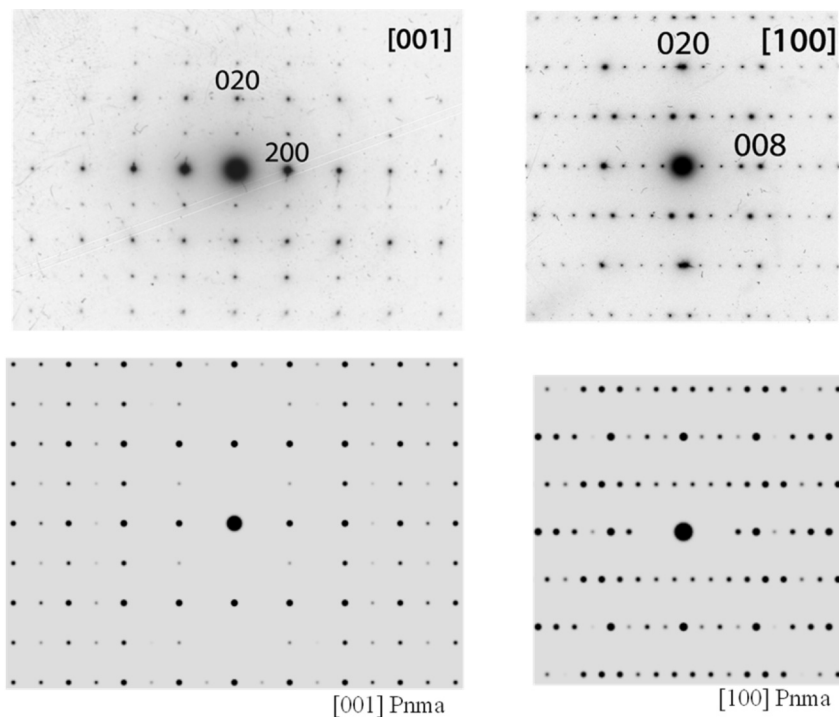
Fig. 2. Experimental and calculated selected area electron diffraction patterns of $PbBaFeCoO_5$ in [001] and [100] directions

sextet (1) to the pyramidal site (Fe-O$_5$) and sextet (2) to the octahedral site (Fe-O$_6$) [14]. The sample with Co shows a significant increase of the resonance line width for both sites: the pyramidal and octahedral ones. There is also a small decrease of the magnetic field at the site of the Fe nucleus when going from Type I (without Co) to Type II (with Co) samples. It should be mentioned some difference of the relative spectral area as well. The sample without Co shows

nearly equal spectral area for both sites, while the sample with Co shows that the pyramidal site is several percent less populated by iron (Fig. 1 and Table 3).

Summarizing all the data we can conclude that cobalt replaces iron in both sites, but with more preference to the pyramidal one. The broadening of the resonance lines for Type II sample is connected with the random distribution of cobalt and different
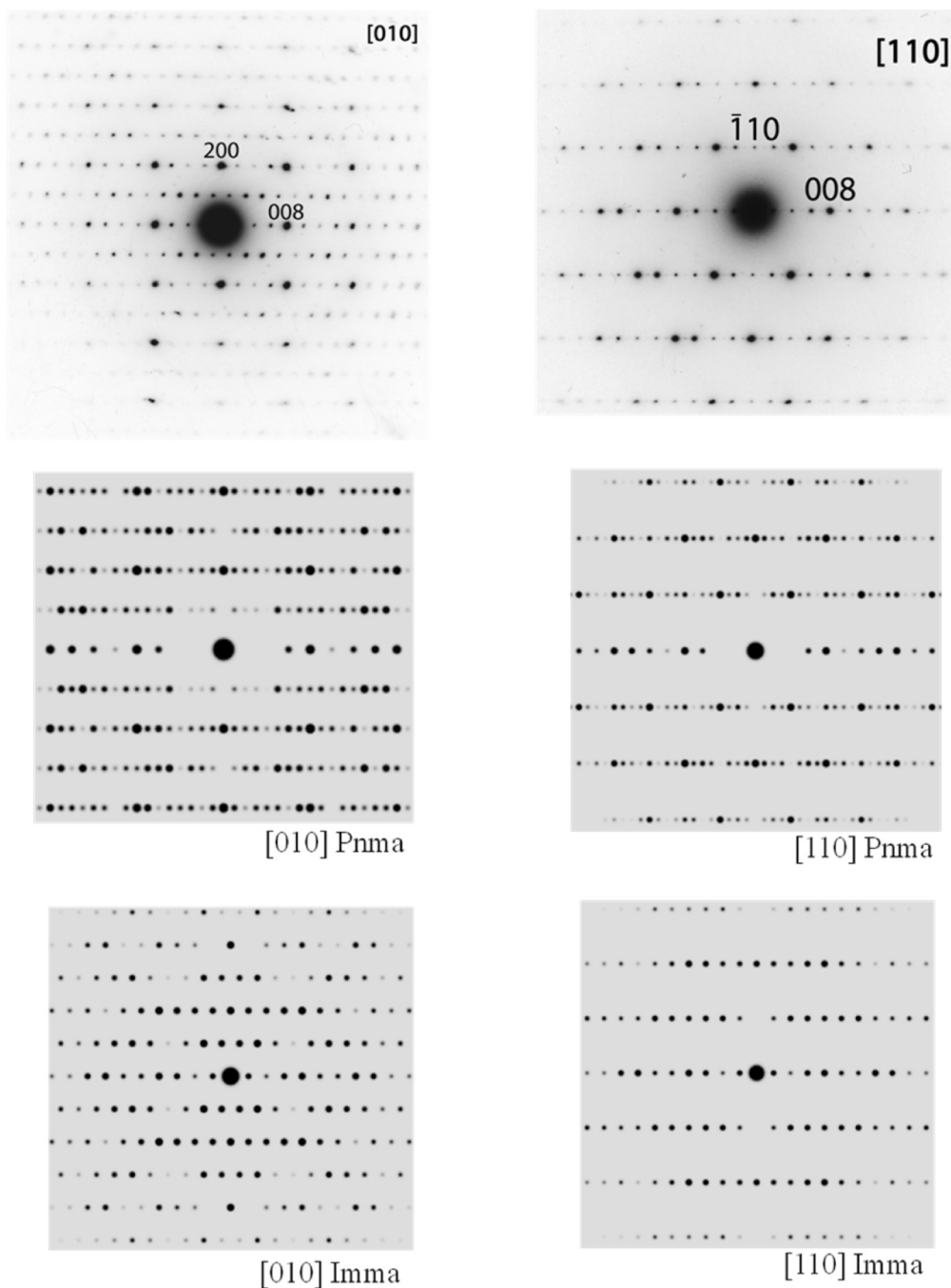
Fig. 3. Experimental and calculated selected area electron diffraction patterns of PbBaFeCoO$_5$. In directions [010] and [110] both low (*Pnma*) and high (*Imma*) temperature phases are observed

exchange interactions Fe–Fe and Fe–Co. The small increase of the cobalt population in the pyramidal site could be explained by the different ion radii of Fe and Co. The cobalt ion has a smaller radius than the iron ion and it is easier for Co ion to be placed into the pyramidal site than iron ion since the pyramidal site volume is smaller than that of the octahedral site. The asymmetric population of cobalt in the octahedral and pyramidal sites is an additional way to assign magnetic sextet (1) to the pyramidal site (Fe-O_5) and sextet (2) to the octahedral site (Fe-O_6).

Experimental and calculated SAED patterns of sample PbBaFeCoO$_5$ are shown in Figs. 2 and 3. The complete indexing of the patterns was performed using an orthorhombic unit cell as determined from the XRD data. The reflection conditions: 0kl:k+l = 2n, hk0:h = 2n, h00:h = 2n, 0k0:k = 2n, 00l:l = 2n are unambiguously derived from the [100] and [001] electron diffraction patterns, in agreement with the proposed *Pnma* space group.

The parent structure PbBaFe$_2$O$_5$ undergoes a phase transition from *Pnma* to *Imma* space group at 270 °C [10]. The same transition was observed for the substituted sample PbBaFeCoO$_5$ during the TEM studies. The SAED patterns for [010] and [110] directions can be indexed by using two sets of diffraction patterns – one for the low-temperature phase and a second one for the high temperature phase. We suppose that this transition is caused by the electron beam irradiation. Experimental [100], [010], [001], [110] SAED patterns are compared with calculated ones and a good accordance is observed.

REFERENCES

1. M. Anderson, J. Vaughey, K. Poeppelmeier, *Chem. Mater.*, **5**, 151 (1993).
2. J. Vaughey, K. Poeppelmeier, *NIST Special Publication*, **804**, 419 (1991).
3. J. Hadermann, G. Van Tendeloo, A. Abakumov, *Acta Cryst. A*, **61,** 77 (2005).
4. E. Antipov, A. Abakumov, S. Istomin, *Inorg. Chem*, **47**, 8543 (2008).
5. C. Bougerol, M. Gorius, I. Grey, *J. Solid State Chem.*, **169**, 131 (2002).
6. A. Abakumov, J. Hadermann, S. Bals, I. Nikolaev, E. Antipov, G. Van Tendeloo, *Angew. Chem. Int. Ed.*, **45**, 6697 (2006).
7. A. Abakumov, J. Hadermann, G. Van Tendeloo, E. Antipov, *J. Am. Ceram. Soc.*, **91**, 1807 (2008).
8. G. Van Tendeloo, J. Hadermann, A. Abakumov, E. Antipov, *J. Mater. Chem.*, **19**, 2660 (2009).
9. V. Raynova-Schwarten, W. Massa, D. Babel, *Z. Anorg. Allg. Chem.*, **623**, 1048 (1997).
10. I. Nikolaev, H. D'Hondt, A. Abakumov, J. Hadermann, A. Balagurov, I. Bobrikov, D. Sheptyakov, V. Pomjakushin, K. Pokholok, D. Filimonov, G. Van Tendeloo, E. Antipov, *Phys. Rev. B*, **78**, 024426 (2008).
11. M. Sekar, K. Pathil, *J. Mater.Chem.*, **2**, 739 (1992).
12. K. Patil, S. Aruna, T. Mimani, *Curr. Opin. Solid State Mater. Sci.*, **6**, 507 (2007).
13. G. Shenoy, J. Friedt, H. Maleta, S. Ruby, *Mössbauer Effect Methodology*, **9**, 277 (1974).
14. T. Cranshaw, *J. Phys. E*, **7**, 122 (1974).
15. TOPAS 3: General profile and structure analysis software for powder diffraction data, Bruker AXS, Karlsruhe, Germany. Menil, F., 1985, *J. Phys. Chem. Solids*, **46**, 763 (2005).
16. R. Shannon, *Acta Cryst. A*, **32**, 751 (1976).

СТРУКТУРНА СТАБИЛНОСТ И КАТИОННО ЗАМЕСТВАНЕ В A₂B₂O₅ ПЕРОВСКИТИ С КРИСТАЛОГРАФСКИ РАВНИНИ НА СРЯЗВАНЕ

П. Цветков[1,*], Д. Ковачева[1], Д. Нихтянова[1,2], Т. Русков[3]

[1] Институт по обща и неорганична химия, Българска академия на науките
1113 София ул. „Акад. Георги Бончев" бл.11
[2] Институт по минералогия и кристалография, Българска академия на науките
1113 София ул. „Акад. Георги Бончев" бл.107
[3] Институт за ядрени изследвания и ядрена енергия, Българска академия на науките 1784 София бул. „Цариградско шосе" 72

(Резюме)

Чрез метода на комбустия от разтвор бяха синтезирани нови перовскитоподобни съединения с обща формула Pb$_{2-x}$Ba$_x$Fe$_{2-y}$Co$_y$O$_5$ (0.67<x<1, 0<y<1). Веществата са характезизирани с X-ray прахова дифракция, SAED TEM и ^{57}Fe Mössbauer спектроскопия. Структурата е близка на други производни структури като Ca$_2$FeAlO$_5$ и Ca$_2$Mn$_2$O$_5$ и може да бъде описана като анионно дефицитен перовскит, в който половината от B^{3+} катиони заемат октаедрична координация, а останалата половина са в петорна координация в изкривени тетрагонални пирамиди. Петорната координация на пирамидите се получава от прихлъзване на един перовскитов блок спрамо съседния на b/2 по направление [010], като резултат от подредени кислородни ваканции. Пирамидите споделят общи ръбове и образуват двойни вериги и канали по дължина на b-оста. Вътре в каналите Pb^{2+} катиони са координирани от шест кислородни атома и една 6s^2 електронна двойка от оловния атом. Втората голяма катионна позиция се намира в перовскитовия блок и има смесено заселване от Pb^{2+} и Ba^{2+} йони. Изследването показва, че заместването на желязо с кобалт е възможно само при високи нива на заместване на олово от барий. Обсъдени са влиянието на състава върху структурните параметри и стабилностт на структурата.

On the relationship crystal structure – properties at flexible chain polymers. I. Polycaprolactam

Chr. Uzov[1]*, B. Bogdanov[1], Y. Denev[1], V. Velev[2], T. Angelov[3], A. Popov[1]

[1] *"Prof. Assen Zlatarov" University-Burgas, 8010 Burgas, Bulgaria*
[2] *"Konstantin Preslavski" University-Shumen, 9712 Shumen, Bulgaria*
[3] *Lukoil Neftohim – Burgas AD, Burgas, Bulgaria*

There are applied different methods as high temperature X–ray, microscopic, spectroscopic, calorimetrical, heat-mechanical etc. There are mostly studied the deformation and destruction of the elementary cells of the polycaprolactam basic crystal forms. By change of the intensity distribution of the powder X-ray diffraction there are controlled as the profile and angle deviation on different diffraction reflections, as well as the alterations in the packing of the macromolecular chain segments in the crystal phase. There are defined the critical deformation values caused the polymorphic transitions. The present results are connected with the crystal phase perfection and with the quantitative proportion of the simultaneously existed crystallographic modifications in the studied objects at the given conditions. There is supposed a mechanism of structural development connected with the specificity in the H-bonds redistribution at the polycaprolactam.

Key words: Polycaprolactam, thin films, structure, polymorphic transitions, X-ray diffraction.

INTRODUCTION

Undoubtedly the structure-properties relationship remains currently actually. At the strongly crystallizable flexible chain polymers and especially at polycaprolactam the studying of the relationship crystal structure/properties is particularly important. The influence of the hydrogen bonds between the amide groups as in the crystal as well as in the amorphous polycaprolactam regions fully defines its strength/deformation properties. The effect multiplies from the fact that the polycaprolactam structure/properties relation is consider in the borders crystal structure in isotropic state – deformation behaviour in oriented state, and includes basic stages as follows: nascent structure – forming conditions – isotropic structure – orientation drawing conditions – structure in oriented state at given drawing stage – utmost drawing conditions – utmost oriented structure – deformation behaviour of utmost oriented polycaprolactam. The studding of the relationships begins with temperature possibilities for optimal modifications of the initial isotropic structures and it can starts with investigation of the

polycaprolactam polymorphism at cyclical repeatedly heating and cooling in the most wide possible temperature interval.

EXPERIMENTAL

There are used different modes polycaprolactam with different molecular masses and molecular-mass distribution (characteristic viscosity in 1% solution of H_2SO_4 $\eta_{rel}=2.11\div2.83$), contents of low-molecular tie in the interval $1.0\div12.0\%$ mass, moisture content from 0,1 to 0,01% mass, as a necessary condition about the obtaining of crystal structures with different perfection. There are formed thin folios in a large diapason of forming conditions: $T_{pr.} = 483\div513$ K и $T_{c.} = 77\div473$ K. The high temperature X-ray investigations are carried out by repeated cyclical heating and cooling in the temperature interval from 293 K to 513 K with heating rate of 5 K/min and 5 min tempering for every scanned temperature at interval of 5 K. The initial isotropic structure of the pressed folios was characterized by light-microscopy, electron-microscopy and with powder X-ray diffraction methods using a polarization light-microscopy Amplival Pol, Karl Zeiss, Jena, Germany, SEM BS – 340, Tesla, Brno, Cheh Republic, TEM Opton 10B, Feintechnik, Oberkochen, Germany. Using

---

* To whom all correspondence should be sent:
E-mail: hristo_uzov@abv.bg

an universal powder X-ray diffractmeters URD 6 ("Präzisionsmechanik – Freiburg", Germany) and ДРОН 3 equipped with a high temperature chamber УВД 2000 ("Буревестник – Санкт Петербург", Русия), at applying of $Cu_{K\alpha}$ radiation (β-filtered by Ni filter, $\lambda = 1.5418$ Å) there are obtained low- and high-temperature X-ray diffraction curves under different time/temperature conditions of simultaneous modification. The crystal phase perfection was defined by the packing compactness of the macromolecular chain segments in the crystal phase of the α-crystal modification [1, 2]. The deformation/strength investigations are carried out at differen temperatures by an apparatus "Tiratest-102", Germany.

RESULTS AND DISCUSSION

The intensity distribution of the diffracted from isotropic structures X-ray beam is basically concentrated in the angle interval 18–19 ÷ 25–26 °2θ. In that interval appear the fundamental diffraction reflections of the all known polymorphous forms (α, α*, β, β*, γ, γ*), the other possible meso-states, as well as the known as overcooling melt δ-phase [3–11]. Because of that the powder diffraction in the interval 15÷30 °2θ is fully sufficient about polymorphous phase investigations in the studying of its structure rearrangement. The relation structure – properties investigation needs of a detailed notion about the polycaprolactam crystal structure, because of the existence of direct connection with the morphology and determining of its mechanical behaviour amorphous regions. The obtained experimental data show that the most using morphologic structures cause the simultaneously existence of more than one crystal forms. Usually it can be observed the simultaneously existence of all possible polymorphous forms and mesophases in different
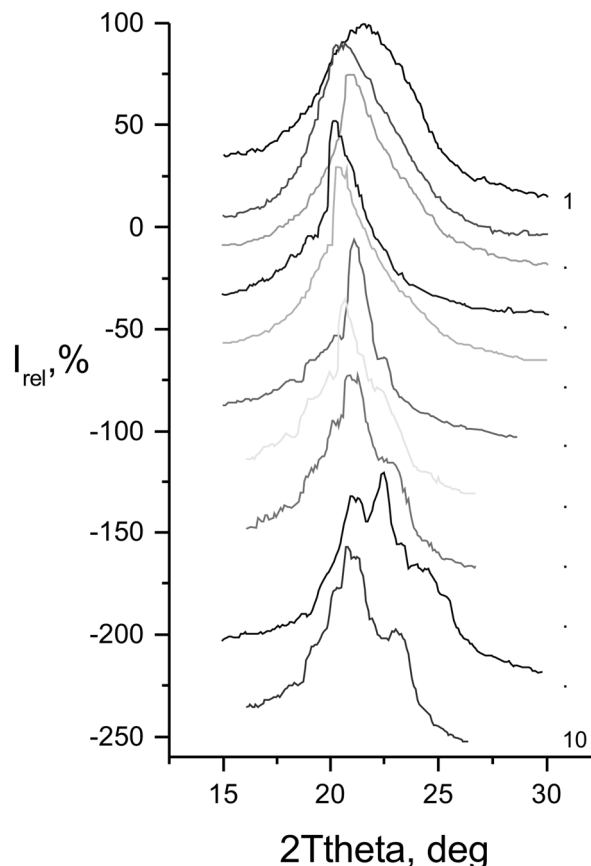
Fig. 1. High temperature X-ray diffractograms of thin PCL folios formed and scanned at different conditions:

1) PCL-2, Tpr = 220 °C, Tcool = 0 °C, Tsc = 20 °C;
2) PCL-2, Tpr = 230 °C, Tcool = 0 °C, Tsc = 20 °C;
3) PCL-2, Tpr = 240 °C, Tcool = 0 °C, Tsc = 20 °C;
4) PCL-1, Tpr = 240 °C, Tcool = 20 °C, Tsc = 180 °C;
5) PCL-2, Tpr = 240 °C, Tcool = 0 °C, Tsc = 20 °C;
6) PCL-2, Tpr = 240 °C, Tcool = 20 °C, Tsc = 20 °C;
7) PCL-2, Tpr = 240 °C, Tcool = 20 °C, Tsc = 200 °C;
8) PCL-2, Tpr = 240 °C, Tcool = 20 °C, Tsc = 180 °C;
9) PCL-2, Tpr = 240 °C, Tcool = 20 °C, Tsc = 240 °C;
10) PCL-2, Tpr = 240 °C, Tcool = 20 °C, Tsc = 140 °C.

Table 1. Crystallographic and morphological information for some of the investigated objects

Object, №	$T_{pr.}$, K	$T_{cry.}$, K	$T_{sc.}$, K	α_c,%	α::γ:δ	Initial morphology	CPI*	ICP**
1. PCL-1	230	−196	120	4	3:8:89	Fine spherolitic Narrow size distribution	0.367	0.5
2. PCL-1	230	200	160	49	2:11:87	Large spherolitic lamellar Wide size distribution	0.704	1
3. PCL-2	240	20	180	41	19:38:43	Middle spherolitic Middle size distribution	0.604	0.846
4. PCL-2	240	200	210	1.5	94:2:4	Large spherolitic Wide size distribution	0.424	0.583

*Crystalline Perfection Index (CPI)
**Index of Chain Packing (ICP)

The large-spherolitic structures with narrow size-distribution possess high (490 MPa) and lower strength characteristics (31–37 MPa). The large-spherolitic structures with very widely size-distribution of the morphological components are characterized with better mechanical features (E_{el} = 430 MPa, σ_{ext} = 42 MPa) in comparison with the structures having whopping morphological components but with narrow size-distribution. The biggest spherolitic and lamellar polycaprolactam structures (Fig. 4a) with a little dispersion show very high modulus (1.6 GPa) only in the little deformations range (ε = 0.01÷0.5%).

It was found, that it is easy to find out forming conditions for every kind of polycaprolactam with purpose to obtain the desired isotropic structure with crystallographic modifications in the crystal phase are connected with the morphologi-

Fig. 2. High temperature X-ray diffractograms of thin PCL folios formed and scanned at different conditions:

1) PCL-2, Tpr = 200 °C, Tcool = 20 °C, Tsc = 20 °C;
2) PCL-2, Tpr = 240 °C, Tcool = 25 °C, Tsc = 25 °C;
3) PCL-2, Tpr = 240 °C, Tcool = 20 °C, Tsc = 100 °C;
4) PCL-2, Tpr = 240 °C, Tcool = 20 °C, Tsc = 140 °C;
5) PCL-2, Tpr = 240 °C, Tcool = 20 °C, Tsc = 50 °C;
6) PCL-1, Tpr = 240 °C, Tcool = 20 °C, Tsc = 20 °C;
7) PCL-2, Tpr = 245 °C, Tcool = 25 °C, Tsc = 30 °C;
8) PCL-2, Tpr = 240 °C, Tcool = 20 °C, Tsc = 20 °C;
9) PCL-1, Tpr = 215 °C, Tcool = 20 °C, Tsc = 210 °C;
10) PCL-1, Tpr = 220 °C, Tcool = –95 °C, Tsc = 20 °C.

quantitative proportions. The specific conditions just strongly increase the content of some of them (Table 1). So by changing of the forming conditions of different structures is possible to affect strongly the properties of the polycaprolactam materials and products. It is possible by reason of the fact that every determining the mechanical behaviour morphology is genetically connected with own crystallographic content. For example the known with the better mechanical behaviour fine spherolitic structure with not so large as a size of the morphological components distribution (Fig. 4d) is described with significant presence of almost every polycaprolactam polymorphous forms and mesophases and approximately equally content of α- and γ-forms (Curve 1, Fig. 2; Fig. 4c; Table 1, № 3).

Fig. 3. High temperature X-ray diffractograms of thin PCL folios formed and scanned at different conditions:

1) PCL-1, Tpr = 240 °C, Tcool = 20 °C, Tsc =230 °C;
2) PCL-1, Tpr = 220 °C, Tcool = –95 °C, Tsc =230 °C;
3) PCL-1, Tpr = 220 °C, Tcool = –95 °C, Tsc =200 °C;
4) PCL-1, Tpr = 220 °C, Tcool = –95 °C, Tsc =160 °C;
5) PCL-1, Tpr = 220 °C, Tcool = –95 °C, Tsc =220 °C;
6) PCL-1, Tpr = 220 °C, Tcool = –95 °C, Tsc =140 °C;
7) PCL-1, Tpr = 220 °C, Tcool = –95 °C, Tsc =100 °C;
8) PCL-1, Tpr = 220 °C, Tcool = –95 °C, Tsc =20 °C;
9) PCL-1, Tpr = 220 °C, Tcool = –95 °C, Tsc =120 °C;
10) PCL-1, Tpr = 230 °C, Tcool = –196 °C, Tsc =20 °C.
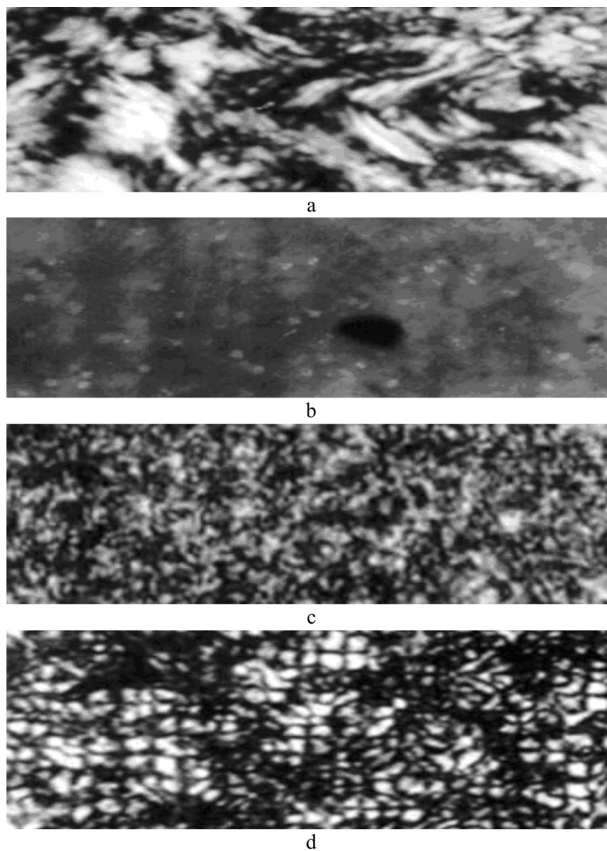
Fig. 4. Polarization microphotos of thin PCL folios Formed by pressing at: a) Tpr =240 °C, Tcool = 0 °C; b) Tpr = 240 °C, Tcool = 20 °C; c) Tpr = 200 °C, Tcool = 20 °C; d) Tpr = 230 °C, Tcool = –196 °C. Micr. magnification 200×.

cal type, and respectively with the mechanical behaviour, too. On the basis of the initial isotropic structure 3 (Table 1, Curve 1, Fig. 2, Fig 4c) subjected to gradually orientated drawing in the temperature interval from 393 K to 433 K were reached $E_{el.}$ = 1.1 GPa and σ_{ext} = 350 MPa at 7.2 multiple extension. Besides, every structure can be easy temperature modified in other desired one using different modes. It is most important the circumstance that at one and the same conditions it can be formed different structures (with different quantitative proportion of crystal forms) or at different conditions – identical structures, depending on the objects preliminary history. As a result of heating, for example of the amorphous δ-phase forming itself γ-modification, turns into the polycaprolactam α-form. Up to 140–160 °C there are running improving processes of the both co-existence modification. At farther temperature raising begins increase of the γ-form contents. Over 180 °C starts the crystal phase melting that is finish around 220–230 °C. The first cooling

forms first of all the α-form that is perfecting up to room temperature.

At variance of the time/temperature modification conditions at different temperatures and different heating and cooling cycles it can be obtain different structures with different perfection (Fig. 1–3, Table 1). Namely the different quantity and quality of the crystallographic modifications determine the suitable density and mode of the segments packing for different structural reorganizations depending on the implement conditions. Their big multiform and complexity should to be investigated concrete in detail for all used in the practice polycaprolactam materials. On Figures 1–3 are present a number of powder diffractograms of thin polycaprolactam folios formed under different conditions. Accepting the β-form [3] as an α- and γ-forms blend, supplemented up to 100% with the δ-phase, we can characterize the roughly presented isotropic structures in first approach by the quantitative proportion of the α- and γ-forms. If accept the basic peaks of the crystal forms appears in the angle intervals 20.1–20.2° ± 0.4–0.8° 2θ for 200_α, 21.6–21.8 ± 0.4–0.8° 2θ for 100_γ and 23.4–23.8⁰ ± 0.4–0.8° 2θ for 002_α, 020_α we can interpret qualitative, or with some approximation, their quantitative content in the experimental powder diffractograms. As it can be seen from the shown diffractograms there are observed one-, two-, three- and multilineal polycaprolactam models in the studied diffraction interval 18–19÷25–26°. It is not easy to interpret similar multiplicity in the light of the polycaprolactam complicated polymorphism, that is strongly dependent on different physics influences. By the realizing of different degrees and modes of overcooling during the initial isotropic structure forming, is possible to obtain various variants of the diffracted beam intensity distribution. It turned out, that the same or similar pictures can be obtained by means of different hating and cooling modes. I.e., from every one obtained initial isotropic structure, using different modes of temperature modification, it is possible to receive another possible from that group isotropic structure. Moreover, with different degree of perfection.

CONCLUSION

Depending on the forming conditions of thin folios by pressing and basically, from the overcooling ratio at the recrystallization processes it is possible to obtain strongly different isotropic structures, that contains all known polycaprolactam polymorphous phases, with differently quantitative proportion and perfection. By different modes of heating and cooling of the initial polycaprolactam

phases it can be received various desired isotropic structures;

There are observed at first sight illogical polymorphous transitions, namely – form more steadily to less steadily crystal modifications, depending on the initial structure, time-temperature pre-history and the transition scheme, as well as from the perfection of the α- and γ-crystal modification at the moment of the polymorphic transition. The present diffractograms, connected with the relevant forming conditions, can be obtained with a good repetition at consecutively heating and cooling cycles in the temperature interval 20–240 °C.

REFERENCES

1. J. Baldrian, Z. Pelzbauer, *J. of Polym. Sci. Part C.*, **38**, 289 (1972).
2. P. F. Dismore, W .O. Statton, *J. of Polym. Sci. Part C.*, **13**, 133 (1966).
3. A. Sh. Goyihman, T. P. Tantstyura, in Visokomol. Soed., **A**, т. **10**, 1968, p. 724.
4. F. Danausso, in: Uspehi Himii, т. **39**, 1970, p. 304.
5. H. Arimoto, M. Ishibashi, M. Hirai, *J. Polym. Sci. A*, **3**, 317 (1965).
6. R. Brill, *Z. Phys. Chem. B* (Leipzig), **53**, 61 (1942).
7. D. R. Holmes, C. Bunn, D. Y. Smith, *J. Polym. Sci.*, **17**, 159 (1955).
8. I. Kinoschita, *Makromol. Chem.*, **33**, 1 (1959).
9. Ch. Ruscher, V. Gröbe, H. Versaumer, *Faserforsch. und Textiltechn.*, **12**, 214 (1961).
10. D. Vogelsang, *J. Polym. Sci. A*, **1**, 1055 (1963).
11. L. G. Wallner, *Makromol. Chem.*, **79**, 279 (1948).

ВЪРХУ ВРЪЗКАТА МЕЖДУ КРИСТАЛНАТА СТРУКТУРА И СВОЙСТВАТА ПРИ ГЪВКАВОВЕРИЖНИТЕ ПОЛИМЕРИ. I. ПОЛИКАПРОЛАКТАМ

Х. Узов[1], Б. Богданов[1], Й. Денев[1], В. Велев[2], Т. Ангелов[3], А. Попов[1]

[1] *Университет „Проф. д-р Асен Златаров" – Бургас, 8010 Бургас, България*
[2] *Университет „Епископ Константин Преславски" – Шумен, 9712 Шумен, България*
[3] *Лукойл Нефтохим Бургас АД, Бургас, България*

(Резюме)

Използвани са високотемпературни рентгенови, микроскопски и деформационно-якостни методи и методики за изследване полиморфизма на поликапролактама. Изучавани са, основно, деформацията и разрушението на елементарните клетки на основните кристални форми на поликапролактама при прехода им в други кристални модификации. Контролирани са, посредством изменение на интензитетното разпределение на праховата рентгенова дифракция, профила и ъгловата девиация на определени дифракционни отражения, отразяващи промените в опаковката на макромолекулните верижни сегменти в кристалната фаза. Резултатите са свързани със съвършенството на кристалната фаза и с количественото съотношение на едновременно съществуващите кристалографски модификации в изследваните обекти при дадените условия.

BULGARIAN CHEMICAL COMMUNICATIONS

Instructions about Preparation of Manuscripts

General remarks: Manuscripts are submitted in English by e-mail or by mail (in duplicate). The text must be typed double-spaced, on A4 format paper using Times New Roman font size 12, normal character spacing. The manuscript should not exceed 15 pages (about 3500 words), including photographs, tables, drawings, formulae, etc. Authors are requested to use margins of 3 cm on all sides. For mail submission hard copies, made by a clearly legible duplication process, are requested. Manuscripts should be subdivided into labelled sections, e.g. **Introduction, Experimental, Results and Discussion**, *etc*.

The title page comprises headline, author's names and affiliations, abstract and key words.

Attention is drawn to the following:

a) **The title** of the manuscript should reflect concisely the purpose and findings of the work. Abbreviations, symbols, chemical formulas, references and footnotes should be avoided. If indispensable, abbreviations and formulas should be given in parentheses immediately after the respective full form.

b) **The author**'s first and middle name initials, and family name in full should be given, followed by the address (or addresses) of the contributing laboratory (laboratories). **The affiliation** of the author(s) should be listed in detail (no abbreviations!). The author to whom correspondence and/or inquiries should be sent should be indicated by asterisk (*).

The abstract should be self-explanatory and intelligible without any references to the text and containing not more than 250 words. It should be followed by key words (not more than six).

References should be numbered sequentially in the order, in which they are cited in the text. The numbers in the text should be enclosed in brackets [2], [5, 6], [9−12], etc., set on the text line. Refer-ences, typed with double spacing, are to be listed in numerical order on a separate sheet. All references are to be given in Latin letters. The names of the authors are given without inversion. Titles of journals must be abbreviated according to Chemical Abstracts and given in italics, the volume is typed in bold, the initial page is given and the year in parentheses. Attention is drawn to the following conventions:

a) The names of all authors of a certain publications should be given. The use of "*et al.*" in the list of references is not acceptable.

b) Only the initials of the first and middle names should be given.

In the manuscripts, the reference to author(s) of cited works should be made without giving initials, e.g. "Bush and Smith [7] pioneered...". If the reference carries the names of three or more authors it should be quoted as "Bush *et al.* [7]", if Bush is the first author, or as "Bush and co-workers [7]", if Bush is the senior author.

Footnotes should be reduced to a minimum. Each footnote should be typed double-spaced at the bottom of the page, on which its subject is first mentioned.

Tables are numbered with Arabic numerals on the left-hand top. Each table should be referred to in the text. Column headings should be as short as possible but they must define units unambiguously. The units are to be separated from the preceding symbols by a comma or brackets.

Note: The following format should be used when figures, equations, *etc*. are referred to the text (followed by the respective numbers): Fig., Eqns., Table, Scheme.

Schemes and figures. Each manuscript (hard copy) should contain or be accompanied by the respective illustrative material as well as by the respective figure captions in a separate file (sheet). As far as presentation of units is concerned, SI units are to be used. However, some non-SI units are also acceptable, such as °C, ml, l, etc.

The author(s) name(s), the title of the manuscript, the number of drawings, photographs, diagrams, etc., should be written in black pencil on the back of the illustrative material (hard copies) in accordance with the list enclosed. Avoid using more than 6 (12 for reviews, respectively) figures in the manuscript. Since most of the illustrative materials are to be presented as 8-cm wide pictures, attention should be paid that all axis titles, numerals, legend(s) and texts are legible.

The authors are asked to submit **the final text** (after the manuscript has been accepted for publication) in electronic form either by e-mail or mail on a 3.5''

diskette (CD) using a PC Word-processor. The main text, list of references, tables and figure captions should be saved in separate files (as *.rtf or *.doc) with clearly identifiable file names. It is essential that the name and version of the word-processing program and the format of the text files is clearly indicated. It is recommended that the pictures are presented in *.tif, *.jpg, *.cdr or *.bmp format, the equations are written using "Equation Editor" and chemical reaction schemes are written using ISIS Draw or ChemDraw programme.

The authors are required to submit the final text with a list three individuals and their e-mail addresses that can be considered by the Editors as potential reviewers. Please, note that the reviewers should be outside the authors' own institution or organization. The Editorial Board of the journal is not obliged to accept these proposals

EXAMPLES FOR PRESENTATION OF REFERENCES

REFERENCES

1. D. S. Newsome, *Catal. Rev.–Sci. Eng.*, **21**, 275 (1980).
2. C.-H. Lin, C.-Y. Hsu, *J. Chem. Soc. Chem. Commun.*, 1479 (1992).
3. R. G. Parr, W. Yang, Density Functional Theory of Atoms and Molecules, Oxford Univ. Press, New York, 1989.
4. V. Ponec, G. C. Bond, Catalysis by Metals and Alloys (Stud. Surf. Sci. Catal., vol. 95), Elsevier, Amsterdam, 1995.
5. G. Kadinov, S. Todorova, A. Palazov, in: New Frontiers in Catalysis (Proc. 10th Int. Congr. Catal., Budapest, 1992), L. Guczi, F. Solymosi, P. Tetenyi (eds.), Akademiai Kiado, Budapest, 1993, Part C, p. 2817.
6. G. L. C. Maire, F. Garin, in: Catalysis. Science and Technology, J. R. Anderson, M. Boudart (eds), vol. 6, Springer-Verlag, Berlin, 1984, p. 161.
7. D. Pocknell, *GB Patent* 2 207 355 (1949).
8. G. Angelov, PhD Thesis, UCTM, Sofia, 2001.
9. JCPDS International Center for Diffraction Data, Power Diffraction File, Swarthmore, PA, 1991.
10. CA **127**, 184 762q (1998).
11. P. Hou, H. Wise, *J. Catal.*, in press.
12. M. Sinev, private communication.
13. http://www.chemweb.com/alchem/articles/1051611477211.html.

CONTENTS

СЪДЪРЖАНИЕ